The Astrophysical Journal Supplement Series, 182:216–309, 2009 May doi:10.1088/0067-0049/182/1/216

STRUCTURE AND FORMATION OF ELLIPTICAL AND SPHEROIDAL GALAXIES*,†,‡

John Kormendy[1,2,3], David B. Fisher[1,2,3], Mark E. Cornell[1], and Ralf Bender[1,2,3]
[1] Department of Astronomy, University of Texas, Austin, TX 78712, USA; kormendy@astro.as.utexas.edu, dbfisher@astro.as.utexas.edu, cornell@astro.as.utexas.edu
[2] Universitäts-Sternwarte, Scheinerstrasse 1, München D-81679, Germany; bender@usm.uni-muenchen.de
[3] Max-Planck-Institut für Extraterrestrische Physik, Giessenbachstrasse, D-85748 Garching-bei-München, Germany; bender@mpe.mpg.de
Received 2006 September 2; accepted 2008 October 7; published 2009 April 30

ABSTRACT

New surface photometry of all known elliptical galaxies in the Virgo cluster is combined with published data to derive composite profiles of brightness, ellipticity, position angle, isophote shape, and color over large radius ranges. These provide enough leverage to show that Sérsic $\log I \propto r^{1/n}$ functions fit the brightness profiles $I(r)$ of nearly all ellipticals remarkably well over large dynamic ranges. Therefore, we can confidently identify departures from these profiles that are diagnostic of galaxy formation. Two kinds of departures are seen at small radii. All 10 of our ellipticals with total absolute magnitudes $M_{VT} \leqslant -21.66$ have cuspy cores—"missing light"—at small radii. Cores are well known and naturally scoured by binary black holes (BHs) formed in dissipationless ("dry") mergers. All 17 ellipticals with $-21.54 \leqslant M_{VT} \leqslant -15.53$ do not have cores. We find a new distinct component in these galaxies: all coreless ellipticals in our sample have extra light at the center above the inward extrapolation of the outer Sérsic profile. In large ellipticals, the excess light is spatially resolved and resembles the central components predicted in numerical simulations of mergers of galaxies that contain gas. In the simulations, the gas dissipates, falls toward the center, undergoes a starburst, and builds a compact stellar component that, as in our observations, is distinct from the Sérsic-function main body of the elliptical. But ellipticals with extra light also contain supermassive BHs. We suggest that the starburst has swamped core scouring by binary BHs. That is, we interpret extra light components as a signature of formation in dissipative ("wet") mergers.

Besides extra light, we find three new aspects to the ("E–E") dichotomy into two types of elliptical galaxies. Core galaxies are known to be slowly rotating, to have relatively anisotropic velocity distributions, and to have boxy isophotes. We show that they have Sérsic indices $n > 4$ uncorrelated with M_{VT}. They also are α-element enhanced, implying short star-formation timescales. And their stellar populations have a variety of ages but mostly are very old. Extra light ellipticals generally rotate rapidly, are more isotropic than core Es, and have disky isophotes. We show that they have $n \simeq 3 \pm 1$ almost uncorrelated with M_{VT} and younger and less α-enhanced stellar populations. These are new clues to galaxy formation. We suggest that extra light ellipticals got their low Sérsic indices by forming in relatively few binary mergers, whereas giant ellipticals have $n > 4$ because they formed in larger numbers of mergers of more galaxies at once plus later heating during hierarchical clustering.

We confirm that core Es contain X-ray-emitting gas whereas extra light Es generally do not. This leads us to suggest why the E–E dichotomy arose. If energy feedback from active galactic nuclei (AGNs) requires a "working surface" of hot gas, then this is present in core galaxies but absent in extra light galaxies. We suggest that AGN energy feedback is a strong function of galaxy mass: it is weak enough in small Es not to prevent merger starbursts but strong enough in giant Es and their progenitors to make dry mergers dry and to protect old stellar populations from late star formation.

Finally, we verify that there is a strong dichotomy between elliptical and spheroidal galaxies. Their properties are consistent with our understanding of their different formation processes: mergers for ellipticals and conversion of late-type galaxies into spheroidals by environmental effects and by energy feedback from supernovae.

In an appendix, we develop machinery to get realistic error estimates for Sérsic parameters even when they are strongly coupled. And we discuss photometric dynamic ranges necessary to get robust results from Sérsic fits.

Key words: galaxies: elliptical and lenticular, cD – galaxies: evolution – galaxies: formation – galaxies: nuclei – galaxies: photometry – galaxies: structure

Online-only material: machine-readable table

1. INTRODUCTION

This is the first of a series of papers in which we study elliptical galaxies by combining new surface photometry with published data to construct composite brightness profiles over large radius ranges. This approach has two strengths. Combining data from many sources allows us to reduce systematic errors arising (e.g.) from imperfect sky subtraction. Having accurate profiles over large radius ranges provides leverage necessary for reliable conclusions about profile shapes and what they tell us about galaxy formation.

* Based on observations made with the NASA/ESA *Hubble Space Telescope*, obtained from the Data Archive at STScI, which is operated by AURA, Inc., under NASA contract NAS 5-26555. These observations are associated with program numbers 5999, 6107, 6357, 6844, 7868, 8686, 9401, and 10558.
† Based on observations obtained at the Canada–France–Hawaii Telescope (CFHT), which is operated by the National Research Council of Canada, the Institut National des Sciences de l'Univers of the Centre National de la Recherche Scientifique of France, and the University of Hawaii.
‡ Based in part on observations obtained with the Hobby–Eberly Telescope (HET), which is a joint project of the University of Texas at Austin, the Pennsylvania State University, Stanford University, Ludwig-Maximilians-Universität München, and Georg-August-Universität Göttingen.

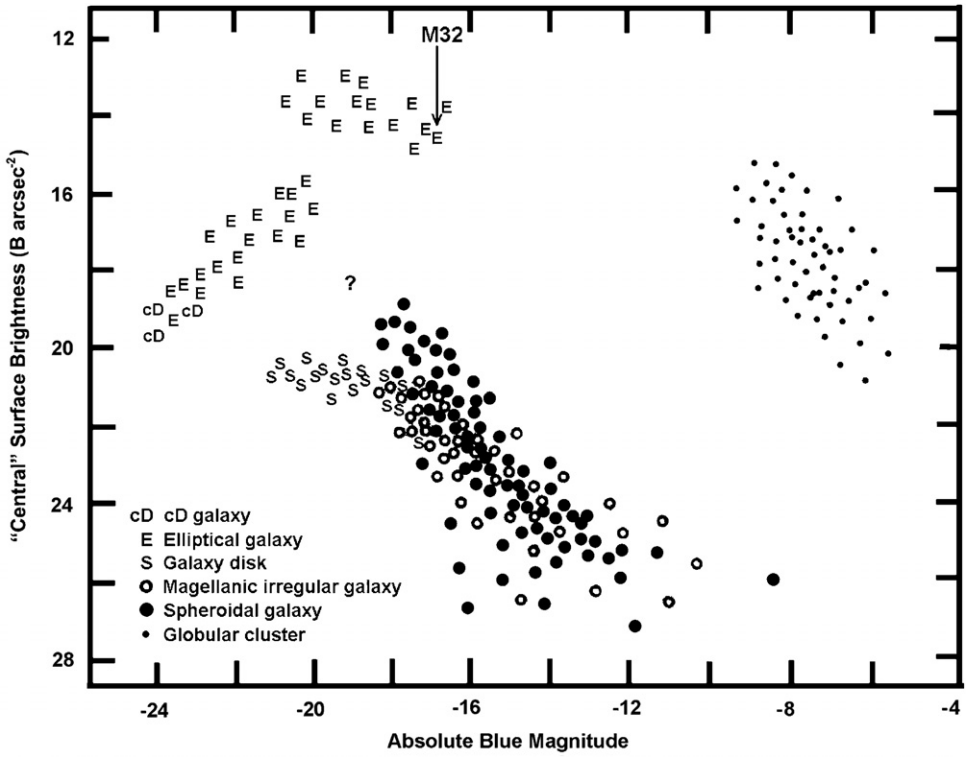

Figure 1. Schematic illustration of the dichotomies discussed in this paper. The figure sketches the correlation between the total absolute magnitude and central surface brightness (for spheroidal and irregular galaxies, galaxy disks, and globular clusters), or the highest surface brightness resolved by the *Hubble Space Telescope* (for elliptical and cD galaxies). Surface brightnesses apply to the main bodies of the galaxies; that is, nuclear star clusters and AGNs are omitted. This figure is adapted from Binggeli (1994) but with the dichotomy between "core" and "power-law" ellipticals—i.e., the discontinuity in E points at $M_B \sim -20.5$—added from Faber et al. (1997). M 32 is one of the lowest-luminosity true ellipticals; the arrow points from the maximum surface brightness observed at a distance of 0.8 Mpc to the lower limit that would be observed if the galaxy were moved to the Virgo cluster. M 32 resembles the faintest ellipticals in Virgo. The distribution of Sph and S+Im galaxies is disjoint from that of ellipticals. Sph and S+Im galaxies have similar global parameters at low luminosities, but the most luminous spheroidals "peel off" of the distribution of late-type galaxies toward higher surface brightness. Spheroidals with $M_B \lesssim -18$ are rare, so the degree to which the Sph sequence approaches the E sequence is poorly known (see the question mark). Note: Binggeli (1994) and some other authors call spheroidal galaxies "dwarf ellipticals" (dEs). We do not do this, because correlations like those in this figure and in Figures 34–38 and 41, as well as the considerations discussed in Sections 2.1 and 8, persuade us that they are not small ellipticals but rather are physically related to late-type galaxies.

What is at stake? We have a formation paradigm. We believe that galaxies grow as part of the hierarchical clustering that makes all structure in the universe. Ellipticals form in violent galaxy mergers that often include gas dissipation and star formation (Toomre 1977; White & Rees 1978; Joseph & Wright 1985; Schweizer 1990; Kauffmann et al. 1993; Steinmetz & Navarro 2002). What questions remain unanswered?

We focus on two well-known dichotomies. We confirm that there is a physical difference between elliptical and spheroidal galaxies. This has been much criticized in recent literature. With photometry over large dynamic ranges, we find that elliptical and spheroidal galaxies have very different parameter correlations. This result is consistent with our understanding of their different formation processes. Spheroidals are not low-luminosity ellipticals but rather are defunct late-type galaxies transformed by internal and environmental processes. A second dichotomy is the main focus of this paper. Why are there two kinds of elliptical galaxies? We suggest an explanation—that the last major mergers that determined the present-day structure either did or did not involve cold gas dissipation and starbursts.

2. TWO DICHOTOMIES

2.1. Elliptical Versus Spheroidal Galaxies

In a pioneering paper, Wirth & Gallagher (1984) suggested that compact dwarf ellipticals like M 32 and not—as previously thought—diffuse "spheroidal" dwarfs like NGC 205 are the extension to low luminosities of the family of giant ellipticals. This was based on the identification of several free-flying M 32 analogs, implying that the compactness of the best known dwarf Es—M 32, NGC 4486B, and NGC 5846A (Faber 1973)—is not due only to tidal pruning by their giant galaxy neighbors. Wirth and Gallagher hypothesized that ellipticals and spheroidals form disjoint families overlapping for $-15 \gtrsim M_B \gtrsim -18$ but differing in mean surface brightness at $M_B = -15$ "by nearly two orders of magnitude." This implied that the luminosity function of true ellipticals is bounded and that M 32 is one of the faintest examples. The latter result was confirmed for the Virgo cluster by Sandage et al. (1985a, 1985b) and by Binggeli et al. (1988).

Kormendy (1985a, 1985b, 1987b) used the high spatial resolution of the Canada–France–Hawaii Telescope (CFHT) to obtain surface photometry of the cores of bulges and elliptical galaxies. He showed in larger galaxy samples that ellipticals form a well-defined sequence in parameter space from cD galaxies to dwarfs like M 32. Lower-luminosity ellipticals are more compact; they have smaller core radii and higher central surface brightnesses. These are projections of the core fundamental plane correlations (Lauer 1985b). Kormendy found a clearcut dichotomy between E and Sph galaxies. Fainter spheroidals have lower central surface brightnesses. In fact, spheroidals have almost the same parameter correlations as spiral-galaxy disks and Magellanic irregular galaxies. These results are most clearly seen in correlations between central

properties, but they are also evident in global properties (Kormendy 1987b; Binggeli & Cameron 1991; Bender et al. 1992, 1993). The brightest spheroidals "peel off" of the correlations for late-type galaxies and approach the E sequence, but they are rare, and the two sequences remain distinct (Kormendy & Bender 1994). The E–Sph dichotomy is illustrated in Figure 1.

Kormendy (1985b, 1987b) concluded that E and Sph galaxies are distinct types of stellar systems with different formation processes. Spheroidals are physically unrelated to ellipticals; Figure 1 hints that they are related to S+Im galaxies. They may be late-type galaxies that lost their gas or processed it all into stars. Relevant evolution processes include supernova-driven energy feedback (Saito 1979a, 1979b; Dekel & Silk 1986; Navarro et al. 1996; Klypin et al. 1999; Veilleux et al. 2005), ram-pressure gas stripping (Lin & Faber 1983; Kormendy 1987b; van Zee et al. 2004a, 2004b; Chung et al. 2007), stochastic starbursts (Gerola et al. 1980), and galaxy harassment (Moore et al. 1996, 1998).

Additional differences diagnostic of formation processes include luminosity functions (Section 8) and rotation properties. Faint Es are rotationally supported, and some Sph galaxies are also (Pedraz et al. 2002; van Zee et al. 2004b), but many are nonrotating and anisotropic (Bender & Nieto 1990; Bender et al. 1991; Held et al. 1992; Geha et al. 2002, 2003, 2006; Thomas et al. 2003, 2006). Possible explanations include galaxy harassment (González-García et al. 2005) and rapid expansion after baryonic blowout (Dekel & Silk 1986; Hensler et al. 2004).

The dichotomy has been challenged by Jerjen & Binggeli (1997), Graham & Guzmán (2003), Graham et al. (2003), Trujillo et al. (2004), and Gavazzi et al. (2005). They argue that Sph parameters are continuous with those of low-luminosity Es, while bright Es deviate from these correlations only because scouring by binary supermassive black holes (BHs) excavates cores. Another argument is that the correlation between brightness profile shape and galaxy luminosity is continuous from Es through Sphs. Recently, Ferrarese et al. (2006a)[4] argue forcefully against the E–Sph dichotomy based on their *Hubble Space Telescope* (*HST*) photometry of Virgo cluster galaxies. For these reasons, and because we need to settle the controversy in order to define our sample of ellipticals, we return to the issue in Section 8. Because the fundamental plane of ellipticals is so thin (Section 3), we will find that E and Sph galaxies are cleanly distinguishable.

At stake are the different formation mechanisms of small ellipticals and big spheroidals. We have good reasons to believe that ellipticals form via galaxy mergers. We also know that many spheroidal satellites of our Galaxy are defunct irregulars. Their intermediate-age stellar populations (see Da Costa 1994 for a review) tell us that dIm galaxies have gradually converted themselves into dSph galaxies via episodic star formation. For example, the Carina dSph is made up of two stellar populations: 15–20% of the stars are 12–15 Gy old, but $> 80\%$ of the stars are 6–8 Gy old. Kormendy & Bender (1994) emphasize that there must have been gas ~ 7 Gyr ago to make these stars. Gas-rich, star-forming dwarfs are Magellanic irregulars. We know less about the formation of spheroidals in Virgo, although additional signs that Sph galaxies are related to late-type galaxies are observations of spiral structure (Jerjen et al. 2000; Lisker & Fuchs 2009) and star formation (Lisker et al. 2006). It is natural to expect that galaxy harassment would convert larger late-type galaxies into Sphs in Virgo than in the Local Group. Moreover, one effect is to concentrate gas toward the center before star formation happens (Moore et al. 1996, 1998). This provides a natural explanation for why the Sph sequence peels off the S+Im sequence at high galaxy luminosities (Figure 1).

If E and Sph galaxies formed a continuous family, it would be surprising to conclude that different formation processes dominated at high and low luminosities, with major mergers making ellipticals but not spheroidals (Section 13, Tremaine 1981).

2.2. *The Dichotomy into Two Kinds of Elliptical Galaxies*

There are two kinds of elliptical galaxies: (1) normal- and low-luminosity ellipticals rotate rapidly; they are relatively isotropic, oblate-spheroidal, and flattened (E3); they are coreless, and they have disky-distorted isophotes. Most bulges of disk galaxies are like low-luminosity ellipticals. In contrast, (2) giant ellipticals are essentially nonrotating; they are anisotropic and triaxial; they are less flattened (E1.5); they have cuspy cores, and they have boxy-distorted isophotes. These results are established in Davies et al. (1983), Kormendy & Illingworth (1982), Bender (1987, 1988a), Bender et al. (1987, 1989), Nieto & Bender (1989), Nieto et al. (1991), Kormendy et al. (1994, 1996a), Lauer et al. (1995, 2005, 2007b), Kormendy & Bender (1996), Tremblay & Merritt (1996), Gebhardt et al. (1996), Faber et al. (1997), Rest et al. (2001), Ravindranath et al. (2001), Emsellem et al. (2007), and Cappellari et al. (2007). The differences between the two kinds of ellipticals are fundamental. They motivated Kormendy & Bender (1996) to suggest that the Hubble sequence be revised (Figure 2) so that rotation increases in importance and random motions decrease in importance along the Hubble sequence from boxy Es through Scs. The "E–E dichotomy" is the main subject of this paper.

3. REGULARITY IN THE STRUCTURE OF ELLIPTICAL GALAXIES

Why do we think that surface brightness profiles can tell us about the formation of elliptical galaxies?

Our picture of hierarchical clustering implies that different galaxies are the products of different merger histories in which different progenitor morphologies and encounter geometries produced a variety of results. It is remarkable that the remnants of such varied mergers show regularity that we can interpret. In fact, ellipticals show surprising regularity in structure. Interpreting these regularities—and departures from them—has been a profitable way to study galaxy formation.

A well-known example is the "fundamental plane" of elliptical galaxies. Their half-light radii r_e, effective surface brightnesses $\mu(r_e)$, and velocity dispersions σ interior to r_e lie in a tilted plane in parameter space (Djorgovski & Davis 1987; Faber et al. 1987; Dressler et al. 1987; Djorgovski et al. 1988; Djorgovski 1992; Bender et al. 1992, 1993), $r_e \propto \sigma^{1.4\pm0.15} I_e^{-0.9\pm0.1}$, whose scatter is similar to the parameter measurement errors (Saglia et al. 1993; Jørgensen et al. 1996). This is a consequence of the virial theorem and the fact that ellipticals are nearly homologous over a wide range in luminosities L. Slow variations with L in density profiles, velocity structure, and mass-to-light ratio $M/L \propto L^{0.2}$ combine to give the fundamental plane slopes

[4] Ferrarese et al. (2006a) argue against both dichotomies discussed in this paper. We discuss our procedures and analysis in the main text and save a comparison of our differences with Ferrarese et al. (2006a) for Appendix B. Our paper and theirs are independent looks at the same science using similar analysis techniques.

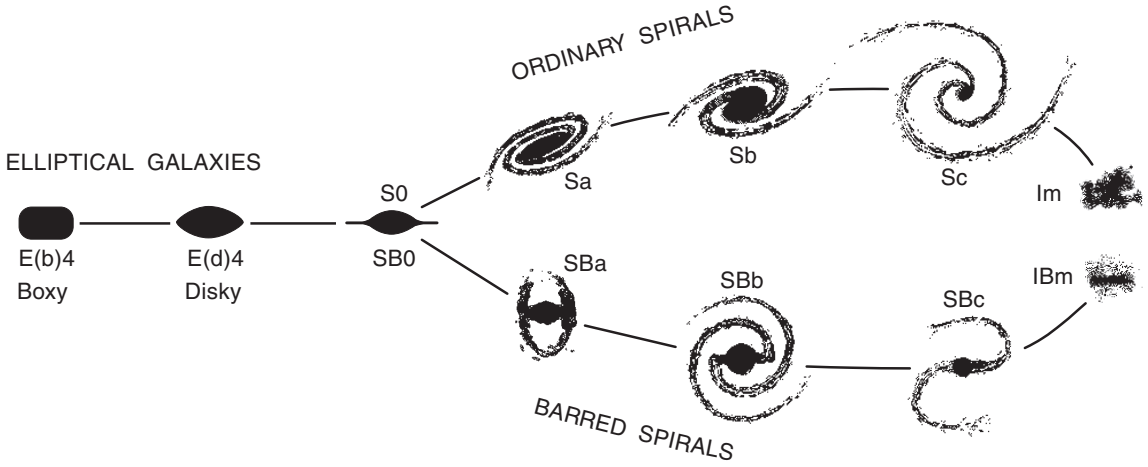

Figure 2. Revision of Hubble's (1936) morphological classification scheme proposed by Kormendy & Bender (1996). Here ellipticals are not classified by apparent flattening, which in large part encodes our viewing geometry. Rather, they are classified according to whether they show boxy or disky isophote distortions. This is also the dichotomy between ellipticals that do and do not have cuspy cores (Figure 1); it is the one summarized in Section 2.2. Boxy-core galaxies tend to rotate less and to be more dominated by velocity dispersion anisotropies than are disky-coreless galaxies. Therefore, the revised classification orders galaxies along the Hubble sequence by physically fundamental properties, i.e., by the increasing importance from left to right of ordered rotation as compared with random internal velocities.

that are slightly different from the virial theorem prediction, $r_e \propto \sigma^2 I_e^{-1}$, for exactly homologous galaxies.

The part of the near-homology that concerns us here is the slow variation of profile shape with L. Kormendy (1980), Michard (1985), and Schombert (1986, 1987) found that the de Vaucouleurs (1948) $r^{1/4}$ law fits ellipticals best at $M_B \simeq -20.2$ ($H_0 = 70$ km s^{-1} Mpc^{-1}; Komatsu et al. 2009). More (less) luminous ellipticals have brighter (fainter) outer profiles than the extrapolation of the best-fitting $r^{1/4}$ law. Schombert (1986, 1987) provides a nonparametric illustration by deriving average profiles for ellipticals binned by luminosity. *Nothing guarantees that any simple parameterization of profile variations describes the results of mergers and dissipative starbursts.* However, Nature proves to be extraordinarily kind. *The theme of this paper is that Sérsic (1968)* $\log I(r) \propto r^{1/n}$ *functions fit most ellipticals remarkably well. The result is that local departures from the fits and correlations involving the fit parameters provide new insights into galaxy formation.*

Caon et al. (1993) were the first to prove that $r^{1/n}$ functions fit ellipticals better than do $r^{1/4}$ laws. This is not a surprise—$r^{1/n}$ laws have three parameters while $r^{1/4}$ laws have two. Kormendy (1980, 1982) and Kormendy & Djorgovski (1989) emphasized that elliptical galaxy profiles are close enough to $I \propto r^{-2}$ power laws—which have only one parameter—so that accurate photometry over a large radius range is required to derive even two parameters. Three-parameter fits can involve so much parameter coupling that the results are useless. This was true in the era of photographic photometry (see Figure 12 in Kormendy 1982 for an example). It is no longer true, because CCDs provide more accurate photometry and because the *HST* has greatly increased the dynamic range by providing point-spread function (PSF)-corrected photometry inward to radii $r \simeq 0\farcs1$. Improved data now support three-parameter fits, and Caon and collaborators argue convincingly that the Sérsic index n has physical meaning. For example, n correlates with the effective radius r_e and total absolute magnitude M_B of the elliptical or bulge. The usefulness of Sérsic functions and the importance of the above correlations have been confirmed by D'Onofrio et al. (1994), Graham et al. (1996), Graham & Colless (1997), Graham (2001), Trujillo et al. (2001, 2002), Ferrarese et al. (2006a), and others.

This rapid progress slowed down as the easy results enabled by CCDs were derived. Now, however, an important iteration in quality is within reach. The shortcoming of most CCD photometry is limited field of view. Many published profiles do not reach large radii and may be affected by sky subtraction errors. However, images are now available from a variety of wide-field, mosaic detectors and surveys such as the Two Micron All Sky Survey (2MASS; Jarrett et al. 2003; Skrutskie et al. 2006) and the Sloan Digital Sky Survey (SDSS; Stoughton et al. 2002; Abazajian et al. 2003, 2004, 2005).

Our aim is to exploit the significant improvements in the dynamic range of brightness profiles that can be gained by combining data from a variety of telescopes. Intercomparison of these data allows us to reduce systematic errors. Confirming previous work, we find that Sérsic functions fit many ellipticals over large radius ranges. As a result, we can derive more accurate values of r_e, μ_e, and Sérsic index n. This allows us to improve the derivation of parameter correlations. Most important, the robust detection of Sérsic profiles over large radius ranges allows us reliably to see departures from these profiles that are diagnostic of galaxy formation mechanisms.

One purpose of this paper is to expand on a result summarized in Section 4.2. We enlarge the sample on which it is based by measuring all known elliptical galaxies in the Virgo cluster as listed in Binggeli et al. (1985) and as confirmed by radial velocities. The sample and the new photometry are discussed in Sections 5 and 6. Tables of composite profiles are included. Section 7 illustrates the composite profiles of all the galaxies. Sections 8–13 discuss our conclusions.

4. CUSPY CORES AND "EXTRA LIGHT" AT THE CENTERS OF ELLIPTICAL GALAXIES

4.1. A Digression on Analytic Fitting Functions

"Cuspy cores" are defined to be the region interior to the "break radius" r_b where $I(r)$ breaks from a steep outer power law, $I \propto r^{-\beta}$, to a shallow inner cusp, $I \propto r^{-\gamma}$. This region of the profile can conveniently be parameterized as

$$I(r) = I_b 2^{\frac{\beta-\gamma}{\alpha}} \left(\frac{r}{r_b}\right)^{-\gamma} \left[1 + \left(\frac{r}{r_b}\right)^{\alpha}\right]^{\frac{\gamma-\beta}{\alpha}}, \qquad (1)$$

where I_b is the surface brightness at r_b and α measures the sharpness of the break (Kormendy et al. 1994; Lauer et al. 1995; Byun et al. 1996; see Lauer et al. 1992b; Ferrarese et al. 1994 for earlier, simpler versions).

Since Equation (1) is asymptotically a power law at large r, it does not fit Sérsic profiles, nor was it devised to do so. Rather, it was devised to fit central profiles in the vicinity of the break radius in order to derive core parameters. This was done in Byun et al. (1996) and in Lauer et al. (2005, 2007b) and used to study core parameter correlations in Faber et al. (1997) and Lauer et al. (2007a). Graham et al. (2003, 2004) and Trujillo et al. (2004) advocate replacing Equation (1) with an analytic "core-Sérsic function" that becomes Sérsic at large r. This is a plausible idea, but making it uncovers a problem with any attempt to fit cores and outer profiles with a single analytic function. Analytic functions are stiff. Their core and outer parameters are coupled in a way that depends on the chosen fitting function. This is why Trujillo et al. (2004) get slightly different parameter values than those derived using Equation (1). Core parameters inevitably depend on the parameterization; Lauer et al. (2007b) provide further discussion. The solution is to avoid fitting functions that are complicated enough to result in large, coupled errors in the derived parameters.

Therefore, we do not use one fitting function to parameterize all of a profile whose form is nowhere analytic and whose underlying distribution function is controlled by different physics at different radii. Rather, we fit the profile piecewise. That is, we fit the outer profile using a Sérsic function over the radius range where it fits well (Section 7.2; Appendix A). Departures from these fits are measured nonparametrically.

4.2. "Extra Light" at the Centers of Elliptical Galaxies

One new result of this paper is confirmation in a larger sample of galaxies of an effect seen by Kormendy (1999). It is illustrated in Figure 3. NGC 4621, NGC 3377, and M 32 are normal ellipticals with absolute magnitudes $M_V = -21.54$, -20.18, and -16.69, respectively. Their main bodies are well fitted by Sérsic functions. At small radii, the behavior of the profile is opposite to that in a core galaxy—there is extra light compared to the inward extrapolation of the outer Sérsic fit.

Kormendy (1999) pointed out that the extra light is similar to predictions by Mihos & Hernquist (1994) of high-density centers produced by dissipative mergers (Figure 4). In their simulations, the excess light is a result of rapid inward transport of gas during the merger followed by a starburst. The transition from the starburst center to the outer profile occurs at $\sim 4\%$ of the effective radius r_e. The radii of the observed breaks from the $r^{1/n}$ laws bracket $0.04r_e$ in Figure 3. The observed transitions are less sharp than those in the simulations, but the numerical prescriptions used for star formation and energy feedback were approximate. Interestingly, the observed departures from Sérsic function fits are larger in smaller galaxies; observations imply more dissipation at lower galaxy luminosities (e.g., Kormendy 1989). It was too early to be sure of an interpretation, but Kormendy (1999) noted that the observations are suggestive of dissipative starbursts. Further observations along these lines are discussed in Rothberg & Joseph (2004, 2006) and in Côté et al. (2006, 2007; note that these papers include disk-dominated S0s which are not primarily merger remnants).

We will reach the same conclusions.

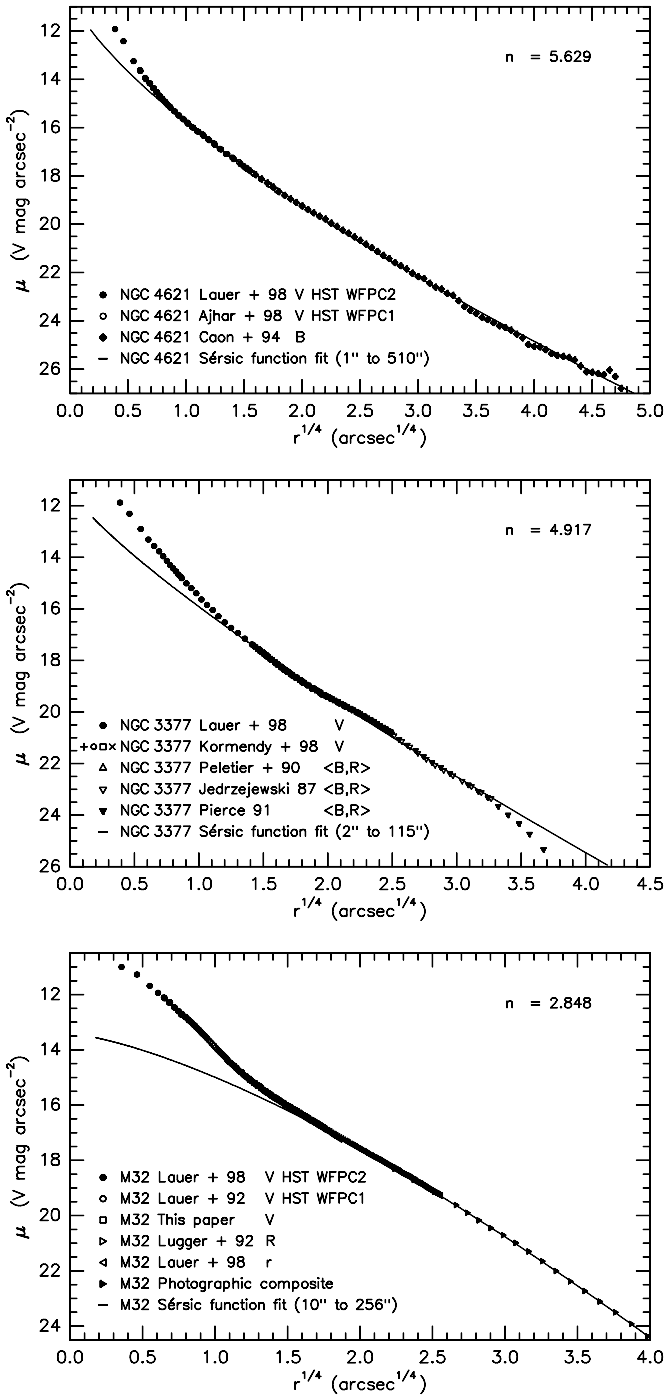

Figure 3. Composite major-axis brightness profiles of coreless elliptical galaxies fitted with Sérsic functions (solid curves) with index n (see the key). This figure is from Kormendy (1999).

5. GALAXY SAMPLE

Table 1 lists our sample ordered by total absolute magnitude M_{VT} (Column 11) determined from our photometry. The Virgo cluster has depth along the line of sight, so we use individual galaxy distances from Mei et al. (2007) or from Tonry et al. (2001). Galactic extinctions are from Schlegel et al. (1998).

We wish to study all elliptical galaxies in the Virgo cluster. Distinguishing elliptical (E), S0, and spheroidal (Sph) galaxies is nontrivial but important, because different types of galaxies are likely to have different formation processes. To construct a

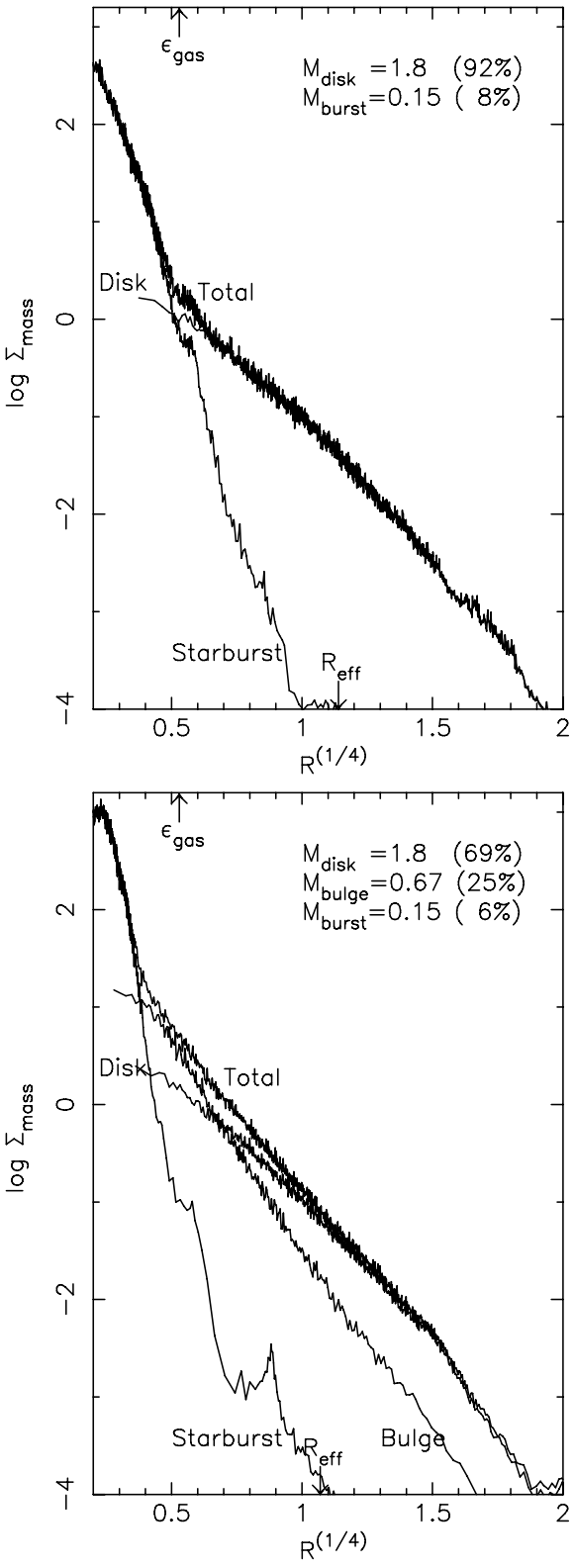

Figure 4. Luminous mass density profiles of merger remnants for progenitor galaxies consisting of (top) a disk and a dark halo and (bottom) a disk, a bulge, and a dark halo. These results are based on *N*-body simulations with gas. During the merger, the gas falls to the center and produces the "Starburst" density distribution. Note that the outer profiles are better described by Sérsic functions than by $r^{1/4}$ laws. This is Figure 1 from Mihos & Hernquist (1994).

pure sample of ellipticals, we erred on the side of caution and included galaxies with uncertain classifications (e.g., E/S0). We then used the photometry to resolve problem cases. How we distinguish E and Sph galaxies is discussed in Section 8. How we distinguish E and S0 galaxies is discussed here.

5.1. The Distinction Between Ellipticals and S0 Galaxies

If we want our classification to distill clean physics, we should not mix disks with ellipticals. When both are present, as in an S0 galaxy, we need to make a photometric decomposition and analyze the bulge and disk separately. However, the distinction between Es, which by definition are supposed not to contain disks, and S0s, which by definition do contain disks, has been blurred in recent years by the recognition of "disky ellipticals" whose isophotes are distorted from ellipses by $\sim$ 1–2% as they would be if they contained embedded disks (Carter 1978; Lauer 1985c; Bender & Möllenhoff 1987; Bender et al. 1987, 1988, 1989; Franx et al. 1989a; Peletier et al. 1990). Photometric decompositions imply that the difference between an underlying, exactly ellipsoidal galaxy and the observed, disky-distorted object is typically $\sim$ 10% and sometimes as much as 40% (Scorza & Bender 1995). This does not prove that the disky distortions formed like the disks of spiral galaxies. Disky distortions could instead be a natural consequence of gas-rich mergers, if stars rain out of the gas distribution while dissipation causes it to flatten. In simulations, even dissipationless mergers can make disky ellipticals (Naab et al. 1999; Burkert & Naab 2003; Naab & Burkert 2003). On the other hand, the above "disk fractions" are well within the range of disk contributions in S0s (Simien & de Vaucouleurs 1986). Also, bulge-dominated S0s are easily recognized when seen edge-on (e.g., NGC 3115) but not when seen face-on. Then their disks perturb the bulge profile by only small amounts at intermediate radii (Hamabe 1982). Capaccioli et al. (1991) even suggest that NGC 3379, often called a prototypical elliptical, is a bulge-dominated S0. In our sample, NGC 4636 may be such a galaxy (Figure 55).

Distinguishing E and S0 galaxies is therefore tricky. We are saved by our result (Section 9.1; Appendix A) that ellipticals are accurately described by Sérsic functions except near their centers; only a few galaxies with extra halos compared to the outward extrapolation of inner Sérsic fits require interpretation. To recognize S0s, we use the ellipticity and isophote distortion profiles as discussed in Section 7. Disks should be more flattened than bulges, and they should—except when nearly face-on—be disky by $\gtrsim$ a few percent. And S0 disks live at large radii; *nuclear* disks do not disqualify a galaxy from being an elliptical.

Fortunately, distinguishing ellipticals from bulge-dominated S0s is not critical to our results, because the Hubble sequence is continuous between them (Kormendy & Djorgovski 1989; Kormendy & Bender 1996). The bulge-dominated S0s that are most easily confused with ellipticals behave like ellipticals of similar luminosity. They reinforce our conclusions.

5.2. Construction of Galaxy Sample

Our sample was constructed as follows. We started with the 30 galaxies that Binggeli et al. (1985) classify as E and list as Virgo cluster members. We added M 32 analogs from Binggeli's Table XIII after eliminating S0, Sph, and background galaxies, provided that *HST* photometry is available. We added S0s with $M_V \lesssim -21.5$ and checked to see which ones are ellipticals using our photometry. The tendency to classify giant Es as S0s results mainly from the M_V–n correlation. Giant ellipticals have Sérsic $n > 4$, i.e., shallow brightness profiles at large radii. Absent quantitative photometry, these halos look similar to S0

Table 1
Virgo Cluster Galaxy Sample

											Parameters from Major-Axis Sérsic Fit				Parameters from 2D Profile Integration			
Galaxy	VCC	Type RC3	Type VCC	Type Adopted	D (Mpc)	V	ΔV	V_T	A_V	M_{VT}	n	μ_{eV} (arcsec^{-2})	r_e (arcsec)	$\log(r_e)$ (kpc)	μ_{eV} (arcsec^{-2})	r_e (arcsec)	$\log(r_e)$ (kpc)	Percentage Extra Light
(1)	(2)	(3)	(4)	(5)	(6)	(7)	(8)	(9)	(10)	(11)	(12)	(13)	(14)	(15)	(16)	(17)	(18)	(19)
NGC 4472	VCC 1226	E2	E2/S0$_1$(2)	E2	17.14	8.12	−0.12	8.00	0.072	−23.24	$5.99^{+0.31}_{-0.29}$	$23.37^{+0.17}_{-0.14}$	$269.29^{+23.6}_{-18.6}$	$1.350^{+0.037}_{-0.031}$	22.73 ± 0.18	194.44 ± 17.0	1.208 ± 0.040	-0.50 ± 0.05
NGC 4486	VCC 1316	E$^+$0-1pec	E0	E1	17.22	8.30	−0.00	8.30	0.072	−22.95	$11.84^{+1.79}_{-1.19}$	$25.71^{+0.54}_{-0.32}$	703.91^{+203}_{-102}	$1.769^{+0.110}_{-0.068}$	23.16 ± 0.78	194.41 ± 63.3	1.210 ± 0.171	-4.2 ± 1.0
NGC 4649	VCC 1978	E2	S0$_1$(2)	E2	17.30	8.66	−0.13	8.53	0.086	−22.75	$5.36^{+0.38}_{-0.32}$	$22.41^{+0.18}_{-0.15}$	$132.05^{+11.6}_{-9.3}$	$1.044^{+0.037}_{-0.032}$	22.34 ± 0.20	128.16 ± 11.1	1.031 ± 0.039	-1.05 ± 0.07
NGC 4406	VCC 0881	E3	S0$_1$(3)/E3	E3	16.83	8.56	−0.03	8.53	0.096	−22.69	$10.27^{+0.49}_{-0.35}$	$27.63^{+0.41}_{-0.30}$	2341.62^{+625}_{-357}	$2.281^{+0.103}_{-0.072}$	22.85 ± 0.10	202.69 ± 14.6	1.218 ± 0.032	-0.17 ± 0.01
NGC 4365	VCC 0731	E3	E3	E3	23.33	9.46	−0.19	9.27	0.068	−22.63	$7.11^{+0.40}_{-0.35}$	$23.80^{+0.16}_{-0.15}$	$184.22^{+14.4}_{-12.2}$	$1.319^{+0.033}_{-0.030}$	23.04 ± 0.21	128.06 ± 11.3	1.161 ± 0.040	-0.63 ± 0.07
NGC 4374	VCC 0763	E1	E1	E1	18.45	9.03	−0.20	8.83	0.131	−22.63	$7.98^{+0.71}_{-0.56}$	$23.09^{+0.27}_{-0.20}$	$142.08^{+19.3}_{-13.3}$	$1.104^{+0.055}_{-0.043}$	22.69 ± 0.23	113.71 ± 10.8	1.007 ± 0.043	-1.52 ± 0.05
NGC 4261	VCC 0345	E2$^+$	E2	E2	31.6	10.22	−0.26	9.96	0.059	−22.60	$7.49^{+0.82}_{-0.60}$	$23.26^{+0.31}_{-0.23}$	$99.97^{+15.8}_{-10.5}$	$1.185^{+0.064}_{-0.048}$	22.59 ± 0.16	72.96 ± 6.4	1.048 ± 0.040	-1.84 ± 0.05
NGC 4382	VCC 0798	SA0$^+$pec	S0$_1$(3)pec	E2	17.86	8.93	−0.11	8.82	0.101	−22.54	$6.12^{+0.31}_{-0.27}$	$22.80^{+0.17}_{-0.16}$	$128.89^{+10.2}_{-8.8}$	$1.048^{+0.033}_{-0.031}$	21.65 ± 0.12	102.28 ± 6.3	0.947 ± 0.028	-0.18 ± 0.06
NGC 4636	VCC 1939	E0$^+$	E1/S0$_1$(1)	E3	14.7	8.97	−0.14	8.83	0.090	−22.10	$5.65^{+0.48}_{-0.38}$	$24.42^{+0.35}_{-0.27}$	$336.03^{+65.7}_{-43.8}$	$1.379^{+0.078}_{-0.061}$	23.14 ± 0.16	183.35 ± 14.6	1.116 ± 0.036	-0.22 ± 0.04
NGC 4552	VCC 1632	E0$^+$	S0$_1$(0)	E1	15.85	9.67	−0.20	9.47	0.133	−21.66	$9.22^{+1.13}_{-0.83}$	$23.72^{+0.44}_{-0.34}$	$138.60^{+33.4}_{-21.5}$	$1.027^{+0.094}_{-0.073}$	23.04 ± 0.24	94.96 ± 11.3	0.863 ± 0.055	-1.23 ± 0.09
NGC 4621	VCC 1903	E5	E4	E4	14.93	9.57	−0.13	9.44	0.107	−21.54	$5.36^{+0.30}_{-0.28}$	$22.03^{+0.14}_{-0.13}$	$74.63^{+4.62}_{-3.96}$	$0.733^{+0.026}_{-0.024}$	22.54 ± 0.21	95.84 ± 8.07	0.841 ± 0.038	0.27 ± 0.06
NGC 4459	VCC 1154	SA0$^+$	S0$_3$(2)	E2	16.07	10.30	−0.06	10.24	0.149	−20.94	$3.17^{+0.34}_{-0.27}$	$21.45^{+0.10}_{-0.10}$	$42.97^{+1.90}_{-1.90}$	$0.525^{+0.019}_{-0.020}$	21.41 ± 0.07	41.57 ± 1.85	0.510 ± 0.020	4.30 ± 0.56
NGC 4473	VCC 1231	E5	E5	E4	15.28	10.19	−0.09	10.10	0.092	−20.91	$4.00^{+0.18}_{-0.16}$	$21.63^{+0.20}_{-0.19}$	$51.79^{+4.15}_{-3.56}$	$0.584^{+0.034}_{-0.031}$	21.46 ± 0.10	47.71 ± 2.54	0.548 ± 0.024	8.8 ± 1.0
NGC 4478	VCC 1279	E2	E2	E2	16.98	11.46	−0.01	11.45	0.080	−19.78	$2.07^{+0.08}_{-0.07}$	$19.95^{+0.05}_{-0.05}$	$13.43^{+0.28}_{-0.28}$	$0.044^{+0.009}_{-0.009}$	19.85 ± 0.07	13.28 ± 0.43	0.039 ± 0.014	1.12 ± 0.15
NGC 4434	VCC 1025	E	E0/S0$_1$(0)	E0	22.39	12.28	−0.02	12.26	0.072	−19.56	$3.34^{+0.20}_{-0.18}$	$20.65^{+0.10}_{-0.09}$	$10.80^{+0.41}_{-0.41}$	$0.069^{+0.016}_{-0.017}$	20.80 ± 0.09	11.33 ± 0.48	0.090 ± 0.019	0.82 ± 0.20
NGC 4387	VCC 0828	E	E5	E4	17.95	12.27	−0.02	12.25	0.107	−19.13	$2.03^{+0.06}_{-0.06}$	$20.59^{+0.04}_{-0.04}$	$14.37^{+0.22}_{-0.22}$	$0.097^{+0.007}_{-0.007}$	20.56 ± 0.06	14.33 ± 0.52	0.096 ± 0.016	0.93 ± 0.11
NGC 4551	VCC 1630	E:	E2	E3	16.14	12.09	−0.01	12.08	0.125	−19.09	$1.98^{+0.06}_{-0.06}$	$20.75^{+0.04}_{-0.04}$	$15.51^{+0.29}_{-0.29}$	$0.084^{+0.008}_{-0.008}$	20.76 ± 0.07	15.79 ± 0.54	0.092 ± 0.015	2.15 ± 0.10
NGC 4458	VCC 1146	E0$^+$	E1	E1	16.37	12.26	−0.07	12.19	0.077	−18.96	$2.53^{+0.14}_{-0.13}$	$21.66^{+0.05}_{-0.05}$	$18.57^{+0.43}_{-0.43}$	$0.168^{+0.010}_{-0.010}$	21.57 ± 0.07	17.96 ± 0.69	0.154 ± 0.017	6.75 ± 0.35
NGC 4486A	VCC 1327	(E2)	E2	E2	18.28	12.55	−0.02	12.53	0.077	−18.86	$2.04^{+0.15}_{-0.13}$	$19.54^{+0.10}_{-0.12}$	$6.99^{+0.36}_{-0.36}$	$-0.208^{+0.022}_{-0.023}$	19.63 ± 0.06	7.44 ± 0.26	-0.181 ± 0.015	2.82 ± 0.32
NGC 4515	VCC 1475	S0$^-$:	E2	E2	16.60	12.68	−0.03	12.65	0.101	−18.56	$3.36^{+1.42}_{-0.67}$	$21.64^{+0.50}_{-0.89}$	$14.19^{+3.23}_{-4.41}$	$0.058^{+0.089}_{-0.161}$	20.82 ± 0.10	10.10 ± 0.40	-0.090 ± 0.018	12.6 ± 1.1
NGC 4464	VCC 1178	(E3)	E3	E3	15.85	12.67	−0.01	12.66	0.071	−18.40	$2.45^{+0.08}_{-0.08}$	$19.86^{+0.06}_{-0.06}$	$7.28^{+0.19}_{-0.19}$	$-0.252^{+0.011}_{-0.011}$	19.92 ± 0.08	7.55 ± 0.28	-0.236 ± 0.016	5.38 ± 0.21
NGC 4486B	VCC 1297	cE0	E1	E1	16.29	13.43	−0.01	13.42	0.069	−17.71	$2.20^{+0.13}_{-0.11}$	$18.40^{+0.11}_{-0.11}$	$2.51^{+0.12}_{-0.12}$	$-0.704^{+0.020}_{-0.021}$	18.45 ± 0.07	2.54 ± 0.09	-0.698 ± 0.016	5.77 ± 0.43
IC 3653	VCC 1871	E?	E3	E1	15.49	13.72	−0.01	13.71	0.101	−17.34	$1.73^{+0.09}_{-0.09}$	$20.73^{+0.06}_{-0.06}$	$6.74^{+0.17}_{-0.17}$	$-0.296^{+0.011}_{-0.011}$	20.77 ± 0.05	7.13 ± 0.21	-0.271 ± 0.013	1.56 ± 0.02
NGC 4467	VCC 1192	E2	E3	E2	16.53	14.29	−0.05	14.24	0.074	−16.92	$1.91^{+0.05}_{-0.05}$	$20.51^{+0.03}_{-0.03}$	$4.89^{+0.06}_{-0.06}$	$-0.406^{+0.005}_{-0.005}$	20.91 ± 0.07	5.86 ± 0.18	-0.328 ± 0.013	2.33 ± 0.07
IC 0798	VCC 1440	(E0)	E0	E0	16.00	14.35	−0.09	14.26	0.088	−16.85	$3.37^{+0.19}_{-0.16}$	$22.14^{+0.12}_{-0.10}$	$8.38^{+0.45}_{-0.38}$	$-0.187^{+0.023}_{-0.020}$	22.08 ± 0.09	7.92 ± 0.35	-0.212 ± 0.020	0.91 ± 0.01
...	VCC 1627	(E0)	E0	E0	15.63	14.67	−0.01	14.66	0.127	−16.44	$2.13^{+0.08}_{-0.08}$	$20.51^{+0.04}_{-0.04}$	$3.71^{+0.06}_{-0.06}$	$-0.552^{+0.007}_{-0.007}$	20.57 ± 0.07	3.86 ± 0.13	-0.534 ± 0.015	2.19 ± 0.05
...	VCC 1199	(E2)	E2	E1	16.53	15.64	−0.01	15.63	0.071	−15.53	$1.90^{+0.05}_{-0.05}$	$20.14^{+0.04}_{-0.04}$	$2.09^{+0.04}_{-0.04}$	$-0.775^{+0.007}_{-0.008}$	20.28 ± 0.06	2.22 ± 0.07	-0.749 ± 0.014	5.10 ± 0.30
NGC 4482	VCC 1261	E	d:E5,N	Sph,N	18.11	13.06	−0.02	13.04	0.092	−18.35	$1.40^{+0.06}_{-0.06}$	$22.33^{+0.04}_{-0.04}$	$24.75^{+0.43}_{-0.43}$	$0.337^{+0.008}_{-0.008}$	22.22 ± 0.06	23.22 ± 0.73	0.309 ± 0.014	4.0 ± 0.5
IC 3381	VCC 1087	E$^+$:	dE3, N	Sph, N	16.67	13.61	−0.13	13.48	0.085	−17.71	$1.54^{+0.07}_{-0.07}$	$22.73^{+0.08}_{-0.07}$	$21.88^{+0.78}_{-0.72}$	$0.248^{+0.015}_{-0.014}$	22.82 ± 0.05	22.66 ± 0.72	0.263 ± 0.014	0.27 ± 0.01
IC 3442	VCC 1355	E0:	dE2, N	Sph, N	16.90	13.94	−0.14	13.80	0.111	−17.45	$1.45^{+0.05}_{-0.05}$	$23.97^{+0.07}_{-0.06}$	$30.81^{+0.91}_{-0.84}$	$0.402^{+0.013}_{-0.012}$	24.21 ± 0.06	33.93 ± 0.92	0.444 ± 0.012	0.17 ± 0.01

Table 1
(Continued)

Galaxy	VCC	Type RC3	Type VCC	Type Adopted	D (Mpc)	V	ΔV	V_T	A_V	M_{VT}	Parameters from Major-Axis Sérsic Fit				Parameters from 2D Profile Integration			Percentage Extra Light
											n	μ_{eV} (arcsec^{-2})	r_e (arcsec)	log(r_e) (kpc)	μ_{eV} (arcsec^{-2})	r_e (arcsec)	log(r_e) (kpc)	
(1)	(2)	(3)	(4)	(5)	(6)	(7)	(8)	(9)	(10)	(11)	(12)	(13)	(14)	(15)	(16)	(17)	(18)	(19)
IC 0809	VCC 1910	E	dE1, N	Sph, N	16.07	13.74	−0.02	13.72	0.098	−17.41	$1.41^{+0.03}_{-0.03}$	$21.87^{+0.03}_{-0.03}$	$12.14^{+0.12}_{-0.12}$	$-0.024^{+0.004}_{-0.004}$	22.02 ± 0.05	13.19 ± 0.35	0.012 ± 0.012	0.47 ± 0.03
IC 3470	VCC 1431	E?	dE0, N	Sph, N	16.14	13.87	−0.02	13.85	0.175	−17.36	$1.49^{+0.04}_{-0.03}$	$21.68^{+0.03}_{-0.03}$	$9.87^{+0.11}_{-0.11}$	$-0.112^{+0.005}_{-0.005}$	21.63 ± 0.05	9.83 ± 0.28	-0.114 ± 0.012	0.64 ± 0.03
IC 3509	VCC 1545	(E4)	E4	Sph,N	16.83	14.35	−0.10	14.25	0.134	−17.02	$2.73^{+0.05}_{-0.05}$	$23.05^{+0.05}_{-0.05}$	$15.20^{+0.30}_{-0.30}$	$0.094^{+0.008}_{-0.009}$	22.88 ± 0.08	14.15 ± 0.56	0.062 ± 0.018	0.15 ± 0.01
IC 3461	VCC 1407	E?	dE2, N	Sph, N	16.75	14.56	−0.05	14.51	0.101	−16.71	$1.82^{+0.12}_{-0.11}$	$23.01^{+0.09}_{-0.08}$	$13.82^{+0.47}_{-0.43}$	$0.050^{+0.014}_{-0.014}$	22.95 ± 0.07	13.16 ± 0.43	0.029 ± 0.015	0.40 ± 0.02
IC 3635	VCC 1828	(dE, N)	dE2, N	Sph, N	16.83	14.73	−0.08	14.65	0.119	−16.61	$1.63^{+0.07}_{-0.07}$	$23.67^{+0.07}_{-0.07}$	$20.06^{+0.61}_{-0.52}$	$0.214^{+0.013}_{-0.011}$	23.67 ± 0.07	19.37 ± 0.63	0.199 ± 0.014	0.21 ± 0.01
...	VCC 1185	E?	dE1, N	Sph, N	16.90	14.99	−0.07	14.92	0.073	−16.30	$1.50^{+0.04}_{-0.04}$	$24.03^{+0.04}_{-0.04}$	$18.44^{+0.27}_{-0.25}$	$0.179^{+0.006}_{-0.006}$	24.02 ± 0.06	18.11 ± 0.53	0.171 ± 0.013	0.52 ± 0.01
IC 3490	VCC 1489	E?	dE5, N?	Sph, N	16.53	15.51	−0.04	15.47	0.120	−15.75	$1.12^{+0.03}_{-0.03}$	$23.58^{+0.04}_{-0.04}$	$15.77^{+0.22}_{-0.21}$	$0.102^{+0.006}_{-0.006}$	23.51 ± 0.04	15.13 ± 0.40	0.084 ± 0.012	0.17 ± 0.02
NGC 4570	VCC 1692	S0/	$S0_1(7)$/E7	S0	17.06	10.98	−0.02	11.67	0.071	−19.56	3.69 ± 0.50	19.77	11.5	−0.022	...	...	...	...
NGC 4660	VCC 2000	E:	E3/$S0_1(3)$	S0	15.00	11.28	−0.07	11.51	0.107	−19.48	4.43 ± 0.38	19.57	10.5	−0.117	...	...	...	...
NGC 4564	VCC 1664	E	E6	S0	15.85	11.25	−0.09	11.66	0.113	−19.45	4.69 ± 0.20	20.81	16.8	0.112	...	...	...	...
NGC 4489	VCC 1321	E	$S0_1(1)$	S0	15.42	12.32	−0.01	13.53	0.090	−17.50	3.22 ± 0.57	20.04	4.7	−0.453	...	...	...	...
NGC 4318	VCC 0575	E?	E4	S0	22.08	13.36	−0.01	15.53	0.081	−16.27	2.05 ± 0.37	18.00	0.88	−1.025	...	...	...	...

Notes. Galaxy types in Columns 3, 4, and 5 are from RC3 (or, if in parentheses, from NED), from the VCC catalog (Binggeli et al. 1985) and as adopted based on our photometry. Isophotal magnitudes V (Column 7) are calculated by integrating our observed V-band surface brightness and ellipticity profiles out to the last data point in Table 3 (available in full in the online version). Column 8 gives an approximate correction from V to the total magnitude (Column 9), calculated by integrating the best-fit Sérsic function (or, in the case of S0s, the sum of the best-fit Sérsic function and exponential disk profile) from the last profile data point to very large radii. Galactic absorptions are from Schlegel et al. (1998). We use individual distances D (Column 6) from Mei et al. (2007) or, for NGC 4261 and NGC 4636, from Tonry et al. (2001). VCC 1192, VCC 1199, and VCC 1489 do not have distance measurements in Mei et al. (2007); for these, we used the mean distance for "all [79] galaxies (no W′ cloud)" given in Table 3 of Mei et al. (2007). Note that four galaxies with $D > 20$ Mpc are in the background of the main Virgo cluster. Then the total absolute magnitudes M_{VT} in Column 11 are based on V_T, A_V, and D. For S0 galaxies, V and ΔV refer to the whole galaxy, but V_T and M_{VT} refer to the bulge component. Adopted bulge-to-total luminosity ratios are $B/T = 0.63$ from our decomposition for NGC 4564 (cf. 0.71 in Scorza et al. 1998 via a decomposition based on reducing a_4 to zero), 0.75 from our decomposition for NGC 4660 (cf. 0.78 in Scorza & Bender 1995), 0.33 for NGC 4489 (this paper), 0.52 for NGC 4570 (this paper; cf. 0.36 in Burstein 1979), and 0.13 for NGC 4318 (this paper). Column 12 gives the Sérsic index of the major-axis profile fit illustrated in Figures 11–32 and 49–72, and Columns 13–15 give the corresponding major-axis V-band effective brightness μ_{eV} not corrected for Galactic extinction and effective (half-light) radius r_e. Note that these are not estimates of the true half-light radii and surface brightnesses but rather are parameters of the major-axis profile. True major-axis half-light radii and surface brightnesses are calculated "nonparametrically" by integrating the two-dimensional brightness profiles (that is, μ_V and ϵ) and are tabulated in Columns 16–18. Finally, Column 19 gives the percentage of the total light (Column 9) that is present near the center above the inward extrapolation of the Sérsic function fit. It is calculated from the fit and from the two-dimensional brightness profile including $\epsilon(r)$. It is < 0 for core galaxies. The quoted errors are internal. They are dominated by the uncertainty in what value(s) of ellipticity we should use for the Sérsic profile that "underlies" the galaxy profile. For the calculation of extra or missing light, we generally assumed that ϵ is the value at r_{min}, the minimum radius of the profile points used in the Sérsic fit. The error bars are based on reasonable extrapolations of $\epsilon(r)$ from the Sérsic region into the region of extra light. For NGC 4459 and NGC 4486A, the percent extra light is corrected approximately for residual dust absorption in the profile using a Sérsic function interpolation between the central brightness and the innermost profile points outside the prominent dust disk. The percent extra light for NGC 4482 is calculated consistently with the other values, but it should not be interpreted in the same way as for the other spheroidals. Figure 25 shows that the profile of the main body of NGC 4482 is not a Sérsic function, and the extra light above the Sérsic fit but outside the prominent nucleus has been included in Table 1. Interior to 1″ radius, the "extra light" in the nucleus is consistent with values given in Table 1 for other spheroidals. We emphasize that the missing or extra light percentages and their errors quoted above are based on the Sérsic function fits at large radii and are therefore model dependent. For this reason, external errors cannot realistically be estimated.

Table 2
Data Sources

No.	Telescope and Instrument	Filter	Scale (arcsec pixel^{-1})	Field of View (arcmin)	References	Number of Galaxies
1	CFHT AOB Pueo	K	0.035	0.15 × 0.15	1, 8	1
2	*HST* WFPC1 PC	F555W, F785LP	0.043	1.1 × 1.1	6, 10, 11	15
3	*HST* WFPC2 PC	F555W, F675W, F702W, F814W	0.046	0.6 × 0.6	1, 12	20
4	*HST* ACS	F475W, F850LP → V	0.050	3.5 × 3.4	1	40
5	*HST* NICMOS	F160W, F205W	0.075	0.3 × 0.3	1	2
6	CFHT HRCam	V, I	0.110	1.9 × 1.2	1	18
7	CFH12K	R	0.21	42 × 28	1	23
8	CFHT Cass	V	0.22	7.0 × 7.0	1	21
9	ESO/MPI 2.2 m	B	0.351	3.0 × 1.9	3	8
10	KPNO 2.1 m	B, R→ V	0.38	3.2 × 2.0	15	4
11	SDSS	g, z → V	0.396	...	1	31
12	Lick 1 m	R	0.43	3.6 × 3.6	9	1
13	ESO 1.5 m Danish	B	0.463	4.0 × 2.5	4	5
14	KPNO 4 m	C, T_1→ V	0.48	16.4 × 16.4	7	1
15	Hawaii 2.2 m	B, R → V	0.595	5.1 × 5.1	2	3
16	KPNO 0.9 m	B, R→ V	0.86	7.3 × 4.6	5, 15	11
17	McDonald 0.8 m PFC	V	1.36	46 × 46	1	31
18	CWRU 0.6 m Burrell Schmidt	M → V	1.45	90 × 45	14	2
19	Hawaii 0.6 m	B, R → V	1.6	13.3 × 13.3	2	9
20	NAO China 60 cm Schmidt	Various → R	1.7	58 × 58	13	1

Notes. The Caon et al. (1990, 1994) CCD data at small r were augmented by photographic data at large radii taken with the 1.8 m UK Schmidt telescope. Most Caon et al. (1990) galaxies were observed with the ESO/MPI 2.2 m telescope, but five of 33 galaxies were observed with the ESO 1.5 m Danish telescope (entry 13). The paper does not specify which galaxies were observed with which telescope, so all Caon et al. (1990) galaxies are credited to the ESO 2.2 m telescope. Similarly, six of 19 Virgo galaxies discussed in Caon et al. (1994) were observed with the Steward Observatory 2.3 m telescope (scale = 0.″3 pixel^{-1}; field size 1.9 × 2.0 arcmin), but the paper does not specify which ones. All Caon et al. (1994) galaxies are therefore credited to the ESO 1.5 m Danish telescope. The uncertainty in the telescope is unimportant here, because Caon data are used only at intermediate and large radii; the large-radius data are in any case dominated by the photographic results. Further discussion is given in Appendix A.3.

References: (1) This paper; (2) R. Bender et al. 2008, in preparation; (3) Caon et al. 1990; (4) Caon et al. 1994; (5) Davis et al. 1985; (6) Ferrarese et al. 1994; (7) Kim et al. 2000; (8) Kormendy et al. 2005; (9) Lauer 1985a; (10) Lauer et al. 1992a; (11) Lauer et al. 1995; (12) Lauer et al. 2005; (13) Liu et al. 2005; (14) Mihos et al. 2005; (15) Peletier et al. 1990.

disks when galaxies are seen not nearly edge-on. Ellipticals can also get misclassified as S0s when they contain prominent nuclear dust disks (NGC 4459) or asymmetries diagnostic of unfinished mergers (NGC 4382). We obtained photometry of the combined sample plus the most elliptical-like Sph galaxies (called dE in Binggeli et al. 1985) as identified by previous authors in parameter correlations. We then identified S0 and Sph galaxies based on our photometry. However, we retain Sph and S0 galaxies in Figures 34–38 to illustrate how we distinguish the different types. This procedure resulted in the sample of 27 elliptical galaxies in Table 1. Three are now known to be background galaxies; we keep them but do not include them in Virgo statistics.

Clearly, we cannot be sure that we found all Virgo ellipticals. Some omitted galaxies that Binggeli et al. (1985) list as possible members will prove to be members. Some spheroidals listed by Binggeli may turn out to be misclassified ellipticals. We describe our sample as "all known Virgo ellipticals," recognizing that future work may find a few more. We defined our sample carefully and tried not to omit galaxies with special properties whose lack would bias our conclusions.

6. SURFACE PHOTOMETRY

Throughout this work, our aim is to improve the accuracy of galaxy photometry as much as possible. For each galaxy, we combine photometry from a wide range of sources to provide independent consistency checks and thereby to reduce systematic errors. The sources include published data, our photometry of images available in public archives, and our photometry of images from our own observing programs. All magnitude zero points come from *HST* images, but many have been checked against ground-based sources. Both our relative brightness profiles and our zero points should be substantially more accurate than data available in the literature. We cannot, of course, exclude the possibility that a small number of errors that are larger than our error estimates have "slipped through the cracks." But for most galaxies, the results have survived more consistency checks and comparisons of independent data sources than other photometry in the literature.

6.1. Sources

Data sources are listed in Table 2 and cited in the keys to Figures 11–32 (Section 7). Comments on individual sources follow.

HST WFPC2 data provide the highest spatial resolution (Lauer et al. 2005) with scale = 0.″0456 pixel^{-1} for the Planetary Camera (hereafter PC). All WFPC1 and WFPC2 PC profiles from Lauer et al. (1995, 2005) are based on PSF-deconvolved images. They allow us reliably to identify central departures from Sérsic functions fitted to the main body of each galaxy. However, the PC field of view is small, so it is important to supplement *HST* data with wide-field photometry.

The ACS Virgo cluster survey by Côté et al. (2004) provides high-quality, archival images of almost all of our sample

galaxies. Because it is uniform in quality, it is our best source of color profiles. Good resolution (scale $0\farcs05$ pixel^{-1}) means that it provides an important supplement to the WFPC1 and WFPC2 photometry of the brighter galaxies and the best photometry of the centers of faint galaxies that were not previously observed by *HST*. The ACS images have high signal-to-noise ratios (S/Ns) and a reasonably large field of view, so they also yield the deepest profiles for some of the smallest galaxies in our sample.

We have *HST* WFPC1, WFPC2, or ACS profiles for all of our galaxies. Note, however, that we did not carry out PSF deconvolution of the ACS images. Therefore, the ACS profiles have slightly lower spatial resolution than the WFPC profiles. For many of the fainter galaxies, we have *HST* profiles only from ACS. The lower resolution affects how well we do or do not spatially resolve any extra light or nuclei. But it does not compromise our estimates of the amount of extra light, and it has no effect on any conclusions in this paper.

HST NICMOS images allow us to correct the optical *HST* profiles of NGC 4261 and NGC 4374 for dust absorption. Comparison of the NICMOS F160W or F205W profiles and ACS z-band profiles shows that any residual absorption in the near-infrared is small. NGC 4261 and NGC 4374 both have cuspy cores. The NICMOS profiles are used only at small radii; they affect our calculation of the total amount of light "missing" because of the presence of the core (Section 10.1), but they do not affect the Sérsic fits or the determination of global parameters.

Adaptive optics observations obtained in the K band with the CFHT and PUEO (Arsenault et al. 1994) were used to minimize absorption seen in NGC 4486A. This is a small elliptical galaxy with an edge-on stellar disk that is bisected by a strong dust lane (Kormendy et al. 2005). Again, use of a central infrared profile improves our estimate of the amount of extra light in the galaxy, but it does not affect the determination of global parameters.

We include the CFHT photometry obtained in 1982–1994 by Kormendy with the Cassegrain CCD camera and the High Resolution Camera (HRCam; Racine & McClure 1989; McClure et al. 1989). Kormendy & McClure (1993) discuss image reduction. HRCam includes tip-tilt image stabilization. We also measured images obtained by Wainscoat and Kormendy in 2000–2002 with the CFHT 12K CCD mosaic.

For as many galaxies as possible and especially for all of the largest galaxies, we obtained V-band images using the McDonald Observatory 0.8 m telescope. These data generally provide the deepest profiles and thus are important for constraining the Sérsic fits. We reach especially low surface brightnesses with the 0.8 m telescope because we can accumulate long exposures and because the wide unvignetted field ($46' \times 46'$) allows accurate sky subtraction.

When papers published profiles or archives contained images in two bandpasses that bracket V, we used the bracketing profiles to calculate a V profile using standard calibrations.

6.2. Surface Photometry

Most profile calculations are based on isophote fits using the algorithm of Bender (1987), Bender & Möllenhoff (1987), and Bender et al. (1987, 1988) as implemented in the ESO image processing system `MIDAS` (Banse et al. 1988) by Bender and by R. P. Saglia (2003, private communication). The software fits ellipses to the galaxy isophotes; it calculates the ellipse parameters and parameters describing departures of the isophotes from ellipses. The ellipse parameters are surface brightness, isophote center coordinates $X_{\rm cen}$ and $Y_{\rm cen}$, major and minor axis radii, and hence ellipticity ϵ and position angle P.A. of the major axis.

The radial deviations of the isophotes from the fitted ellipses are expanded in a Fourier series of the form

$$\Delta r_i = \sum_{k=3}^{N} [a_k \cos(k\theta_i) + b_k \sin(k\theta_i)] \,. \quad (2)$$

The most important of these parameters is a_4, expressed in the figures as a percent of the major-axis radius a. If $a_4 > 0$, the isophotes are disky-distorted; large a_4 at intermediate or large radii indicates an S0 disk. If $a_4 < 0$, the isophotes are boxy. The importance of boxy and disky distortions is discussed in Bender (1987), Bender et al. (1987, 1988, 1989), Kormendy & Djorgovski (1989), Kormendy & Bender (1996), and below.

Some profiles were measured using Lauer's (1985a) program `profile` in the image processing system `VISTA` (Stover 1988). The interpolation scheme in `profile` is optimized for high spatial resolution, so it is best suited to high-S/N images of galaxy centers. The isophote calculation is Fourier based, so it is less well suited to measuring outer parts of galaxies, where low S/N results in noisy isophotes or where star removal or limited field of view results in incomplete isophotes.

Some profiles were calculated with the isophote ellipse fitting program `GASP` (Cawson 1983; Davis et al. 1985). `GASP` does not provide isophote distortion parameters, but it is the most robust of our isophote fitters at low S/N, and it handles nonmonotonic brightness profiles without problems. Therefore, it was sometimes the program of choice at large radii.

Finally, in some cases (e.g., NGC 4486A), it was impossible to calculate reliable ellipse fits because of dust absorption or because of overlapping galaxies or bright foreground stars. In these cases, we calculated cut profiles by averaging the surface brightness in one- to several-pixel-wide cuts through the galaxy center. Cut profiles are identified in the keys to Figures 11–32.

Some profiles showed a few glitches produced, for example, by imperfectly masked foreground stars. By this, we mean that one value of μ (rarely), ϵ, or P.A. among a set of smoothly varying values was much different from the adjacent values. These values were replaced by the average of the adjacent points when it was clear that they were measurement errors.

6.3. Photometric Zero Points

All zero points are based on *HST* images. When available, WFPC1 or WFPC2, F555W zero points were used. For most galaxies with these zero points, the keys to Figures 11–32 list Lauer et al. (1995, 2005) as data sources. Then V-band profiles were taken directly from these papers. For a few galaxies, we measured and zero-pointed WFPC2 images ourselves.

We have a particularly good external check of the WFPC1 and WFPC2 zero points. Many Virgo galaxies were observed during an excellent, seven-night observing run with the CFHT (1984 March 6/7–12/13). The entire run was photometric. We observed large numbers of V- and I-band standard stars to tie our photometry to Landolt (1983). Most standards were in M 67 (Schild 1983). The CFHT and *HST* zero points agree very well. In obvious notation, the mean difference in zero point for three WFPC1 values is $V_{HST} - V_{\rm CFHT} = +0.004 \pm 0.002$ mag arcsec^{-2} ($\sigma/\sqrt{3}$). The mean difference in zero point for 11 WFPC2 values is $V_{HST} - V_{\rm CFHT} = -0.009 \pm 0.004$ mag arcsec^{-2} ($\sigma/\sqrt{11}$).

All galaxies in our sample that do not have zero points from WFPC1 or WFPC2 were observed in the Virgo cluster ACS

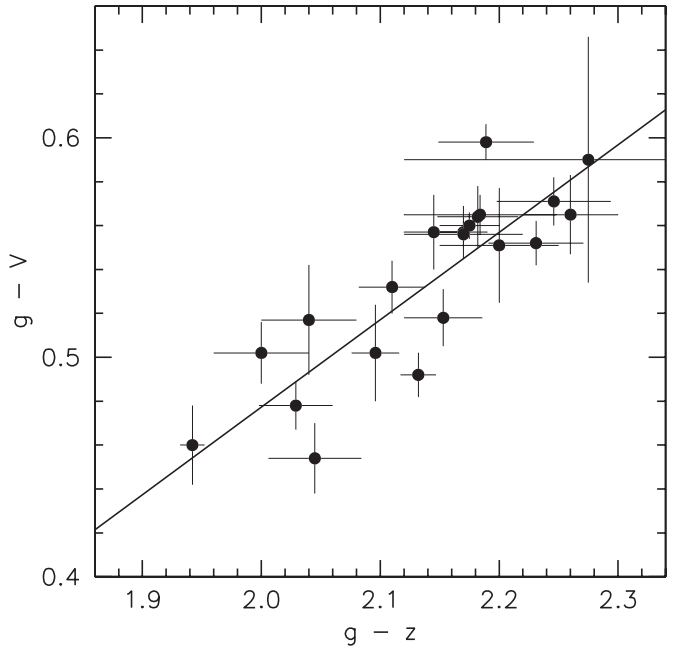

Figure 5. Calibration of *HST* ACS F475W g and F850LP z magnitudes to WFPC1 and WFPC2 V band. The ACS magnitude system used is VEGAmag with zero points from Sirianni et al. (2005). Each point represents one galaxy for which we can compare the g profile from ACS with a V profile from Lauer et al. (1995, 2005). The least-squares fit to the points (straight line) is our adopted transformation, Equation (3).

survey. However, the profiles are not tabulated in Ferrarese et al. (2006a). We remeasured the g- and z-band images using the Bender code to ensure consistent a_4 values. Zero points were taken from Sirianni et al. (2005):[5] $g = -2.5 \log \mathrm{ADU} + 26.168$ and $z = -2.5 \log \mathrm{ADU} + 24.326$, where ADU represents counts s^{-1} in the F475W or F850LP band, as appropriate. The g and $g - z$ profiles were converted to V as follows.

Most galaxies with WFPC1 or WFPC2 zero points were also observed with ACS. We calibrated g and $g - z$ against V by comparing our g profiles to Lauer's V profiles. The results are shown in Figure 5. Our adopted transformation is

$$V = g + 0.320 - 0.399\,(g - z). \tag{3}$$

Similar calibrations have been derived using standard stars (Smith et al. 2002; Sirianni et al. 2005), but Equation (3) is more relevant here, because it is based on the composite, old, metal-rich stellar populations that make up elliptical galaxies. The scatter in Figure 5 is 0.021 mag arcsec^{-2} in $g - V$. Figure 5 does not reach the bluest colors of our galaxies; some extrapolation is required. We have an external check of our $g - z$ colors: after converting their AB magnitudes to VEGAmag, we can compare Ferrarese et al. (2006a) color measurements $(g - z)_{\mathrm{VEGA,F}}$ to ours $(g - z)_{\mathrm{VEGA,KFCB}}$ over the radius range $1'' \leqslant r \leqslant 16''$. For 34 E + Sph galaxies, the mean difference is

$$(g - z)_{\mathrm{VEGA,F}} - (g - z)_{\mathrm{VEGA,KFCB}} = +0.015 \pm 0.004\,(\sigma/\sqrt{34}). \tag{4}$$

[5] The currently adopted ACS zero points (http://www.stsci.edu/hst/acs/analysis/ zeropoints) are different from the above. These changes have no effect on the present paper: the zero point that we adopted for each galaxy is the one that we calibrated to V. However, readers who wish to use Equation (3) to calibrate current photometry using updated *HST* zero points need to correct it for the changes in zero points from Sirianni et al. (2005) values.

The dispersion, $\sigma = 0.024$ mag arcsec^{-2}, includes our errors in measuring Ferrarese colors by hand in their published plots. Figure 5 suggests no reason to believe that ACS g zero points converted to V are less accurate than WFPC1 and WFPC2 zero points. Galaxies with ACS zero points are identified in Figures 11–32: the keys list "ACS V" but not Lauer et al. (1995, 2005) as a data source.

How accurate are our zero points? The answer is notoriously difficult to determine. Our comparison of WFPC and CFHT photometry was reassuring, but the agreement was fortuitously good. The ground-based standard star system was uncertain by several percent (e.g., Joner & Taylor 1990). The same is true of *HST*. Photometric standards and science targets are observed at different times, and the telescope plus instruments show short-term instabilities and long-term sensitivity trends of a few percent or occasionally more (Baggett & Gonzaga 1998; Heyer et al. 2004; Biretta 2005; Bohlin 2007). Aperture effects are nontrivial (Holtzman et al. 1995). Ground-based, WFPC, and ACS standard star measurements are made within apertures of different sizes, but the total amount of light at large radii in a PSF can be surprisingly large (King 1971; Kormendy 1973). The outer PSF halo is often unmeasurably faint, but its light is taken away from the central profile, so it affects the zero point. Given these considerations and our tests, we estimate that the random errors in our zero points are ± 0.03 mag arcsec^{-2} and the systematic errors are $\lesssim 0.05$ mag arcsec^{-2}. These are better than the science requirements of this paper.

6.4. Construction of Composite Profiles

Composite profiles were constructed from as many data sources as possible (Table 2), including our own and published photometry. Our emphasis was on accuracy. For example, almost all photographic profiles and many early CCD results proved not to be accurate enough to add weight to modern CCD data.

To construct composite profiles, we began with *HST* profiles, including zero points. We then added profiles one at a time, starting with the highest-accuracy ones measured with the highest spatial resolution. Each profile was shifted in surface brightness to minimize the scatter with the previous composite over the largest possible radius range. This must be done "by hand," because at this stage, the deviations of individual profiles from the composite reveal systematic errors. Only a few of these can be anticipated. For example, ground-based profiles "peel off" the *HST* profiles near the center when atmospheric seeing or telescope aberrations become important. But it is not obvious a priori—although it becomes clear in carrying out the exercise—that ellipticities are more sensitive to seeing than are surface brightnesses. P.A.s are most robust. Another problem was that WFPC1 profiles are generally not accurate at large tabulated radii. In general, it quickly became clear that some profile sources (e.g., Peletier et al. 1990) are more reliable than others (e.g., our CFHT Cassegrain camera profiles, which are excellent at small radii, but which have poor sky subtraction at large radii when the field of view is too small for the galaxy). Since we have many data sources at most radii in most galaxies, we were draconian in our pruning of individual profiles that did not agree with the means. The final composite profiles are the means of the individual μ-shifted profile points that were not pruned, i.e., the data identified by asterisks in the keys to Figures 11–32. The averages were carried out in $\log r$ bins of 0.04. These profiles are illustrated in Figures 11–32 and used in all analysis. They are published in the online version of ApJS. Table 3 provides a sample.

Table 3
NGC 4486 = M 87 Composite Surface Photometry

Galaxy	r (arcsec)	μ_V (mag arcsec^{-2})	ϵ	P.A. (deg E of N)	Galaxy	r (arcsec)	μ_V (mag arcsec^{-2})	ϵ	P.A. (deg E of N)
NGC 4486	0.017	16.266	...	...	NGC 4486	26.318	19.560	0.050	−17.72
NGC 4486	0.044	16.358	0.160	163.60	NGC 4486	29.040	19.716	0.051	−18.93
NGC 4486	0.088	16.511	0.161	163.60	NGC 4486	31.750	19.860	0.052	−18.86
NGC 4486	0.176	16.589	0.161	187.60	NGC 4486	35.015	20.016	0.059	−19.82
NGC 4486	0.220	16.646	0.161	146.70	NGC 4486	38.371	20.161	0.064	−19.03
NGC 4486	0.264	16.700	0.162	136.60	NGC 4486	42.073	20.318	0.072	−21.15
NGC 4486	0.308	16.746	0.162	125.50	NGC 4486	45.779	20.455	0.076	−22.77
NGC 4486	0.352	16.788	0.162	119.00	NGC 4486	50.855	20.631	0.078	−21.66
NGC 4486	0.396	16.838	0.138	118.40	NGC 4486	56.040	20.794	0.082	−23.00
NGC 4486	0.440	16.889	0.131	118.40	NGC 4486	61.094	20.936	0.086	−22.84
NGC 4486	0.484	16.927	0.118	114.00	NGC 4486	67.531	21.097	0.096	−23.61
NGC 4486	0.548	16.953	0.109	110.95	NGC 4486	72.277	21.217	0.100	−23.49
NGC 4486	0.604	16.966	0.097	118.40	NGC 4486	77.179	21.331	0.099	−23.19
NGC 4486	0.660	16.996	0.094	118.40	NGC 4486	84.918	21.499	0.109	−24.58
NGC 4486	0.727	17.031	0.084	126.35	NGC 4486	93.972	21.693	0.114	−24.82
NGC 4486	0.795	17.062	0.090	147.40	NGC 4486	104.954	21.912	0.128	−25.22
NGC 4486	0.867	17.091	0.087	147.60	NGC 4486	116.011	22.116	0.139	−24.22
NGC 4486	0.950	17.114	0.079	147.60	NGC 4486	127.938	22.317	0.153	−25.73
NGC 4486	1.038	17.134	0.075	111.15	NGC 4486	139.798	22.515	0.157	−25.18
NGC 4486	1.147	17.165	0.071	68.83	NGC 4486	154.170	22.714	0.171	−24.06
NGC 4486	1.254	17.195	0.072	62.30	NGC 4486	166.341	22.870	0.185	−24.52
NGC 4486	1.365	17.210	0.049	63.83	NGC 4486	180.926	23.019	0.206	−24.98
NGC 4486	1.515	17.241	0.030	67.50	NGC 4486	200.909	23.220	0.222	−24.33
NGC 4486	1.669	17.270	0.023	53.80	NGC 4486	222.587	23.420	0.237	−23.90
NGC 4486	1.825	17.290	0.015	57.60	NGC 4486	242.103	23.573	0.254	−23.52
NGC 4486	1.998	17.318	0.007	94.75	NGC 4486	265.053	23.742	0.275	−24.12
NGC 4486	2.196	17.346	0.018	94.62	NGC 4486	293.990	23.934	0.293	−23.47
NGC 4486	2.419	17.371	0.015	86.82	NGC 4486	321.366	24.096	0.303	−23.70
NGC 4486	2.640	17.399	0.012	115.62	NGC 4486	346.737	24.257	0.313	−23.83
NGC 4486	2.835	17.418	0.008	91.40	NGC 4486	381.651	24.441	0.329	−24.78
NGC 4486	3.218	17.470	0.005	59.60	NGC 4486	419.276	24.658	0.337	−25.59
NGC 4486	3.823	17.538	0.012	25.40	NGC 4486	462.914	24.820	0.348	−23.58
NGC 4486	4.546	17.613	0.010	20.40	NGC 4486	502.343	25.011	0.370	−23.56
NGC 4486	5.413	17.715	0.017	12.50	NGC 4486	541.377	25.090	0.381	−23.84
NGC 4486	6.092	17.790	0.021	12.38	NGC 4486	593.608	25.288	0.388	−24.66
NGC 4486	7.118	17.913	0.028	10.27	NGC 4486	653.131	25.486	0.398	−25.78
NGC 4486	7.780	17.991	0.023	5.66	NGC 4486	719.449	25.697	0.427	−27.03
NGC 4486	8.610	18.086	0.028	5.82	NGC 4486	794.328	25.917	0.447	−26.86
NGC 4486	9.441	18.183	0.020	−1.00	NGC 4486	878.348	26.100	0.454	−26.75
NGC 4486	10.304	18.277	0.026	0.12	NGC 4486	946.237	26.328	0.447	−26.57
NGC 4486	11.552	18.409	0.030	−1.06	NGC 4486	1046.325	26.620	0.457	−26.88
NGC 4486	12.322	18.489	0.026	−7.05	NGC 4486	1145.513	26.848	0.464	−27.50
NGC 4486	13.715	18.622	0.030	−5.10	NGC 4486	1230.269	26.995	0.454	...
NGC 4486	15.109	18.749	0.030	−5.23	NGC 4486	1336.595	27.180	0.443	−29.80
NGC 4486	16.615	18.879	0.032	−8.61	NGC 4486	1479.109	27.305	0.439	...
NGC 4486	18.249	19.009	0.036	−9.85	NGC 4486	1621.810	27.535	0.436	...
NGC 4486	19.971	19.143	0.036	−12.95	NGC 4486	1778.279	27.715	0.433	...
NGC 4486	21.945	19.284	0.040	−15.19	NGC 4486	1995.262	27.755	0.429	...
NGC 4486	23.961	19.415	0.043	−17.19	NGC 4486	2443.700	28.045	0.422	−34.10

Notes. Radius r is measured along the major axis. The central ϵ and P.A. gradients may be caused by AGN jet contamination. In the online table, the profile labeled NGC 4486A is the V-band profile of NGC 4486A. Profile NGC 4486AK is an alternative profile of NGC 4486A with V-band zero point and V-band data used at large radii but with the CFHT deconvolved K-band profile (brown points in Figure 20) substituted at $r \leqslant 1''.4$ to minimize the effects of dust absorption.
(This table is available in its entirety in a machine-readable form in the online journal. A portion is shown here for guidance regarding its form and content.)

Some profile data are plotted in Figures 11–32 but were not included in the averaging. They are not accurate enough to add significantly to our results, but they provide important consistency checks. These are identified in Figures 11–32: the keys do not have asterisks at the end of the source references.

The accuracy of the final profiles is difficult to estimate. However, we have many external checks. The residual plots in Figures 11–32 illustrate with an expanded μ scale how well the individual profiles agree with each other. At small radii, our composite profiles should be accurate to a few percent or better. At large radii, the number of independent data sources decreases. It is even possible that, among (say) three sources, two agreed fortuitously but were less accurate than the third. The agreement of different data sources provides a guide to the accuracy at large r, but it is not bombproof. When we discard a few points from the Sérsic fits at large radii, this implies that we

do not trust the sky subtraction. In general, we believe that our profiles are accurate to $\lesssim 0.1$ mag arcsec^{-2} at large radii.

7. PHOTOMETRY RESULTS

7.1. Composite Brightness Profiles and Photometric Data

Figures 11–15, 16–24, 25–29, and 30–32 illustrate the photometry of the core ellipticals, the extra light ellipticals, the spheroidals, and the S0 galaxies, respectively.

The bottom three panels show the V-band, major-axis brightness profile μ, the isophote ellipticity ϵ, and the major-axis P.A. The next two panels are the isophote shape parameters a_4 and a_3. Parameter a_3 shows that isophotes have reasonably pure boxy or disky distortions that are aligned with the major axes; they generally have no triangular (a_3) or rotated (b_n) components. Second from the top is the $g - z$ color profile from the *HST* ACS and SDSS surveys. The top panel shows the deviations of the individual profiles in the bottom panel from the adopted Sérsic function fit shown by the black curve. The Sérsic index n is given in the key.

7.2. Sérsic Function Fits to the Profiles

Appendix A discusses our Sérsic fits. Figures 49–72 show all of the fits and the χ^2 hyperellipses of the three fit parameters. They show that the parameter errors are often strongly coupled. In this situation, parameter errors can only be estimated from the maximum half-widths of the χ^2 hyperellipses. Appendix A also explores the dependence of the fit parameters on the radial range in which we make the fit. We show that the parameters are robust provided that the fit range is large enough. This is why we aim to measure profiles that are reliable over large dynamic ranges. No conclusions of this paper are vulnerable to small changes in fit ranges. To aid users of Sérsic functions, Appendix A presents guidelines on dynamic ranges needed to get reliable fits. Parameters of our fits including error estimates are listed in Figures 49–72 and in Table 1.

We fit Sérsic functions over the largest radius ranges over which the fit residuals are (i) not systematic and (ii) roughly in agreement with our profile measurement errors. The median root mean square (rms) of the 27 E fits is 0.040 V mag arcsec^{-2}, and the dispersion in rms values is 0.019 V mag arcsec^{-2}. One of the main conclusions of this paper is that *Sérsic functions fit the main parts of the profiles of both elliptical and spheroidal galaxies astonishingly well over large ranges in surface brightness. For most galaxies, the Sérsic fits accurately describe the major-axis profiles over radius ranges that include* $\sim$ *93%–99% of the light of the galaxies* (see Figure 41).

At small r, all profiles deviate suddenly and systematically from the best fits. This is the signature of a core or extra light. Including either one in the fit produces large systematic residuals that are inconsistent with our measurement errors. Figure 64 (Appendix A) shows an example. We emphasize in Section 4.1 that we choose not to use fitting functions that combine (say) a central core with a Sérsic envelope: the resulting parameters are too strongly coupled. Our fits are robust descriptions of the main bodies of the galaxies. In later sections, we measure and interpret the amount of extra or missing light with respect to the inward extrapolation of the fits.

7.3. Galaxy Magnitudes

Galaxy apparent magnitudes V (Table 1, Column 7) are calculated by integrating the two-dimensional mean brightness

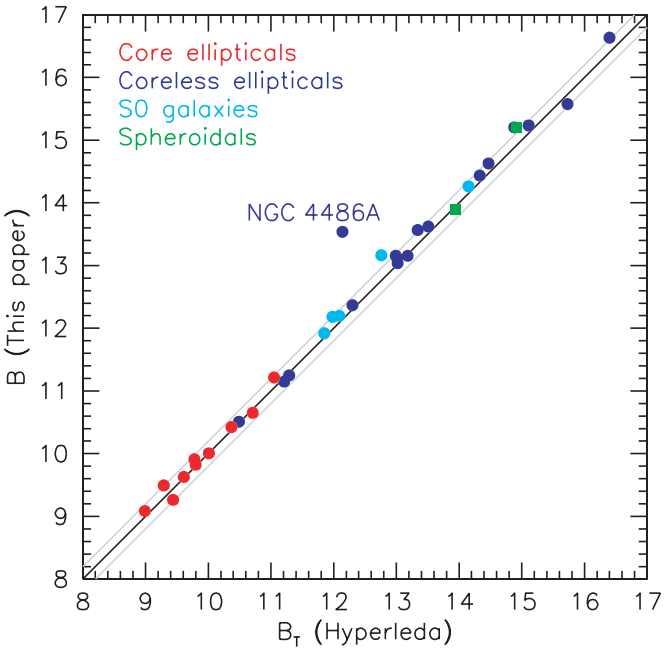

Figure 6. Comparison of our galaxy magnitudes with total B_T magnitudes from Hyperleda (Paturel et al. 2003: their "integrated photometry" values). Our V magnitudes from Table 1 are converted to B using total $B - V$ colors from RC3 when possible or colors within the effective radius from Hyperleda in a few cases. Galaxy classifications are from Table 1. The black line indicates equality, and fiducial gray lines are drawn at ± 0.2 mag to facilitate interpretation. NGC 4486A deviates because a bright foreground star (see Kormendy et al. 2005) is imperfectly removed from the Hyperleda photometry.

profiles including ellipticities $\epsilon(r)$. That is, V is the magnitude interior to the outermost nearly-elliptical isophote for which we have data. These magnitudes, after conversion to B using total $(B - V)$ colors, are compared to Hyperleda total magnitudes in Figure 6. Our iophotal magnitudes B are slightly fainter than Byperleda total magnitudes B_T. For 10 core galaxies, the average difference is $\langle B - B_T \rangle = 0.045 \pm 0.035$ mag; for 15 coreless ellipticals (omitting NGC 4486A) and two Sphs, $\langle B - B_T \rangle = 0.087 \pm 0.031$ mag, and for five S0 galaxies, $\langle B - B_T \rangle = 0.180 \pm 0.060$ mag. It is not surprising that our magnitudes are fainter, because they certainly do not include all of the light of the galaxies. Our limiting surface brightnesses are 25.5–28 V mag arcsec^{-2} for E and Sph galaxies and about 1 mag arcsec^{-2} brighter for S0s. Galaxy surface brightnesses do not drop suddenly to zero outside these isophotes. The corrections to total magnitudes are not very large, because the surface brightnesses that we fail to reach are faint. But the corrections are not negligible, either, because the area of the outer isophotes is large.

We concluded in Section 7.2 that Sérsic functions fit the major-axis brightness profiles of our E and Sph galaxies very well, including the outermost points that we trust in our photometry. Ellipticals are hot stellar systems; they cannot easily have sharp features in their brightness profiles. It is therefore reasonable to estimate corrections from our isophotal magnitudes to nearly total magnitudes by integrating extrapolations of our Sérsic function fits, as long as we do not need to extrapolate too far. Figure 7 shows such magnitude corrections ΔV. They capture most of the missing light. This is especially true for small-n systems: their outer profiles cut off steeply, so their corrections are small. The ΔV values also are reasonable for giant ellipticals with large Sérsic indices. Their corrections are larger

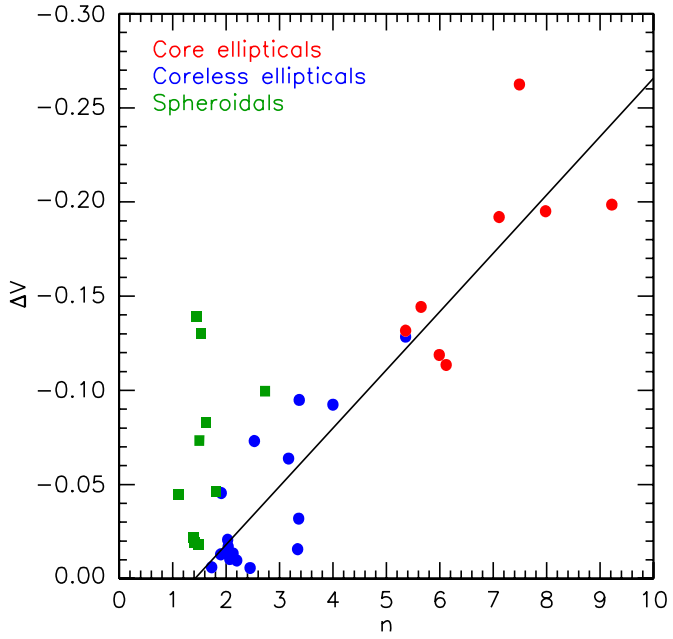

Figure 7. Corrections to convert our measured V-band galaxy magnitudes interior to the outermost elliptical isophotes in Figures 11–32 to almost-total magnitudes interior to a surface brightness of ~ 29.7 V mag arcsec^{-2} for core Es and out to an arbitrarily faint surface brightness for coreless Es and Sphs. Each correction is calculated by integrating the extrapolation of our Sérsic function fit with the ellipticity fixed at the value in the outermost observed isophotes. The corrections depend on n as expected: larger n means brighter, more extended outer halos and therefore larger ΔV. The correction is larger for Sph galaxies than for Es of the same Sérsic index in part because Sph galaxies have low surface brightnesses at small radii (Figures 34–36), so the relative contribution from large radii is large. In addition to this effect, the scatter results mostly from the fact that our observations reach different limiting surface brightnesses in different galaxies; ΔV is small (large) when our photometry is deep (shallow). However, the scatter for ellipticals is small. We use a least-squares fit to the points for ellipticals (straight line) only to note that the rms scatter about the line is 0.027 mag arcsec^{-2}.

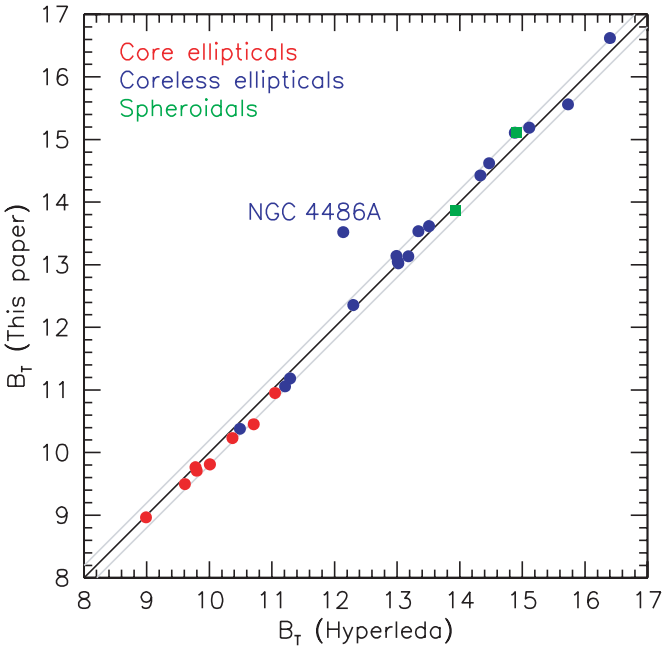

Figure 8. Comparison of our extrapolated, "total" galaxy magnitudes with total magnitudes from Hyperleda. Our V-band magnitudes from Table 1 have been corrected individually with the ΔV values plotted in Figure 7 and converted to B as in Figure 6. The black line indicates equality, and fiducial gray lines are drawn at ± 0.2 mag to facilitate interpretation.

and more uncertain, but we already approach the intracluster background light (e.g.) in our profiles of M 87 and NGC 4406 (see Mihos et al. 2005 and note that we include several isophotes from that paper in our profiles). At radii not much larger than these, total magnitudes become ill defined, because stars there do not "belong" exclusively to the galaxy under study but also feel the gravitational potential of the cluster and especially of the nearest neighbors.

Figure 8 plots total magnitudes $B_T = V + \Delta V + (B-V)_T$ from our photometry versus values from Hyperleda. The scatter is remarkably small and the agreement is remarkably good, given that both sources have measurement errors and that Hyperleda data are very heterogeneous. The small systematic differences now have exactly the sense that we would expect. Hyperleda aperture magnitudes are extrapolated to total magnitudes using mean growth curves for each galaxy type; for ellipticals, the growth curves are based on $n = 4$ de Vaucouleurs (1948) laws (Prugniel & Héraudeau 1998). One of the main conclusions of this paper will be that core ellipticals have $n > 4$ whereas almost all coreless ellipticals have $n \leqslant 4$. Therefore, our total magnitudes should be slightly brighter than Hyperleda's for core galaxies and slightly fainter than Hyperleda's for coreless galaxies. This is exactly what Figure 8 shows. For eight core ellipticals plus NGC 4621 (a coreless galaxy which, in exception to the above conclusion, has $n = 5.36$) but omitting M 87 and NGC 4406 (see below), the average difference is

$$\langle B_T - B_{T,\mathrm{Hyperleda}} \rangle = -0.116 \pm 0.026. \quad (5)$$

For five coreless ellipticals with $3 < n < 5$ (i.e., bracketing $n = 4$),

$$\langle B_T - B_{T,\mathrm{Hyperleda}} \rangle = +0.064 \pm 0.080. \quad (6)$$

For 12 coreless Es and 2 Sphs ("E" in Hyperleda) with $n < 3$,

$$\langle B_T - B_{T,\mathrm{Hyperleda}} \rangle = +0.056 \pm 0.033. \quad (7)$$

Equations (5)–(7) imply that our photometric system is consistent with the heterogeneous but large database in Hyperleda; recall that our zero points were estimated to be good to $\pm$ 0.05 mag. For coreless ellipticals and for Sph galaxies, our corrections ΔV should be accurate roughly to the rms = 0.027 mag in Figure 7. It is unlikely that they are much worse than $\pm$ 0.05 mag even for giant ellipticals, although one cannot be certain about extrapolations. We therefore adopt the individual corrections plotted in Figure 7 for these galaxies to get total magnitudes V_T and hence total absolute magnitudes M_{VT} in Columns 9 and 11 of Table 1, respectively.

Three ellipticals in Table 1 require special attention and were omitted from the above statistics. NGC 4486A has a bright star superposed near its center that is imperfectly removed from the Hyperleda photometry. The galaxy is therefore an outlier in Figures 6 and 8. However, our *HST* photometry should be unaffected by the star, so we corrected V to V_T as normal using our Sérsic fit to the profile. Second, the giant elliptical NGC 4406 in the main chain of galaxies near the center of the Virgo cluster is surrounded on all sides by other galaxies. Either because these are imperfectly removed from the photometry or because the profile is affected by tides from its neighbors, NGC 4406 has an outer profile that cuts off strongly compared to the outward extrapolation of the inner Sérsic fit (Figure 12). Therefore, the normal magnitude correction is not valid. Based on a Sérsic fit to the steep outer profile, we derive $\Delta V = -0.03$. Finally, M 87 almost certainly contains a faint cD halo (Section 7.4). We should not include intracluster light in M_{VT}. Based on Figure 7 and on the two fits in Figure 50, we adopt $\Delta V = 0$.

The total absolute magnitudes that result from the above procedures are used throughout this paper. Including zero point errors but not distance errors, we conservatively estimate that M_{VT} has errors of ~ 0.07 mag for galaxies with $n < 4$, ~ 0.1 mag for galaxies with $n \geqslant 4$, and 0.2 mag for M 87.

7.4. The cD Halo of M 87

M 87 = NGC 4486 is the *second*-brightest galaxy in Virgo. However, it is the central giant elliptical in the cluster, and it is surrounded by an enormous X-ray halo which shows that the galaxy is at the bottom of a deep potential well (e.g., Fabricant & Gorenstein 1983; Böhringer et al. 1994, 2001; Forman et al. 2007). In richer clusters, such galaxies are often cDs (Matthews et al. 1964; Morgan & Lesh 1965), i.e., giant ellipticals that have extra light at large radii in an enormous halo that belongs more to the cluster than to the central galaxy. "Extra light" with respect to what? The answer is best quantified by Schombert (1986, 1987, 1988). He showed that E profile shapes depend on luminosity; he constructed template mean profiles in different luminosity bins, and he identified as cDs those giant Es that have extra light at large radii with respect to the template that best fits the inner parts of the profiles. Recasting this statement in the language of Sérsic functions, cD galaxies are giant Es that have cluster-sized extra light at large radii with respect to the outward extrapolation of a Sérsic function fitted to the inner profile. cD halos are believed to consist of stars that were stripped from individual galaxies by collisions (Gallagher & Ostriker 1972; Richstone 1976).

Whether M 87 is a cD has been uncertain. This appears to be settled by the remarkably deep photometry by Liu et al. (2005) and Mihos et al. (2005). Both are included in Figure 11. Liu and collaborators, like de Vaucouleurs & Nieto (1978) and others, conclude that M 87 is a cD. We agree, but not for the reasons given in their papers. They conclude that the profile of M 87 shows extra light at large radii with respect to an $r^{1/4}$ law fitted to the inner parts. This is true, but it is true for all galaxies that have Sérsic $n > 4$. As reviewed in Section 3 and confirmed again in this paper, essentially all giant ellipticals have $n > 4$. The evidence that M 87 has a cD halo is more indirect. It is shown in Figure 50. A Sérsic function fits the whole profile with entirely acceptable residuals outside the core (rms = 0.0448 mag; see the top panels in Figure 50). However, $n = 11.8^{+1.8}_{-1.2}$ is formally much larger than in any other galaxy in our sample. When the outer end of the fit range is decreased below $\sim 900''$, n drops rapidly. By construction, such fits have extra light at large radii. An example is shown in the bottom panels of Figure 50. Fitting the profile out to $419''$ results in Sérsic index $n = 8.9^{+1.9}_{-1.3}$ that is more consistent with the values for the other giant ellipticals in Virgo. If this fit is adopted, then the galaxy has a faint extra halo at large radii. It is similar to but (by construction) fainter than the cD halos advocated by Liu and de Vaucouleurs. We emphasize that this fit is not unique. It is an interpretation, not a proven result. However, based on such fits, we do suggest that M 87 is marginally a cD galaxy. And we regard the detection of intracluster light by Mihos et al. (2005) as definitive proof.

These results are consistent with Oemler's (1976) conclusion that cD envelope luminosity $L_{\rm env}$ depends strongly on cluster luminosity, $L_{\rm env} \propto L^{2.2}_{\rm cluster}$. The total luminosity of Virgo is near the low end of the range for clusters that contain cDs. That M 87 is a weak cD is interesting in its own right, but it plays no direct role in this paper. Either set of fit parameters in Figure 50 is comfortably consistent with the fundamental plane correlations discussed in Section 8. Our estimate of the amount of missing light that defines the core is essentially unaffected. And n is robustly larger than 4, consistent with our conclusion that Sérsic index participates in the E–E dichotomy.

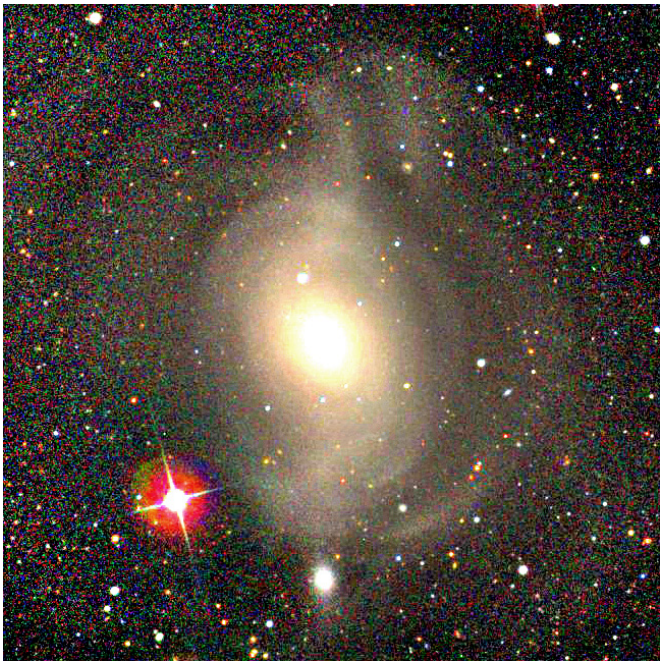

Figure 9. Contrast-enhanced gri-band color image of NGC 4382 from the SDSS online site http://www.wikisky.org. Strong fine-structure features are signs that the galaxy has not finished relaxing after a recent merger.

7.5. Comments on Individual Ellipticals

Profile properties that are common to many galaxies are discussed in Section 9. Here and in Section 7.6, we comment on galaxies whose classification (E versus S0) has been uncertain. When we assign a different morphological type to a galaxy than the catalog types (Columns 3 and 4 in Table 1), we give the reasons. This section involves details; readers who are interested in our main science results can jump to Section 8.

NGC 4382 is classified as SA0$^+$pec in RC3. Figure 14 shows that it has a very unusual brightness profile. It has extra light at intermediate radii, but the a_4 profile indicates that a slight disky distortion at smaller radii disappears here. This suggests that the extra light is not an S0 disk. Also, when the profile is decomposed into a Sérsic function bulge and an exponential disk, the disk parameters are very abnormal (cf. Freeman 1970). Finally, the galaxy is asymmetric and shows fine-structure features indicative of a recent merger (Figure 9). Schweizer & Seitzer (1992) quantify such features for 69 E and S0 galaxies; only three galaxies, two of them obvious mergers-in-progress, have larger fine-structure indices than does NGC 4382. The galaxy gets bluer and shows enhanced Hβ and depressed Mg b spectral lines near the center (Fisher et al. 1996; Lauer et al. 2005; Kuntschner et al. 2006), consistent with a younger stellar population. We conclude that the galaxy is an elliptical—a recent (damp?) merger remnant that has not fully settled into equilibrium. Aguilar & White's (1986) N-body simulations show that tidal stretching and shocking can produce features like the "extra halo" in Figure 14. Similarly, Navarro's (1990) N-body simulations show that merger remnants relax violently from the center outward, with waves in the density (see Figure 14) that propagate outward during the relaxation process.

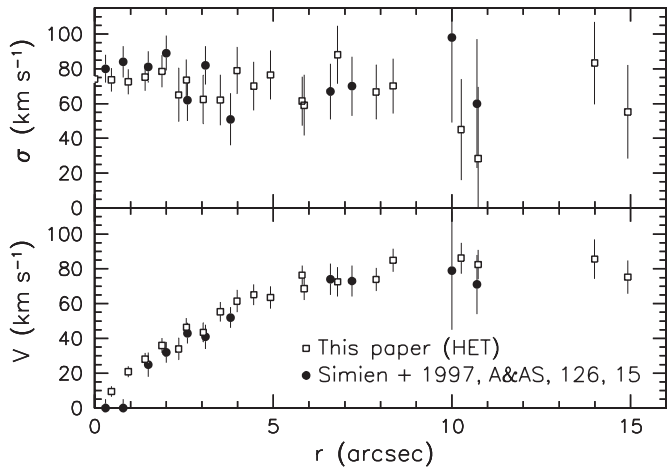

Figure 10. Absorption-line rotation curve $V(r)$ and velocity dispersion profile $\sigma(r)$ along the major axis of NGC 4318.

NGC 4406 is classified as $S0_1(3)$/E3 in the VCC and E3 in RC3. We see no sign of an S0 disk in the surface brightness or a_4 profiles (Figure 12). In particular, a_4 shows boxy—not disky—isophotes at large radii. The galaxy is zooming through Virgo at ~ 1400 km s^{-1}, and it is bracketed closely by NGC 4374, by the pair NGC 4435 + NGC 4438, and by many other, not much smaller galaxies. Its isophotes overlap at large radii with those of the adjacent galaxies (Kormendy & Bahcall 1974; Mihos et al. 2005), so the outermost profile is uncertain. This or else the nonequilibrium tidal distortion that can result from a rapid encounter with its neighbors (Aguilar & White 1986) could account for the slightly non-Sérsic profile at large radii and for the unusually large value of $n = 10.27^{+0.49}_{-0.35}$. Note that the profile is very concave upward in Figure 12.

NGC 4459 is classified S0 in the VCC and RC3 because of its nuclear dust ring. Figure 16 shows no evidence of a stellar disk in the form of profile departures from a Sérsic function. The isophotes are not disky. We classify the galaxy as an elliptical.

7.6. Comments on Individual S0s

NGC 4318 is classified "E?" in the RC3 and E4 in the VCC. However, its brightness, ellipticity, and P.A. profiles show a strongly two-component structure (Figure 32). The outer component has a disky signature ($a_4 > 0$) and an exponential profile (Figure 32). This suggests that the galaxy is an S0.

We can check this by measuring the rotation velocity and velocity dispersion of the outer component. Simien & Prugniel (1997, 1998) took spectra of NGC 4318 using the 1.93 m telescope of the Observatoire de Haute-Provence. The latter work used a dispersion of 52 km s^{-1} pixel^{-1} and got a central velocity dispersion of $\sigma_0 = 77 \pm 17$ km s^{-1}. The former paper quoted a maximum rotation velocity of 75 ± 20 km s^{-1}, but the observations did not clearly reach a flat part of the rotation curve (Figure 10). We therefore remeasured NGC 4318 with the Low Resolution Spectrograph (LRS; Hill et al. 1998) on the 9.2 m HET. The slit P.A. was 65°, the slit width was 1.″5, and the exposure time was 900 s. The standard spectrum was a mean of the spectra of the K0 III stars η Cyg and HD 172401. The results are the open squares in Figure 10. Our dispersion, 116 km s^{-1} pixel^{-1}, is substantially worse than that of Simien & Prugniel, so their velocity dispersion measurements are more reliable than ours. But our S/N is higher, so we reach the $V \simeq$ constant part of the rotation curve. We adopt our measurement of the maximum rotation velocity, $V_{\rm max} = 82.4 \pm 2.3$ km s^{-1}. Then, $V_{\rm max}/\sigma_0 = 1.07 \pm 0.24$. For an ellipticity of $\epsilon = 0.35$ in the outer component, the "oblate line" in the $V_{\rm max}/\sigma_0$–ϵ diagram (Binney 1976, 1978a, 1978b; Illingworth 1977; Kormendy 1982) implies that an isotropic, oblate spheroid should have $V_{\rm max}/\sigma_0 = 0.73$. The outer component of NGC 4318 rotates $(V_{\rm max}/\sigma_0)^* = 1.46 \pm 0.32$ times faster than this. In practice, we should use a mean velocity dispersion inside approximately the half-light radius; from Figure 10, this would be smaller than σ_0. Moreover, since the outer velocity dispersion is small and the S/N of the Simien & Prugniel measurements is low, the true velocity dispersion may be even smaller. Therefore, the outer component clearly rotates more rapidly than an isotropic oblate spheroid with the observed flattening. This is a disk signature.

Taking all these signs together, we identify NGC 4318 as a low-luminosity S0 galaxy. Figure 32 shows a decomposition into a Sérsic function bulge and an exponential disk. The bulge has an entirely normal Sérsic index of $n = 2.1 \pm 0.4$.

NGC 4489 is classified E in the RC3 and S0 in the VCC. It appears in our photometry to consist of two components (Figure 31). The galaxy is reasonably isolated. It is very round, so the a_4 profile is not informative. We classify it as an S0, but this is uncertain. There is a sharp isophote twist of $\sim 80°$ between the "bulge" and the "disk" implied by the profile decomposition in Figure 31. Given suitable structure and viewing geometry, this could be consistent with either an E or an S0 classification.

NGC 4564 is classified E in the RC3 and E6 in the VCC, but the brightness profile has the two-component structure of a bulge plus disk, and the a_4 profile shows a strong disky distortion at the radii of the extra light (Figure 31). This is clearly an almost-edge-on S0. Scorza et al. (1998) observed a similar a_4 profile; by decomposing the two-dimensional brightness distribution into an elliptical galaxy component with exactly elliptical isophotes and a disk that accounts for the observation that $a_4 > 0$, they estimated that the bulge-to-total luminosity ratio is 0.71. This is probably an underestimate, because low-luminosity, coreless ellipticals have isophotes that are intrinsically disky, and all of the disky distortion was ascribed to the S0 disk in the decomposition. The disk of NGC 4564 is also detected in the Doppler asymmetry in the spectral line profiles (Gauss–Hermite moment h_3: Halliday et al. 2001).

NGC 4660 is classified E: in the RC3 and E/S0 in the VCC, but it is a bulge-dominated S0. Figure 30 shows that extra light above an almost-$r^{1/4}$ brightness profile coincides with a maximum in the ϵ profile and a very disky value of a_4. These features are well known (Bender et al. 1988; Rix & White 1990; Scorza & Bender 1995); a photometric decomposition implies that the disk contains $\sim 1/4$ of the light. As in NGC 4564, the spectral line profiles of NGC 4660 show the kinematic signature of a dynamically cold, rapidly rotating component added to a dynamically hot, slowly rotating component (Bender et al. 1994; Scorza & Bender 1995).

8. PHOTOMETRY RESULTS. I. PARAMETER CORRELATIONS AND THE DICHOTOMY BETWEEN ELLIPTICAL AND SPHEROIDAL GALAXIES

One principal result of this paper is to verify the dichotomy between elliptical and spheroidal galaxies (Section 2.1) with modern, accurate photometry. This is done in Figures 34–39. It is a necessary step in refining our sample of elliptical galaxies.

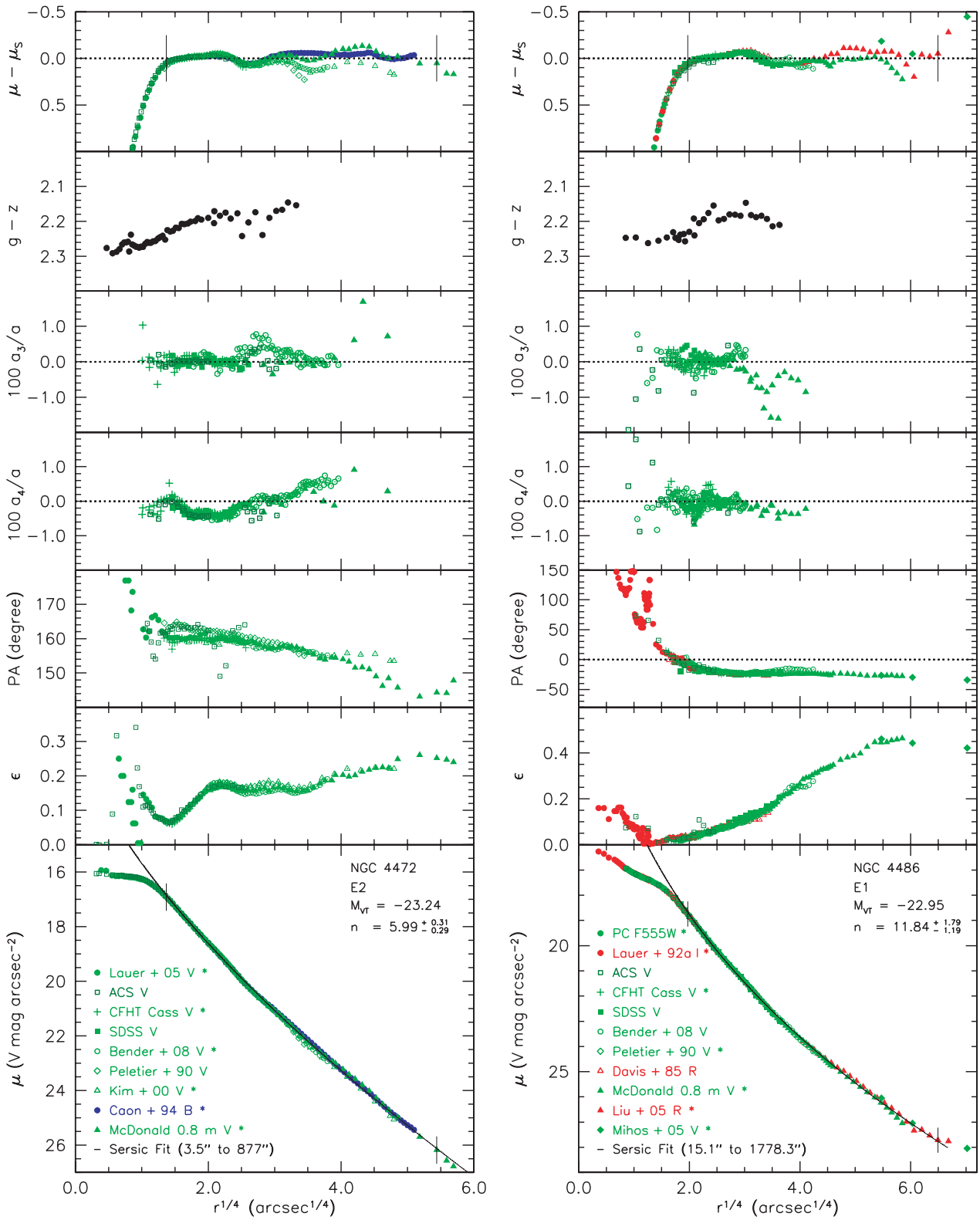

Figure 11. Composite brightness profiles of Virgo cluster elliptical galaxies ordered by total absolute magnitude M_{VT} (Column 11 of Table 1). For each galaxy, the panels show, from bottom to top, surface brightness μ, ellipticity ϵ, P.A. of the major axis east of north, the isophote shape parameters a_4 and a_3 (as percentages of the major-axis radius a $\equiv r$), the $g - z$ color profile from *HST* ACS and from the SDSS, and the deviations of the individual profiles in the bottom panel from the best Sérsic function fit shown by the black curve (n is in the key). The Sérsic function is fitted between the vertical dashes crossing the profiles in the top and bottom panels. Note that $a_4 > 0$ implies disky isophotes and $a_4 < 0$ implies boxy isophotes. The profile data are color coded so that blue corresponds to B band, green corresponds to g or V band, red corresponds to R or I band, and brown corresponds to H or K band. These are the brightest core galaxies in Virgo. Inside the core of NGC 4486, the apparent gradients and discontinuities in ϵ and P.A. may be due to contamination of the photometry by the AGN and jet.

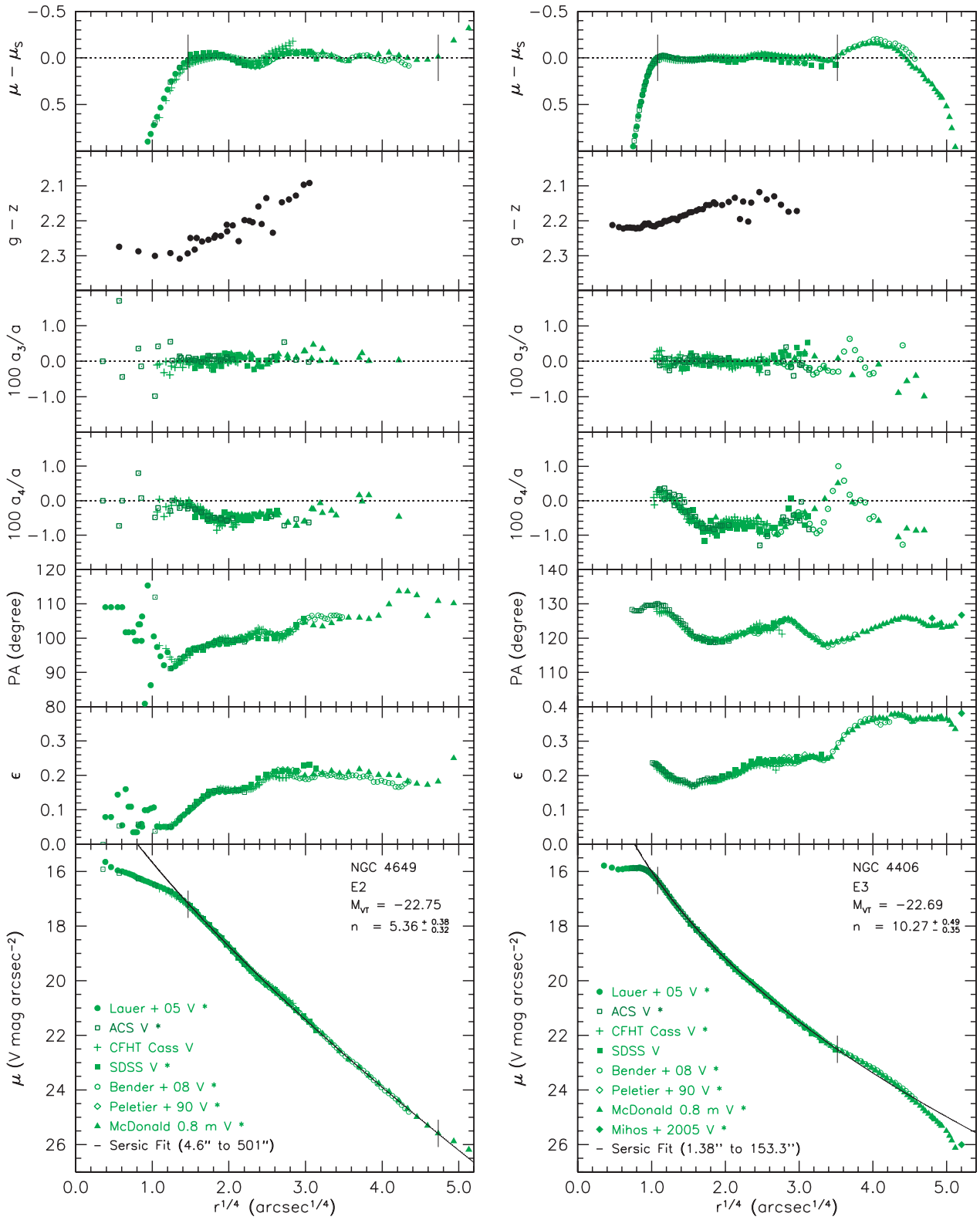

Figure 12. Photometry of Virgo cluster core ellipticals. Inside the core of NGC 4406, the surface brightness drops slightly toward the center, making this a "hollow core" galaxy (Lauer et al. 2002). The outer profile of NGC 4406 is affected by many bracketing galaxies (see the text and Figure 1 in Elmegreen et al. 2000).

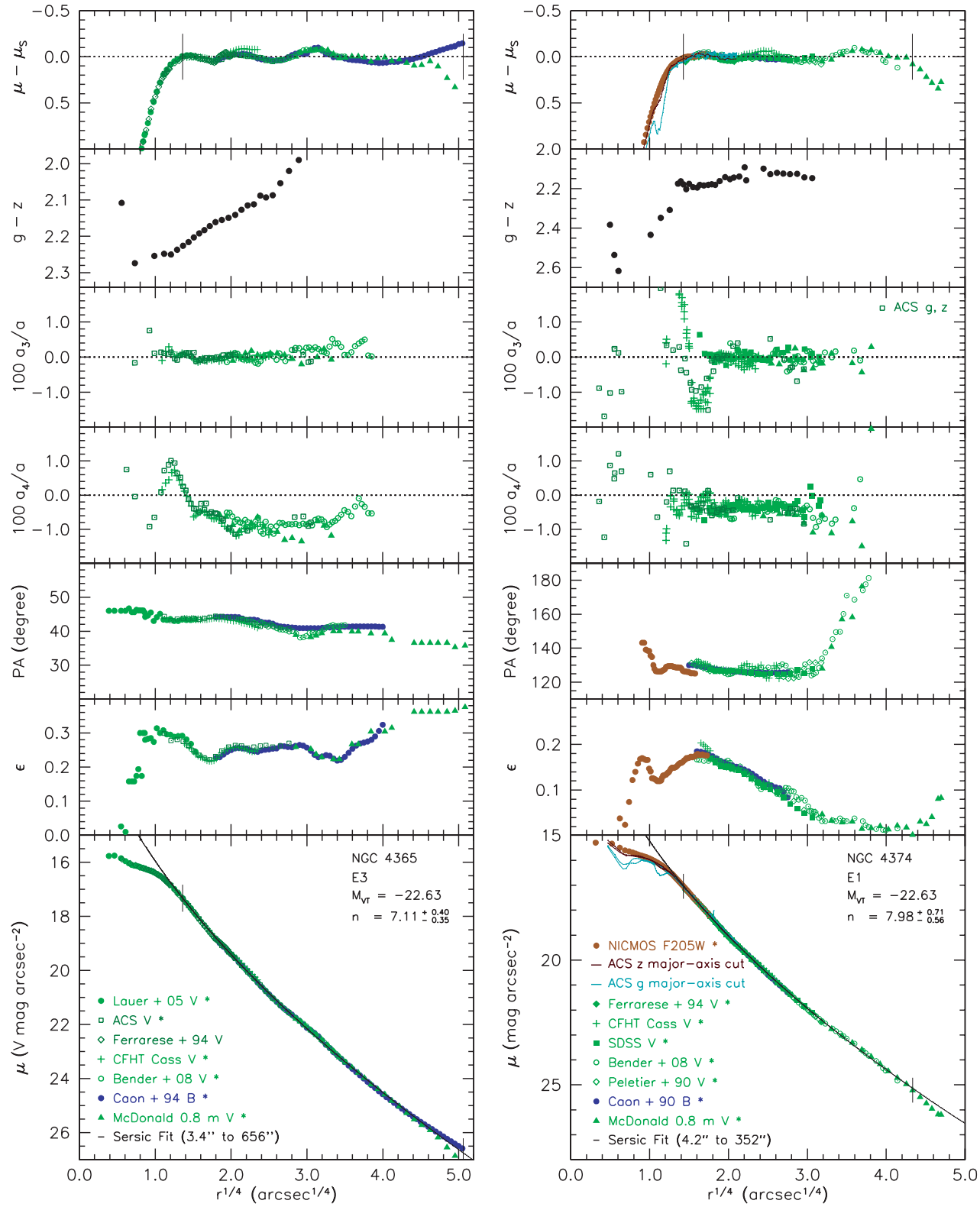

Figure 13. Photometry of Virgo cluster ellipticals with cuspy cores. For NGC 4374, the ACS *g*-band (folded) cut profile illustrates the well-known dust features (Véron-Cetty & Véron 1988; Jaffe et al. 1994; van Dokkum & Franx 1995; Bower et al. 1997; Ferrarese et al. 2006a, and references therein), but the *HST* NICMOS F205W profile is almost unaffected by absorption.

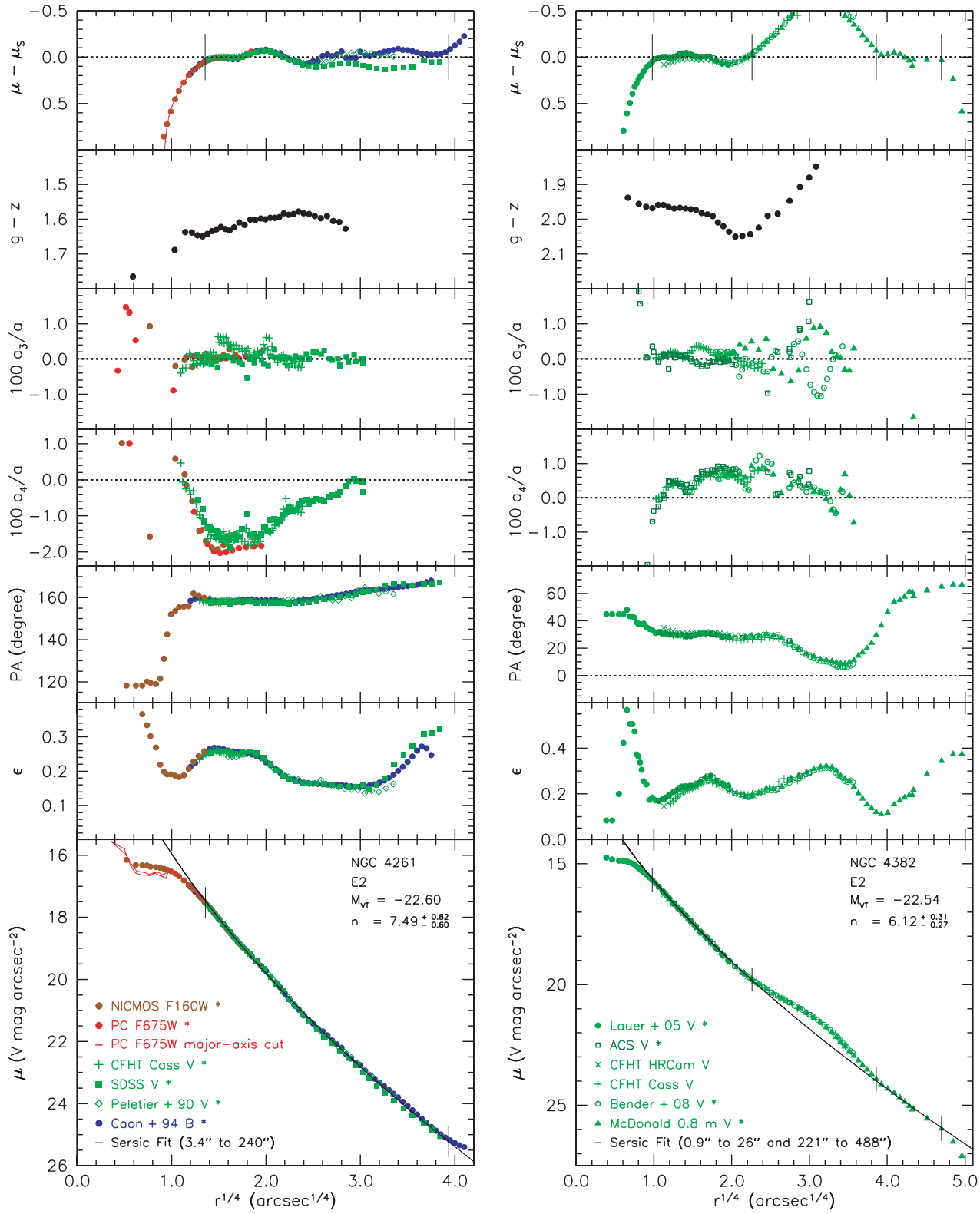

Figure 14. Photometry of elliptical galaxies with cuspy cores. The central dust disk of NGC 4261 (Kormendy & Stauffer 1987; Möllenhoff & Bender 1987a, 1987b; Jaffe et al. 1993, 1994, 1996; van Dokkum & Franx 1995; Ferrarese et al. 1996; Martel et al. 2000) is evident in the (folded) PC F675W cut profile. However, the NICMOS F160W profile is almost unaffected by absorption; the identification of the core is not in doubt. NGC 4261 is in the background of the Virgo cluster ($D = 31.6$ Mpc; Tonry et al. 2001). NGC 4382 has a complicated profile that we interpret as the signature of an unrelaxed recent merger (Section 7.5). Two alternative Sérsic fits to the galaxy are discussed in Appendix A; all are consistent with the fundamental plane projections discussed in Section 8.

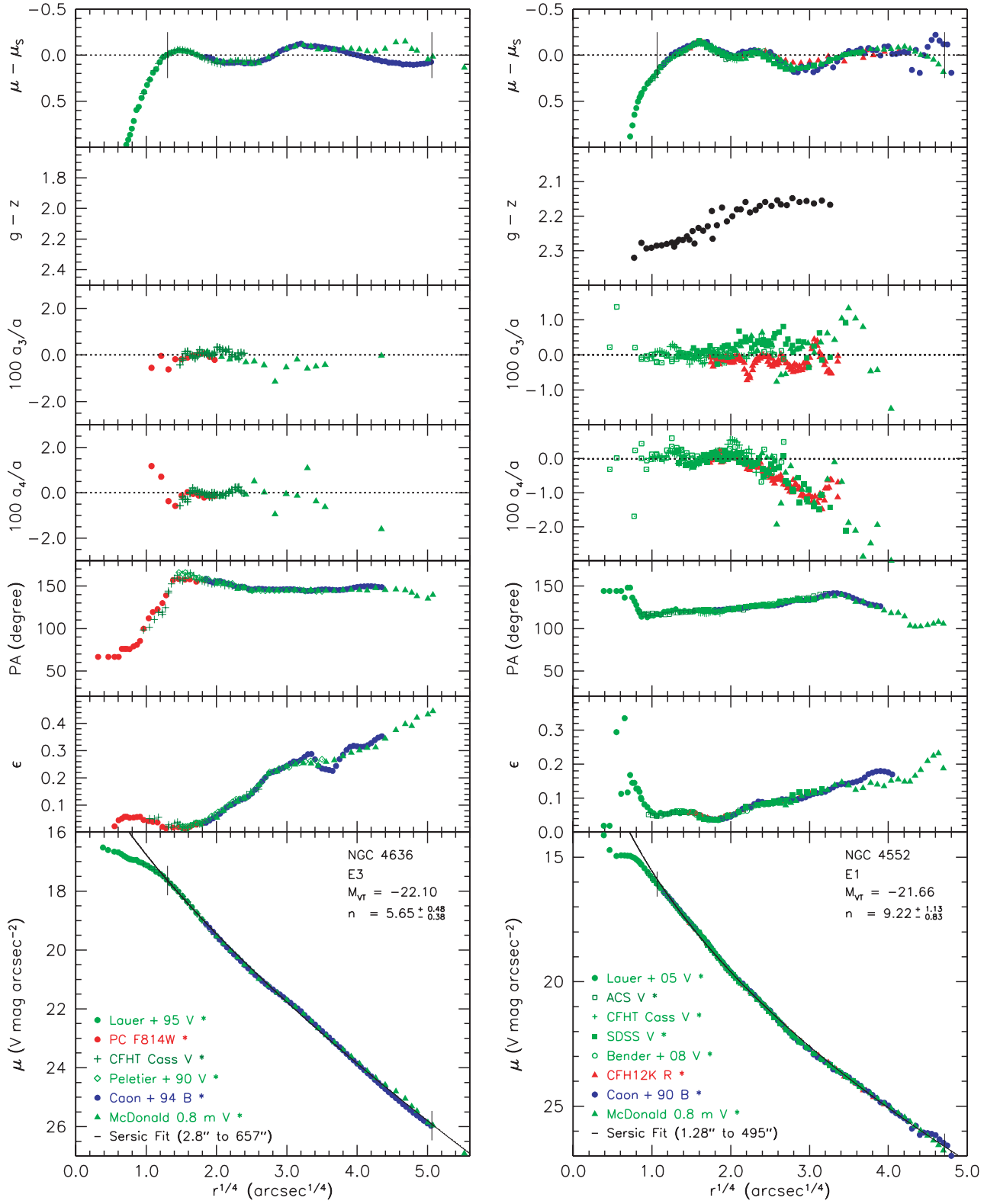

Figure 15. Photometry of the lowest-luminosity core ellipticals in the Virgo cluster.

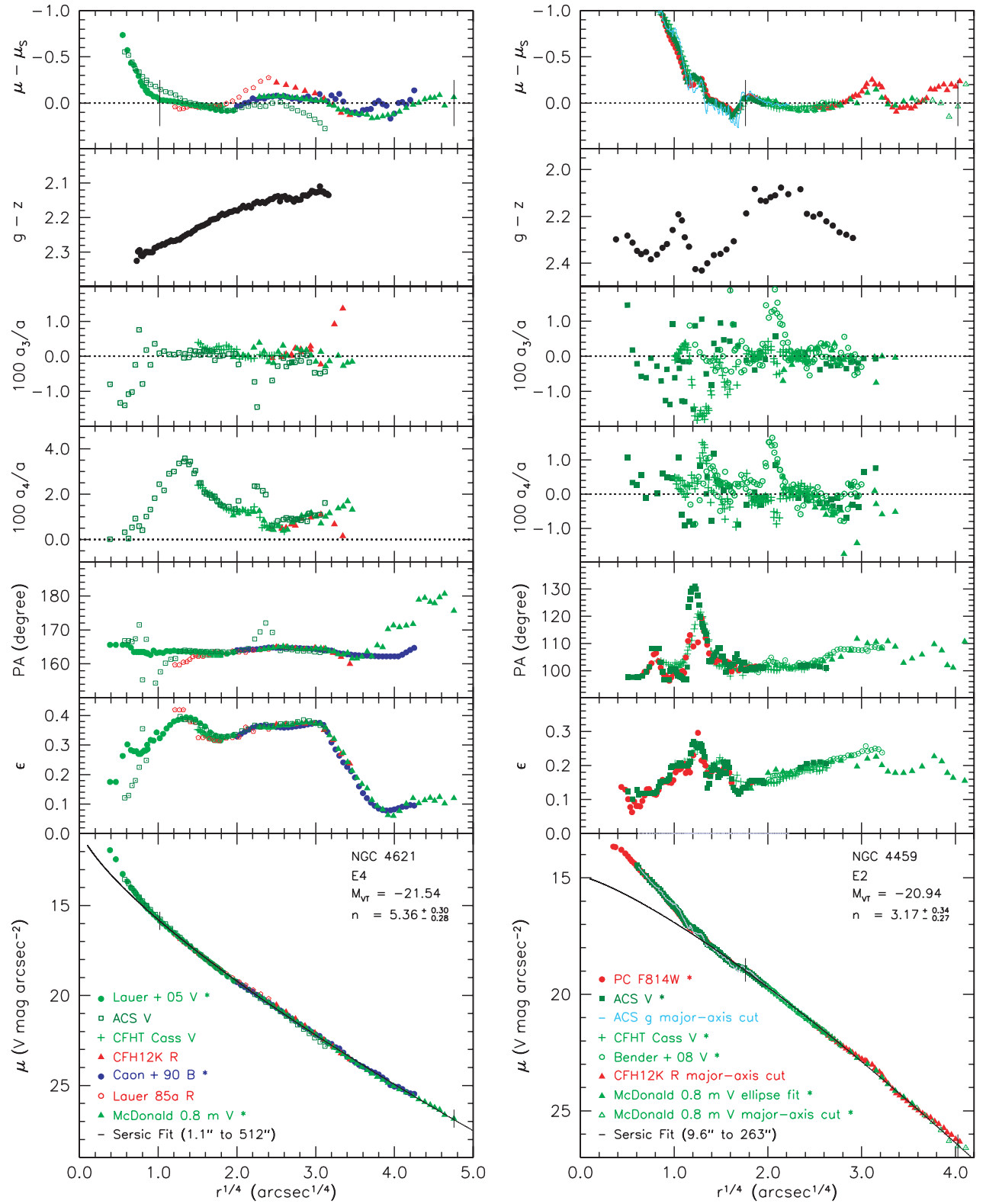

Figure 16. Photometry of the highest-luminosity extra light ellipticals in the Virgo cluster. NGC 4621 is the exception to the correlation between n and core properties discussed in Section 9. NGC 4459 has a prominent dust disk at $1'' \lesssim r \lesssim 10''$ (e.g., de Vaucouleurs 1959; Sandage 1961; Sandage & Bedke 1994; Sarzi et al. 2001; Ferrarese et al. 2006a). Therefore, a major-axis, g-band cut profile is shown as well as the ellipse fit results. It shows that the dust absorption is only ~ 0.3 mag deep and is easily avoided. The profile is fitted only exterior to the dust disk; the Sérsic index is robustly less than 4. There is substantial extra light near the center for any Sérsic fit to the profile outside the dust disk.

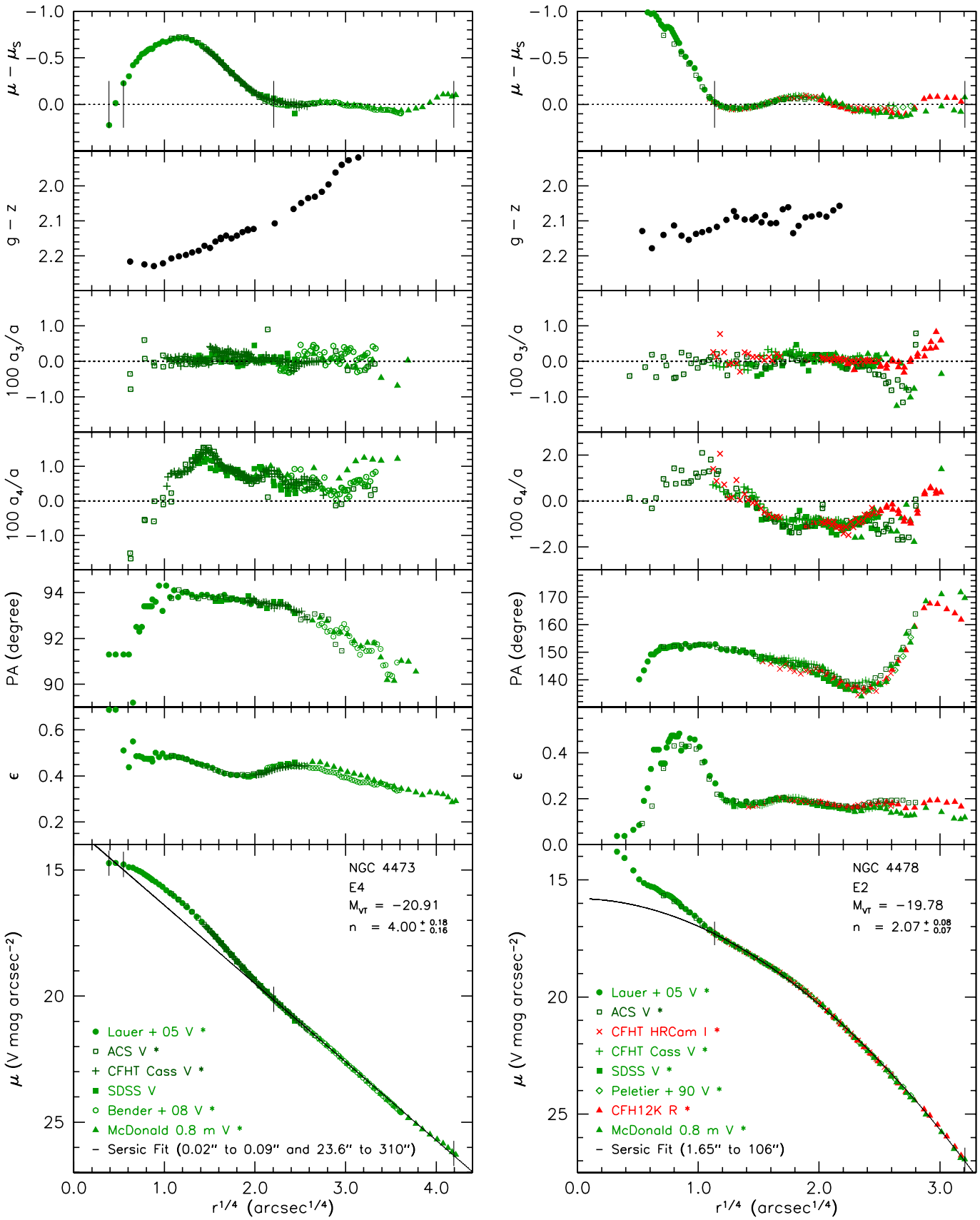

Figure 17. Photometry of Virgo cluster ellipticals with extra light near the center. In NGC 4473, this takes the unusual form of a counter-rotating stellar disk (Cappellari et al. 2004, 2007; Cappellari & McDermid 2005; see Section 9.2 here for discussion).

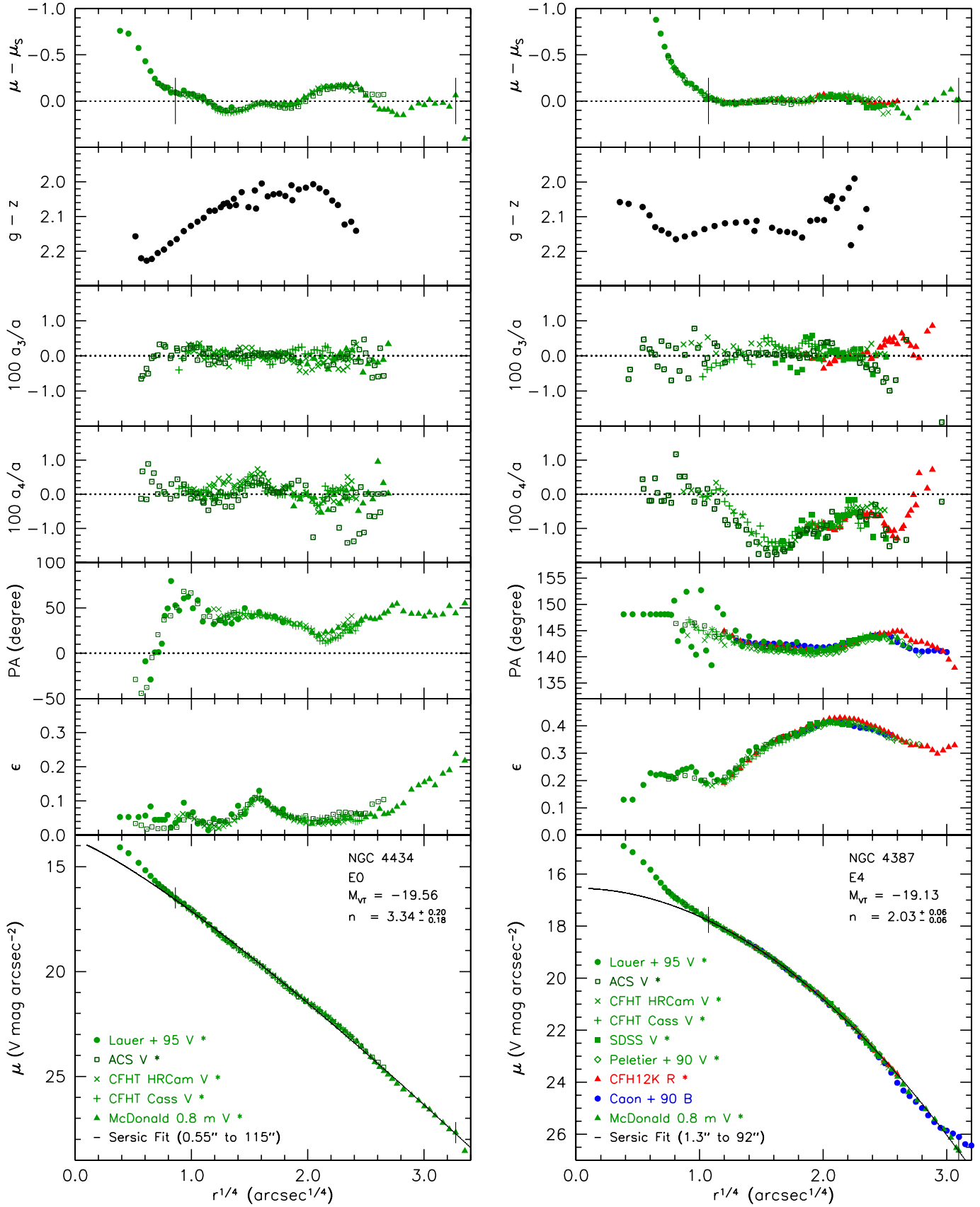

Figure 18. Photometry of extra light ellipticals. NGC 4434 is in the background of the Virgo cluster ($D = 22.4$ Mpc; Mei et al. 2007), but it behaves like other faint ellipticals.

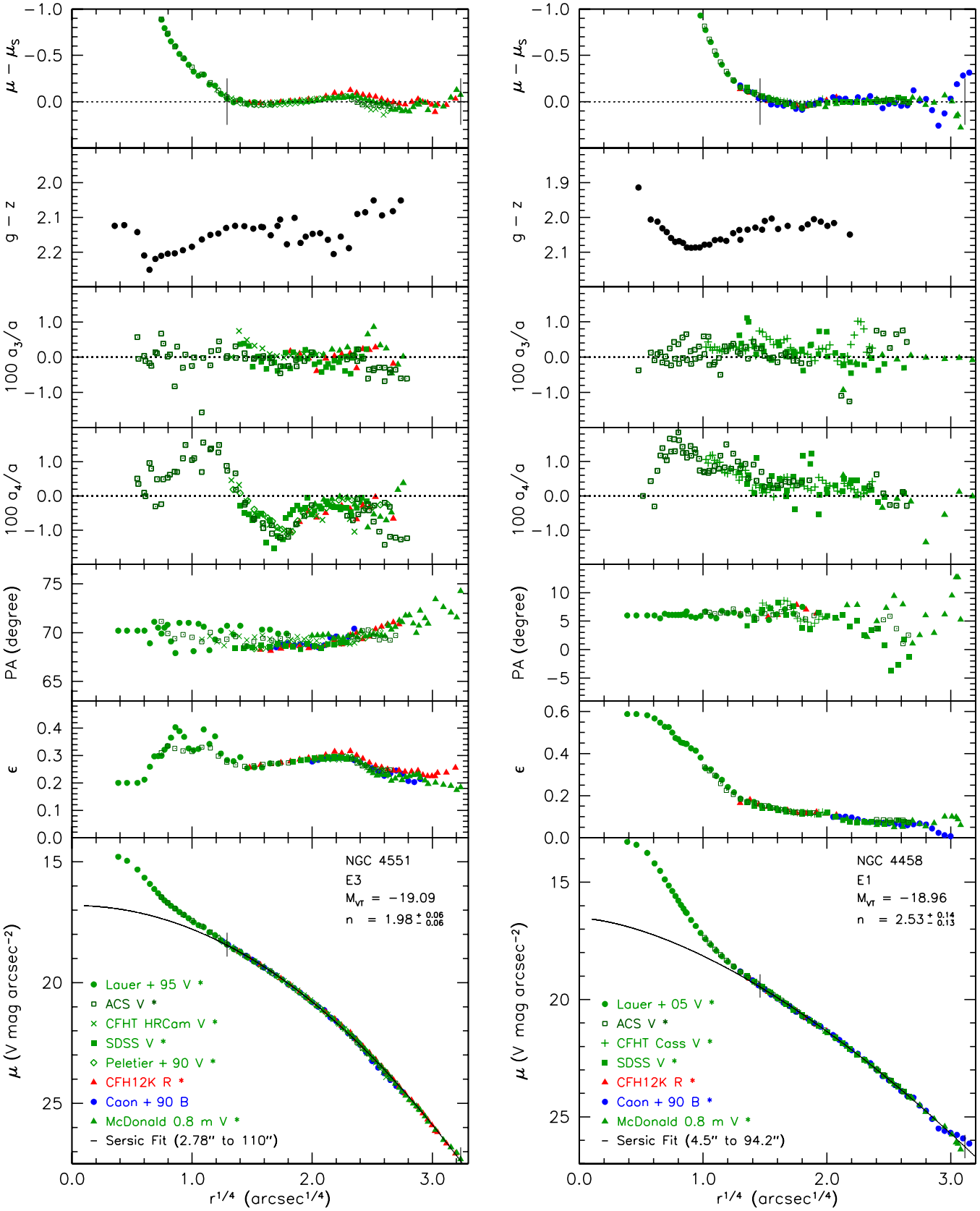

Figure 19. Photometry of Virgo cluster ellipticals with central extra light. Note that the extra light component in NGC 4458—like that in M 32 (Figure 3)—is especially well resolved spatially. "Extra light" is very different from "nuclei," that is, tiny nuclear star clusters such as that in M 33 (Kormendy & McClure 1993; Lauer et al. 1998; see Section 9.7 and Hopkins et al. 2009a for further discussion).

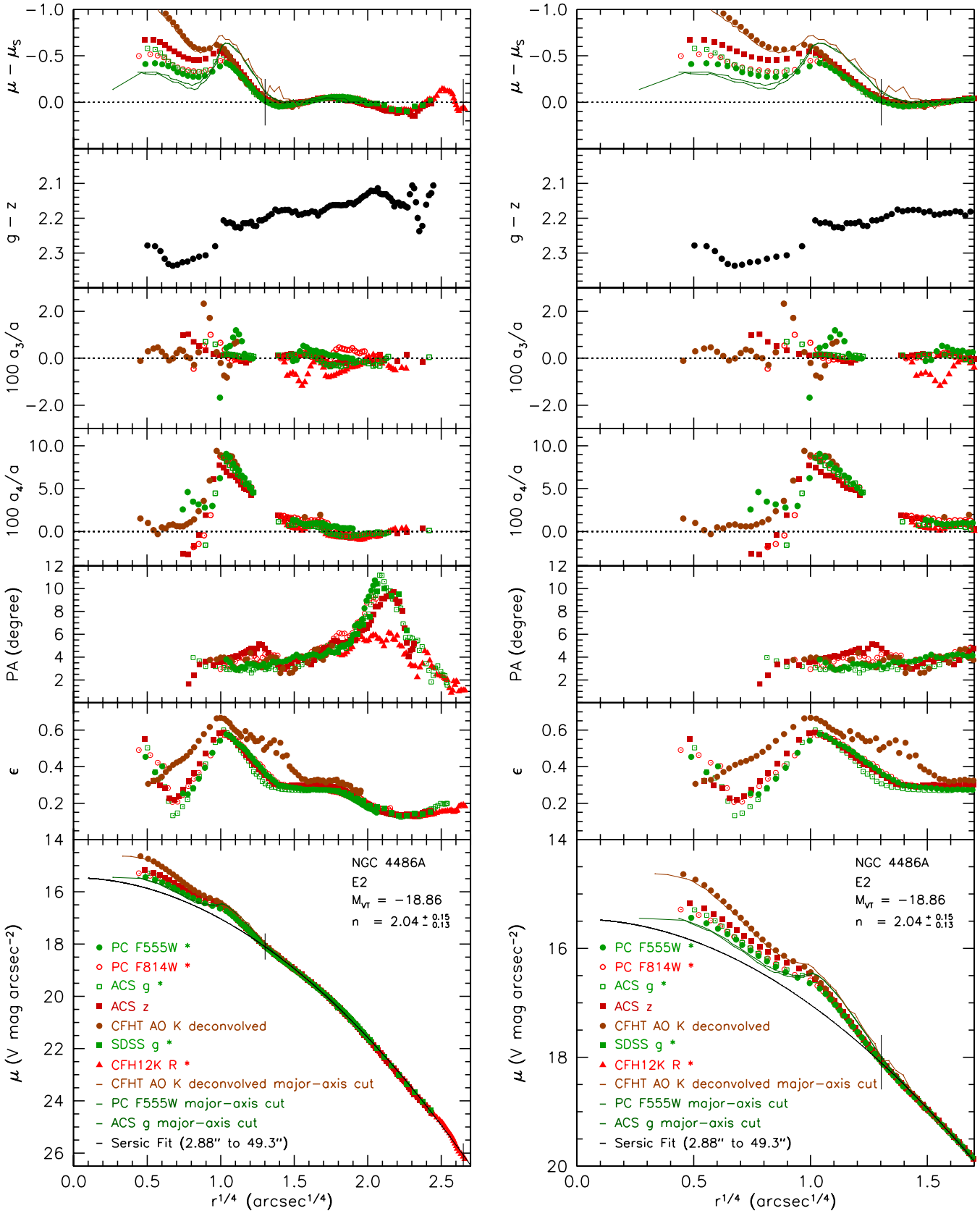

Figure 20. Photometry of Virgo cluster dwarf elliptical NGC 4486A plotted to show the overall profile (left) and an expanded region near the center (right). The major-axis cut profiles derived from the *HST* PC (F555W) and ACS (*g*-band) provide and are illustrated with independent *V*-band zero points. We adopt the mean of these two zero points. The amount of extra light at the center is underestimated by the *V* profiles, because the extraordinarily strong nuclear disk (note that a_4/a reaches almost 10%) has an embedded, edge-on dust lane at radii $r \lesssim 1''$ (Kormendy et al. 2005). The absorption is more obvious in major-axis cut profiles (lines) than in ellipse-fit profiles (points). Also, as expected, the absorption is strongest in *V* and *g*, less strong in ACS *z*, and least strong in the CFHT adaptive optics *K*-band image. But the kink in the profile at $1''$ suggests that there is some absorption even in the *K* band (see Kormendy et al. 2005 for further discussion). The online tables provide both a pure *V*-band profile and one ("NGC 4486AK") that has a *V*-band zero point but the *K*-band profile substituted at $r^{1/4} \leqslant 1.1$.

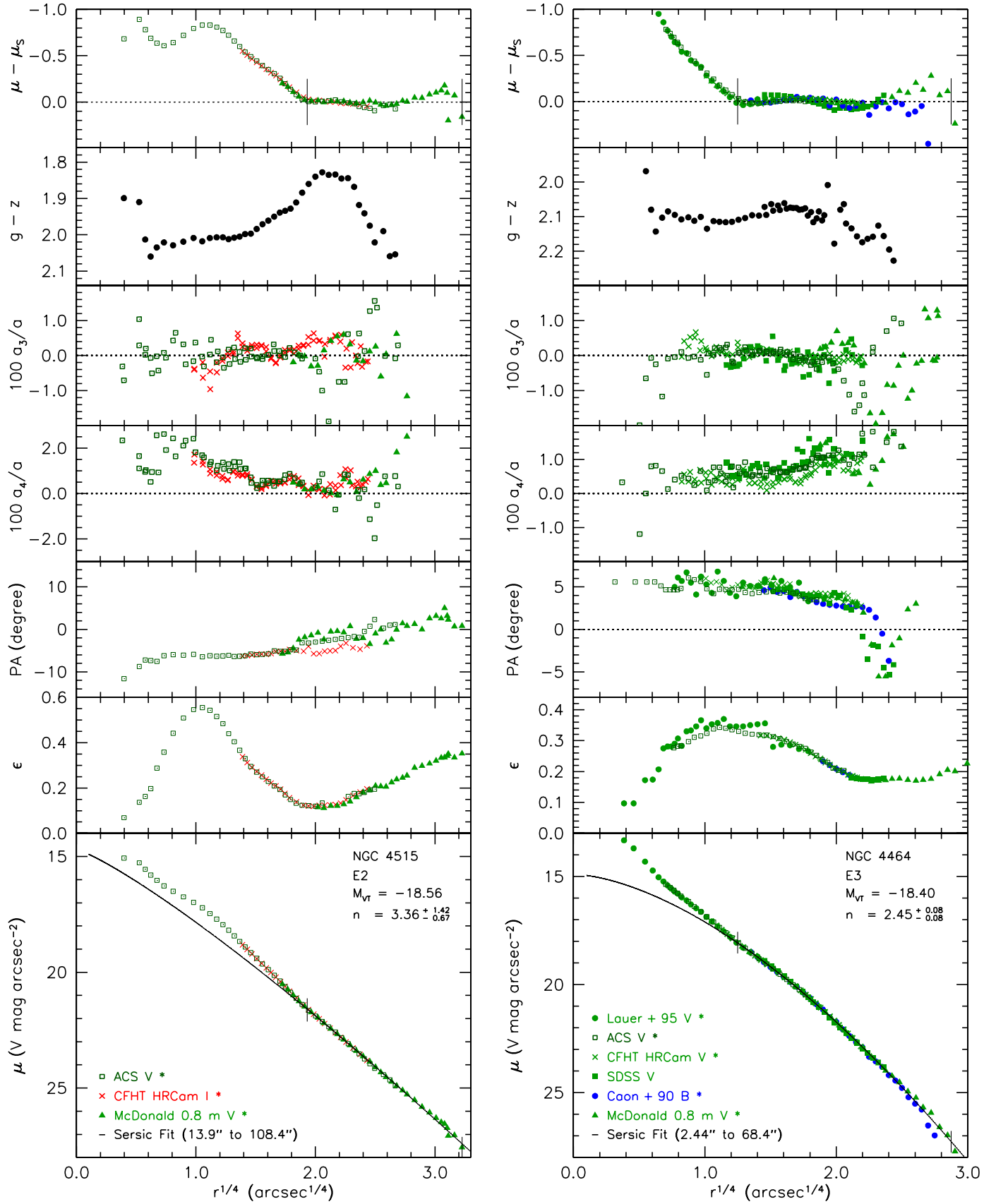

Figure 21. Photometry of Virgo cluster ellipticals with central extra light. For NGC 4415, the choice of fit range is discussed in Figures 62 and 63 (Appendix A). These show two alternative fits to the major-axis profile and a fit to the minor-axis profile. For NGC 4464, the P.A. glitch at $r^{1/4} \simeq 2.4$ is probably not real.

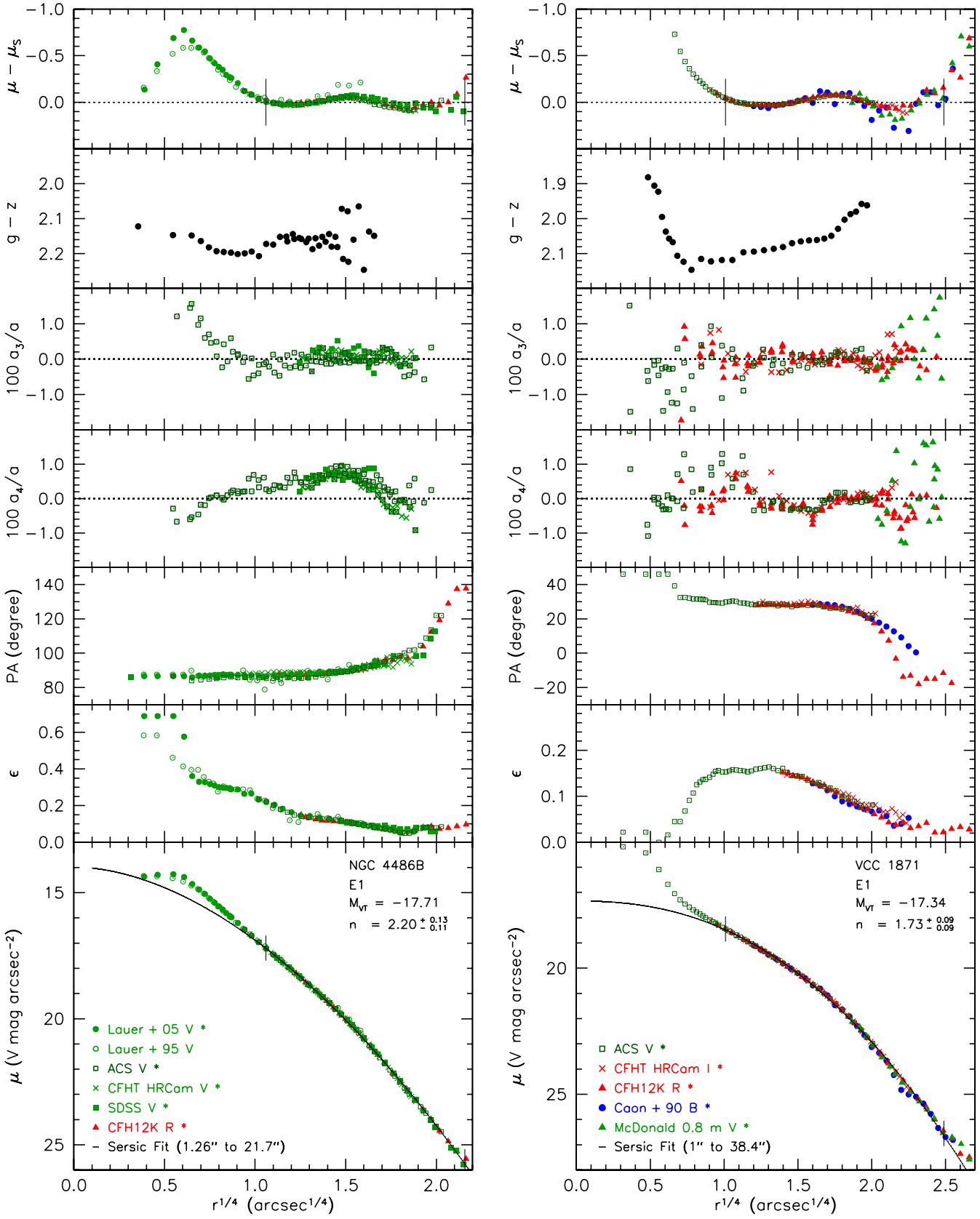

Figure 22. Photometry of Virgo elliptical galaxies. These are typical M 32-like, dwarf ellipticals with extra light near the center. NGC 4486B does not—contrary to appearances—have a core; the central flattening of the profile is an effect of the double nucleus (Lauer et al. 1996). Exterior to the double nucleus, the profile shows extra light, as usual for a low-luminosity elliptical. The isophotes of NGC 4486B twist toward M 87 at large radii. This appears to be real and not an effect of the overlapping isophotes of the larger galaxy. We had to model and subtract the overlapping light from M 87, but it varies on such a large scale, and NGC 4486B is so small, that it is routine to produce images that have flat sky surrounding the smaller galaxy. Four images from three telescopes give consistent P.A. measurements.

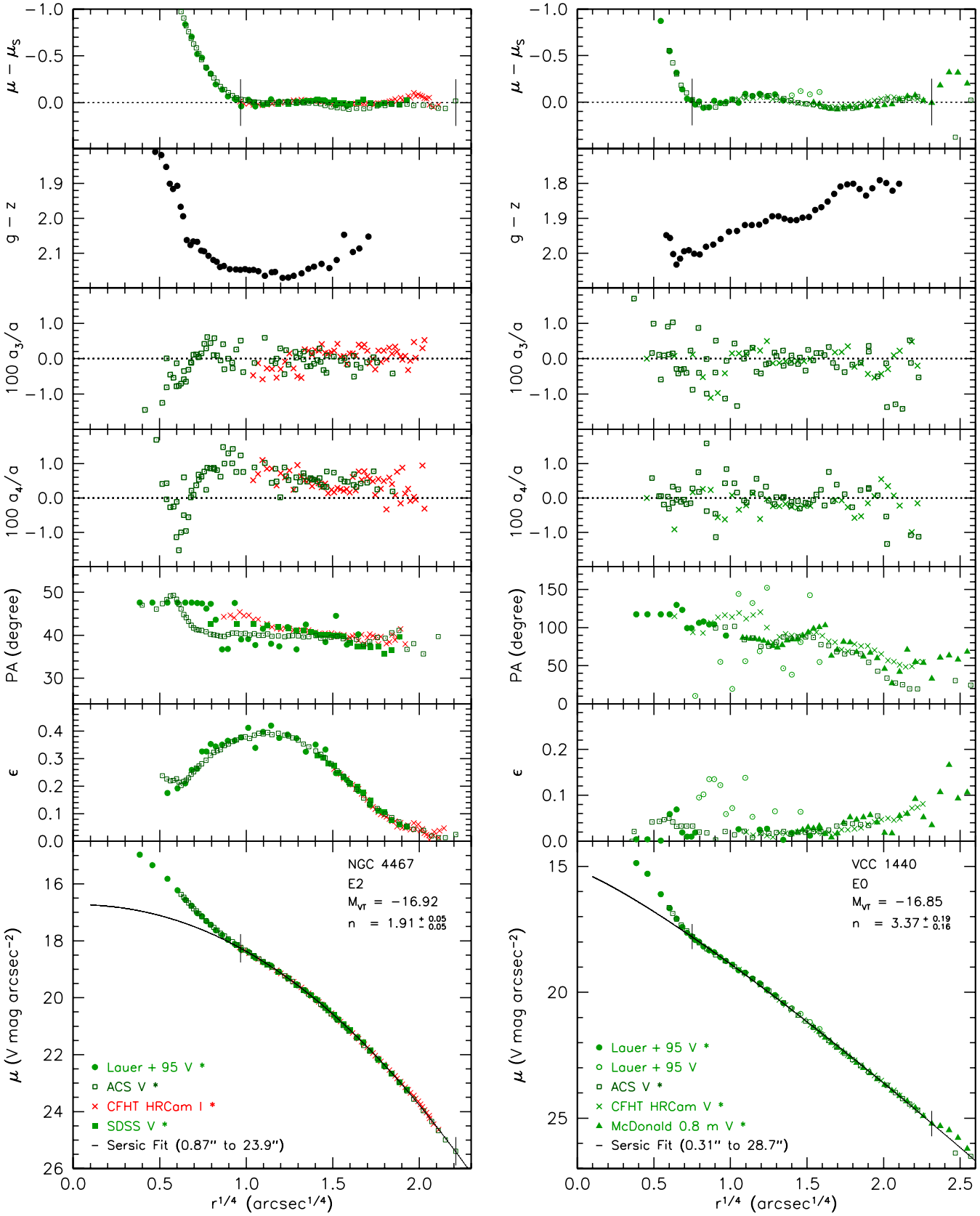

Figure 23. Photometry of Virgo cluster ellipticals. These galaxies and the two on the next page are the faintest ellipticals known in the Virgo cluster. All four have extra light near the center with respect to the inward extrapolations of well-defined Sérsic function fits to the outer profiles. These galaxies are very similar to M 32; recall that M 32 has $M_{VT} = -16.69$ and $n = 2.82 \pm 0.07$.

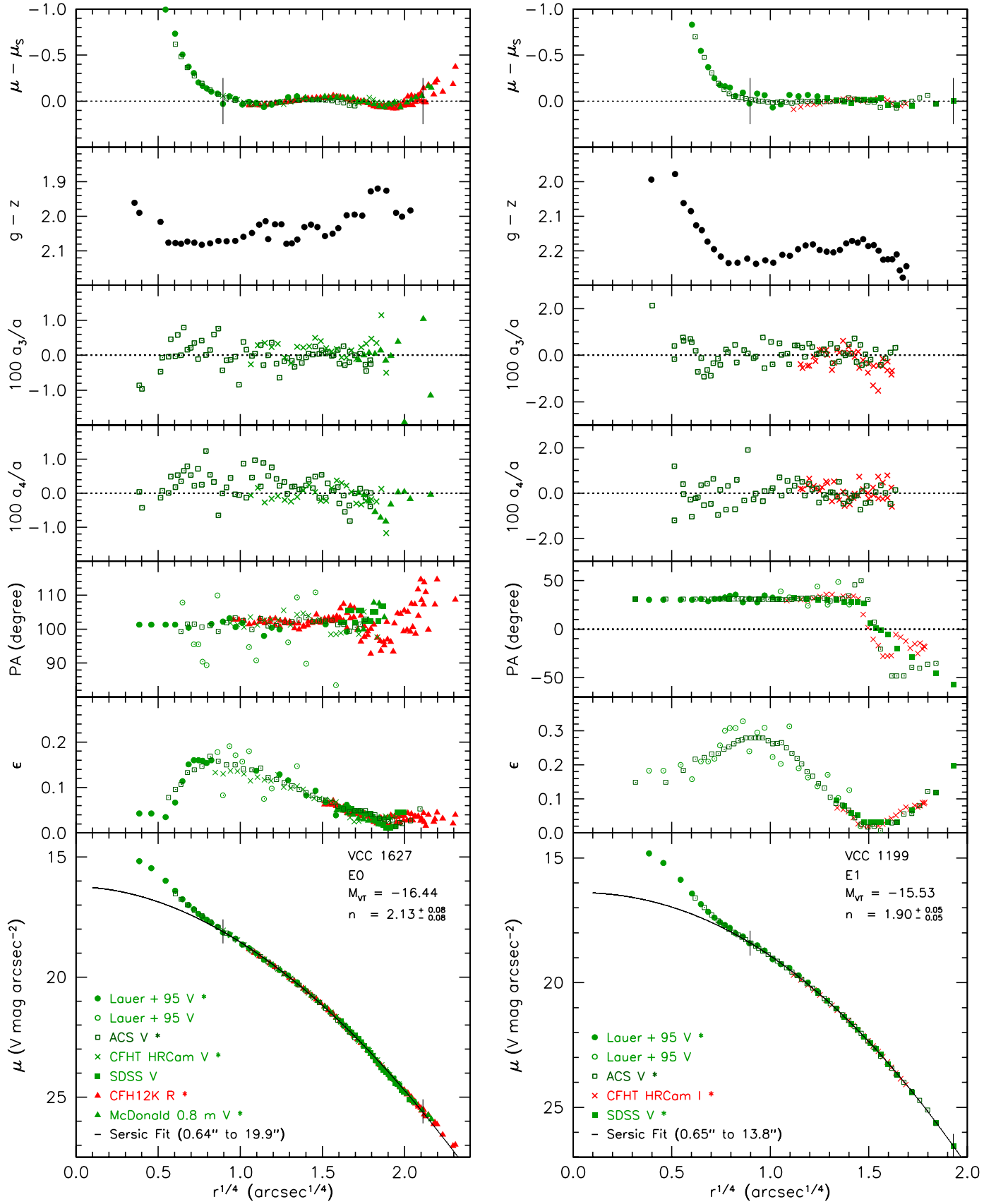

Figure 24. Photometry of faintest known ellipticals in the Virgo cluster. They are slightly fainter than M 32, which has $M_{VT} = -16.69$ and $n = 2.82 \pm 0.07$.

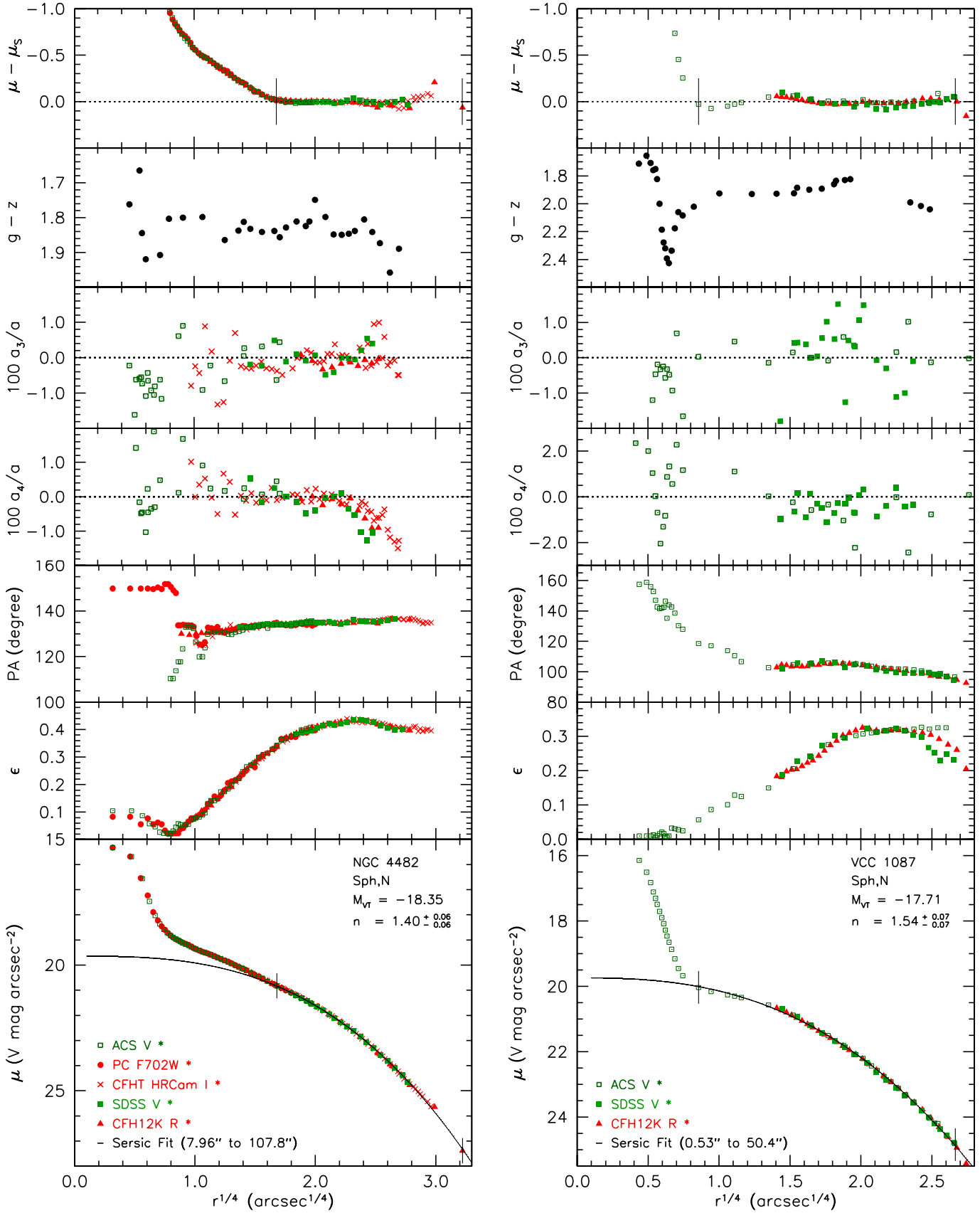

Figure 25. Composite brightness profiles of Virgo cluster spheroidal (Sph) galaxies ordered by total absolute magnitude M_{VT}. Symbols, parameters, and color coding are as in Figures 11–24.

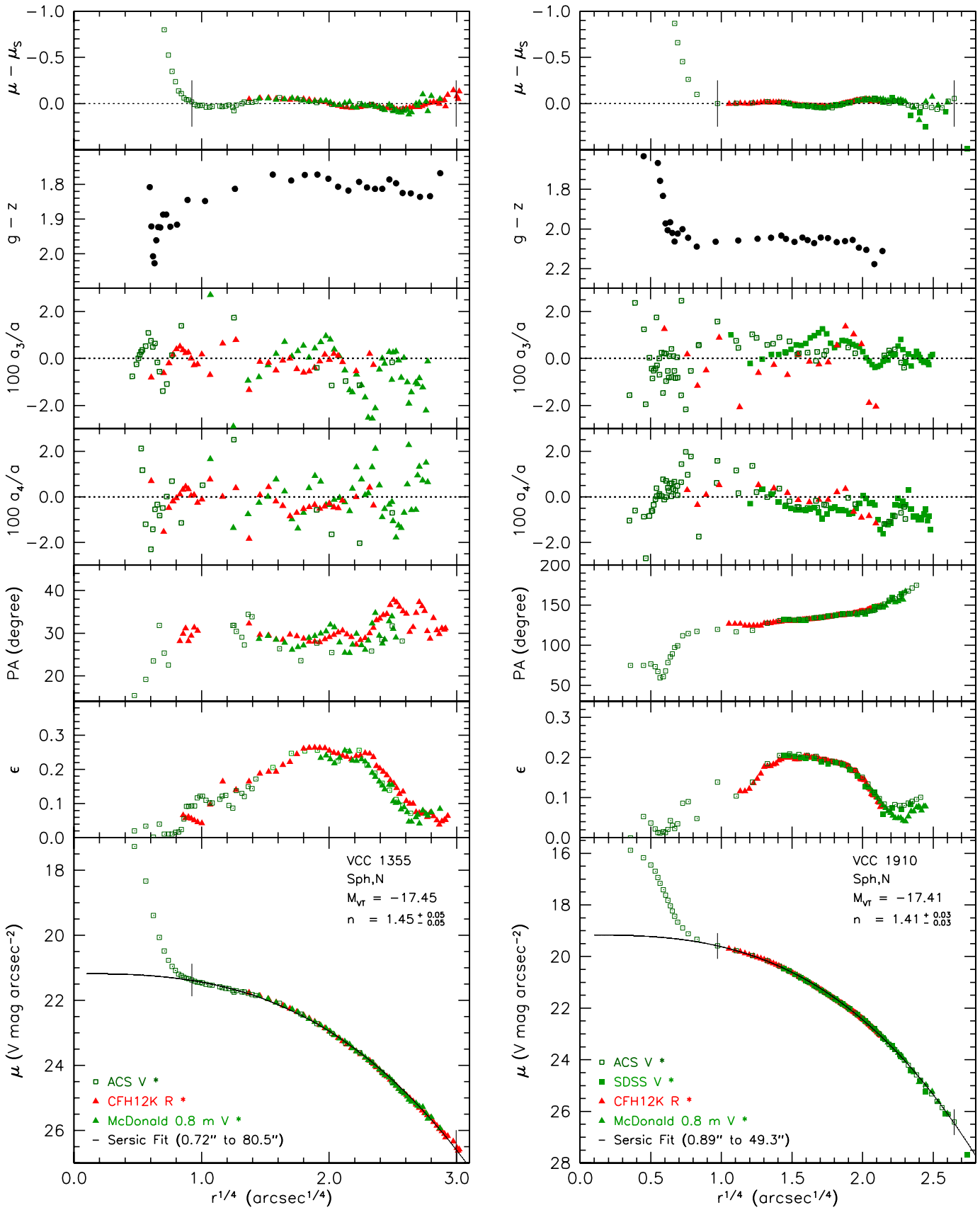

Figure 26. Photometry of Virgo cluster Sph galaxies. In VCC 1910, the outermost part of the P.A. twist and the outer rise in ϵ may be spurious (caused by PSF overlap with a nearby star).

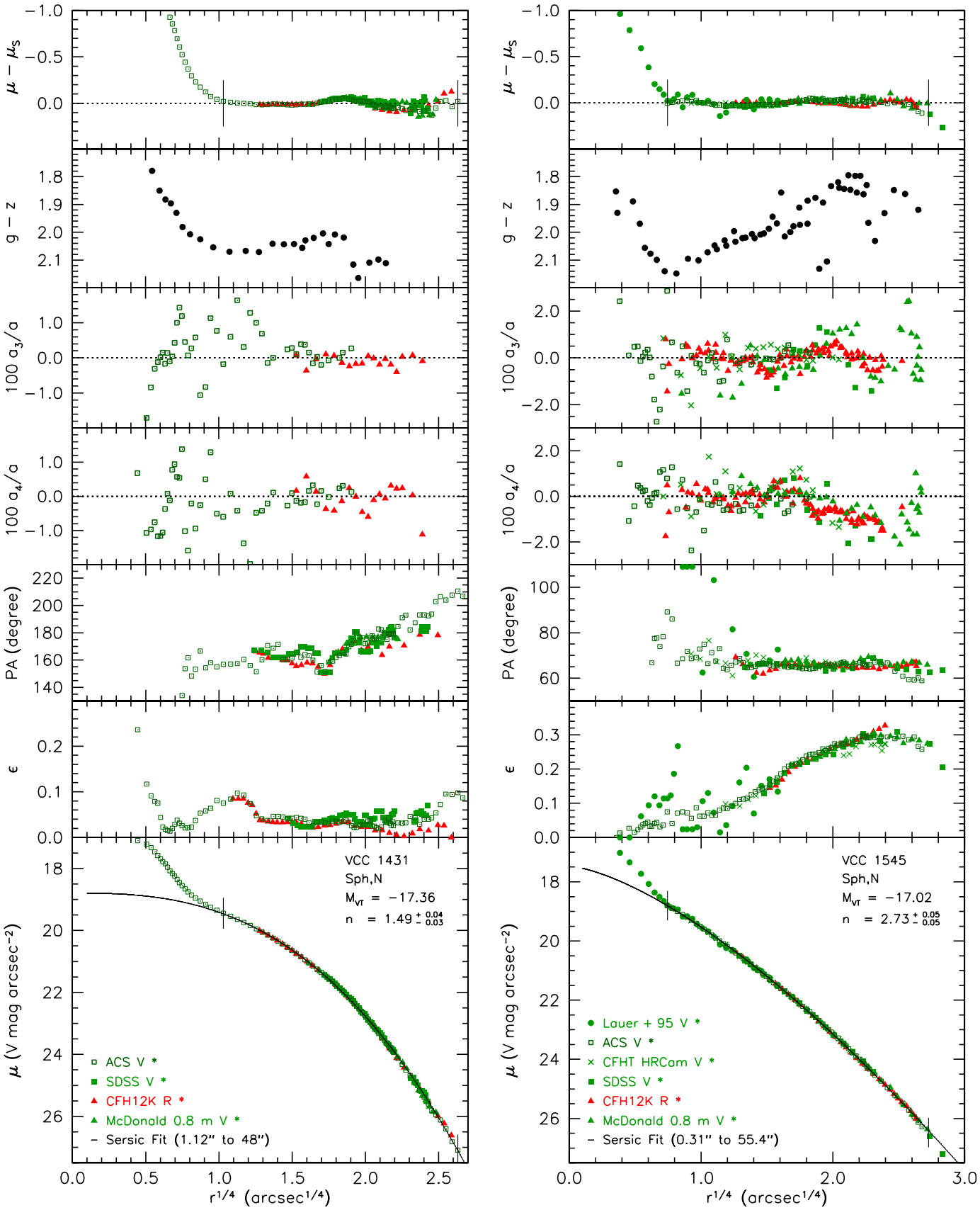

Figure 27. Photometry of Virgo cluster Sph galaxies.

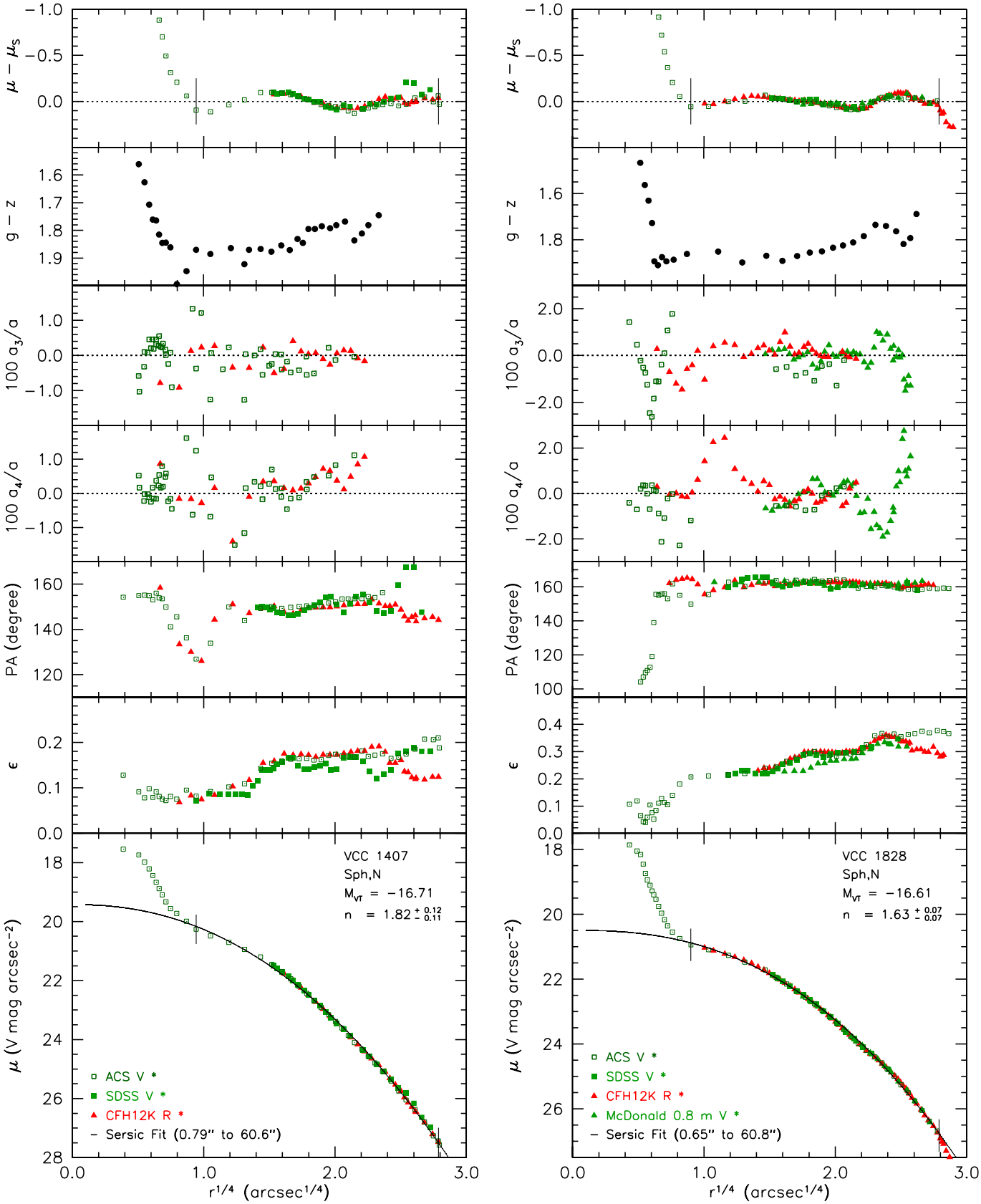

Figure 28. Photometry of Virgo cluster Sph galaxies. The outer CFH12K *R*-band profile of VCC 1828 is not accurate because the galaxy falls on one of the poor CCD chips of the mosaic: the sky values are mottled and the sky subtraction is not as reliable as normal.

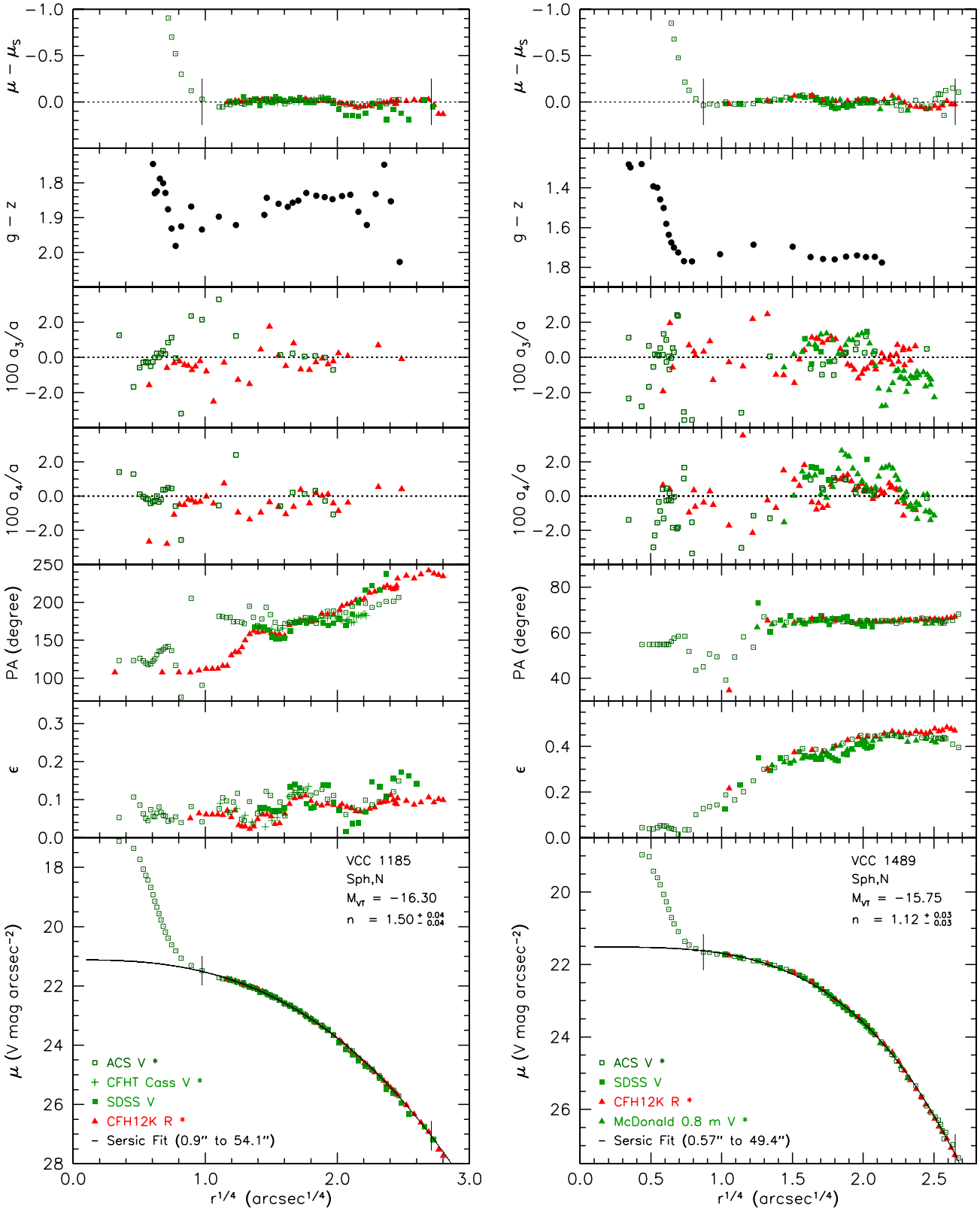

Figure 29. Photometry of Virgo cluster Sph galaxies. VCC 1185 and VCC 1489 have almost the same absolute magnitudes as the faintest dwarf ellipticals in our sample, VCC 1627 ($M_{VT} = -16.44$), VCC 1199 ($M_{VT} = -15.53$), and M 32 ($M_{VT} = -16.69$). But the spheroidals have very different brightness profiles than the ellipticals. Contrast especially the faint extrapolated central surface brightness of the Sérsic fits to VCC 1185 ($\mu = 21.12$ V mag arcsec^{-2}) and VCC 1489 ($\mu = 21.52$ V mag arcsec^{-2}) with the 100-times-brighter values for VCC 1627 ($\mu = 16.24$ V mag arcsec^{-2}) and VCC 1199 ($\mu = 16.38$ V mag arcsec^{-2}) and the still brighter value in M 32 ($\mu = 13.42$ V mag arcsec^{-2}). The dichotomy between E and Sph galaxies is particularly clearcut in central parameters (Section 2.1 and Figures 34–36), although it is also seen in global parameters (Figures 37 and 38). VCC 1489 is the lowest-luminosity Sph galaxy in our sample, which favors spheroidals that most resemble M 32-like ellipticals. Nevertheless, it is brighter than the majority of spheroidals in the Virgo cluster (see Figures 34, 37, and 38).

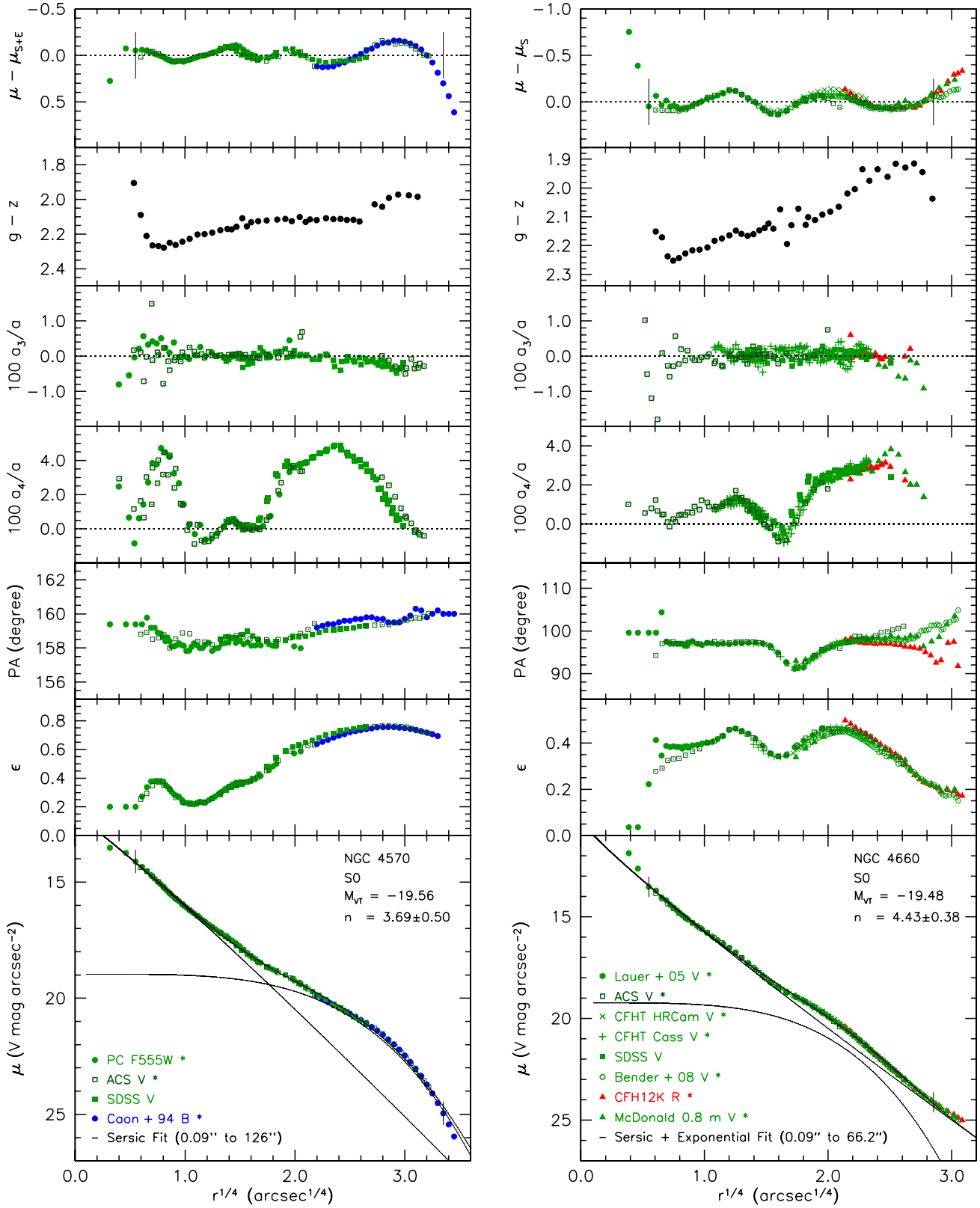

Figure 30. Photometry of Virgo cluster S0 galaxies. Symbols, parameters, and color coding are as in Figures 11–29. The absolute magnitudes quoted in the keys of Figures 30–32 refer to the bulge only (see notes to Table 1). Note the obvious disk signatures in the a_4 profiles of both galaxies. Both galaxies are highly inclined. In contrast, NGC 4489 (next page) is almost round and shows no $a_4 > 0$ disk signature. NGC 4570 obviously looks like an edge-on S0 in images and is normally classified as such. But NGC 4660 is a good example of an S0 galaxy that is traditionally misclassified as an elliptical (Table 1). Its disk contributes relatively little light, and the galaxy is seen far enough from edge-on so that the disk is evident mostly from the a_4 profile. The S0 nature of NGC 4660 was established by Rix & White (1990) and by Scorza & Bender (1995).

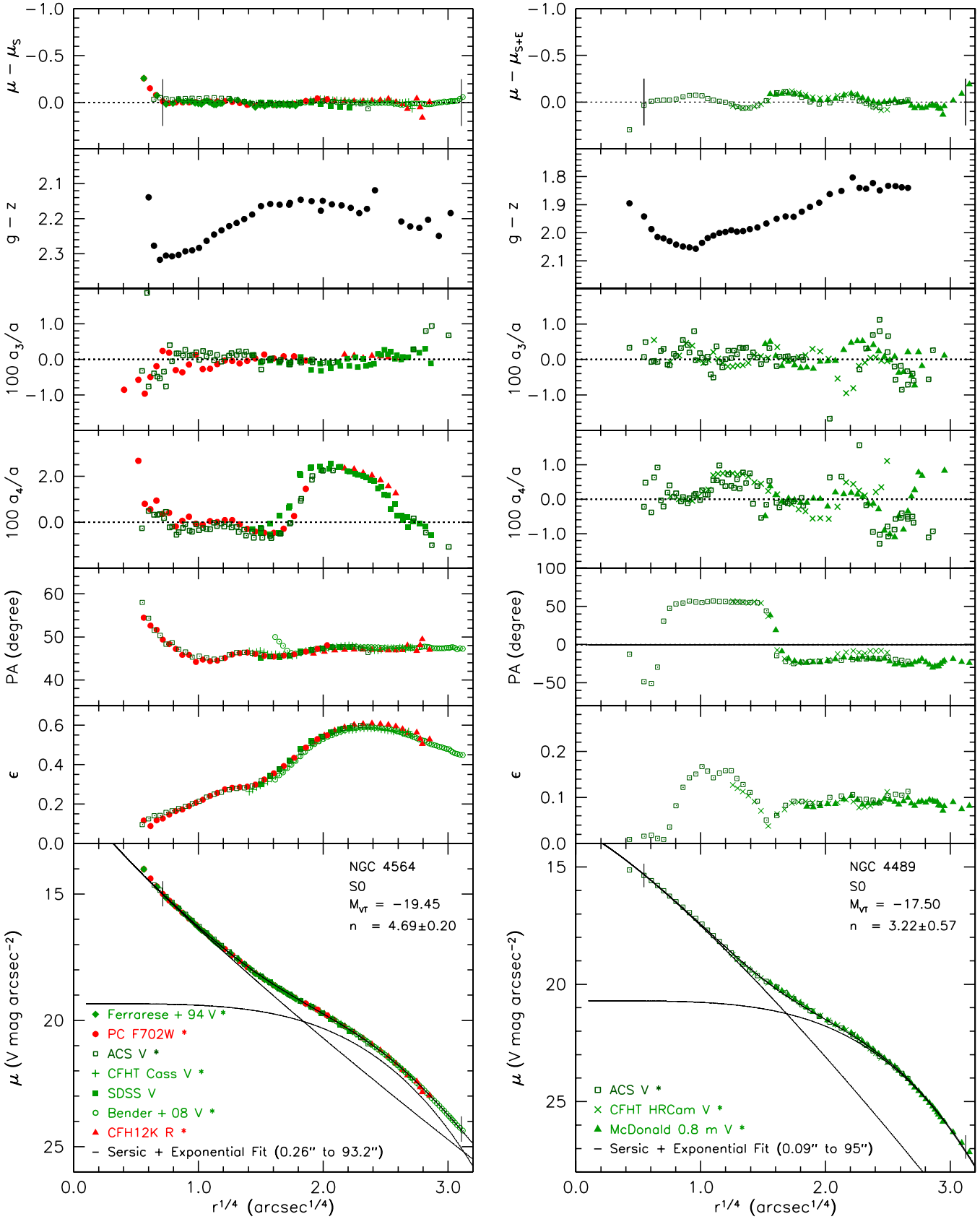

Figure 31. Photometry of Virgo cluster S0 galaxies. Note that the highly inclined galaxy NGC 4564 shows a strong disky $a_4 > 0$ signature, but the much rounder, presumably nearly face-on galaxy NGC 4489 does not (see also Bender et al. 1989; Kormendy & Bender 1996).

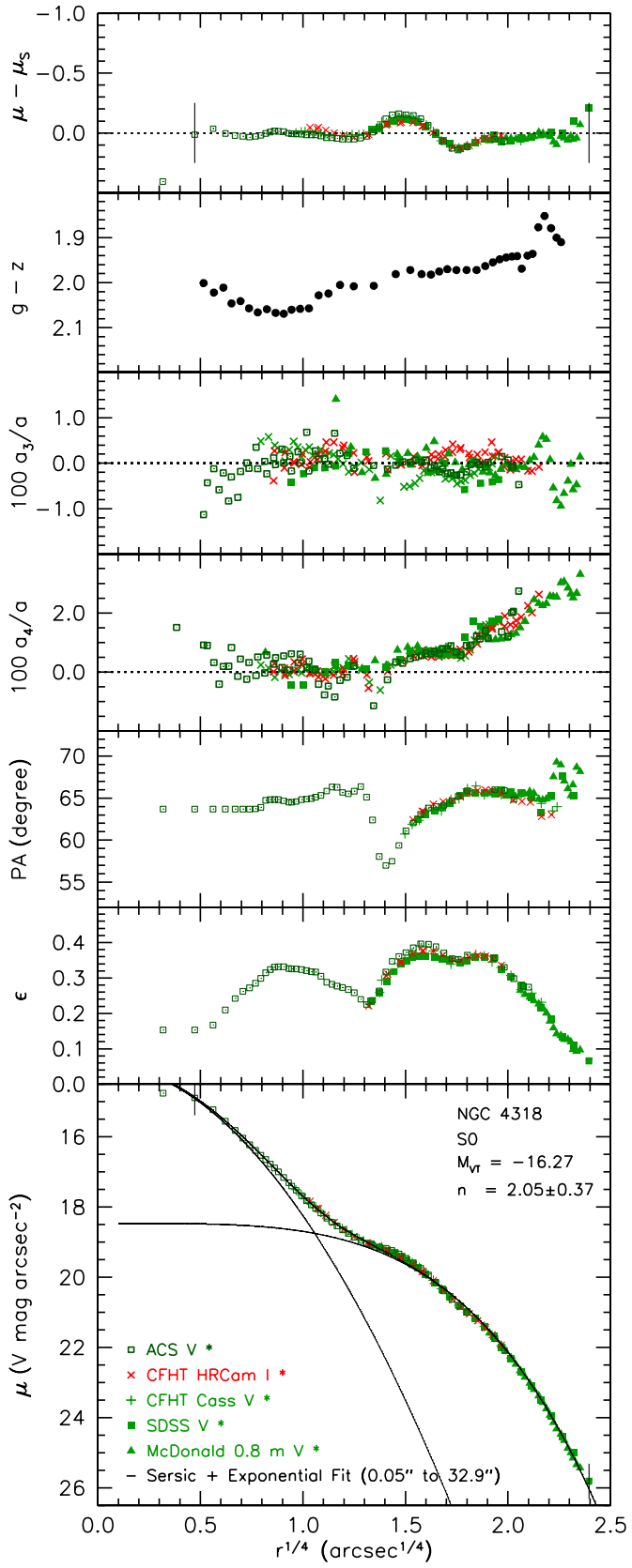

Figure 32. Photometry of Virgo cluster S0 galaxies. NGC 4318 is a good example of a tiny S0 galaxy that is easily misclassified as an elliptical. High-resolution photometry is required to distinguish the small bulge, and spectroscopy is required to verify that the outer component is a disk (see Section 7.6).

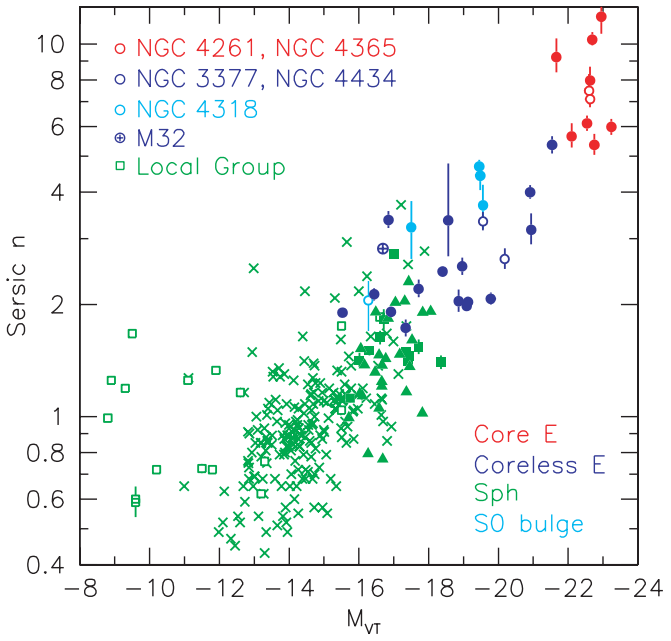

Figure 33. Correlation between Sérsic index n and M_{VT}: red, blue, green, and turquoise points show our core Es, extra light Es, Sph galaxies, and S0 bulges. The green triangles show all spheroidals from Ferrarese et al. (2006a) that are not in our sample. Crosses show all spheroidals from Gavazzi et al. (2005) that are not in our sample or Ferrarese's. The open squares are for Local Group spheroidals (Caldwell 1999; Jerjen et al. 2000). The open symbols refer to galaxies that are not Virgo cluster members.

Challenges to the E–Sph dichotomy are based mostly on two claims: (1) that the correlation between Sérsic index n and galaxy luminosity is continuous from spheroidals through ellipticals and (2) that other parameter correlations are continuous between spheroidals and low-luminosity ellipticals. With more accurate parameter measurements, we can better test these claims. We agree with (1) but not with (2).

Figure 33 shows the correlation between n and M_{VT}. Blind to the E–Sph distinction shown in Figures 34–39, we would conclude that the n–M_{VT} correlation is continuous over all luminosities. But this does not prove that E and Sph galaxies are related. If they are different, then Figure 33 just tells us that the n–M_{VT} correlation is not sensitive to the physics that makes them different. There are other, similar correlations. Viewed morphologically blindly, E, Sph, and even Im galaxies are continuous in the correlations between metallicity and galaxy luminosity or velocity dispersion (Bender 1992; Bender et al. 1993; Mateo 1998; Tremonti et al. 2004; Veilleux et al. 2005). Again, this does not mean that E, Sph, and Im galaxies are the same. The conclusion is that gravitational potential well depth and not the details of galaxy structure governs the degree to which metals returned to the interstellar medium during stellar evolution are retained by a galaxy (Dekel & Woo 2003). So all galaxies roughly satisfy the same metallicity–luminosity correlation. Looking at the correlations with morphology in mind, Mateo (1998) and Grebel (2004) find that Sph galaxies are slightly more metal-rich than Im galaxies of the same luminosity. Similarly, ellipticals generally have higher Sérsic indices than spheroidals of the same luminosity.

To distinguish galaxy types, we need to use all parameter correlations. We need to find out which ones are sensitive to formation physics. Given how the E–Sph dichotomy was discovered, we expect that some of the relevant correlations will involve nearly-central surface brightnesses and radii.

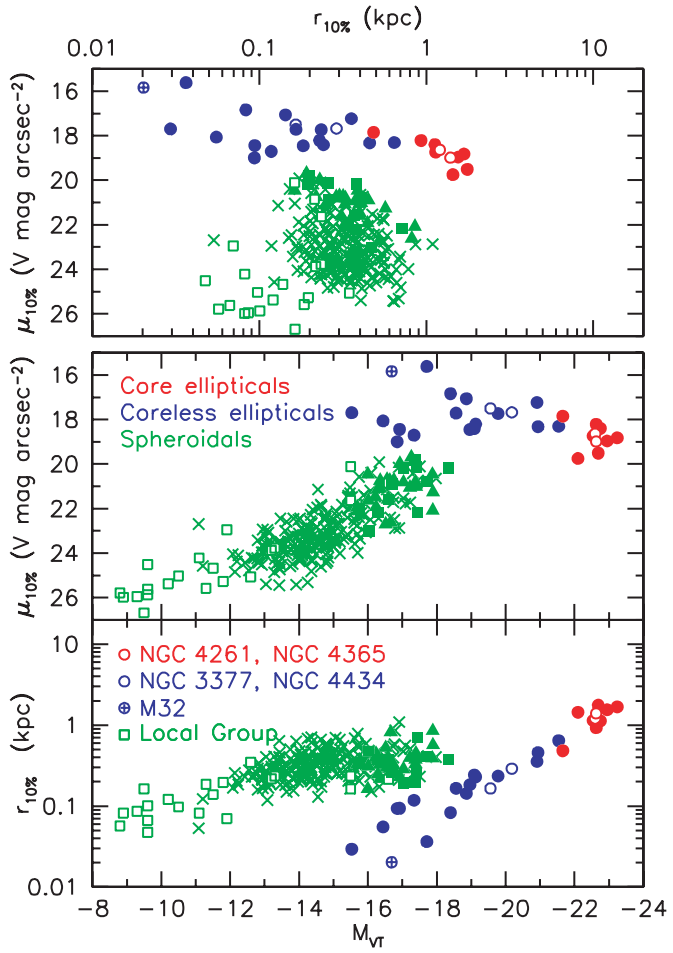

Figure 34. "Central" parameter correlations for the main bodies of elliptical and spheroidal galaxies. Here $r_{10\%}$ is the major-axis radius of the elliptical isophote that contains 10% of the light of the galaxy and $\mu_{10\%}$ is the surface brightness at that radius corrected for Galactic extinction. The 10%-light radius is approximately the smallest radius that is outside the nucleus in Sph galaxies and outside cores and extra light in Es. The center panel shows $\mu_{10\%}$ vs. total V-band absolute magnitude M_{VT}. The bottom panel shows $r_{10\%}$ vs. M_{VT}. The symbols are as in Figure 33. The open squares are Local Group spheroidals from Mateo (1998) and McConnachie & Irwin (2006).

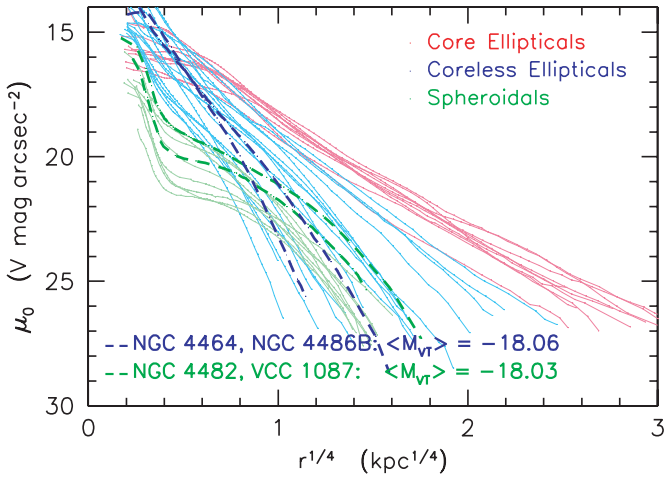

Figure 35. Major-axis profiles of all E and Sph galaxies in our sample corrected for Galactic absorption and scaled so that radius is in kpc. Plotted with thick dashed lines are the profiles of the two brightest Sph galaxies in our sample and the two extra light ellipticals that have nearly the same mean M_{VT}.

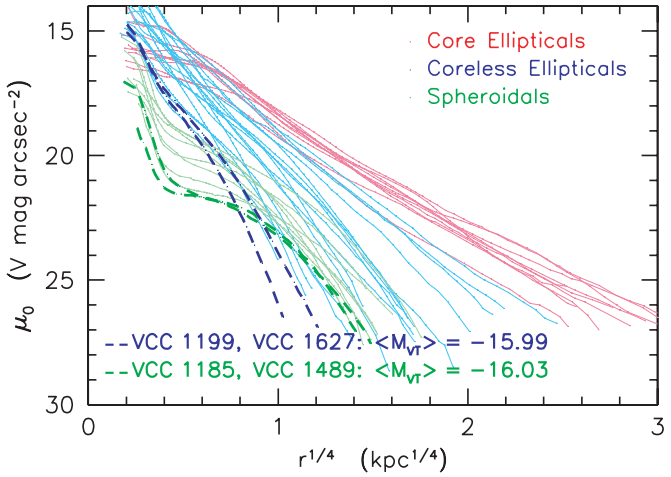

Figure 36. Major-axis profiles of all E and Sph galaxies in our sample corrected for Galactic absorption and scaled so that radius is in kpc. Plotted with thick dashed lines are the two faintest Sph galaxies and the two faintest extra light ellipticals in our sample. They happen to have the same mean M_{VT}.

Figure 34 shows such correlations. We also show in Figures 35 and 36 that E and Sph galaxies can be distinguished by their qualitatively different surface brightness profiles, and in Figures 37 and 38 that we reach similar conclusions using global parameters.

The top panel of Figure 34 shows the surface brightness $\mu_{10\%}$ at the isophote that contains 10% of the light of the galaxy versus the radius $r_{10\%}$ of that isophote. The central panel shows $\mu_{10\%}$ versus M_{VT}. It is analogous to Figure 1, which shows values or limits at the smallest radii reached by the observations. Here, we prefer to measure parameters at the 10%-light radius, even though they are less sensitive to the E–Sph distinction than are parameters measured at smaller radii. There are two reasons. First, these parameters are completely insensitive to PSF smoothing. Second, they measure nearly central properties of the main bodies of the galaxies outside the radii of extra or missing light near the center. Our conclusions are not sensitive to the choice of the fraction 10%; for example 5% gives similar results. We calculated $r_{10\%}$ and $\mu_{10\%}$ for our galaxies directly from the photometry without using analytic fitting functions and without interpreting the profiles.

All panels of Figure 34 show two distinct, often nearly perpendicular sequences of galaxies, as in Kormendy (1985b, 1987b). The high-density sequence consists only of ellipticals. The other sequence initially consisted mostly of spheroidals (called dE or dS0 in Binggeli et al. 1985, Gavazzi et al. 2005, and Ferrarese et al. 2006a) plus a few galaxies that were classified by Binggeli et al. (1985) as low-luminosity, M 32-like Es. We included all of these, because we did not know which were E and which were Sph—or, indeed, whether the two types could be distinguished—until Figures 34–38 were constructed. We included as many E–Sph transition objects identified by other authors as we could. Our sample is strongly biased in favor of spheroidals that are most like ellipticals. Despite this bias, *the E and Sph sequences are clearly distinct. The differences between E and Sph galaxies do not depend on how we measure parameters; E and Sph profiles are qualitatively different (Figures 35 and 36).* We therefore use Figure 34 to reclassify as Sph the few galaxies that have parameters in the Sph sequence but that were called E by other authors (Table 1).

Figures 37 and 38 are analogous to Figure 34 but show global parameters (Table 1). Figure 37 is based on Sérsic fits to

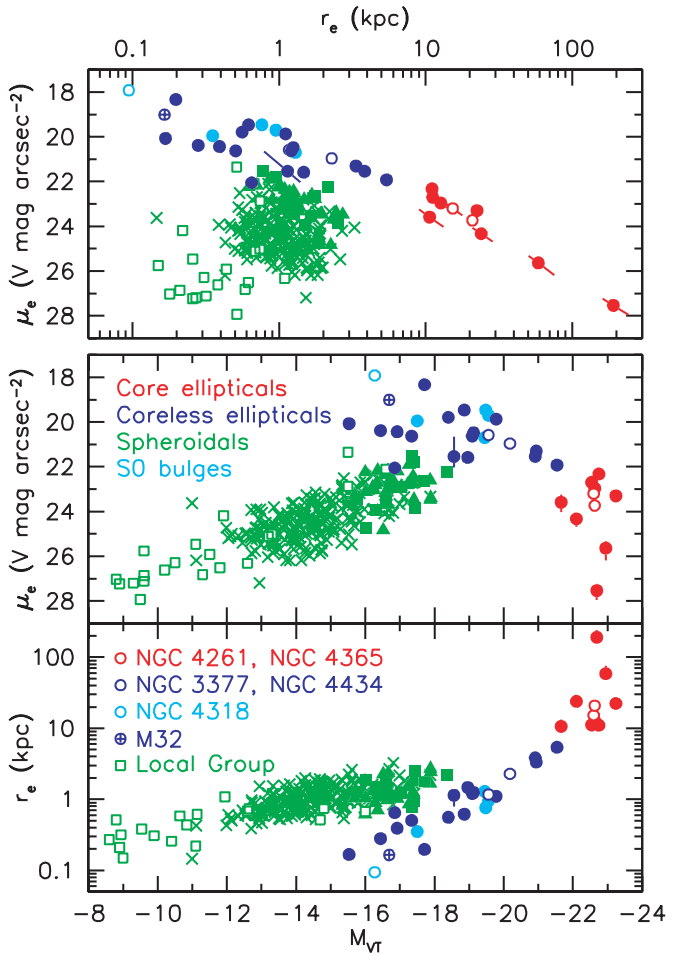

Figure 37. Global parameter correlations for elliptical and spheroidal galaxies and for S0 bulges. The panels are analogous to those in Figure 34, but r_e is the effective radius that contains 50% of the light of the galaxy and μ_e is the surface brightness at r_e. These are the parameters of the Sérsic fits to the major-axis profiles (Table 1); as a result, we can include S0 bulges, which require a profile decomposition that is based on a Sérsic fit to the bulge. Otherwise, the symbols are as in Figures 33 and 34. The E and Sph points in our sample have error bars; most are too small to be visible. The blue point among the green points in Figures 37 and 38 is for VCC 1440. It is clearly classified E in Figure 34, but its position is symptomatic of the fact that the Sph sequence approaches the E sequence near its middle (not its faint end).

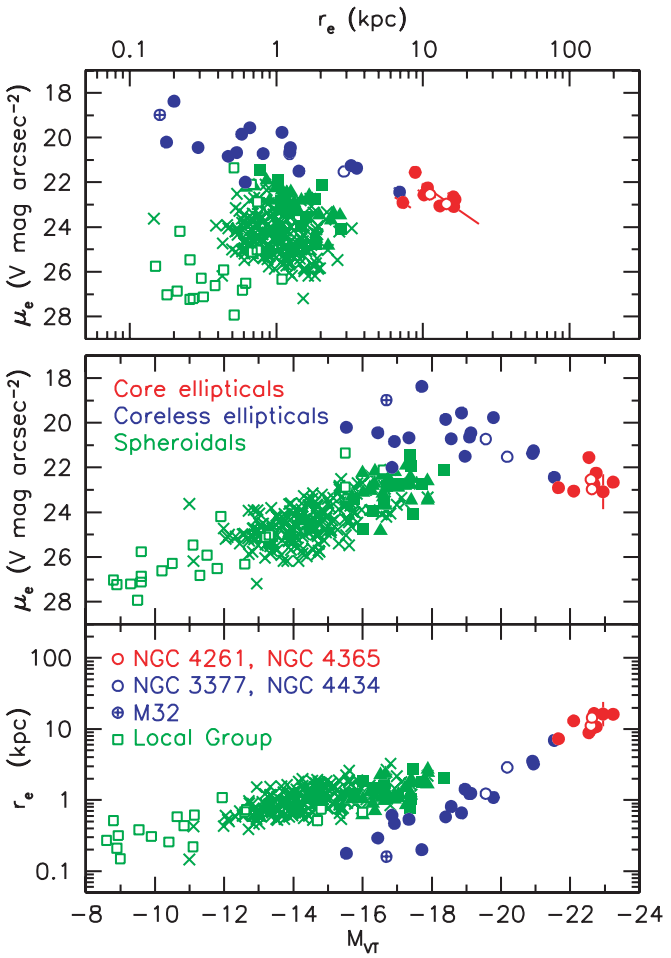

Figure 38. Global parameter correlations for elliptical and spheroidal galaxies. The symbols are as in Figures 34 and 37. Effective surface brightnesses μ_e and major-axis effective radii r_e are calculated by integrating isophotes with the observed brightness and ellipticity profiles out to half of the total luminosity. S0 bulges are omitted, because bulge–disk decomposition requires assumptions that we do not wish to make for this figure—either that the bulge and disk profiles have pre-chosen analytic functional forms or that ellipticity is constant for each of the components. Thus for our sample, r_e, μ_e, and M_{VT} are independent of Sérsic fits. For the other samples, the parameters are based on Sérsic fits and are corrected to the major axis when necessary.

the major-axis profiles. Figure 38 is based on integrations of the brightness profiles and is independent of fitting functions. The top panels show effective brightness versus effective radius—the Kormendy (1977) relation. It shows the fundamental plane close to edge-on. The bottom panels show the correlations of μ_e and r_e with total or (for S0s) bulge absolute magnitude.

Figures 37 and 38 further confirm the distinctions illustrated in Figures 1 and 34–36 between elliptical and spheroidal galaxies. Our results are clearcut because we have a large range in M_{VT} and because we have accurate brightness profiles over large radius ranges. We can derive accurate galaxy parameters, so we can see that the scatter in the μ_e–r_e correlation for ellipticals is small. This confirms the fundamental plane results of Saglia et al. (1993) and Jørgensen et al. (1996). The scatter increases slightly toward the faintest galaxies. This is expected, because they form in fewer mergers than do giant galaxies, so the details of different merger histories matter more.

The scatter in Figures 37 and 38 is small enough and the spatial resolution of *HST* photometry is good enough to show that the lowest-luminosity Virgo ellipticals extend the elliptical galaxy correlations continuously and with almost no change in slope from typical giant ellipticals all the way to M 32. That is, M 32 is a normal, tiny—and hence "dwarf"—elliptical galaxy.

Most important, the sequence of ellipticals is well enough defined so we can see with confidence that the Sph sequence approaches it not at its faint end but rather near its middle. It is not the case, as suggested by Graham & Guzmán (2003), Graham et al. (2003), and Gavazzi et al. (2005), that E and Sph galaxies define a single set of correlations from which giant ellipticals deviate only because they have cores. Cores are "missing" $\sim 1 \pm 1\%$ of the galaxy light (Table 1). They have negligible effects on global parameters.

This confirmation of the E–Sph dichotomy is not new; it is just better defined by our photometry. The middle panels of Figures 37 and 38 can be compared with Figure 1a and the bottom panels can be compared with Figure 1b in Binggeli & Cameron (1991). They did not have *HST* photometry, so the faint part of their E sequence is not well defined and the degree to which M 32 is a normal dwarf elliptical is not obvious. Nevertheless, they,

too, interpreted[6] their results as indicative of a "dichotomy [that] appears strongest in the King core parameter diagrams but [that] is basically *model independent*" (their emphasis). Bender et al. (1992) also emphasized that, in addition to elliptical galaxies, "a second major sequence is comprised of dwarf ellipticals[7] and dwarf spheroidals. These systems populate an elongated locus running at right angles to the main elliptical locus" in the κ fundamental plane parameters defined in their paper. The different loci of E and Sph galaxies in parameter space can also be seen in many other papers (e.g., Capaccioli et al. 1993; Chilingarian et al. 2007, 2008), including the ones that criticize the existence of the dichotomy. How clearly it is seen depends on sample selection (particularly on whether low-luminosity Es are included) and on the spatial resolution available for the lowest-luminosity ellipticals (see Appendix B).

The E–Sph dichotomy is also evident in their different luminosity functions. Our figures, Ferrarese et al. (2006a), Kormendy & Bender (1994), and Binggeli & Cameron (1991) show that a small number of Sph galaxies closely approach the E sequence as defined by global parameters. They are rare—the luminosity function of Sph galaxies falls rapidly toward higher luminosities at $M_{VT} < -18$ (Sandage et al. 1985a, 1985b). But it rises dramatically toward lower L, as hinted at by the samples in Figures 34, 37, and 38 until they reach tiny dwarfs that are rarely studied outside the Local Group. In contrast, the luminosity function of elliptical galaxies has a broad maximum near where the Sph sequence approaches it and is bounded at both bright and faint magnitudes. Dwarfs like M 32 and giants like M 87 are rare. These results are clearly demonstrated in Sandage et al. (1985a, 1985b) and reviewed in Binggeli et al. (1988). Sandage et al. (1985b) conclude that the difference in luminosity functions "suggests that dEs do not form a continuum with the giant Es but rather [that they] form separate families" as argued by Wirth & Gallagher (1984) and by Kormendy (1985b). Binggeli et al. (1988) reach the same conclusion.

We believe that the E–Sph dichotomy is a secure result.

Nevertheless, by using the word "dichotomy," we do not mean to imply there is an empty gap between the E and Sph sequences in global parameter space. A few galaxies are close enough to both sequences so that their classifications are uncertain. This is most evident for VCC 1440, which is clearly in the E sequence in Figure 34 but which plots among the Sph galaxies in Figures 37 and 38. What does this mean?

These galaxies are not a problem for the developing scenario of E and Sph formation. For example, in galaxy harassment, it is not unreasonable to expect that gas dissipation, inflow, and star formation will be most vigorous in the biggest Sph progenitors. These events may not be completely different from the starbursts that accompany dissipative mergers. The same may be true for the biggest starbursts in blue compact dwarfs. So it is reasonable that E and Sph galaxies have fundamentally different formation mechanisms but that a few of the biggest Sphs end up not too different from some ellipticals.

9. PHOTOMETRY RESULTS. II. BRIGHTNESS PROFILES OF ELLIPTICAL GALAXIES

This section presents our results on the systematic properties of the brightness distributions of elliptical galaxies. Interpretations are discussed in Sections 10–12.

[6] They have since changed their minds (Jerjen & Binggeli 1997).

[7] Bender et al. (1992) use the terminology of the Sandage–Binggeli Virgo cluster survey papers (Sandage & Binggeli 1984; Binggeli et al. 1985, and references therein) in which bright spheroidals are called "dwarf ellipticals" (dEs).

9.1. Sérsic Profiles of the Main Bodies of Elliptical Galaxies

Figures 11–24 in Section 7 and Figures 49–67 in Appendix A show that Sérsic functions fit the major-axis brightness profiles of the main bodies of elliptical galaxies remarkably well. This is a resounding confirmation of the studies reviewed in Section 3. With the improved accuracy and dynamic range provided by composite profiles, we now see quantitatively how well this single, three-parameter fitting function works. Appendix A provides details. For nine giant ellipticals with cores (omitting NGC 4382), Sérsic functions fit the major-axis profiles with a mean rms dispersion of 0.042 ± 0.006 mag arcsec^{-2} over a mean surface brightness range of $\Delta\mu_V = 8.7 \pm 0.4$ mag arcsec^{-2}. For the 16 extra light ellipticals (omitting NGC 4515), Sérsic functions fit the major-axis profiles with a mean rms dispersion of 0.045 ± 0.005 mag arcsec^{-2} over a mean $\Delta\mu_V$ that is also 8.7 ± 0.4 mag arcsec^{-2}. That is, Sérsic functions fit the brightness profiles to 4% (sometimes 2%) over a range of 3000 (sometimes > 10,000) in surface brightness.

This result is remarkable because there is no astrophysical basis for the Sérsic function. We know no reason why violent relaxation, dissipation, and star formation should conspire—surely in different ways in different galaxies—to produce so simple and general a density profile. We note in Section 10.4 that merger simulations make profiles that are more nearly Sérsic functions than $r^{1/4}$ laws. The reasons why Sérsic functions work so well deserve further investigation.

Even if we do not have an explanation, the empirical result that Sérsic functions fit well has an important consequence. It allows us confidently to identify and interpret departures from these fits. Otherwise—if the best analytic representation of the profile were only marginally applicable, with profile wiggles above and below that function seen in most galaxies and at many radii—the use of an analytic fitting function would be nothing more than fancy numerology.

We discuss departures from Sérsic profiles in Sections 9.2–9.7.

9.2. Cuspy Cores in Giant Ellipticals: The Definition of Cores

Cores occur in all of the 10 brightest ellipticals in our sample: eight are in Virgo and two are in the background. Our faintest core galaxy is NGC 4552 at $M_{VT} = -21.66$. We find no cores in fainter galaxies; our brightest coreless galaxy is NGC 4621 at $M_{VT} = -21.54$. The perfect separation at $M_{VT} = -21.6$ between core and coreless galaxies is a fortuitous feature of our sample (see below). Nevertheless, the degree to which one concludes that core and coreless galaxies overlap in galaxy luminosity is affected by the definition of what constitutes a core:

We define a core as the central region in a bulge or elliptical galaxy where the brightness profile breaks away from and drops below a Sérsic function fitted to the outer profile. This is the definition adopted by Kormendy (1999): "Elliptical galaxies are divided into two types: galaxies with steep profiles that show no breaks in slope or that have extra light at small radii compared to a Sérsic function fit and galaxies that show a break from steep outer profiles to shallow inner profiles." Figure 3 in that paper demonstrates that the breaks in the projected profiles of cores correspond to real breaks in the deprojected profiles. This confirms analyses of the Nuker galaxies by Gebhardt et al. (1996) and by Lauer et al. (2007b). Similar definitions of cores based on profile breaks have recently been adopted by Graham et al. (2003), Trujillo et al. (2004), and Ferrarese et al. (2006a).

The Nuker team definition is different: a galaxy has a core if the inner slope of a Nuker function fit (Equation (1)) is $\gamma < 0.3$ (Kormendy et al. 1994; Lauer et al. 1995, 2002, 2005, 2007b; Byun et al. 1996; Faber et al. 1997). This definition is not different in spirit from ours. It is also based on the detection of an inner, downward break in the profile from an outer power law that fits profiles well just outside the break radius r_b. Most profiles wiggle: a fit of Equation (1) almost always spits out a value of r_b. A quantitative criterion was needed to decide when the break was strong enough to justify the identification of a core. There is no a priori way to choose a numerical criterion. The decision to use $\gamma < 0.3$ was based on the observation that γ values are bimodal and that there is physics in this. Is there any collision between the Nuker definition and ours?

The answer is "no," because both definitions are designed to capture the same physics. They agree on most galaxies. They disagree on a few objects. But both definitions occasionally produce unphysical results, if they are applied blindly, without taking other information into account. The objects involved tend to be the ones on which the two definitions disagree. We illustrate this with a few examples.

The most remarkable example is NGC 4473. Lauer et al. (2005, 2007b) classify it as a core galaxy; Ferrarese et al. (1994) reached the same conclusion based on a related definition. We can do so too: Figure 58 (top) in Appendix A shows an excellent fit of a Sérsic function with rms = 0.043 mag arcsec^{-2} between 2.″9 and 311″ radius. The fit has $n = 6.1 \pm 0.4$ and implies a core. It looks consistent with our other core fits except that the onset of the core is more gradual than normal as $r \to 0$. There is no operational reason to discard this fit. Indeed, it is substantially nicer than the fit that we adopt (Figure 58, bottom), which has rms = 0.070 mag arcsec^{-2} over a much smaller radius range. This fit gives $n = 4.00^{+0.18}_{-0.16}$ and no core. Instead, there is "extra light" interior to 23″. Why do we prefer the inferior-looking fit? The reason is that SAURON observations show that the galaxy contains a counter-rotating embedded disk: added to the main galaxy, it results in a large apparent velocity dispersion along the major axis but not above and below it (Emsellem et al. 2004; Cappellari & McDermid 2005; Cappellari et al. 2004, 2007). Figure 5 in Cappellari et al. (2007) shows that the counter-rotating disk is important from small radii out to 19″ but not at larger r. It is associated with a strong disky signature in Figure 17. The counter-rotating disk is presumably the result of a late accretion. It does not contain much mass, and it has nothing to do with the basic structure of the galaxy. We therefore fit the profile from $r \simeq 24''$ outward, excluding the counter-rotating disk (see Figure 58). As a result, our interpretation changes. With the $n = 6.1$ fit, it would have been an unusually faint core galaxy with profile systematics that disagree strongly with Figure 40. There are well-known virtues to the application of analysis machinery without premature interpretation. But in this case, the addition of kinematic information dramatizes how apparent virtue can lead one astray. We adopt the $n = 4$ fit in Figure 17 and Table 1. Then NGC 4473 is a slightly unusual extra light elliptical.

NGC 4486B (Figure 22) is a simpler example. The double nucleus (Lauer et al. 1996) makes the major-axis profile flatten out near the center. So the Nuker definition says that the galaxy has a core (Lauer et al. 1996, 2005, 2007b; Faber et al. 1997). Of course, the complication of the double nucleus was known. Interestingly, Figure 22 now shows that the central profile flattening and double nucleus are features in an extra light component (see below) that is very well defined.

Finally, consider NGC 4458 (Figure 19). Lauer et al. (1996) call it a power-law galaxy based on *HST* WFPC1 photometry. Based on higher-resolution WFPC2 data, Lauer et al. (2005) see a small core. Figure 19 shows that the galaxy has a remarkably clearcut extra light component. But at the center, the profile clearly flattens. This may be an example of an interesting phenomenon that is allowed but not predicted by the formation scenario suggested in this paper. Suitable tuning of the relative timescales of merger-induced starbursts (which, we suggest, make extra light components) and the orbital decay of binary BHs (which, we suggest, scour cores) might make it possible to grow a core in an extra light galaxy. The disadvantage of the Nuker definition of cores is that, without using the whole profile, it misses the fact that NGC 4458 *also* contains an extra light component.

One advantage of our definition is that it eliminates confusion about the existence of cores in Sph galaxies. Trujillo et al. (2004) and Ferrarese et al. (2006a) criticize the Nuker definition because it "identifies" cores in Sph galaxies: most of them have Sérsic indices $n \sim 1$, so they have shallow profiles with $\gamma < 0.3$ near the center. As a result, the γ–M_V correlation is not monotonic. Trujillo et al. (2004) note that this could be interpreted as part of a dichotomy between E and Sph galaxies, but they do not believe in this dichotomy, so they interpret it as a shortcoming of the Nuker definition. We show in Kormendy (1985b, 1987b) and in Section 8 that the E–Sph dichotomy is real. So the issue of almost-flat central profiles in Sph galaxies is moot anyway. Sph structure is related to disk structure—disks have $n \sim 1$ profiles too (Freeman 1970)—and neither are related to E structure. In addition, Sph profiles generally show no breaks; they are well fitted by single Sérsic functions at all radii outside their nuclei (Figures 25–29). By our definition, they would not have cores even if they were related to ellipticals.

Finally, we return to the luminosity overlap between core and coreless galaxies, $\Delta M_V \sim 2 \pm 0.5$ mag (Faber et al. 1997; Ravindranath et al. 2001; Laine et al. 2003; Lauer et al. 2007b). With the above tweaks in core classification and distances based on surface brightness fluctuations (Tonry et al. 2001; Mei et al. 2007), the overlap region in the Faber et al. (1997) sample—which we can study in detail—is reduced to ~ 0.7 mag. But it is certainly not zero: NGC 3379 is robustly a core galaxy with $M_V \simeq -21.0$ and NGC 4621 is robustly a coreless galaxy with $M_V = -21.5$. The larger sample of Lauer et al. (2007b) shows overlap mainly at $-20.5 \gtrsim M_V \gtrsim -23$ (Figure 48 here). These classifications have not been repeated with the present definition, but we find in Section 12.3.1 that NGC 6482 is an extra light galaxy with $M_V \simeq -22.3$. There are interesting hints that "poor galaxy groups can harbor more luminous power-law galaxies than clusters" (Quillen et al. 2000; see also Faber et al. 1997). We agree: the unusually bright coreless galaxies NGC 6482 and NGC 4125 (Figure 48) are in poor environments. On the other hand, some power-law galaxies are also brightest cluster members. The environmental dependence of the E–E dichotomy deserves further investigation. We will address this in a future paper.

9.3. Extra Light Near the Centers of Coreless Ellipticals

All the galaxies from NGC 4621 ($M_{VT} = -21.54$) to VCC 1199 ($M_{VT} = -15.53$), that is, all the faint ellipticals in our sample, do not have cores. They are called "power-law" ellipticals in Nuker team papers, because their profiles are approximately featureless power laws over the relatively small radius range studied in those papers.

One of the main results of this paper is that these galaxies do not have simple, almost featureless Sérsic profiles at all r. Instead, *all Virgo ellipticals that do not show cores have extra light near the center above the inward extrapolation of Sérsic functions fitted to their main bodies.* These galaxies behave exactly like the extra light galaxies that are discussed in Kormendy (1999) and illustrated in Figure 3 here. Therefore the results of Kormendy (1999) are not a fluke that applies only to a few, unusual galaxies. Extra light near the center is a general feature of coreless ellipticals.

This adds a new feature to the E–E dichotomy. Table 1 lists the amount of light "missing" or "extra" with respect to the inward-extrapolated Sérsic fit expressed as a percent of total luminosity. Core Es are missing 0.17%–4.2% of their starlight near the center. The mean is 1.15%, the median is 0.84%, and the quartiles are 0.22% and 1.52%. Coreless ellipticals have 0.27%–12.6% extra light near the center. The median is 2.3%; the quartiles are 1.3% and 5.6%. The range is larger than the range of missing light in core ellipticals.

Diagnostic of formation processes, extra light often has disky characteristics. It has $a_4 > 0$ in NGC 4458 and NGC 4478 (see also Morelli et al. 2004), NGC 4464, NGC 4467, NGC 4473, NGC 4486A (see also Kormendy et al. 2005), NGC 4515, NGC 4551 (see also Lauer et al. 1995), NGC 4621, VCC 1627, and VCC 1871. The isophotes remain disky well into the Sérsic part of the profile; in fact, they are sometimes most disky there and not in the "extra light" part of the galaxy.

The extra light is neutral ($a_4 \simeq 0$) or boxy ($a_4 < 0$) in NGC 4459 (which, however, has an embedded dust disk), NGC 4434, NGC 4387 (which otherwise is boxy), NGC 4486B (see below), VCC 1199, and VCC 1440. NGC 4434 and VCC 1440 are almost round; the observed correlation of a_4 with apparent flattening implies that ellipticals are either boxy or disky when seen edge-on but have nearly-elliptical isophotes when seen face-on (Bender et al. 1989; Kormendy & Bender 1996). So these galaxies have no leverage on the question of whether extra light is disky. In NGC 4486B, the extra light includes the double nucleus (Lauer et al. 1996). Tremaine (1995) interprets the analogous double nucleus of M 31 as an eccentric disk. Statler et al. (1999), Kormendy & Bender (1999), Statler (1999), Peiris & Tremaine (2003), and Bender et al. (2005) discuss observational evidence in favor of this model.

We conclude that extra light is usually disky. Ferrarese et al. (1994) reach a more extreme conclusion: they suggest that all power-law galaxies are coreless because of central disks. Lauer et al. (1995) disagree; they show nondisky examples. We do also. Nevertheless, the frequent observation that the extra light is disky is a sign that it was produced by dissipation.

9.4. Kinematic Subsystems in Core and Extra Light Galaxies

Another clue to galaxy formation is the observation that cores and extra light are often associated with kinematic subsystems that are decoupled from the rest of the galaxy. We distinguish kinematic subsystems that are misaligned with the photometric axes from cold, disky subsystems that corotate with the rest of the galaxy. The latter are evidence for dissipative formation, although they do not tell us whether the gas that formed the disk was internal or accreted. In contrast, kinematic misalignments do not necessarily imply dissipative formation, but they have traditionally been interpreted as accretions. Work by the SAURON team now shows that this is not always correct:

Core Es with kinematically decoupled, misaligned centers include NGC 4365, NGC 4382, NGC 4406, NGC 4472, and NGC 4552 (Wagner et al. 1988; Bender 1988b; Jedrzejewski & Schechter 1988; Franx et al. 1989b; Bender & Surma 1992; Bender et al. 1994; Surma & Bender 1995; Davies et al. 2001; de Zeeuw et al. 2002; McDermid et al. 2006; Krajnović et al. 2008). The most thoroughly studied subsystem is in NGC 4365. Its central structure is disky (Figure 13) and rapidly rotating ($V/\sigma \sim 1.4$; Surma & Bender 1995). The main body shows minor-axis rotation (Wagner et al. 1988) and so is triaxial (Statler et al. 2004). NGC 4406 shows similar kinematic decoupling (Bender 1988b, Bender et al. 1994) and minor-axis rotation (Wagner et al. 1988; Jedrzejewski & Schechter 1989; Franx et al. 1989b).

The observation of disky isophotes and $V/\sigma \sim 1.4$ is normally interpreted as an argument for dissipative formation. However, van den Bosch et al. (2008) model two-dimensional SAURON kinematic and photometric observations and show that the almost-90° decoupled central rotation "is not dynamically distinct from [the triaxial structure of] the rest of the galaxy." Its stars are metal-rich, α-element overabundant, and old (Surma & Bender 1995). Davies et al. (2001) remark that "the decoupled core and the main body of the galaxy have the same luminosity-weighted age, $\sim$ 14 Gyr, and the same elevated magnesium-to-iron ratio. The similarity of the stellar populations in the two components suggests that the observed kinematic structure has not changed substantially in 12 Gyr." There is no need to postulate late accretion of a cold component; major mergers can make decoupled kinematic subsystems (Jesseit et al. 2007; Naab et al. 2007). Kinematic subcomponents in core galaxies appear to be no problem for our picture that these galaxies were made in dry mergers.

Still, it would be surprising if late accretions did not occasionally build a nuclear disk in what used to be a core E despite "protection" (Section 12.3) from X-ray gas halos. NGC 4621 may be an example. A more obvious example is NGC 5322 (Bender 1988b, Rix & White 1992; Scorza & Bender 1995). The presence of an edge-on dust disk (Lauer et al. 1995, 2005) guarantees that the subcomponent was formed dissipatively.

Extra light ellipticals with distinct kinematic subsystems include NGC 4473 (Section 9.2) and the following. NGC 4458 has a rapidly rotating center at $r \lesssim 0\farcs5$; at $r > 5''$, the galaxy rotates slowly or in the opposite direction (Halliday et al. 2001; Emsellem et al. 2004; Krajnović et al. 2008). NGC 4458 is one of the clearest examples of extra light (Figure 19); it reaches out to $r > 4''$. Similarly, in NGC 4387, Halliday et al. (2001) suggest that a central decrease in σ implies a rotationally supported subsystem that is confirmed by Emsellem et al. (2004) and Krajnović et al. (2008). NGC 4621 has a rapidly rotating, disky center, as suggested by Bender (1990) and now beautifully shown by two-dimensional SAURON spectroscopy (Emsellem et al. 2004). Figure 16 shows its disky a_4 signature. In all three galaxies, SAURON two-dimensional maps of Hβ line strength reveal no difference in age between the decoupled center and the rest of the galaxy (Kuntschner et al. 2006).

These results further imply that extra light components form dissipatively. Usually (but not always), the stellar population indicators suggest that the central extra light structures formed approximately at the same time as the rest of the galaxies' stars.

9.5. The E–E Dichotomy Illustrated by Scaled Brightness Profiles

The dichotomy between core and extra light ellipticals is illustrated further in Figures 39 and 40. Figure 39 shows all

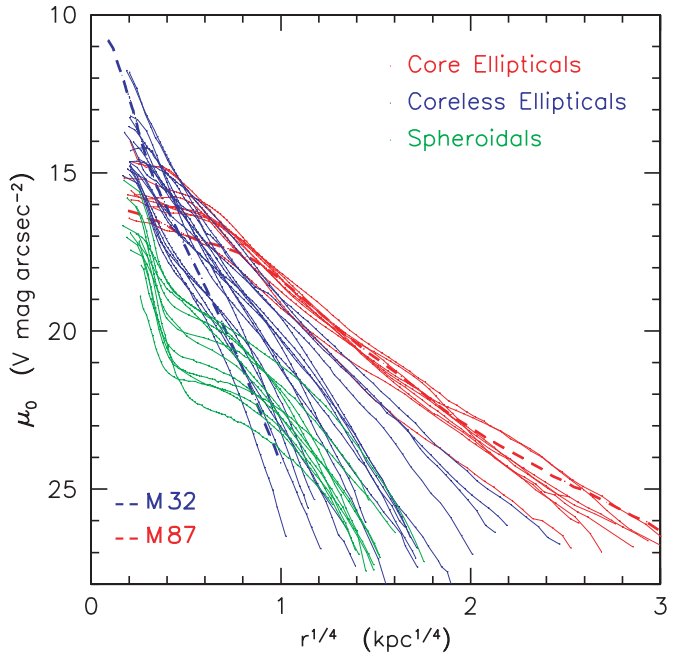

Figure 39. Major-axis profiles of all elliptical and spheroidal galaxies in our sample scaled so that radius is in kpc. The brightness profiles are corrected for Galactic absorption. The fiducial galaxies M 32 and M 87 are plotted with thick dashed lines. The same profiles are shown in Figures 35 and 36; the emphasis here is on comparing the two kinds of ellipticals. As in Figures 34, 37, 38, and 41, M 32 is a normal example of the lowest-luminosity ellipticals.

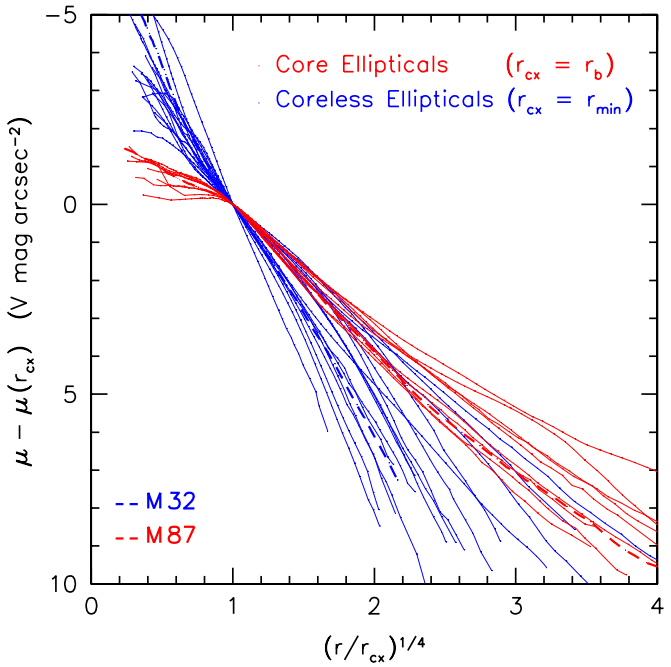

Figure 40. Major-axis profiles of all of our ellipticals scaled together to illustrate the dichotomy between core and coreless ellipticals. Core ellipticals are scaled together at $r_{cx} = r_b$, the break radius given by the Nuker function fit in Lauer et al. (2007b). Coreless ellipticals are scaled together at the minimum radius $r_{\rm min}$ that was used in our Sérsic fits; interior to this radius, the profile is dominated by extra light above the inward extrapolation of the outer Sérsic fit.

profiles in our sample scaled together so that radius is in kpc. Because core ellipticals have $n > 4$ and extra light ellipticals have $n \lesssim 4$, their profiles curve apart at large radii. A larger fraction of the light lives at large radii in core Es, so r_e is larger and μ_e is *fainter* than in extra light Es (Figures 37 and 38). But at almost all metric radii outside the core, *core ellipticals have higher surface brightnesses than do extra light ellipticals at the same metric radius.* This is important, because *n*-body models of galaxy mergers predict that the surface brightness in the merger remnant is higher than the surface brightness of either progenitor at essentially all radii (Hopkins et al. 2009a). Binary BH core scouring is the exception to this prediction, and the relatively low absolute surface brightnesses in cores with respect to extra light is clear in Figures 39 and 40. The important conclusion from Figure 39 is that *surface brightnesses in core galaxies are high enough so that they can be products of dry mergers of extra light ellipticals* (but see Section 11.1).

Figure 40 shows all of our elliptical galaxy profiles scaled together at approximately the radius where the central core or extra light gives way to the outer Sérsic profile. Because the profiles of extra light Es break upward while core profiles break downward near the center, the core and extra light profiles are well separated from each other at small radii. The present sample shows a fortuitously clean separation between core and coreless galaxies; larger samples show a few intermediate cases (Rest et al. 2001; Ravindranath et al. 2001; Lauer et al. 2005, 2007b). We have not yet checked whether these remain ambiguous with the present definition of cores. In any case, the distinction between galaxies with and without cores remains robust (Gebhardt et al. 1996; Lauer et al. 2007b).

9.6. Profile Shape Participates in the E–E Dichotomy

Figure 41 shows again that Sérsic index *n* participates in the E–E dichotomy. Also, E and Sph galaxies are well separated.

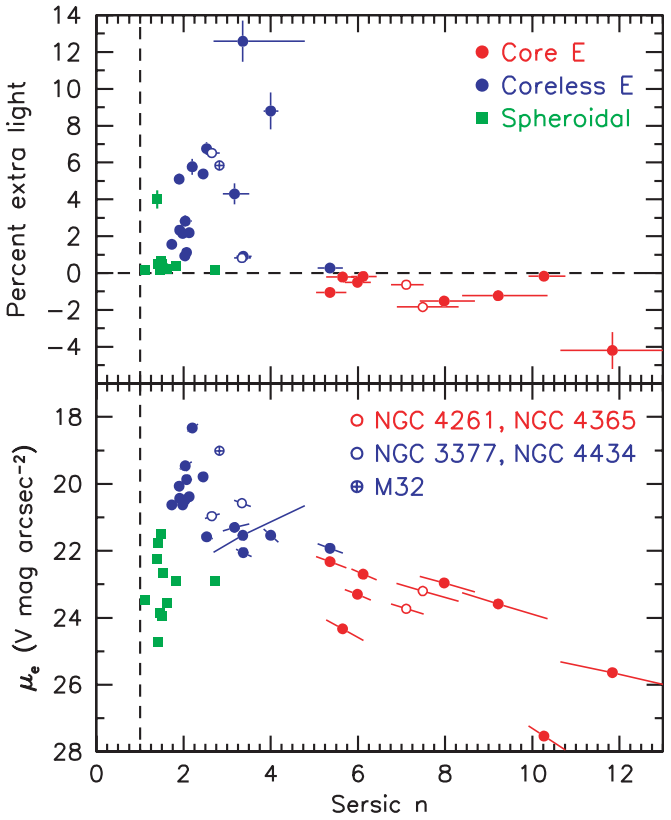

Figure 41. Top: percent of the total *V*-band luminosity that is "missing" in core galaxies or "extra" in coreless galaxies compared to the inward extrapolation of the outer Sérsic fit. Bottom: effective surface brightness μ_e vs. Sérsic index *n*. The symbols are as in Figures 34, 37, and 38.

Figure 41 (top) shows the amount of central extra light above the inward extrapolation of the outer Sérsic fit as a percent

of total galaxy luminosity. It is negative (light is "missing") for core galaxies. The amount of extra light is calculated by integrating the two-dimensional brightness distribution of the galaxy nonparametrically from the center to the inner limit $r_{\rm min}$ of the Sérsic function's radial fit range. From this luminosity, we subtract the integral of the fitted Sérsic function over the same radial range. In the latter integral, the ellipticity ϵ of the Sérsic function is kept fixed at $\epsilon(r_{\rm min})$. Error bars are estimated by substituting plausible (usually small) extrapolations of the outer $\epsilon(r)$ profile into the region of the extra light. These are internal errors only, e.g., the effects of changing the Sérsic fits within the ranges allowed by their error bars are not taken into account. As a result, the error bars in the top panel of Figure 41 are not formally coupled. The error bars in the bottom panel are coupled; they can be correlated or anticorrelated (see Figures 49–72 in Appendix A). All points in Figure 41 have error bars, but most are too small to be seen. Table 1 lists the plotted data.

Note: for M 87, we used the bottom fit in Figure 50, i.e., the one that allows for a cD halo. The top fit in Figure 50 provides the upper error bar on the amount of missing light. That is, for M 87, the error bars are dominated by the choice of Sérsic fit.

Figure 41 demonstrates again that all core galaxies in Virgo (percent extra light < 0) also have Sérsic indices $n > 4$. All of the coreless ellipticals (percent extra light > 0) have $n \leqslant 4$ except NGC 4621. We will use this result in Section 10.3.

The bottom panel of Figure 41 shows effective brightness against Sérsic index. Ellipticals form a well-defined sequence with core and extra light galaxies largely separated. NGC 4621 is an exception to the E–E dichotomy: it has $n > 4$ but is disky and has a little extra light near the center. Otherwise, this Virgo cluster sample shows the dichotomy cleanly, and profile shape in the form of Sérsic n participates in it.[8]

Spheroidal galaxies are well separated from ellipticals in both panels. As in Figures 34–39, they have smaller n and lower central and effective surface brightnesses than extra light ellipticals. This is consistent with their similarity in parameter correlations to galaxy disks (Kormendy 1985b, 1987b).

9.7. Nuclei—Unrelated to Extra Light and Supermassive BHs

Nuclei in spheroidal galaxies are very different from extra light in elliptical galaxies. Hopkins et al. (2009a) show that they have almost orthogonal parameter correlations. Here, Figure 41 shows that nuclei contain a much smaller fraction of the total galaxy light. NGC 4482 (green point at 4% in the top panel) looks like—but is not—an exception; the Sérsic fit in Figure 25 fails at relatively large radii, and the extra light interior to this is included in the 4%. However, the nucleus in NGC 4482 is similar in light fraction to the nuclei of other spheroidals. All of our Sph galaxies are nucleated, and the nuclei all contain similar fractions of the galaxies' light. The mean light fraction of our Sph nuclei is $0.33 \pm 0.06\%$, as found previously by Côté et al. (2006). The analogous fraction for extra light Es is much larger and has a much larger range.

Several authors note that nuclei make up roughly the same fraction of spheroidal galaxy stellar masses as supermassive BHs do of their host bulges ($\sim 0.13\%$: Merritt & Ferrarese 2001; Kormendy & Gebhardt 2001). These authors plot BH and nuclear mass against galaxy absolute magnitude and find a single, continuous correlation (Côté et al. 2006; Wehner & Harris 2006; Ferrarese et al. 2006b; Graham & Driver 2007). They suggest that nuclei and BHs are related—a galaxy contains either a nucleus or a BH, and perhaps nuclei evolve into BHs. We confirm the observational conclusion but suggest that it is an accident. Nuclei constitute a canonical fraction of some Sphs, but others contain no nuclei (Sandage et al. 1985a, 1985b; Binggeli et al. 1985, 1987; Côté et al. 2006). In late-type galaxies, nuclear absolute magnitudes correlate with total magnitudes, but only weakly (Carollo et al. 1998; Böker et al. 2004). Furthermore, BHs exist even in bulgeless disks (Filippenko & Ho 2003; Barth et al. 2004, 2008; Greene & Ho 2004, 2007; Peterson et al. 2005; Greene et al. 2006; Shields et al. 2008; Thornton et al. 2008; see Ho 2008 for a review). But BH masses correlate very little with their host disks (Kormendy & Gebhardt 2001). Finally, some galaxies—including ones with classical bulges—clearly contain both BHs and nuclei. Sometimes the BH mass is much larger than that of the nucleus (NGC 3115: Kormendy et al. 1996b); sometimes the BH mass is similar to that of the nucleus (M 31: Light et al. 1974; Dressler & Richstone 1988; Kormendy 1988; Lauer et al. 1993, 1998; Kormendy & Bender 1999; Bender et al. 2005; NGC 4395: Filippenko & Ho 2003; Peterson et al. 2005); and sometimes the BH mass appears to be less than that of the nucleus (NGC 1042: Shields et al. 2008). We believe that there is no observational reason to suspect more of a physical relationship between nuclei and BHs than the generic likelihood that both are fed with gas from the disk.

10. INTERPRETATION: WET VERSUS DRY MERGERS

10.1. Black Hole Scouring of Cuspy Cores in Giant Ellipticals

Figure 41 shows that a typical core E is missing $1 \pm 1\%$ of its starlight near the center with respect to the inward extrapolation of a Sérsic function fitted to the outer profile. Implicit in this statement is the hypothesis that these ellipticals would have had Sérsic profiles if not for the process that excavates cores. This is consistent with Figure 39, which shows how representative dry-merger progenitor profiles would "fill" core profiles and would approximately continue the outer, high-n Sérsic functions inward. It is also consistent with the canonical explanation of how cores form:

Understanding cores is nontrivial. Observed core parameter relations show that, in higher-luminosity ellipticals, the break in the profile that defines the core occurs at larger radius r_b and fainter surface brightness I_b (see Faber et al. 1997 for *HST* core parameter correlations and Kormendy 1984, 1985b, 1987a, 1987b; Lauer 1985a, 1985b for the analogous ground-based results). Mergers generally preserve the highest-density parts of their progenitors. Therefore, when ellipticals or bulges that satisfy the core parameters correlations merge, this tends to destroy the correlations (Kormendy 1993; Faber et al. 1997). Fluffy cores in high-luminosity ellipticals are not a natural consequence of hierarchical clustering and galaxy merging.

A possible solution to this problem is the suggestion that cores form via the orbital decay of binary supermassive BHs (Begelman et al. 1980; Ebisuzaki et al. 1991; Makino & Ebisuzaki 1996; Quinlan 1996; Quinlan & Hernquist 1997; Faber et al. 1997; Milosavljević & Merritt 2001; Milosavljević et al. 2002; Makino & Funato 2004; Merritt 2006; Merritt et al. 2007). BH binaries form naturally in the galaxy mergers that are believed to make ellipticals. Their orbits decay—the binaries get harder—by flinging stars away. These stars are deposited into a large volume at large radii or are ejected from the galaxy;

[8] Côté et al. (2007, see Section 2.1) find approximately the same result, but the apparent dichotomy is less clearcut, because they derive somewhat different n values (see Figure 75) and somewhat different central profile classifications.

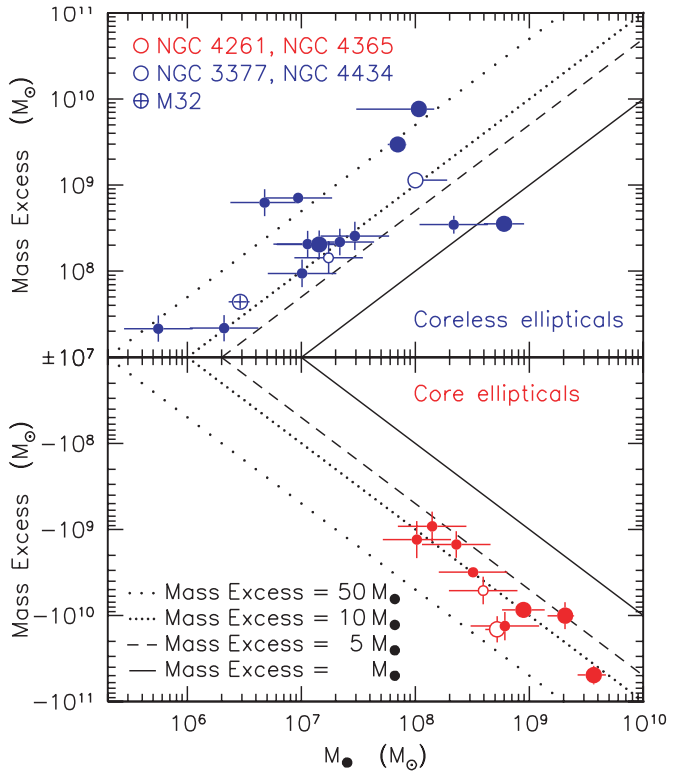

Figure 42. Total stellar mass that is missing in cores (lower panel) or extra in coreless galaxies (upper panel) as a function of BH mass. Large and small symbols denote galaxies with and without dynamical BH detections, respectively. NGC 4486B has the smallest *fractional* excess in the upper panel because $M_\bullet$ is unusually large (Kormendy et al. 1997).

either way, they have little effect on the outer profile. As stars are removed from the small volume near the BHs, the central surface brightness decreases. In this way, the decaying binary excavates a core. The effect of a series of mergers is cumulative; if the central mass deficit after one merger is a multiple f of the BH mass $M_\bullet$, then the mass deficit after N dissipationless mergers should be $M_{\rm def} \simeq NfM_\bullet$. If this picture is correct and if f can be predicted from theory or simulations, then a measure of the observed mass deficit tells us roughly how many dissipationless mergers made the galaxy.

One problem is that f is not well known. Milosavljević & Merritt (2001) estimate that $f \simeq$ 1–2. Milosavljević et al. (2002) get $Nf \simeq 5$ for formation in a hierarchy of mergers. Until recently, the most accurate numerical simulations were those of Merritt (2006), who concluded that $f \simeq 0.5$. Past observations of mass deficits depended on the functional form used to extrapolate the outer profile inward to the center; they are larger for Nuker function extrapolations (Milosavljević & Merritt 2001; Milosavljević et al. 2002; Ravindranath et al. 2002; Lauer et al. 2007a) and smaller for Sérsic function extrapolations. As it became clear that Sérsic extrapolations are both well supported by the data and intrinsically conservative (see Figure 1 in Graham 2004), observations converged on values of $Nf \equiv M_{\rm def}/M_\bullet$ between 1 and 2; most commonly, $M_{\rm def}/M_\bullet \simeq 2$, and values as large as 4.5 are rare (Graham 2004; Ferrarese et al. 2006a; Merritt 2006; Lauer et al. 2007a). The conclusion was that these are consistent with galaxy formation by several successive dry mergers.

With more accurate profiles, we can better measure mass deficits. However, only giant ellipticals have deficits; small ellipticals have mass excesses. So, Figure 42 separately shows central stellar mass deficits (lower panel) and mass excesses (upper panel) against $M_\bullet$. Lines are drawn at $M_{\rm def}/M_\bullet = 1$, 5, 10, and 50. Large symbols denote galaxies with dynamical BH detections; for these, the BH mass and stellar mass-to-light ratio are taken from the BH discovery paper. Small symbols denote galaxies without dynamical BH detections. Then $M_\bullet$ is derived from the correlation between $M_\bullet$ and σ (Ferrarese & Merritt 2000; Gebhardt et al. 2000) as fitted by Tremaine et al. (2002). The estimated error in $\log M_\bullet$ is 0.3. In constructing Figure 42, we converted light excesses (Table 1) to mass excesses using mass-to-light ratios $M/L_V \propto L^{0.36}$ fitted to the SAURON sample of Cappellari et al. (2006) including M 32. The zero point is $M/L_V = 6.07$ at $M_V = -21.6$, i.e., the divide in Table 1 between core and extra light ellipticals. Our error estimate in $\log M/L_V$ is 0.153, the rms scatter of the above fit. This is consistent with the results of Cappellari et al. (2006), who work in the *I* band.

We adopt the Cappellari et al. (2006) M/L ratios because they are based on the most accurate, three-integral models applied to the most detailed, two-dimensional SAURON data. Also, the resulting M/L ratios correlate well with values based on stellar population models, although there is an offset that may imply a dark matter contribution or a problem with the stellar initial mass function used in the population models. The choice of M/L_V critically affects the derived mass excesses, so independent checks are welcome. Many are available. They include additional M/L values based on three-integral models (Gebhardt et al. 2003, 2007; Thomas et al. 2007), two-integral models of galaxies observed to very large radii (Kronawitter et al. 2000; Gerhard et al. 2001), and two-integral models of large galaxy samples (e.g., van der Marel 1991). All authors generally agree well with the steep M/L_V–M_V correlation that we derive from the Cappellari data. Significant caveats still need exploration. For example, dynamical M/L_V values may include a dark matter contribution that depends on M_V. Also, triaxiality is not included in the dynamical models and may depend on M_V. But the mass-to-light ratios that we use in what follows are the most robust ones that are currently available in the literature.

The mass deficits $M_{\rm def}$ that we derive for core galaxies are larger than published values, partly because our M/L_V values are larger and partly as a result of more accurate photometry. They are also remarkably uniform, and—although the sample is small—they show no offset between galaxies with and without dynamical BH detections. In Figure 42, the unweighted mean $\langle \log M_{\rm def}/M_\bullet \rangle = 1.04 \pm 0.07$. The weighted mean is $\langle \log M_{\rm def}/M_\bullet \rangle = 1.07 \pm 0.08$. That is, $M_{\rm def}/M_\bullet \simeq 11$ with an error in the mean of about 18%. The smallest value is $4.9^{+2.4}_{-1.9}$ for NGC 4649, and the largest value is 28^{+13}_{-10} for NGC 4261. These values are very large in comparison to the Merritt (2006) prediction that $M_{\rm def}/M_\bullet \simeq 0.5$ per major merger. However, two recent results help to explain such large $M_{\rm def}/M_\bullet$ values.

First, with a more accurate treatment of the late stages of binary BH mergers, Merritt et al. (2007) find that $M_{\rm def}/M_\bullet$ can be as large as ~ 4 per merger. Then our results are reasonably consistent with estimates (Faber 2005; van Dokkum 2005; Bell et al. 2006) that several dissipationless mergers produced the bright end of the "red sequence" part of the color bimodality of galaxies observed by the SDSS (Strateva et al. 2001; Hogg et al. 2002, 2004; Kauffmann et al. 2003a, 2003b; Blanton et al. 2003b, 2005; Baldry et al. 2004) and by the COMBO-17 survey (Bell et al. 2004). If present-day galaxies provide any guide to the properties of merger progenitors (and they may not—see Section 11.1), then it is essentially required that galaxies as

big as M 87 formed in several successive dry mergers. Giant ellipticals are so big that plausible immediate progenitors are galaxies that contain little or no cold gas.

Second, an additional process has been proposed to make large-$M_{\rm def}/M_\bullet$ cores (Merritt et al. 2004; Boylan-Kolchin et al. 2004; Gualandris & Merritt 2008). Coalescing binary BHs emit gravitational radiation anisotropically; they recoil at velocities comparable to galaxy escape velocities. If they do not escape, they decay back to the center by dynamical friction. In the process, they throw away additional stars. Gualandris & Merritt (2008) estimate that they can excavate as much as $M_{\rm def}/M_\bullet \sim 5$ *in addition to the mass that was already scoured by the pre-coalescence binary.* Any conclusions to be reached from Figure 42 necessarily depend on our choice of Sérsic functions as our models for unscoured merger remnants. But it appears that our observations present no problem for the idea that cores in giant ellipticals are made by a combination of the above two BH scouring mechanisms acting over the course of one or more successive dry mergers.

Kormendy & Bender (2009) further explore the implications of Figure 42, showing that core $L_{\rm def}$ correlates with $M_\bullet$ and σ with scatter similar to that of the well-known $M_\bullet$–σ correlation. They interpret these correlations as the "smoking gun" that connects cores with BHs; that is, as strong support for the binary BH scouring mechanism.

10.2. Extra Light in Low-Luminosity Ellipticals: Implications for Black Hole Scouring and AGN Energy Feedback

Figure 42 (upper panel) shows, for coreless galaxies, the central stellar mass excess $M_{\rm extra}$ above the inward extrapolation of the outer Sérsic profile. Five galaxies (large symbols) have dynamical BH detections, M 32, NGC 3377, NGC 4459, NGC 4486A (Nowak et al. 2007), and NGC 4486B (see Kormendy 2004 for additional references). BHs and extra light are not mutually exclusive. In fact, if essentially all bulges and ellipticals contain BHs (Magorrian et al. 1998), then the other extra light ellipticals are likely to contain BHs too. They are included in Figure 42 with BH masses from the $M_\bullet$–σ relation. The median of $\log M_{\rm extra}/M_\bullet$ is 1.120 (quartiles 0.955, 1.608), i.e., median $M_{\rm extra}/M_\bullet = 13$ (quartiles 9, 41). The mean is $\langle \log M_{\rm extra}/M_\bullet \rangle = 1.159 \pm 0.150$ or $\langle M_{\rm extra}/M_\bullet \rangle = 14^{+6}_{-4}$.

What are the implications of the extra light for our picture of core formation by binary BH scouring? We emphasize: *Extra light ellipticals satisfy the $M_\bullet$–σ correlation as well as do core ellipticals. We believe that they formed in mergers. These mergers cannot all have involved at least one pure-disk, black-hole-less galaxy. Why, then, do coreless ellipticals have extra light, not missing light, in their centers? Why did core scouring by binary BHs fail?* We suggest an answer based in part on the observations in Sections 9.3 and 9.4 that point to dissipational formation of coreless ellipticals. *We suggest that core scouring is swamped by the starburst that results from the rapid infall of gas that occurs in a wet merger* (e.g., Mihos & Hernquist 1994). The mass excesses in coreless Es tend to be somewhat larger than the mass deficits in core Es, when both are expressed as multiples of the BH mass. Our measurements of mass excesses may be slight underestimates (Section 10.3; Hopkins et al. 2009a). This suggests that it is relatively easy for new stars to swamp any core scouring that may have occurred. We pursue the possible starburst formation of the extra light in the next subsection.

First we note an implication for energy feedback from active galactic nuclei (AGNs). A popular hypothesis to explain why giant ellipticals stopped making stars after < 1 Gyr (Bender 1996, 1997; Thomas et al. 1998, 1999, 2005) is that AGN feedback quenched star formation (Springel et al. 2005; Scannapieco et al. 2005; Bower et al. 2006; De Lucia et al. 2006). We suggest in Section 12.3 that AGN feedback is fundamental to the creation of the E–E dichotomy. Here we note that such feedback can easily quench the star formation that—we suggest (Section 10.3)—makes the extra light in coreless galaxies. This implies that the importance of AGN energy feedback is a strong function of galaxy and BH mass. It may have regulated the formation of giant ellipticals, but it cannot have quenched all star formation in coreless ellipticals if our interpretation of the extra light is correct.

10.3. Dissipative Merger Formation of Extra Light in Low-Luminosity Ellipticals

This brings us back to the explanation of the extra light in coreless ellipticals. As reviewed in Section 4.2, Kormendy (1999) found the extra light component in three ellipticals that span the luminosity range over which this paper shows it to occur. In M 32 and NGC 3377, the extra light was well resolved by *HST* photometry. The brightness profiles of all three galaxies closely resemble the density profiles of ellipticals produced in simulations of gas-rich mergers (Mihos & Hernquist 1994: Figure 4 here). The gas sinks rapidly to the center during the merger; the resulting starburst produces an "extra" component of young stars that is clearly distinct from the Sérsic profile ($n < 4$) of the mostly dissipationless part of the merger remnant. Mihos & Hernquist (1994) were concerned that such two-component density profiles were not consistent with the observations. After further simulations confirmed these results, Mihos & Hernquist (1996, see p. 660) remarked, "Perhaps more worrisome are the stellar residuals of the nuclear starbursts....The light profile of the starburst population does not join "seamlessly" onto that of the old stars in the remnant but is instead manifest as a luminosity "spike", in apparent disagreement with the core properties of massive ellipticals (see, e.g., Lauer et al. 1995). What is the significance of this result for the merger hypothesis?". Kormendy (1999) pointed out that the results of the gas-rich-merger simulations look just like the two-component profiles observed in the above galaxies and suggested that the inner component was produced by the merger starburst.

Note that this explanation does not require the extra light to be young. If the merger happened long ago, the age difference between the main body and the extra light would be hard to detect. Worthey (2004) observed a stellar population gradient in M 32 (age 4–6 Gyr at $r \lesssim 5''$ and 8–10 Gyr at larger radii), although he saw no discontinuity at the radius of the break between the extra light and main body of the galaxy. This is consistent with the present formation picture. However, it would be reasonable to expect that, in a large sample, at least some central components should have younger stellar populations than the rest of the galaxy. This is observed (Lauer et al. 2005; Kuntschner et al. 2006; McDermid et al. 2006).

In our sample, we find extra light in all coreless galaxies. Like Kormendy (1999), *we suggest that the extra light in low-luminosity elliptical galaxies generally formed as in the Mihos & Hernquist (1994) models; that is, in the starburst that accompanies the merger that made the elliptical.* Alternatives exist and almost certainly happened in some galaxies. A few extra light components in large ellipticals could be the remnants of the compact and dense centers of dissipationlessly accreted small ellipticals (Kormendy 1984; Balcells & Quinn 1990), provided that they were too massive to be lifted by BH binaries.

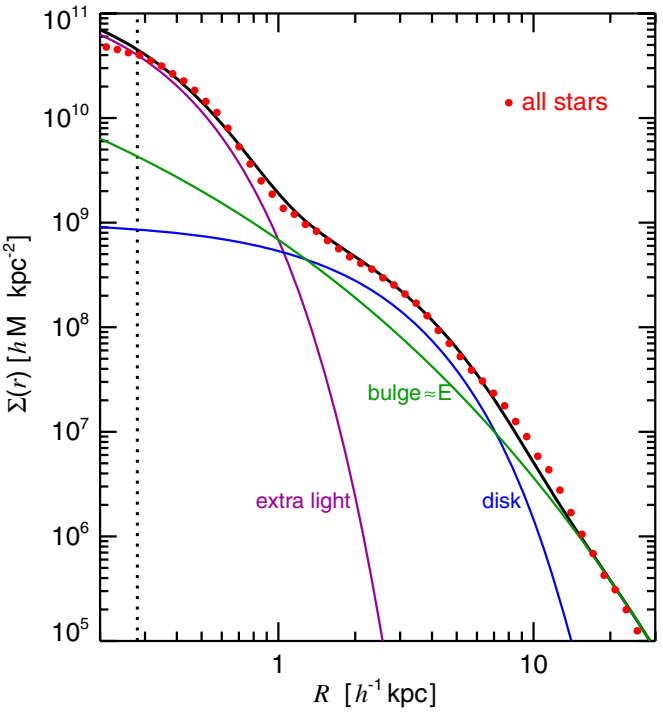

Figure 43. Surface density distribution of the remnant of a gas-rich merger adapted from Figure 3 of Springel & Hernquist 2005, arXiv version; the vertical dotted line is the resolution of the simulation. The progenitors contained no stars, only gas disks embedded in dark halos. Stars that formed in the first, pre-merger encounter later relaxed violently into the density distribution labeled "bulge ≈ E"; it is a Sérsic function with $n < 4$. During the merger, two-thirds of the remaining gas falls to the center, undergoes a starburst, and makes the density distribution labeled "extra light." The remaining gas settles into a new star-forming disk whose stellar density profile is labeled "disk." Note that the ellipsoidal part of the galaxy, that is, the sum of the bulge and extra light, has a two-component density profile like those in Figures 16–24 but with more extra light than is seen in the observations.

However, the frequent observation that the extra light is disky and rapidly rotating argues that it usually forms dissipatively (Scorza & Bender 1995; Sections 9.3 and 9.4 here). So a more likely alternative is that a few extra light components formed via accretions of gas-rich dwarfs (Section 11.2).

More recent simulations of gas-rich mergers also produce an extra component near the center as a result of merger-induced starbursts (e.g., Springel 2000). We illustrate two of these.

Springel & Hernquist (2005) ran a merger simulation in which the progenitors were dark matter halos containing gas disks but no stars. They included star formation according to a Schmidt (1959)–Kennicutt (1998a, 1998b) law, energy feedback from supernovae, and thermal evaporation of cold gas clouds. The density distribution of the merger remnant is shown in Figure 43. Stars that form in an early close passage later relax violently in the merger and produce an almost-$r^{1/4}$-law, elliptical-galaxy-like component; they call this the "spheroid" and we label it "bulge ≈ E" in Figure 43. Inspection of their Figure 3 shows that this component is a Sérsic function with $n < 4$. During the merger, much of the remaining gas falls to the center, and a starburst produces a more compact ellipsoid that Springel & Hernquist call the "bulge" and that we label "extra light" in Figure 43. Gas that survives the merger settles into a new disk that forms stars slowly; this disk has an exponential stellar density distribution and is labeled "disk" in Figure 43. Because the progenitor galaxies contained no stellar disks that could be destroyed in the merger, the final extra light : bulge : stellar disk mass ratios, 0.55 : 0.22 : 0.23, are much different than they are in real galaxies. Nevertheless, the merger remnant has the qualitative character that we see in our data. The nondisk part of the remnant consists of an elliptical-galaxy-like part that is an $n < 4$ Sérsic function plus extra light at the center that gives the sum a two-component look. Enough gas survives the merger to make a new disk. We observe S0 galaxies that have such disks, a bulge that satisfies a Sérsic function, and sometimes extra light (Figures 30–32).

Cox et al. (2006) simulated dissipative mergers with a more detailed treatment of radiative cooling, star formation consistent with a Schmidt–Kennicutt law, and energy feedback from massive stars and supernovae. The progenitor galaxies were realistic approximations to Sbc galaxies, both structurally and in terms of gas content. Moreover, the progenitor disks were constructed to have reasonable Toomre (1964) stability parameters Q and realistic star-formation rates; this required careful tuning of the prescriptions for star formation and energy feedback. A range of parameters that bracket realistic Sbcs was explored to investigate the robustness of the conclusions. Star-formation rates were very sensitive to the details of energy feedback. However, the density profiles of the remnant ellipticals proved to be relatively insensitive to the energy feedback and gas physics (e.g., equation of state). They confirm that star formation in gas that is dumped close to the center by the merger builds a distinct central component in density that is brighter than the inward extrapolation of the density profile of the main body of the remnant. How much of the extra component was built by star formation and how much was the remnant of the progenitor bulges depends on the energy feedback; less efficient feedback results in more star formation near the center. If there is too much feedback, the extra component cannot form.

Since the submission of this paper, the most comprehensive simulations of dissipative mergers are a series of papers by Hopkins et al. (2008a, 2008b, 2009a, 2009b, 2009c) that are motivated directly by the present results and by similar observations of mergers-in-progress by Rothberg & Joseph (2004, 2006). They construct libraries of gas-rich merger simulations in which merger-induced starbursts make extra light components. They match these up with galaxy observations—including ours—and they explore both wet and dry mergers in great detail. They make substantial progress beyond this paper. A review of this progress is beyond the scope of the present paper. But it is important to connect up their results and ours, especially because they are based in part on the same observational data.

Figure 44 shows two examples of model results from Hopkins et al. (2009a). The top panels show decompositions of our profiles into two Sérsic functions; the purpose is to estimate the fraction $f_{\rm extra}$ of the luminosity that is in the extra light. The bottom panels match the observed profiles with the best-fitting results from their simulation library. Unlike the interpretations of the extra light in the top panels and in the present paper, the simulations have known fractions $f_{\rm sb}$ in their starbursts. The extrapolation of the starburst component into the region dominated by the main body of the galaxy is not necessarily matched by the machinery in the top panel, but on the whole, the decompositions and the models give similar results for the starbursts. That is, the behavior of the models fitted to the data in Figure 44 is entirely consistent with the formation picture discussed in the present paper. Since all details of the models are known, Hopkins et al. (2008a, 2008b, 2009a, 2009b, 2009c) can explore how models look from different viewing geometries and demonstrate that the results are consistent with observations of boxy and disky isophote distortions.

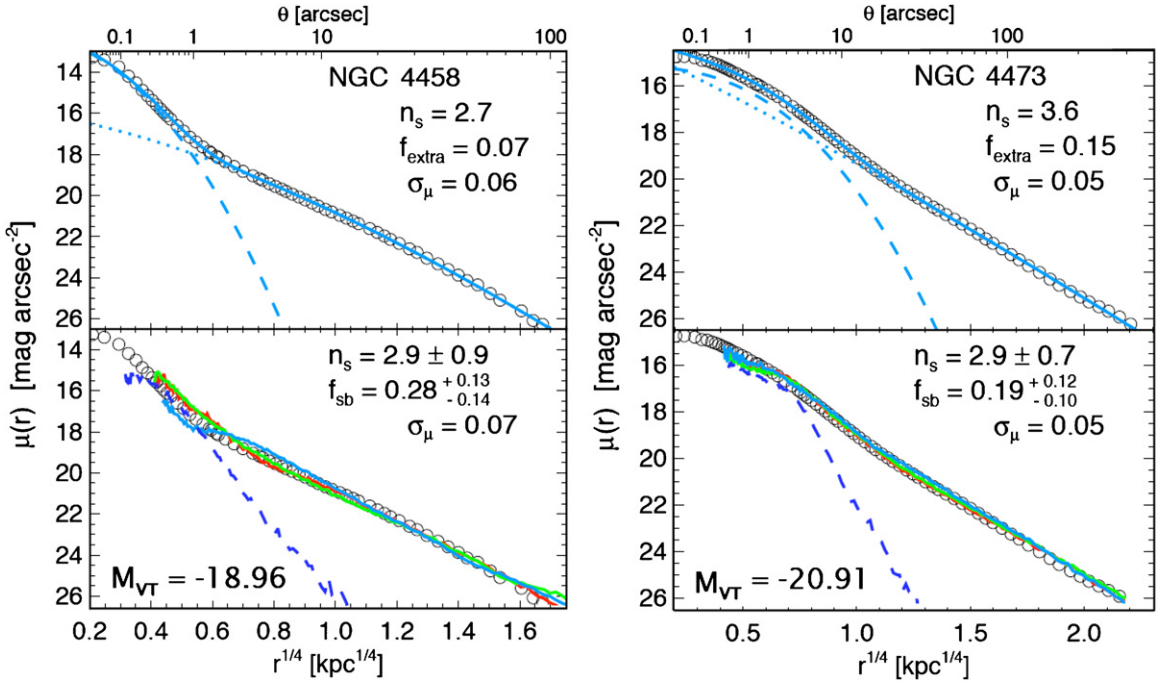

Figure 44. Stellar density profiles of the remnants of dissipative starburst mergers from Hopkins et al. (2009a). The top panels show brightness profiles from the present paper (open circles) decomposed into two Sérsic functions; the Sérsic index n_S of the main body, the fractional contribution $f_{\rm extra}$ of the central extra light, and the rms deviations of the fit (mag arcsec^{-2}) are given in the key. The corresponding values from our analysis are $n = 2.53^{+0.14}_{-0.13}$, $f_{\rm extra} = 0.068 \pm 0.004$, and rms = 0.0295 mag arcsec^{-2} for our fit to the main body of NGC 4458 and $n = 3.9$, $f_{\rm extra} = 0.09$, and rms = 0.048 mag arcsec^{-2} for our decomposition of NGC 4473 (Figure 59). The bottom panels show, in different colors, density profiles from the three library simulations that best fit the galaxy profiles (open circles). Also, the blue dashed line shows the starburst extra light component formed in the best-matching simulation. The range of main-body Sérsic indices for various viewing geometries is given in the key, together with the percent mass contribution f_{sb} of the starburst in these three simulations and the rms deviations of the fits.

It is instructive to compare the extra light fractions derived by Hopkins et al. (2009a) with our estimates. For 10 of the 18 extra light galaxies in common, the agreement is very good; individual ratios of $f_{\rm extra}$ divided by our values range from 0.65 to 1.27 and average 1.00 ± 0.08. For six more, the ratio ranges from 1.7 to 4.2 and averages 2.85 ± 0.40. For the other two, the ratio is 18 for NGC 4434 and 12 for NGC 4486A.

These results are expected. On the whole, the decomposition procedure in Hopkins et al. (2009a) is reasonable,[9] as they demonstrate by comparing to model results. The decomposition is particularly robust for galaxies like those in Figure 44 that have bright and well-resolved extra light and hence good "leverage" on both components. A decomposition tends to give larger fractions of extra light than our estimation procedure. This is expected, because we made no decomposition; instead, we fitted the main body of each galaxy and added up the central light above this fit to estimate the extra component. This almost certainly underestimates the starburst component slightly. On the other hand, we did not make decompositions (except for NGC 4473 in Figure 59), because nothing in the residual profiles in Figures 16–24 and 57–67 demands them. Indeed, our one-component Sérsic fits often have smaller residuals than the two-component decompositions in Hopkins et al. (2009a). Nevertheless, both the above comparisons and the tests done in the above paper show that the decompositions are reasonable interpretations of the data. The most questionable cases (e.g., NGC 4434 and NGC 4486A) are ones where the wiggles in the extra light profile formally cause the decomposition procedure to fit very shallow extra light components. These few objects have little influence on the conclusions.

So, the conclusions from dissipative merger simulations are robust. Some details of remnant structure depend on gas physics and energy feedback. But the simulations very generally predict an extra component near the center that is produced by the merger starburst. Authors of the early papers that showed this worried about whether these extra components are realistic or a problem, because they had not been observed in the published brightness profiles of most ellipticals.

Our results appear to settle this issue, at least for ellipticals in the Virgo cluster. Extra light is almost ubiquitous in coreless ellipticals. Cores are believed to be scoured by binary BHs. The suggestion is that the last major merger that made core ellipticals was dry, whereas the last major merger that made coreless ellipticals was wet and included a substantial central starburst.

[9] We cannot similarly check the decompositions of core galaxies in Hopkins et al. (2009c). As stated in that paper, "all core galaxies are extra light galaxies, too" if their merger progenitors included extra light ellipticals. If the extra light is not scoured away by binary BHs, it contributes to the steep central brightness profiles of giant Es that, together with their shallow halos, gives them their large Sérsic indices. However, most Sérsic fits to core Es have small residuals whose profiles in Figures 11–15 and 49–56 show no significant upward wiggles just outside the core that are suggestive of extra light. The giant elliptical whose residual profile most allows both a core and extra light is NGC 4472 (Figure 49, bottom). However, this figure also shows brightness profiles of candidate extra light progenitors NGC 4459 (which is one of the brightest) and NGC 4458 (which is typical in luminosity but which has an unusually large amount of extra light). In both galaxies, the extra light lives at radii that would be inside the core of NGC 4472. Also, the amount of light that is missing in the core of NGC 4472 (absolute magnitude $M_{V,\rm def} = -17.5$) is comparable to the extra light in NGC 4459 and NGC 4458 ($M_{V,\rm extra} = -17.5$ and -16.0, respectively). Thus, if present-day, extra light ellipticals in Virgo are the dry-merger progenitors of giant core Es, then the extra stars are preferentially scoured away during core formation. It is not clear how much extra light survives.

10.4. Sérsic Index as a Galaxy Formation Diagnostic

One of the clearest conclusions of this paper is that galaxy profile shape as parameterized by the Sérsic index participates in the E–E dichotomy. This changes our view of the well-known correlation that n increases with galaxy luminosity. Figure 33 shows that n does correlate with M_{VT} in Sph galaxies. But elliptical galaxies do not show a continuous correlation. Instead, our observations show two clumps of points: core Es have $n > 4$ but no correlation of n with M_{VT}, and extra light galaxies have $n \simeq 3 \pm 1$ but little correlation between n and M_{VT}. NGC 4621 is the exception; it behaves like a core galaxy that has had its core filled by a late accretion.

Signs of this behavior have been evident from the beginning. The Sérsic indices in Caon et al. (1993) are, on the whole, very accurate (see Figure 74 in Appendix A.3), and they already show two clumps of points in $n - r_e$ plots. Also, Caon et al. (1993) note that "boxy galaxies have larger n than disky galaxies." D'Onofrio et al. (1994) presciently comment that "it is hard to understand whether there is a global trend of [n] with [$\log r_e$] or whether instead there are two distant clusters of points ... corresponding to the two galaxy families, each not presenting any correlation between [n] and [$\log r_e$] within itself, but the relative positions of which mimic the global trend." Their galaxy families are closely related to our E–E dichotomy. In the same vein, Graham et al. (1996) see no correlation of n with luminosity for brightest cluster galaxies (their Figure 8), although they see an $n - r_e$ correlation (their Figure 11) that may be the product of parameter coupling (their Figure 3). In truth, the main reason why people have come to believe in an n–M_V correlation appears to be that they included Sphs—which have nothing to do with ellipticals—and that the n–M_V dichotomy was sometimes blurred by measurement errors.

What do we learn from our Sérsic index results?

A hint can be seen in the earliest simulations constructed to investigate the kinds of mergers that make realistic ellipticals. van Albada (1982) is remembered (Binney & Tremaine 1987) for having shown that larger amounts of dynamical violence—that is, larger collapse factors and lumpier initial conditions—produce ellipticals with more nearly $r^{1/4}$-law profiles. A closer look at his figures shows that van Albada's merger remnants are more consistent with Sérsic functions than with $r^{1/4}$ laws. They depart from $r^{1/4}$ laws such that $n < 4$ for gentle collapses or mergers, whereas $n > 4$ for violent collapses or mergers. This is not surprising, because large collapse factors give some stars total energies that are nearly zero. That is, they fling stars into extended halos with $n > 4$. The hint is that giant, core ellipticals, which have $n > 4$, formed with more dynamical violence than small, coreless ellipticals, which have $n < 4$. Tiny ellipticals have Sérsic indices $n \sim 2$ that are not much higher than $n \simeq 1$ in exponential disks. Little splashing of stars to large radii is required to make these profiles, although large amounts of dissipation are needed to turn low-density disks into high-density ellipticals (Carlberg 1986; Kormendy 1989; Nipoti et al. 2003; Hopkins et al. 2008a, 2008b, 2009a, 2009c).

A comparison of our results with simulations of galaxy mergers and their remnants shows good agreement with the above picture. The simulated merger remnants in Figure 4 have Sérsic function profiles with $n < 4$. Examination of Figure 3 in Springel & Hernquist (2005) shows that the old stars in the remnant ("bulge $\approx$ E" in Figure 43 here) have a Sérsic profile with $n < 4$. This is not obvious in Figure 43 because the radius scale is logarithmic. Extensive simulations of binary mergers by Naab & Trujillo (2006) also tend to produce $n \sim 3$–4. The remnants in Figure 44 have $n \simeq 3$. Hopkins et al. (2009a) emphasize that "the outer shape of the light profile in simulated and observed systems (when fit to properly account for the central light) does not depend on mass, with a mean outer Sérsic index ~ 2.5." We emphasize the same point; excluding NGC 4621, our extra light Es have an unweighted mean Sérsic index of 2.51 ± 0.17 and little dependence on M_{VT}. So there is excellent consistency between observations of extra light galaxies and simulations in which these galaxies were made in a single merger of plausible, gas-rich progenitor galaxies. *We conclude that the structure of extra light galaxies was created by only a few major mergers.*

In contrast, core Es have much larger n values that likely are produced by many successive mergers, lots of merger violence, and—plausibly—later heating and minor galaxy accretion. Simulations of binary dry mergers show only a little redistribution of energy outward, i.e., a small increase in n (Hopkins et al. 2009c). However, repeated minor mergers cause n to evolve toward larger values (Bournaud et al. 2007). The dynamical violence inherent in hierarchical clustering naturally heats the outer halos of giant galaxies; an extreme version of this process is the blending of the outer parts of certain giant ellipticals into their cD halos made of cluster debris (Gallagher & Ostriker 1972; Richstone 1976; Dressler 1979; Kelson et al. 2002). Nevertheless, further study of exactly what combination of physical processes gives core ellipticals their large Sérsic indices would be worth while.

11. COMPLICATIONS

This section highlights complications in our results. They do not threaten our conclusions, but they deserve further work.

11.1. Today's Extra Light Ellipticals are Not the Merger Progenitors of Most Core Ellipticals

Some small core ellipticals may be dry-merger remnants of today's extra light ellipticals. But these cannot be the merger progenitors of most core Es. Figures 45 and 46 show why.

Figure 45 shows the well-known correlation between alpha element overabundance and galaxy velocity dispersion. Galaxies that have cores are shown in red, while galaxies that have coreless central profiles ("power law" in Lauer et al. 2007b or "extra light" here) are shown in blue. We know that cores predominate in giant Es whereas extra light is the rule in low-luminosity Es. We also know that luminosity correlates with velocity dispersion (Faber & Jackson 1976). So it is not surprising that core and power-law galaxies occupy different, slightly overlapping parts of the [Mg/Fe]–σ correlation. However, this correlation and the Faber–Jackson relation have substantial scatter, so the above result is not guaranteed. In fact, Figure 45 demonstrates that [Mg/Fe] enhancement participates in the E–E dichotomy. This is an important new result.

It has implications for the merger formation of ellipticals. Alpha element overabundances tell us the timescales on which the stars formed. Alpha elements like Mg are produced soon after starbursts when massive stars die as supernovae of Type II. They get diluted by Fe produced by Type I supernovae starting $\lesssim 1$ Gyr later. After that, [α/Fe] can never be very enhanced again. So, large [α/Fe] favors short star-formation timescales (Worthey et al. 1992; Terndrup 1993; Matteucci 1994; Bender & Paquet 1995; Thomas et al. 1999, 2002, 2005).

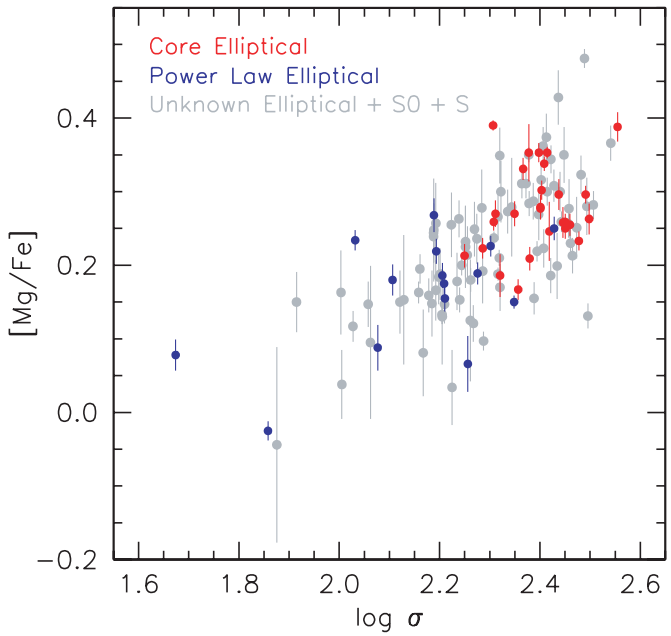

Figure 45. Alpha element overabundance in log solar units vs. velocity dispersion in km s^{-1} (data from Thomas et al. 2005). The red and blue points denote core and power-law ellipticals classified here or by Lauer et al. (2007b).

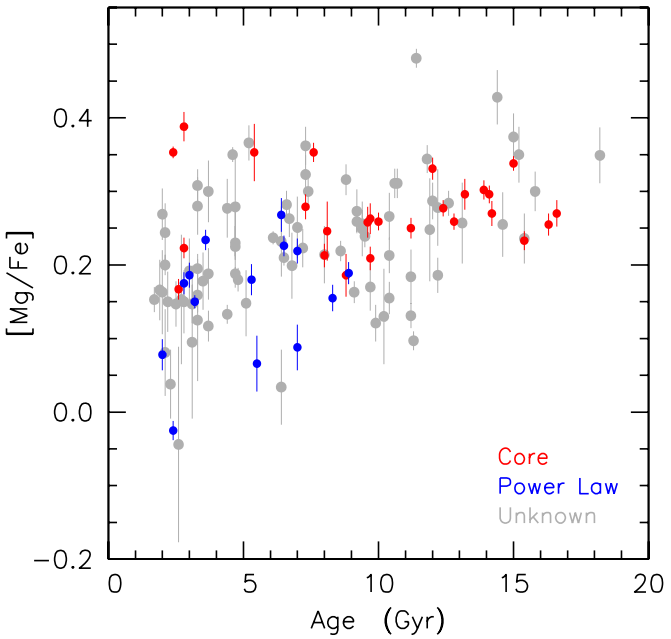

Figure 46. Alpha element overabundance vs. the relative age of the stellar population for the sample in Figure 45 (data from Thomas et al. 2005).

Therefore, Figure 45 implies that the stars in core Es formed over shorter times than did the stars in power-law Es. Neither the observed [Mg/Fe] values nor the inferred star-formation timescales can be altered by dry mergers. If the formation of core Es included any star formation, this is likely to decrease [Mg/Fe] further. So, Figure 45 is consistent with the hypothesis that some small core Es are dry merger products of the biggest power-law ellipticals. But today's power-law Es cannot be the progenitors of most—and especially not the biggest—core Es.

Similarly, *N*-body simulations of dry binary mergers robustly predict that σ in the remnant is similar to σ in the progenitors (see Hopkins et al. 2009c, who also review previous results). Core galaxies generally have larger σ than power-law galaxies. Either their progenitors were not like present-day power-law galaxies or the mergers were not like those that were modeled.

Finally, Figure 46 shows [Mg/Fe] versus relative age. Core and power-law ellipticals overlap only slightly. Stellar population ages are part of the E–E dichotomy (Nipoti & Binney 2007).

Again, the progenitors of most core ellipticals must have been different from today's power-law ellipticals. The latter are mostly younger than the former. Dry mergers cannot age stars.

These results threaten neither the merger picture nor our conclusion that core and extra light Es were made, respectively, in dry and wet mergers. However, they do provide clues about the details of the formation processes. Physics that is missing from our present picture but that almost certainly affected the formation of core ellipticals includes the following:

1. The merger progenitors that made core ellipticals may have been different from all galaxies seen today (e.g., Buitrago et al. 2008; van der Wel et al. 2008; Naab & Ostriker 2009). They could have included an earlier generation of power-law ellipticals, provided that essentially all of them were used up.
2. Quasar-mode AGN feedback (e.g., Cattaneo et al. 2009) is ignored but is believed to have whittled the high-mass end of the galaxy mass function down from the shallow slope predicted from the cold dark matter fluctuation spectrum to the much steeper form observed (Binney 2004). If it could do this, it is easy to believe that it could affect the internal structure of galaxies.
3. We consider only mergers of two galaxies with each other. In the early universe, many galaxies may have merged simultaneously. This affects the structure of the remnant and can change the prediction that σ is unchanged by a dry merger.

These comments should not be interpreted as criticisms of published formation models. Galaxy formation is complicated and not fully constrained by observations. Modeling it is a step-by-step process. Impressive progress has been made by including gas dissipation, star formation, and energy feedback, most recently by Hopkins et al. (2008b, 2009a, 2009c). We hope that the observational constraints discussed here will provide input for the next generation of formation models.

11.2. Do Minor Mergers Build Extra Light Components?

We suggest that extra light was made in starbursts triggered by major mergers. The connection between extra light in Sérsic-function ellipticals and simulations of dissipative mergers is one of the main results of this paper. However, an alternative possibility is that extra light was built out of gas that trickled in during minor mergers. These must happen (e.g., NGC 4473; Section 9.2). In some ellipticals, dust has settled into well-defined, major-axis disks at small radii, where dynamical clocks run quickly, but remains irregular at large radii, where clocks run slowly and galaxies remember accretion geometries for a long time. An example is NGC 315 (Kormendy & Stauffer 1987; Verdoes Kleijn et al. 1999; Capetti et al. 2000).

However, there are signs that minor accretions did not build the extra light in most ellipticals. Often it is as old as the rest of the galaxy (Kuntschner et al. 2006; Section 9.4). Also: *The extra light participates in a dichotomy of physical properties that mostly involves global structure.* Global rotation, isophote shape, and flattening (E3 for coreless Es but E1.5 for core Es; Tremblay & Merritt 1996) are not likely to be affected by minor

accretions. We expect that minor accretions occasionally affect central structure. But the above arguments suggest that they are not the main source of the extra light.

11.3. Uncertainties in Profile Results

Sérsic indices are affected by a number of factors that are not taken into account in the fitting errors listed in Table 1.

First, Figures 11–32 illustrate major-axis profiles, and the Sérsic indices in Table 1 also are for major-axis profiles. We made this choice because we wanted as much radial leverage as possible in distinguishing central and global properties and in recognizing and decomposing bulges and disks. Since ellipticity profiles are not flat, mean- and minor-axis profiles have slightly different Sérsic indices than those along the major axis. However, they agree on the essential question of whether $n < 4$ or $n > 4$ (Figure 63). Since Sérsic index measures how much the outer profile is extended compared to the inner profile, and since an extended outer halo is a natural consequence of dynamical heating (splashing) during violent relaxation, it is reasonable to expect that the major-axis profile is the one that is most sensitive to the physics that we wish to explore.

Second, we measure V-band surface brightness profiles and use them as proxies for projected stellar densities. That is, we assume that mass-to-light ratios are constant with radius. The color gradients illustrated in Figures 11–32 show that this is not quite correct. Converting $g - z$ colors shows that $V - K$ typically varies by a few tenths of a mag arcsec^{-2} over the Sérsic part of the profile. Near-infrared, K-band profiles are insensitive to population differences. Applying $V - K$ colors to the observed profiles would change n by small amounts but would not change the dichotomy that we find between coreless ellipticals with $n < 4$ and core ellipticals with $n > 4$.

A more serious issue is dark matter. Its importance must depend on radius. It is remarkable that there is so much regularity in the light profiles when we do not take dark matter into account. The correlations that we observe are clearcut. But it will be important to investigate how the stellar structure of galaxies is affected by halo structure and dynamics.

Finally, we need to keep in mind that our results are derived almost entirely from galaxies in the Virgo cluster. Work on a larger sample is in progress to check whether ellipticals in other environments are similar to those in Virgo.

12. ELLIPTICAL GALAXY FORMATION

12.1. Summary: New Features of the E–E Dichotomy

We have measured and assembled composite surface photometry from as many sources as possible for all 24 known elliptical galaxies in the Virgo cluster plus three background ellipticals. Because their classifications were unclear at the start of the program, we also included five galaxies that proved to be S0s and 10 galaxies that proved to be spheroidals. Composite photometry over large dynamic ranges provides improved control of systematic problems such as sky subtraction errors. We can derive more accurate profile parameters and use them to investigate galaxy formation. Our conclusions are as follows:

Sérsic functions fit the brightness profiles of the main bodies of 25 of our 27 ellipticals to within $\simeq 0.04$ mag arcsec^{-2} over a mean surface brightness range of 8.7 ± 0.4 mag arcsec^{-2}. In five of the largest-dynamic-range galaxies, the fit range is 10.3–11.5 mag arcsec^{-2}, i.e., factors of 13,000–40,000 in surface brightness. As a result, we can reliably identify departures from Sérsic functions that are diagnostic of formation processes.

The distinction between cuspy core ellipticals and galaxies without cores is well known and clearly evident in our data. We base the distinction on inner departures from outer Sérsic profiles rather than on the slope of the projected brightness profile at small radii as in Nuker papers (Lauer et al. 1995, 2005, 2007b). However, both kinds of analysis machinery usually identify the same galaxies as having cores.

Our results reveal new aspects of the dichotomy (Section 2.2) into two kinds of elliptical galaxies: (1) giant-boxy-core ellipticals have stellar populations that mostly are old and enhanced in α elements. Their main bodies have Sérsic indices $n > 4$, uncorrelated with M_{VT}. The light that is "missing" in cores with respect to the inward extrapolation of the outer Sérsic profile corresponds to a stellar mass—in our sample—about 11 times as big as the masses of the central BHs. (2) Lower-luminosity, disky-coreless ellipticals generally are made of younger stars than are core ellipticals. Their stellar populations also are less enhanced or even Solar in α element abundances. Their main bodies have Sérsic indices $n \leqslant 4$ almost uncorrelated with M_{VT}. And they do not have featureless, nearly power-law central profiles; rather, they show distinct profile breaks and, interior to them, extra light with respect to the inward extrapolation of their outer Sérsic profiles. Previously called "power-law" ellipticals, we refer to them as "extra light ellipticals." The amount of extra light is a larger and more varied fraction of the total light of the galaxy than is the missing light that defines cores. A small number of exceptions to all aspects of the dichotomy are observed. The dividing line between the above types is at absolute magnitude $M_{VT} \simeq -21.6$ and is not sharp.

12.2. How the E–E Dichotomy Arose

We suggest that core and extra light ellipticals formed in dissipationless ("dry") and dissipational ("wet") mergers, respectively.

This idea is not new. The need for dissipation to make the high phase space and mass densities of low-luminosity Es has been recognized for a long time (Ostriker 1980; Carlberg 1986; Gunn 1987; Kormendy 1989; Kormendy & Sanders 1992); it has been connected with the merger picture from the beginning (Toomre & Toomre 1972). So, for example, Faber et al. (1997) concluded that "Disky [power-law] galaxies, including their high central densities, suggest final mergers that were gas rich."

Our observations further strengthen this picture. Numerical simulations of dissipative mergers that include star formation and energy feedback predict extra, dense central components just like the ones that we observe. We interpret the extra light as a "smoking gun" that points to dissipational formation. It frequently has disky structure and kinematic decoupling that are natural consequences of dissipative mergers. Extra light profiles like those that we see in old ellipticals have also been observed in mergers-in-progress (Rothberg & Joseph 2004, 2006). Some simulations suggest further that larger Sérsic indices n are produced by more violent mergers. *Thus numerical simulations and our observations both lead to a picture in which the last merger that made coreless galaxies was relatively gentle and wet, while the last merger that made core galaxies was relatively violent and dry.*

Because in the absence of supermassive BH, mergers of coreless galaxies tend to make coreless galaxies. Therefore, Faber et al. (1997) pointed out that "arguments concerning [the

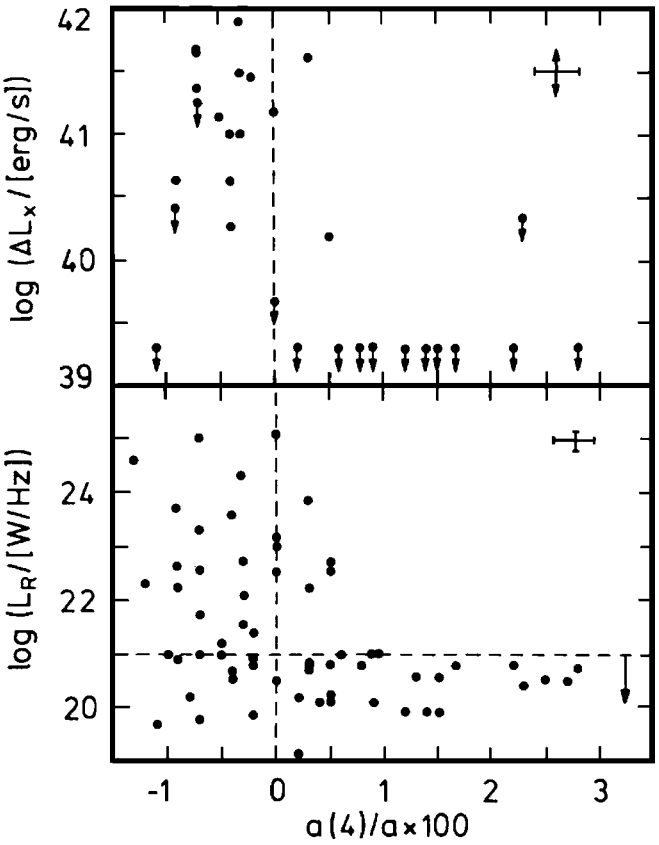

Figure 47. Correlation of X-ray emission from hot gas (top) and radio emission (bottom) with isophote shape parameter a_4 of elliptical galaxies (from Bender et al. 1989). Boxy isophotes have $a_4 < 0$; disky isophotes have $a_4 > 0$.

formation of] boxy [core] galaxies are less clear: the global kinematics of these galaxies suggest final mergers that were gas poor, but forming and preserving cores in such models may be difficult." To solve this problem, the key realization has been that cores may be excavated by binary BHs. This idea, once radical and ad hoc, has become mainstream as we have found a BH in every well-observed elliptical. If we believe that ellipticals form by major mergers, then these must generally make BH binaries. BH scouring, far from being ad hoc, becomes inevitable. While the BHs are well separated, they sink individually by dynamical friction against the background stars. The light distribution of the galaxy is not affected, because the BHs have a small fraction of the mass of the galaxy. But as soon as the BH separation $2R$ is small enough so that the total stellar mass at $r \lesssim R$ is comparable to the mass of the BHs, they must affect the stellar density profile. After several dry mergers, the stars that they have flung to larger radii add up to several times the combined BH masses. The excavated cores can even be hollow, and a few hollow cores have been observed (Lauer et al. 2002). Faber et al. (1997) showed that observed core properties are reasonably consistent with core scouring.

But an important problem remains unsolved. The puzzle is no longer, "How can cores form?" but rather, "How can core excavation by binary BHs be prevented?" Faber et al. (1997) ask the same question and propose the same answer that we do: "...if cores are formed by merging binary BHs, why do power-law galaxies...not have cores? BHs appear to be just as common in power-law galaxies (Kormendy & Richstone 1995). Perhaps power laws can be regenerated by star formation from fresh gas supplied by the latest merger. However, to avoid being ejected by the BH binary, the new stars must form *after* the BH binary shrinks, which poses a timing problem if BHs sink to the center more slowly than gas."

Our observations suggest the same solution. The extra stellar masses in coreless ellipticals tend to be larger than BH masses. BH binaries cannot fling most of it away. We suggest that central starbursts associated with dissipative mergers have swamped BH scouring and filled in any cores. This reduces the timing problem discussed by Faber et al. (1997). It may not prevent the occasional late formation of a new core if the BH binary survives the starburst. In fact, several extra light ellipticals show signs of tiny cores *in the extra light*. NGC 4458 is the best example (Figure 19). The interplay between star formation and BH scouring is likely to be complicated. Any oversimplistic interpretation is likely to suffer exceptions.

Meanwhile, numerical simulations that seek to reproduce orbit structure, rotation, and isophote shapes are most successful when disky Es are made in wet mergers and boxy Es are made in dry mergers (Naab et al. 1999, 2006a, 2006b; Naab & Burkert 2003; Burkert et al. 2008). Making extreme, nonrotating Es is still a challenge (Naab et al. 2008). The solution may be a succession of mergers of several galaxies at once. So,

How the differences between the two kinds of ellipticals arose appears well established by observations and simulations. *Why* they arose is the subject of the next section.

12.3. Why the E–E Dichotomy Arose

12.3.1. X-Ray-Emitting Gas and AGN Energy Feedback Create the E–E Dichotomy

The key observations prove to be two aspects of the E–E dichotomy that are shown in Figure 47. Bender et al. (1987, 1989) discovered (1) that boxy ellipticals tend to be radio-loud while disky ellipticals do not, and (2) that boxy ellipticals mostly contain X-ray-emitting gas while disky ellipticals do not. These correlations were not understood; most subsequent discussions did not mention them but rather concentrated on the structural and dynamical differences between the two kinds of ellipticals. Now the X-ray and radio correlations take center stage.

We suggest that X-ray-emitting gas that is kept hot by AGN feedback is the reason why giant-boxy-core ellipticals formed dissipationlessly. In contrast, disky-extra-light ellipticals and their merger progenitors are too low in mass to hold onto hot gas. Also, we suggest that AGN feedback is weaker in these galaxies; they experienced either weak feedback (Section 10.2) or positive feedback (Silk 2005). As a result, dissipative starbursts were possible. Figure 47 provides the connection between X-ray gas, AGN physics, and the E–E dichotomy.

BH binding energies are enormous; if only a small fraction of the energy released in making them is fed back into gaseous protogalaxies, the effect on galaxy formation is profound (Ostriker & Ciotti 2005). Silk & Rees (1998) make a compelling case that AGN feedback has a major effect on the formation of giant galaxies. Their arguments, the results of galaxy formation models (reviewed by Cattaneo et al. 2009), and Section 10.2 here suggest that AGN feedback is a strong function of galaxy luminosity. The introduction of feedback into formation models is ad hoc—it is tuned to solve specific problems. We do not understand the underlying physics. And AGNs are episodic, with long "down times" between short periods of activity. How can we be sure that an AGN is switched on every time we need one (e.g.) to quench star formation when gas-rich galaxies are accreted by old, α-element-enhanced ellipticals? Therefore,

A welcome watershed in the credibility of AGN feedback was a workshop on "The Role of Black Holes in Galaxy Formation and Evolution" (Potsdam, Germany; 2006 September). McNamara & Nulsen (2007) and Cattaneo et al. (2009) provide reviews. The above problems are plausibly solved if AGN energy is fed into X-ray-emitting gas in giant galaxies and galaxy clusters. As emphasized by Best (2006; see Kauffmann et al. 2008), feedback requires a working surface. Hot gas provides that surface. We suggest that it stores AGN energy and smooths out the episodic nature of the energy input. It quenches star formation in accreted, gas-rich galaxies before that star formation threatens the observation that stars in giant Es are old (Binney 2004; Dekel & Birnboim 2006; Nipoti & Binney 2007). Can radio AGNs keep hot gas hot? We are not sure. But *Chandra* and *XMM-Newton* observations make a strong case that central radio sources heat the X-ray gas in clusters of galaxies. Examples include the Perseus cluster (Böhringer et al. 1993; Fabian et al. 2000, 2003, 2006, 2008; Sanders & Fabian 2007); Hydra A (McNamara et al. 2000); Abell 2052 (Blanton et al. 2003a); M 87 (Forman et al. 2005); and MS0735.6 + 7421 (McNamara et al. 2005). Evidence for shock fronts, bubbles, and compression waves are signs that energy outflow in jets is redistributed more isotropically into the hot gas. The evidence that jets heat gas within galaxies as well as within clusters is less direct. Best et al. (2006) conclude that "the radio sources which give rise to the bulk of radio source heating are low-luminosity sources which tend to be compact and more confined to the host galaxy." Diehl & Statler (2008) also find evidence for AGN feedback within normal Es. These observations make AGN heating of hot gas more believable. *We assume that, for AGN feedback to work, a galaxy needs both an X-ray gas halo and sporadic AGN activity.*

Figure 47 shows that both features are common in boxy and rare in disky galaxies. This is confirmed by Balmaverde & Capetti (2006), Capetti & Balmaverde (2006), and Ellis & O'Sullivan (2006). Almost equivalently, both features are common in big and rare in small galaxies (O'Sullivan et al. 2001; Ellis & O'Sullivan 2006; Best et al. 2005; Pasquali et al. 2009). First consider radio AGN heating. Best et al. (2005) show that the fraction $f_{\rm radio\text{-}loud}$ of galaxies that are radio-loud increases dramatically with increasing stellar mass M_*, $f_{\rm radio\text{-}loud} \propto M_*^{2.5}$. In particular, $f_{\rm radio\text{-}loud}$ rises past 1% at $M_* \simeq 10^{11}\ M_\odot$; this is roughly the transition mass between the two kinds of ellipticals. At the highest M_*, which are generally the oldest (Figure 46), most α-element-enhanced (Figure 45) and most boxy (Figure 47) galaxies, > 30% of ellipticals are radio-loud. Not surprisingly, Best and collaborators conclude that radio-mode heating is also a strong function of galaxy stellar mass. Taking jet properties and AGN duty cycles into account, they estimate that radio-mode heating scales with central BH mass as $M_\bullet^{2.2}$. Therefore, it is similarly a strong function of M_* and M_{VT} (Faber & Jackson 1976; Tremaine et al. 2002).

We can also update the connection between hot gas X-ray luminosity and the E–E dichotomy. Pellegrini (1999, 2005) confirms that X-ray luminosity participates in the dichotomy. Like Bender et al. (1989), she sees a correlation with a_4. She also finds the corresponding correlations with central profile slope and the degree of rotational support. In addition,

Figure 48 shows how the total X-ray emission of elliptical galaxies depends on stellar luminosity. It updates Figure 9 in Ellis & O'Sullivan (2006), which shows the *ROSAT* sample of O'Sullivan et al. (2001) coded according to whether the

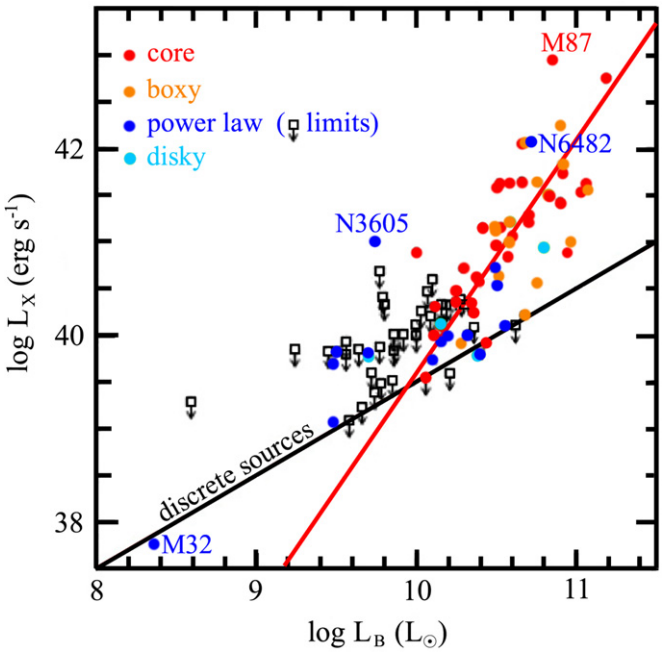

Figure 48. Total observed X-ray emission vs. galaxy *B*-band luminosity (adapted from Figure 9 of Ellis & O'Sullivan 2006). Detections are color coded according to the E–E dichotomy (see the key). New classifications of core and power-law profiles are from Lauer et al. (2007b) and from our photometry. Classifications of boxy and disky structure are from Bender et al. (1989). The contribution from discrete sources is estimated by the black line (O'Sullivan et al. 2001). The red line is a bisector fit to the core-boxy points, i.e., the bisector of regressions of log L_X on log L_B and of log L_B on log L_X. Core-boxy ellipticals statistically reach $L_X = 0$ from hot gas at $\log L_B \simeq 9.94$. This corresponds to $M_V \simeq -20.4$, which is about 1 mag fainter than the stellar luminosity that divides the two kinds of ellipticals. Core and power-law Es clearly overlap in luminosity, but most core galaxies do and most power-law galaxies do not contain significant X-ray-emitting gas. The strongest exceptions, NGC 3605 and NGC 6482, are discussed in Footnote 11.

galaxies have core or power-law profiles. More profile classifications are now available. Also, we can use boxy versus disky structure to distinguish the two types of ellipticals. (Occasionally this conflicts with profile classification; then we use the latter.) The black line shows the O'Sullivan et al. (2001) estimate of the contribution from discrete sources such as X-ray binaries. The discrete source contribution to L_X is proportional to L_B (Fabbiano 2006). Consistent with Bender et al. (1989, Figure 47 here), Figure 48 shows that few coreless-disky galaxies are detected in X-rays and those that are detected mostly are consistent with the discrete source estimate. In contrast, almost all core-boxy galaxies are detected in X-rays and show a steep dependence of L_X on L_B. So Figure 48 further confirms that X-ray luminosity participates in the E–E dichotomy.

The red line crosses the black line at $\log L_B \simeq 9.94$. That is, the X-ray luminosity from hot gas goes to zero at $M_V \simeq -20.4$. This is about 1 mag fainter than the stellar luminosity that divides the two kinds of ellipticals. Core and power-law Es are known to overlap in luminosity (Lauer et al. 1995, 2005, 2007b; Faber et al. 1997), and this is evident in Figure 48. But *Figure 48 suggests that most core galaxies do and most power-law galaxies do not contain significant X-ray-emitting gas.*

A few power-law galaxies may contain small amounts of X-ray gas, including NGC 4387, NGC 4473, NGC 4458, and

NGC 4621 from our sample.[10] However, O'Sullivan et al. (2001) estimate that the contribution from discrete sources varies by a factor of ~ 4 from galaxy to galaxy. It is not certain that these galaxies contain hot gas. More importantly, NGC 4387 is located between the gas-rich, giant Es NGC 4374 and NGC 4406. NGC 4473 is in the chain of Virgo galaxies that has NGC 4374 and NGC 4406 at one end. NGC 4458 forms a close pair with the brighter S0 NGC 4461. All three galaxies benefit from the nearby presence of additional gravitational potential wells.[11] And NGC 4621 has $M_{VT} = -21.54$. It is not surprising if these four galaxies contain a little hot gas. It is also consistent with our formation picture: any merger progenitors of these galaxies were less luminous and less able to hold hot gas; it is plausible that hot gas could be retained only after a merger made a deep enough potential well. Also, from stellar population data, the wet mergers that made these galaxies took place long ago, when the Virgo cluster was less well formed than it is now. This highlights an unavoidable uncertainty in our picture: we interpret the formation physics in terms of X-ray gas that is observed now, but that formation took place long ago. Since then, hot gas content, heating mechanisms, and cooling rates may have evolved. Connecting present-day observations with a formation picture depends on our assumption that mass controls X-ray gas content. It is supported by the conclusion that AGN heating rates can balance cooling rates, so steady state is possible (Best et al. 2006, 2007).

What we find compelling is this: *The transition luminosity between galaxies that should contain X-ray gas and those that should not can be estimated from theory and tested for consistency with observations using semi-analytic models. The results agree with the observed X-ray transition luminosity found above and with the observed E–E transition luminosity.* Birnboim & Dekel (2003) and Dekel & Birnboim (2006, 2008) present theoretical arguments and Kereš et al. (2005) find in SPH simulations of gas accretion in hierarchical clustering that, when gas falls into shallow potential wells, the dynamics are gentle, the inflow stays cold, and it makes star-forming disks. In contrast, when gas accretes onto giant galaxies, a shock develops, the gas is heated to the virial temperature, and star formation is quenched. Dekel & Birnboim (2006, 2008) propose that the gas is maintained at this hot temperature by the heating caused by additional accretion. AGN feedback is an additional heat source (Best et al. 2006; Best 2007a, 2007b). The transition between galaxies with and without X-ray gas is expected to occur at the dark matter halo mass at which the hot gas cooling time is comparable to the infall time. Dekel & Birnboim estimate that this happens at $M_{\rm crit} \simeq 10^{12}\ M_\odot$. Kereš et al. (2005) get $10^{11.4}\ M_\odot$. Implementing $M_{\rm crit}$ quenching proves to allow semi-analytic models of galaxy formation to reproduce the color bimodality of galaxies ("red sequence" versus "blue cloud") as a function of redshift (Cattaneo et al. 2006, 2008, 2009). Using a baryon-to-total mass ratio of 1/6 (Komatsu et al. 2009), $M_{\rm crit} = 10^{12}\ M_\odot$ implies a stellar mass of $M_* = 1.7 \times 10^{11}\ M_\odot$. With a $M/L_B \simeq 8$ (Section 10.1), this corresponds to $M_B = -20.3$ or $M_V = -21.3$. This is almost exactly the absolute magnitude that divides our faintest core galaxy (NGC 4552, $M_{VT} = -21.66$) from our brightest extra light galaxy (NGC 4621, $M_{VT} = -21.54$). The dividing luminosity in Figure 48 is formally a factor of 3 fainter, but L_X is significantly higher than the discrete source estimate only at $M_B \lesssim -20.6$ ($\log L_B \gtrsim 10.4$). This is remarkable agreement.

12.3.2. ULIRGs as Ellipticals in Formation: Do Supernovae Control Dwarf Galaxy Evolution Whereas AGNs Control Giant Galaxy Evolution?

Are low-luminosity ellipticals gas-free? If so, why? Gas shed by dying stars is just as large a fraction of small galaxies as it is of large ones, and galaxies should fill quickly with recycled gas (Ciotti 1991; Ostriker & Ciotti 2005). We suggest that the answer to the first question above is a resounding "yes and no."

First the "yes" part: published work and present results suggest that *the energy feedback that controls galaxy evolution changes fundamentally from supernovae in small galaxies to AGNs in large ones*. We have argued that AGN feedback gets more important at higher galaxy masses. At the highest masses, the case for AGN feedback is compelling (Cattaneo et al. 2009). In dwarfs, it is difficult to doubt the importance of supernova-driven baryonic blowout as one process that gives extreme dwarfs their low baryon densities and that converts irregulars into spheroidals (Sections 2.1 and 8; Dekel & Silk 1986). Very general arguments imply that supernova feedback gets less important at higher galaxy masses (e.g., Dekel & Silk 1986; Somerville & Primack 1999, who review earlier work; Benson et al. 2000, 2003; Garnett 2002; Dekel & Woo 2003; Ostriker & Ciotti 2005; Veilleux et al. 2005).

Provided that star formation is rapid, Dekel & Woo (2003) find that supernovae can unbind the remaining gas if the stellar mass is $M_* \lesssim 3 \times 10^{10}\ M_\odot$. This agrees remarkably well with the mass $M_* \sim 5 \times 10^{10} M_\odot$ at which the L_X–L_B red line in Figure 48 crosses the estimate of L_X from discrete sources. That is, Dekel & Woo suggest that supernovae can drive gas out of galaxies over just the mass range where Figure 48 shows that no hot gas is seen. However, a starburst is necessary so that many supernovae go off together. Absent a starburst, Dekel & Woo assume that supernovae merely regulate star formation. Like Dekel & Silk (1986) and consistent with Garnett (2002), they use supernova-driven baryon ejection and supernova-regulated star formation to explain the low-luminosity, low-surface-brightness sequence

[10] Nine of 17 extra light galaxies in Table 1 are represented in Figure 48; the four detections are discussed in the text; the rest (mostly fainter galaxies) are limits. Three of our five S0s are represented in Figure 48; all are limits. All of our core galaxies except NGC 4382 are represented in Figure 48; all are detections. So our conclusions about the relevance of hot gas to the E–E dichotomy are based very significantly on X-ray observations of the present Virgo cluster sample.

[11] This is also true of NGC 3605, which stands out in Figure 48 as having high L_X at low L_B. But NGC 3605 lives inside the X-ray halo of the much brighter elliptical NGC 3607. It is not clear that NGC 3605 perturbs the X-ray contours of NGC 3607 (Fabbiano et al. 1992). At best, measuring a separate X-ray luminosity for NGC 3605 is tricky. But also, NGC 3605 benefits from the deep potential well of the bigger galaxy. So rather than being an exception to our conclusions, it is a good example of the importance of high mass in retaining hot gas. A possible real exception is NGC 4125, the highest-L_X disky galaxy in Figure 48. A not-yet-relaxed merger in progress (Schweizer & Seitzer 1992), the observation of nuclear dust (Rest et al. 2001; Lauer et al. 2005; Draine 2007)—which prevents us from classifying the central profile—suggests that the merger involved some cold gas. The disky structure may be temporary, and the X-ray luminosity may be temporarily enhanced. However, the galaxy may settle down to be a weak exception to our conclusions; that is, the remnant of a merger that was at least damp in a galaxy that ends up luminous enough to contain some X-ray gas. Finally, NGC 6482 is not a problem in terms of L_X (L_B is certainly high enough), but it is a *bona fide* exception to the usual luminosity at which the E-E dichotomy happens. It is very disky (Bender et al. 1989). From archival *HST* images, we find that it has a extra light and a normal small Sérsic index of 2.4 ± 0.2. It is an example of a "fossil group" (Khosroshahi et al. 2004). We interpret it as the fossil of the merger(s) of several progenitors that were too low in mass to have hot gas and that therefore could merge dissipatively. After the merger, the remnant is much more massive than a normal remnant of a wet merger. Given that ellipticals have a great variety of merger histories, we expect a few exceptions to all aspects of the E–E dichotomy, including the luminosity at which it happens. That is, it seems inevitable that a few outliers like NGC 6482 will have formed in rare variations on the merger theme.

of spirals, irregulars, and spheroidals that form one side of our E–Sph dichotomy.

Fundamental to the physical picture that we suggest in this paper is a merger-induced starburst that makes the extra light component in coreless galaxies. This may be the rapid star-formation event that Dekel & Woo need in order that supernovae can clean low-mass merger remnants of their gas.

Doing so is not a trivial issue:

Ultraluminous infrared galaxies (ULIRGs) are mergers-in-progress (Joseph & Wright 1985; Sanders et al. 1988a, 1988b; Sanders & Mirabel 1996; Rigopoulou et al. 1999; Dasyra et al. 2006a) that are prototypes of the formation of ellipticals in the local universe (Kormendy & Sanders 1992). They are rich in gas and dust. Their structural parameters are consistent with the fundamental plane (Kormendy & Sanders 1992; Doyon et al. 1994; Genzel et al. 2001; Tacconi et al. 2002; Veilleux et al. 2006; Dasyra et al. 2006a, 2006b). Stellar velocity dispersions $\sigma \simeq 100$–230 km s^{-1} show that local ULIRGs are progenitors of moderate-luminosity ellipticals; i.e., the disky-coreless side of the E–E dichotomy and *not* boxy-core ellipticals (Genzel et al. 2001; Tacconi et al. 2002; Dasyra et al. 2006b, 2006c). So *ULIRGs are consistent with our formation picture: they are merger-induced starbursts that are making* $\sigma \sim 160 \pm 60$ *km s*$^{-1}$ *and hence coreless-disky ellipticals*. After much debate about what energy source dominates ULIRGs (Joseph 1999; Sanders 1999), it has become clear that starbursts dominate energetically in almost all cases (Lutz et al. 1996; Genzel et al. 1998, 2000; Downes & Solomon 1998; Joseph 1999; Rigopoulou et al. 1999; Tran et al. 2001; Spoon et al. 2007; Netzer et al. 2007; Vega et al. 2008; Nardini et al. 2008). ULIRGs are rare locally, but they get more common rapidly with increasing redshift (Sanders & Mirabel 1996; Le Floc'h et al. 2005). This is consistent with the protracted overall star-formation histories of disky-coreless but not boxy-core Es (see Renzini 2006 for a review). On the other hand, the timescales of individual starbursts in ULIRGs are a few tens of millions of years (Lutz et al. 1996; Genzel et al. 1998), not much longer than the lifetimes of the stars that die as supernovae and short enough for Dekel & Woo's argument. ULIRGs are exactly the ellipticals-in-formation that we propose. That's the good news. Here is the bad news:

It is a big step to understand how these intermediate-mass mergers-in-progress lose their gas, as they must do if they are to form extra light ellipticals. A plausible picture is this: (1) star formation in the infalling gas in a merger efficiently converts much of the gas into stars; (2) the observed, strong winds from ULIRGs—driven mainly by hot stars and supernovae—are beginning the process of gas ejection (see Veilleux et al. 2005 for a review), and (3) Dekel & Woo's argument tells us the mass range over which this process will ultimately be successful. Their estimate is consistent with our conclusion that a change in dominance from supernova to AGN feedback happens over a range of several magnitudes between $M_V \simeq -20.4$ and -21.6.

This helps: We have come to think that all dissipative mergers are like ULIRGs. Because of their extraordinary infrared luminosities, they deservedly attract attention. But there exist many less spectacular dissipative mergers with easily enough central star formation for our picture but less of a gas cleaning problem (e.g., Schweizer 1980, 1982, 1987, 1990, 1996, 1998; Hibbard et al. 1994; Hibbard & van Gorkom 1996). It is not necessary always to be *soaking* wet.

A caveat is the possible "no" answer above. Gas may not be completely absent in low-L galaxies; it may just get too cool to radiate X-rays. After all, there are strong reasons to believe that a warm-hot intergalactic medium surrounds even small galaxies (e.g., Danforth & Shull 2008; see Bregman 2007 for a review). But the good correlation of L_X with the E–E dichotomy suggests that a small amount of hot gas in low-luminosity Es (Ho 2008) is no problem for our formation picture. Still-smaller galaxies that were their merger progenitors can easily have contained the cold gas necessary to make wet mergers wet.

12.3.3. Perspective

In summary, we suggest that X-ray gas prevented star formation in the last mergers that made giant-boxy-core Es. And we suggest that AGN feedback is the main process that keeps hot gas hot. Thus, $M_{\rm crit}$ quenching is the fundamental reason *why* the E–E dichotomy arose. It is not necessary that both merger progenitors lacked cold gas, since hot gas can prevent star formation even when some cold gas is present. Metaphorically, there are three ways to be dry: water can be absent, frozen, or steam. This section was about steam.

Our picture of the formation of elliptical galaxies is closely similar to that advocated by Dekel and Cattaneo and collaborators on theoretical and modeling grounds and by Faber (2005) and Faber et al. (2007) based on observations of SDSS and distant galaxies. Their picture of "$M_{\rm crit}$ quenching" of star formation was developed to explain specific observational puzzles, mainly the color bimodality of galaxies and the surprising observation that the biggest ellipticals formed their stars quickly and long ago. Much effort has gone into showing that it explains the properties of galaxies as a function of redshift. These are important accomplishments. They account for the well deserved popularity of this formation picture.

Our results lead to the same bottom line via a different route. Independently of the above work, this paper has developed an observational picture of what it means to be an elliptical galaxy. We confirm that ellipticals form a well-defined structural sequence distinct from that of spheroidal galaxies. Its luminosity function is bounded at low luminosities approximately by M 32 and at high luminosities by M 87 and by still brighter cD galaxies. Ellipticals formed via major mergers; this was known. We have added to the evidence that ellipticals come in two varieties that have interpretably different properties. Among these are the distinction into core galaxies, which (if scoured by binary BHs) require dry mergers, and extra light ellipticals, where the extra light is a "smoking gun" that implies dissipative formation. This strengthens the conclusion—otherwise not new—that the reason for the E–E dichotomy is dry versus wet mergers. Why there is such a dramatic wet-versus-dry distinction and why it depends on galaxy mass was not known. Also, while it was known that the E–E dichotomy includes the presence or not of X-ray gas and the importance or not of radio AGNs, the relevance of these observations was not understood. We connect them into a coherent picture in which the X-ray dichotomy is central to our understanding of *why* the E–E dichotomy developed. Fundamental to the explanation is a transition from supernova-driven energy feedback in small galaxies to AGN feedback in large ones. We suggest that X-ray gas is the essential agent that makes dry mergers dry and that AGN feedback is important only in giant galaxies and keeps hot gas hot. The essential property that allows a galaxy to retain an X-ray halo is mass. The mass necessary for the observations that we have discussed is exactly the critical mass in the $M_{\rm crit}$ quenching picture. The two pictures have converged "for free."

12.4. Context: Summary of Elliptical Galaxy Formation

Our results contribute to a picture of elliptical galaxy formation that now encompasses a broad range of phenomena. Hierarchical clustering (White & Rees 1978) leads to galaxy mergers that scramble disks and make ellipticals (Toomre 1977; Schweizer 1990). Merger progenitors usually contain gas; gravitational torques drive it to the center (Barnes & Hernquist 1991, 1996) and feed starbursts (Mihos & Hernquist 1994, 1996). ULIRGs are local examples of dissipative mergers. With intermediate masses, their descendants correspond to the extra light–disky part of the E–E dichotomy. Observations (reviewed in Section 12.3.2) and theoretical models (Kauffmann & Haehnelt 2000; Hopkins et al. 2005a, 2005b, 2006a, 2006b) imply that ULIRGs are related to quasars. The consequences for galaxy evolution are not clear. AGNs are seen to be more important in more luminous ULIRGs (Lutz et al. 1998; Genzel et al. 2000; Tran et al. 2001; Farrah et al. 2002; Veilleux et al. 2006; Schweitzer et al. 2006; Netzer et al. 2007). But most ULIRGs are energetically dominated by starbursts. It is clear that merger-induced starbursts like those discussed in this paper as the origin of "extra light" in coreless ellipticals have not been prevented by AGN feedback; nor do the papers reviewed in the previous section find any correlation of AGN importance with the dynamical stage (early or late) of the host merger. Altogether, it appears likely that quasar energy feedback has a major effect on the formation of bright ellipticals (Silk & Rees 1998; Ciotti & Ostriker 2001; Ostriker & Ciotti 2005) but not faint ellipticals (this paper). This helps to explain why supermassive BHs correlate with bulges (Kormendy & Richstone 1995; Ferrarese & Merritt 2000; Gebhardt et al. 2000; Tremaine et al. 2002) but not disks (Kormendy & Gebhardt 2001)—bulges and ellipticals are made in mergers, but disks are not. So, while many details remain to be worked out, our picture of the formation of extra light-disky ellipticals is becoming well articulated. Now our understanding of core-boxy ellipticals is catching up. Critically important is the observation that essentially all of their star formation happened quickly and long ago (Bower et al. 1992; Bender 1996, 1997; Thomas et al. 1999, 2005; Bernardi et al. 2003; Renzini 2006). We know little about their merger progenitors. Nevertheless, parallel investigations of the theory of gas accretion during hierarchically clustering (Birnboim & Dekel 2003; Dekel & Birnboim 2006, 2008), simulations of the accretion (Kereš et al. 2005), semi-analytic models of galaxy formation including energy feedback (Cattaneo et al. 2006, 2008), observations of galaxy evolution with redshift (Faber 2005; Faber et al. 2007), and archaeology of galaxy structure (this paper) have converged on an "$M_{\rm crit}$ quenching picture" in which total mass M is the main parameter that controls galaxy evolution. Only at $M > M_{\rm crit}$ can galaxies create, continually reheat, and hold onto hot gas halos at X-ray temperatures; they keep them hot via a combination of AGN feedback and cosmological infall, and they use them to quench star formation and make subsequent mergers dry. We show that this picture accounts naturally for the observed dichotomy of elliptical galaxies into dry-merger remnants that contain cores and wet-merger remnants that contain extra central components that are the signatures of merger starbursts. Merger simulations that are motivated by these results and that incorporate the above physics do remarkably well in reproducing the different properties of core and extra light ellipticals (Hopkins et al. 2008a, 2008b, 2009a, 2009b, 2009c).

13. THE E–SPH DICHOTOMY

Fundamental to the above discussion is the conclusion that elliptical and spheroidal galaxies are physically different. This result, presciently guessed by Wirth & Gallagher (1984), demonstrated by Kormendy (1985b, 1987b), and confirmed by Binggeli & Cameron (1991) and Bender et al. (1992), has been much criticized in recent years. With high-dynamic-range brightness profiles, we show in Figures 34–38 that the E–Sph dichotomy is real. In correlations such as effective brightness versus effective radius and effective brightness versus absolute magnitude, ellipticals and spheroidals form almost perpendicular sequences. These sequences approach each other at $M_{VT} \simeq -18$, near the maximum of the luminosity function for ellipticals but at a luminosity where spheroidals are rare. The dichotomy is not a result of a biased sample; in fact, our sample is biased in favor of finding the spheroidals that are most like ellipticals.

This result is critically important to our understanding of galaxy formation. Consider the contrary: if spheroidal galaxies and all ellipticals except those with cores formed a continuous Sph–E sequence in parameter space, then that sequence would be completely different from the fundamental plane discovered by Djorgovski & Davis (1987) and Faber et al. (1987) and studied by many others (e.g., Bender et al. 1992, 1993). That Sph–E sequence would be almost perpendicular to our fundamental plane, $r_e \propto \sigma^{1.4\pm0.15} I_e^{-0.9\pm0.1}$. Its interpretation that structure is controlled by the Virial theorem, $r_e \propto \sigma^2 I_e^{-1}$, modified by small nonhomologies would be wrong. A Sph–E sequence would be inconsistent with the well established result that the scatter in the E–E fundamental plane is small (Saglia et al. 1993; Jørgensen et al. 1996). Merger simulations (Boylan-Kolchin et al. 2006; Robertson et al. 2006; Hopkins et al. 2008a, 2009a) reproduce the E–E fundamental plane, not a set of Sph–E correlations. Equating spheroidals with low-luminosity ellipticals would imply that they formed similarly, but we are confident that ellipticals formed by mergers, and we believe that dwarf spheroidals cannot have formed by mergers (Tremaine 1981). Continuous Sph–E correlations are inconsistent with almost everything that we know about galaxy formation.

However, our results confirm that elliptical galaxies of both types together define the classical fundamental plane in which lower-luminosity galaxies have smaller r_e and brighter I_e (Kormendy 1977) all the way from giants like M 87 to dwarfs like M 32. Spheroidals overlap this sequence in luminosity, but much below the brightness of M 32 ($M_{VT} = -16.7$), where we find no ellipticals, their luminosity functions rise steeply all the way to the faintest galaxies known ($M_{VT} > -9$). Along this sequence, visible matter densities decrease rapidly with decreasing galaxy mass, consistent with the progressive loss of more and more baryons as gravitational potential wells get shallower and as supernovae get more effective in ejecting gas (e.g., Dekel & Silk 1986; Dekel & Woo 2003). For our overall understanding of galaxy formation, confirmation of the E–Sph dichotomy is the most important result of this paper.

This paper has dominated J.K.'s and D.B.F.'s research for more than three years, and it has been a recurring theme for J.K. and R.B. for periods as long as 25 years. During this long gestation, many people have helped us and deserve our sincere thanks. Most importantly, we thank the anonymous referee for an extraordinarily helpful report. This report, our own in-

clinations, and input from several readers (notably Karl Gebhardt and Tod Lauer) motivated the addition of Appendix A on Sérsic function fitting machinery, as well as numerous other improvements. We are grateful to Sandra Faber, Luis Ho, Tod Lauer, Joe Silk, and Scott Tremaine for helpful comments on the MS. Incisive questions by Sandy Faber particularly helped us to refine the conclusions of Section 12. J.K. thanks Josh Barnes, Philip Best, Andi Burkert, Michele Cappellari, Andrea Cattaneo, Avishai Dekel, Bill Forman, Karl Gebhardt, Lars Hernquist, Philip Hopkins, Miloš Milosavljević, Richard Mushotzky, Jerry Ostriker, and Remco van den Bosch for helpful conversations. D.B.F. thanks Roberto Saglia for his detailed introduction to the Bender/Saglia surface photometry code as implemented in MIDAS. Finally, it is appropriate here to thank George Djorgovski, whose emphasis on thoroughness on many occasions (e.g., Djorgovski & King 1986) reinforced our own and had a significant effect on this paper.

The CFH12K observations of the Virgo cluster were made in collaboration with Richard Wainscoat; we are grateful to him for agreeing to let us use the images here. We thank Ying Liu for sending the *R*-band, major-axis profile of M 87 as derived from his multiband photometry. This work makes extensive use of the data products from the *HST* image archive and from the Two Micron All Sky Survey (2MASS). 2MASS is a joint project of the University of Massachusetts and the Infrared Processing and Analysis Center/California Institute of Technology, funded by NASA and the NSF. We also made extensive use of the digital image database of the Sloan Digital Sky Survey. Funding for the SDSS and SDSS-II has been provided by the Alfred P. Sloan Foundation, the Participating Institutions, the National Science Foundation, the U.S. Department of Energy, the National Aeronautics and Space Administration, the Japanese Monbukagakusho, the Max Planck Society, and the Higher Education Funding Council for England. The SDSS is managed by the Astrophysical Research Consortium for the Participating Institutions. The Participating Institutions are the American Museum of Natural History, Astrophysical Institute Potsdam, University of Basel, University of Cambridge, Case Western Reserve University, University of Chicago, Drexel University, Fermilab, the Institute for Advanced Study, the Japan Participation Group, Johns Hopkins University, the Joint Institute for Nuclear Astrophysics, the Kavli Institute for Particle Astrophysics and Cosmology, the Korean Scientist Group, the Chinese Academy of Sciences (LAMOST), Los Alamos National Laboratory, the Max-Planck-Institute for Astronomy (MPIA), the Max-Planck-Institute for Astrophysics (MPA), New Mexico State University, Ohio State University, University of Pittsburgh, University of Portsmouth, Princeton University, the United States Naval Observatory, and the University of Washington.

The NGC 4318 spectrum was obtained with the Marcario LRS and the Hobby–Eberly Telescope (HET). LRS is named for Mike Marcario of High Lonesome Optics; he made optics for the instrument but died before its completion. LRS is a project of the HET partnership and the Instituto de Astronomía de la Universidad Nacional Autónoma de México. The HET is a project of the University of Texas at Austin, Pennsylvania State University, Stanford University, Ludwig-Maximilians-Universität München, and Georg-August-Universität Göttingen. The HET is named in honor of its principal benefactors, William P. Hobby and Robert E. Eberly.

This work would not have been practical without extensive use of the NASA/IPAC Extragalactic Database (NED), which is operated by the Jet Propulsion Laboratory and the California Institute of Technology under contract with NASA. We also used the HyperLeda electronic database (Paturel et al. 2003) at http://leda.univ-lyon1.fr and the image display tool SAOImage DS9 developed by Smithsonian Astrophysical Observatory. Figure 9 was adapted from the WIKISKY image database (www.wikisky.org). Finally, we made extensive use of NASA's Astrophysics Data System bibliographic services.

J.K.'s ground-based CFHT photometry was supported by NSF grant AST-9219221. Also, NSF support under grant AST-0607490 during the late stages of this work is gratefully acknowledged. J.K.'s *HST* photometry work as a member of Nuker team GO programs 2600, 3912, 5512, and 6099 was supported by NASA through grants from the Space Telescope Science Institute (STScI). STScI is operated by AURA under NASA contract NAS5-26555. M.E.C. was supported in part by a generous and much appreciated donation to McDonald Observatory by Mr. Willis A. Adcock. Finally, we acknowledge that this multi-year research program would not have been possible without the long-term support provided to J.K. by the Curtis T. Vaughan, Jr. Centennial Chair in Astronomy. We are most sincerely grateful to Mr. and Mrs. Curtis T. Vaughan, Jr. for their continuing support of Texas astronomy. It is a pleasure to dedicate this paper to them.

Facilities: HST: WFPC1; *HST*: WFPC2; *HST*: ACS; *HST*: NICMOS; CFHT: Cassegrain camera; CFHT: HRCam; CFHT: 12K camera; SDSS: digital image archive; McDonald Observatory: 0.8 m telescope; HET: LRS

APPENDIX A

SÉRSIC FUNCTION FITS TO THE ELLIPTICAL AND SPHEROIDAL GALAXIES

Appendix A documents our Sérsic (1968) function fits to the major-axis brightness profiles $I(r)$ of elliptical and spheroidal galaxies (Figures 49–72). We test the robustness of our fits to changes in the adopted fit range. We provide a summary (Figures 73) with which users of Sérsic functions can judge whether or not the dynamic range of their profile data are adequate for reliable fits.

The Sérsic function is

$$I(r) = I_e \mathrm{dex}\left\{-b_n\left[\left(\frac{r}{r_e}\right)^{1/n} - 1\right]\right\}, \qquad \text{(A1)}$$

where b_n is chosen so that $r_e \equiv$ "effective radius" contains half of the total light of the model profile and $I_e \equiv$ "effective brightness" is the surface brightness at r_e. Over the range of Sérsic indices $0.5 \leqslant n \leqslant 16.5$, numerical integration gives the approximation formula, $b_n \simeq 0.868n - 0.142$ (Caon et al. 1993). That paper, Ciotti (1991), Graham et al. (1996), Ciotti & Bertin (1999), Trujillo et al. (2001), and Graham & Driver (2005) discuss Sérsic functions in detail. They have become popular machinery to describe the profiles of E and Sph galaxies and to derive parameters n, r_e, and $\mu_e \equiv -2.5 \log I_e$ for structural analyses such as fundamental plane studies (see Section 3 for a review).

This appendix concentrates on two aims that are not discussed in previous literature. We illustrate each fit, including χ^2 ellipses in the fit parameters. These provide realistic error estimates (Appendix A.1) that take the (often very strong) parameter coupling into account. Second (Appendix A.2), we explore the

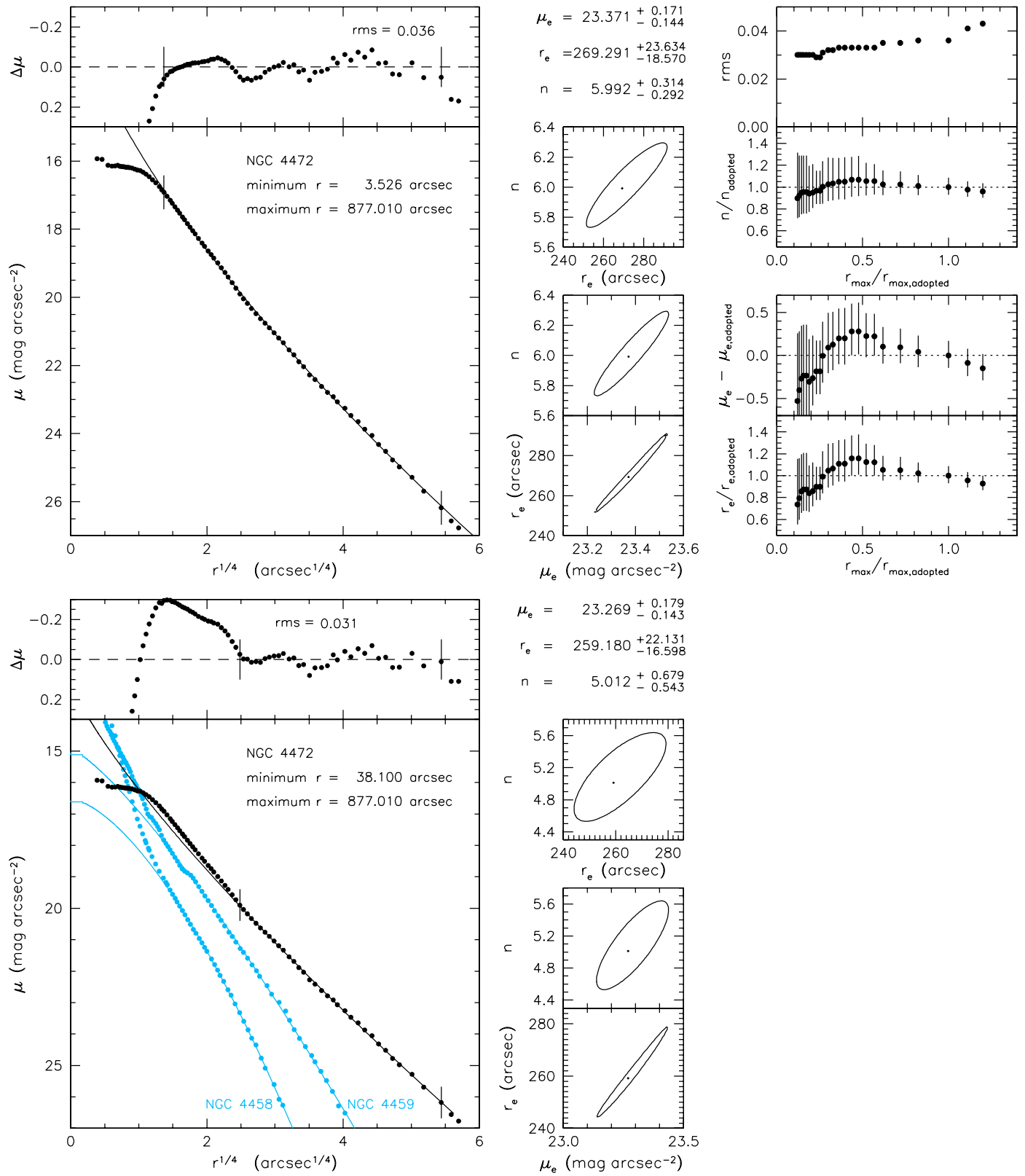

Figure 49. Sérsic (1968) function fits to the major-axis profile of NGC 4472 (also fits to NGC 4458 and NGC 4459, for comparison, at the bottom). This figure and the ones that follow show all known elliptical-galaxy members of the Virgo cluster in order of decreasing luminosity, followed by our spheroidal galaxies also in order of decreasing luminosity. In this and the following figures, the large panel shows the fit (solid curve) to the profile used in all calculations; it is the average of the individual profiles illustrated in Figures 11–29, as discussed in the text. The top-left panel shows the deviations of the profile from the fit and lists the rms deviation in mag arcsec^{-2}. In both panels, the fit range is shown by vertical dashes. The fit parameters are listed in the middle at the top. The small panels in the middle show the three-dimensional, 1σ χ^2 contours projected into two dimensions. They illustrate the parameter coupling. Appendix A shows two kinds of fits, the adopted fits for all galaxies (e.g., at top) and, for some galaxies, one or more additional fits that are designed to illustrate specific astrophysical issues discussed in the text (e.g., bottom fit here). For the final fits but not for the illustrative fits, the right-hand panels test the effect of changing the outer radius r_{max} of the fit range from the adopted value $r_{max,adopted}$ listed in the key of the large panel. As a function of $r_{max}/r_{max,adopted}$, they show how the fit rms and the fit parameters (e.g., r_e) change from the adopted value (e.g., $r_{e,adopted}$) listed above the middle panels. The NGC 4458 and 4459 profiles are discussed in Section 10.3, Footnote 9.

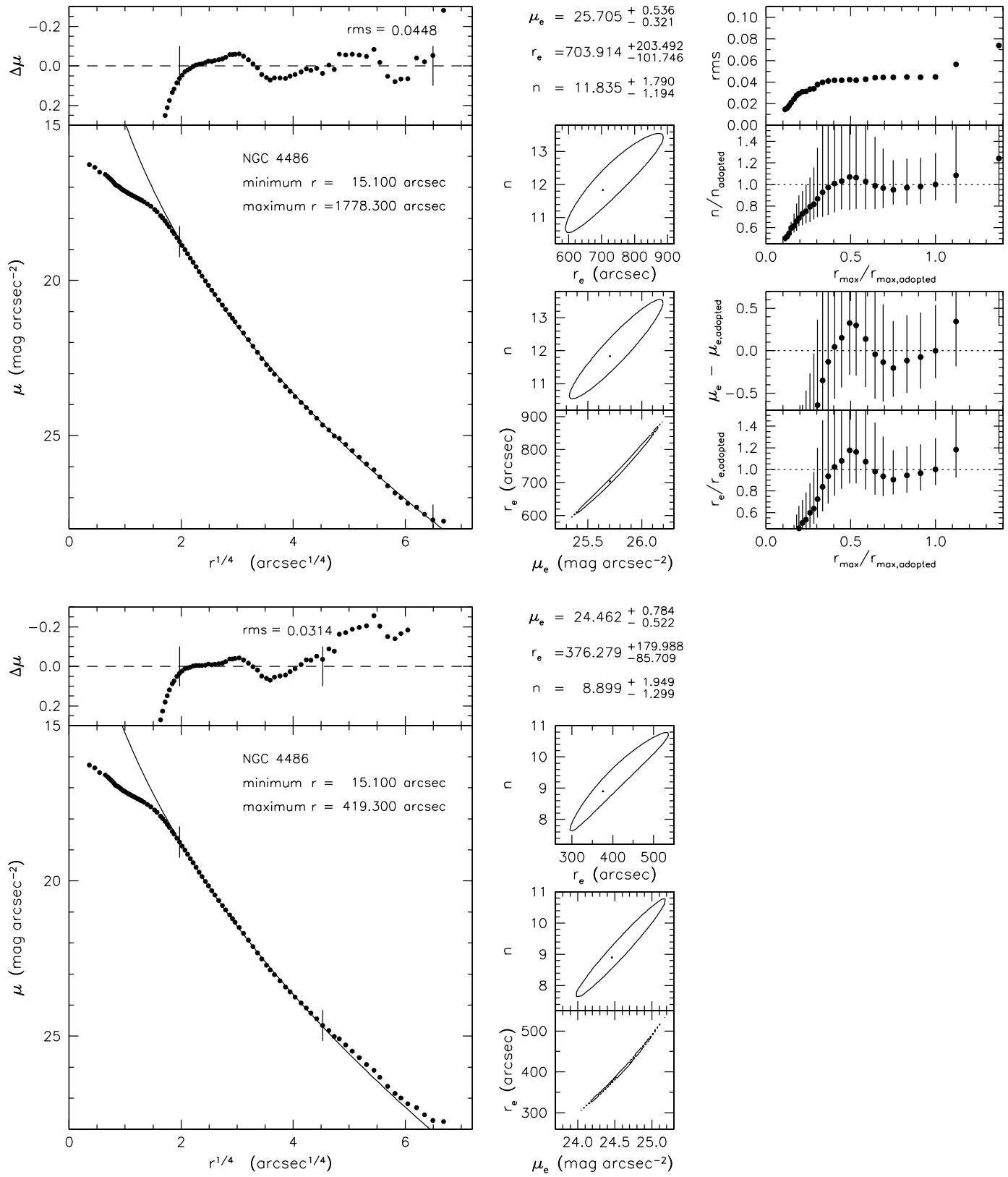

Figure 50. Sérsic function fits to the major-axis profile of NGC 4486 (M 87). The layout is as in Figure 49. In some χ^2-contour figures here and on the following pages, the `sm` contouring routine has difficulty with the thinnest χ^2 contours. They are plotted as distinct "pearls" but of course are continuous. The contours also are approximate when they have sharp, pointed ends. The extraordinarily large n value in the upper fit may be due to the inclusion of a low-surface-brightness cD halo. At the bottom, we illustrate a plausible fit over a smaller radius range that excludes such a halo.

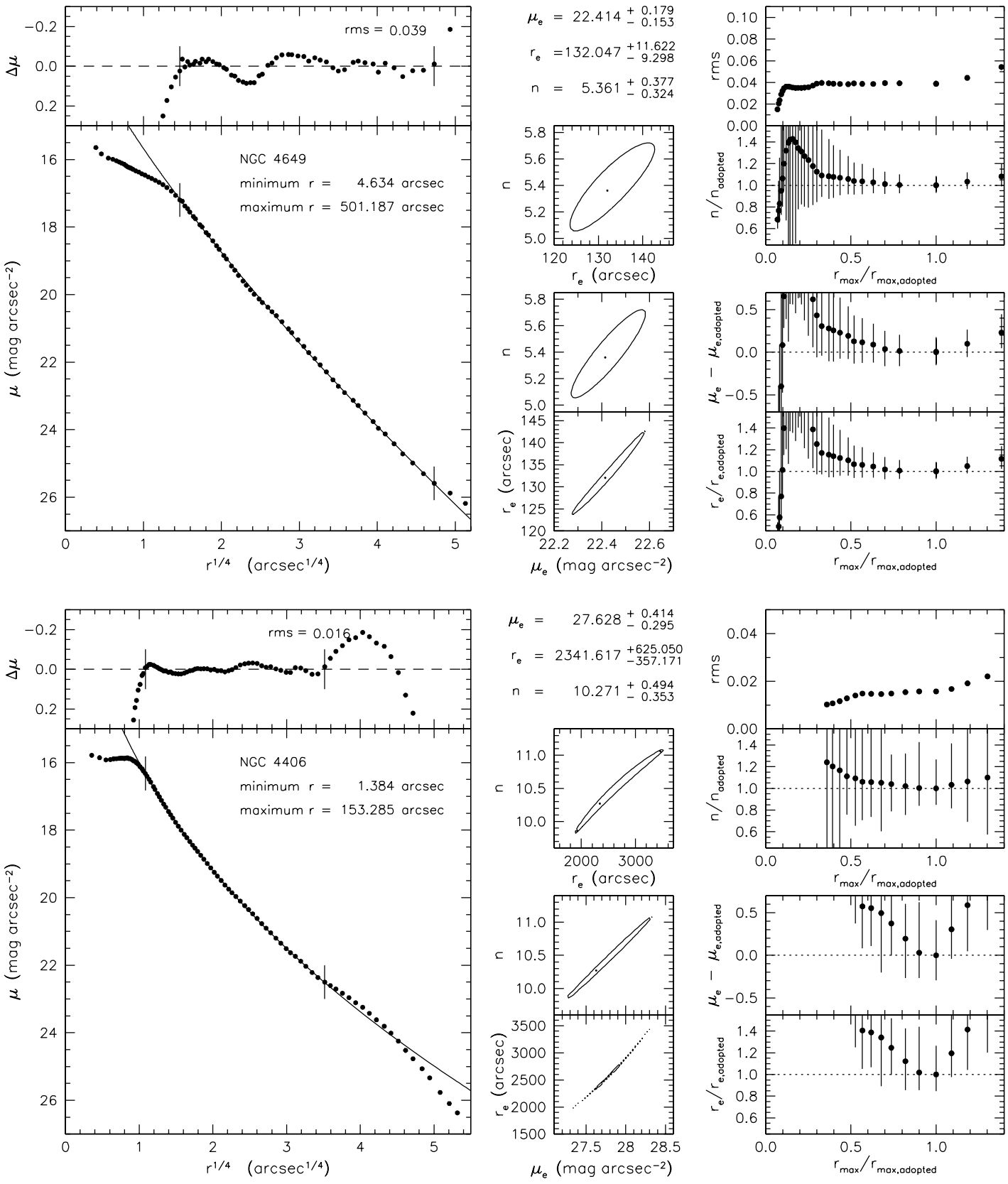

Figure 51. Sérsic function fits to the major-axis profiles of NGC 4649 and NGC 4406. The layout is the same as in Figure 49. Note the extraordinarily strong parameter coupling in the NGC 4406 fit. This is characteristic of fits with large Sérsic indices.

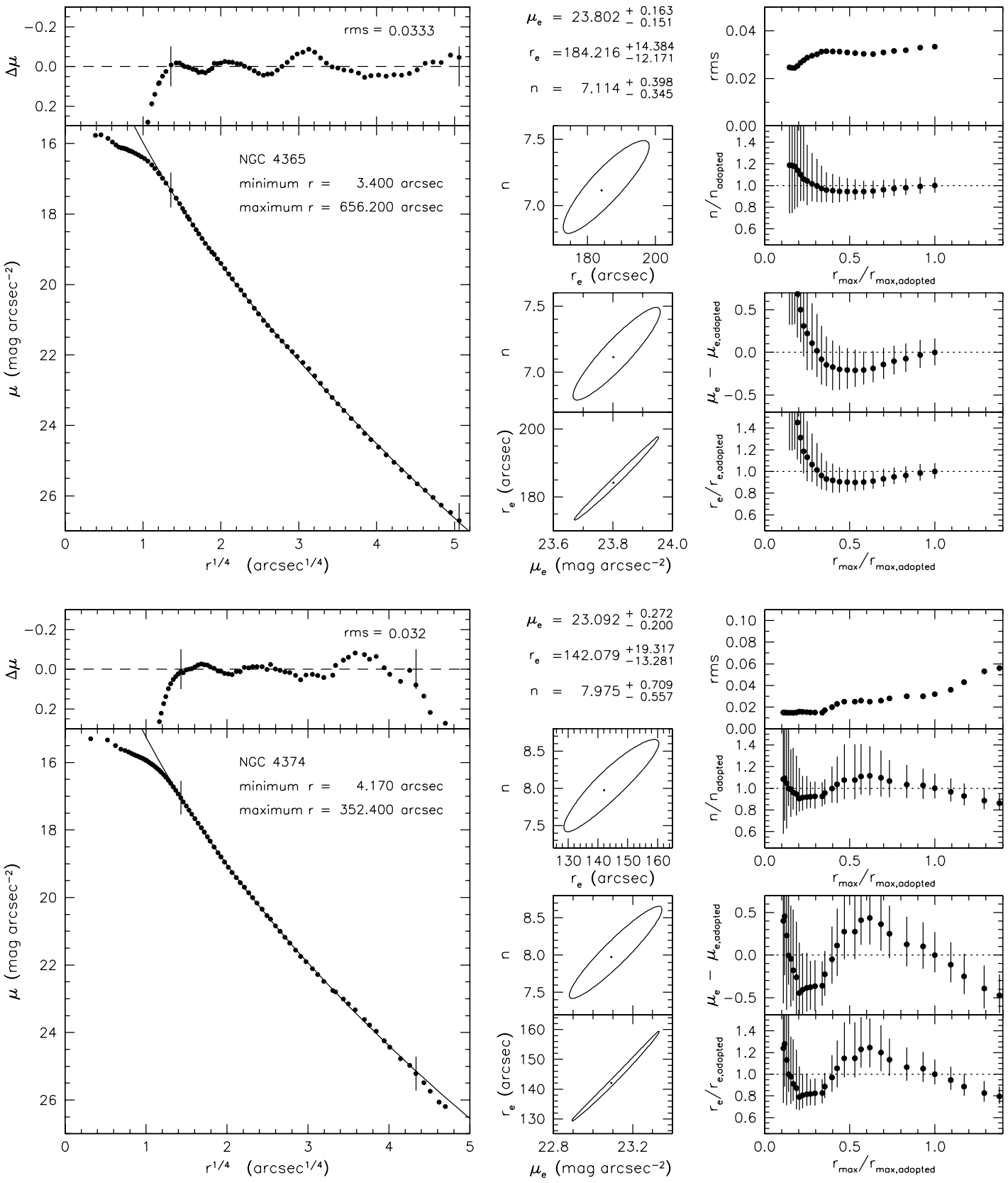

Figure 52. Sérsic function fits to the major-axis profiles of NGC 4365 and NGC 4374. The figure layout is the same as in Figure 49.

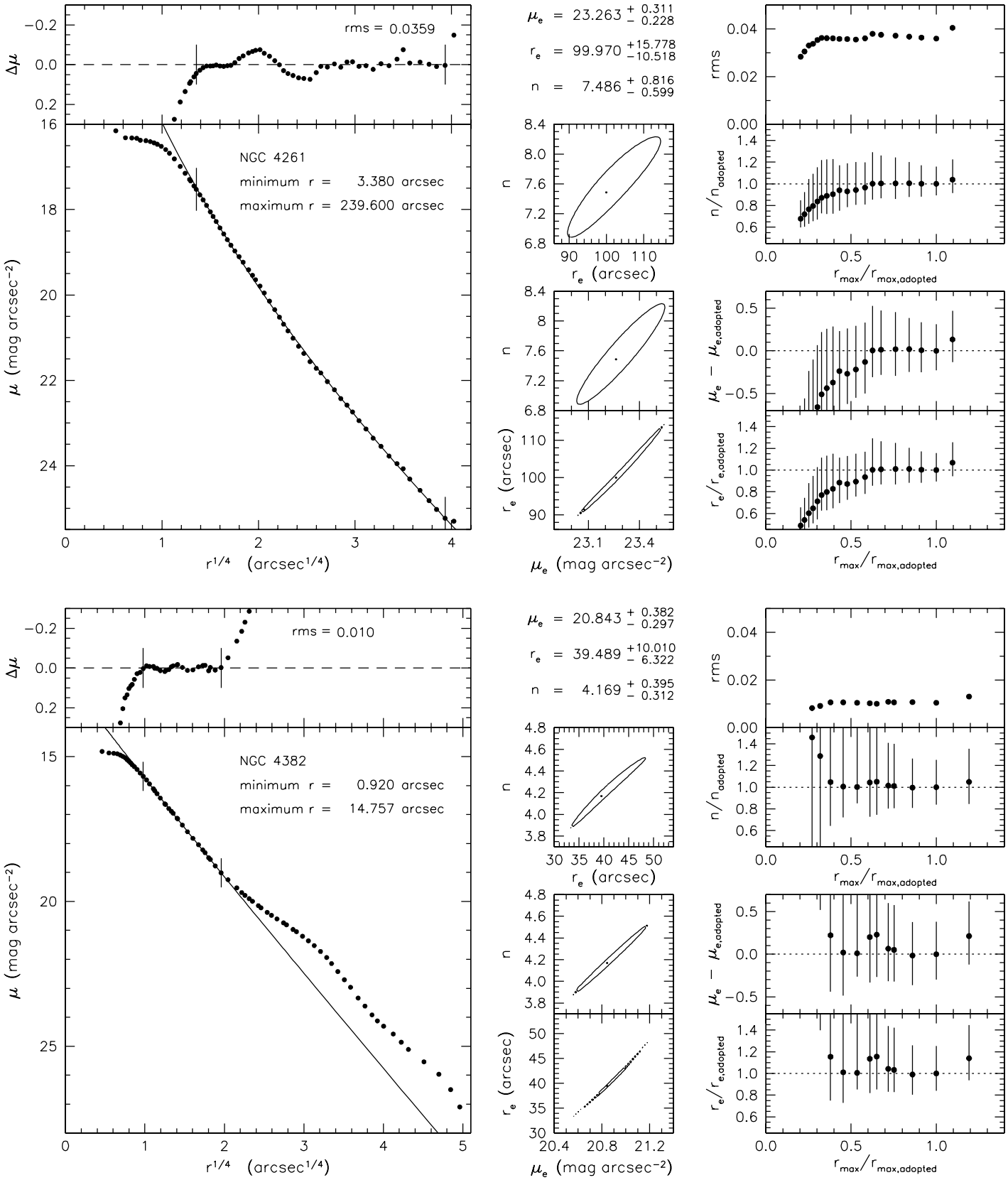

Figure 53. Sérsic function fits to the major-axis profile of NGC 4261 (top) and an illustrative fit to the inner part of the profile of NGC 4382 (bottom). The adopted fit to the profile of NGC 4382 is shown on the next page. The layout is as in Figure 49. Note that NGC 4261 is in the background of the Virgo Cluster (see distances in Table 1).

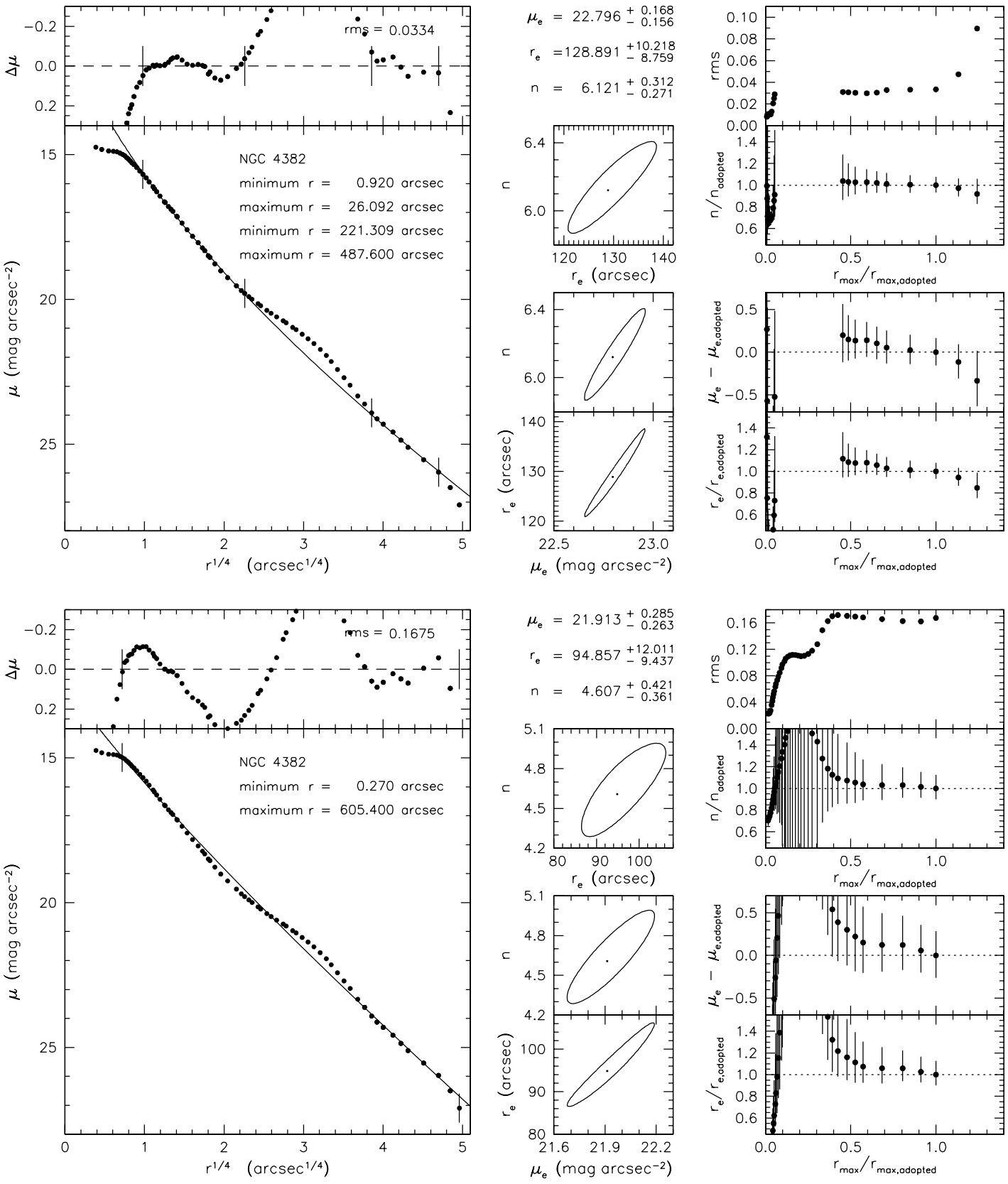

Figure 54. Alternative Sérsic function fits to the major-axis profile of NGC 4382. The layout is as in Figure 49. The top panels show a fit to the inner and outer profile omitting intermediate points between 28″ and 202″ inclusive. This is the adopted fit whose parameters are listed in Table 1. The bottom panels show an overall fit, giving triple weight to the points at $202'' \leqslant r \leqslant 552''$ to ensure a good fit at large radii.

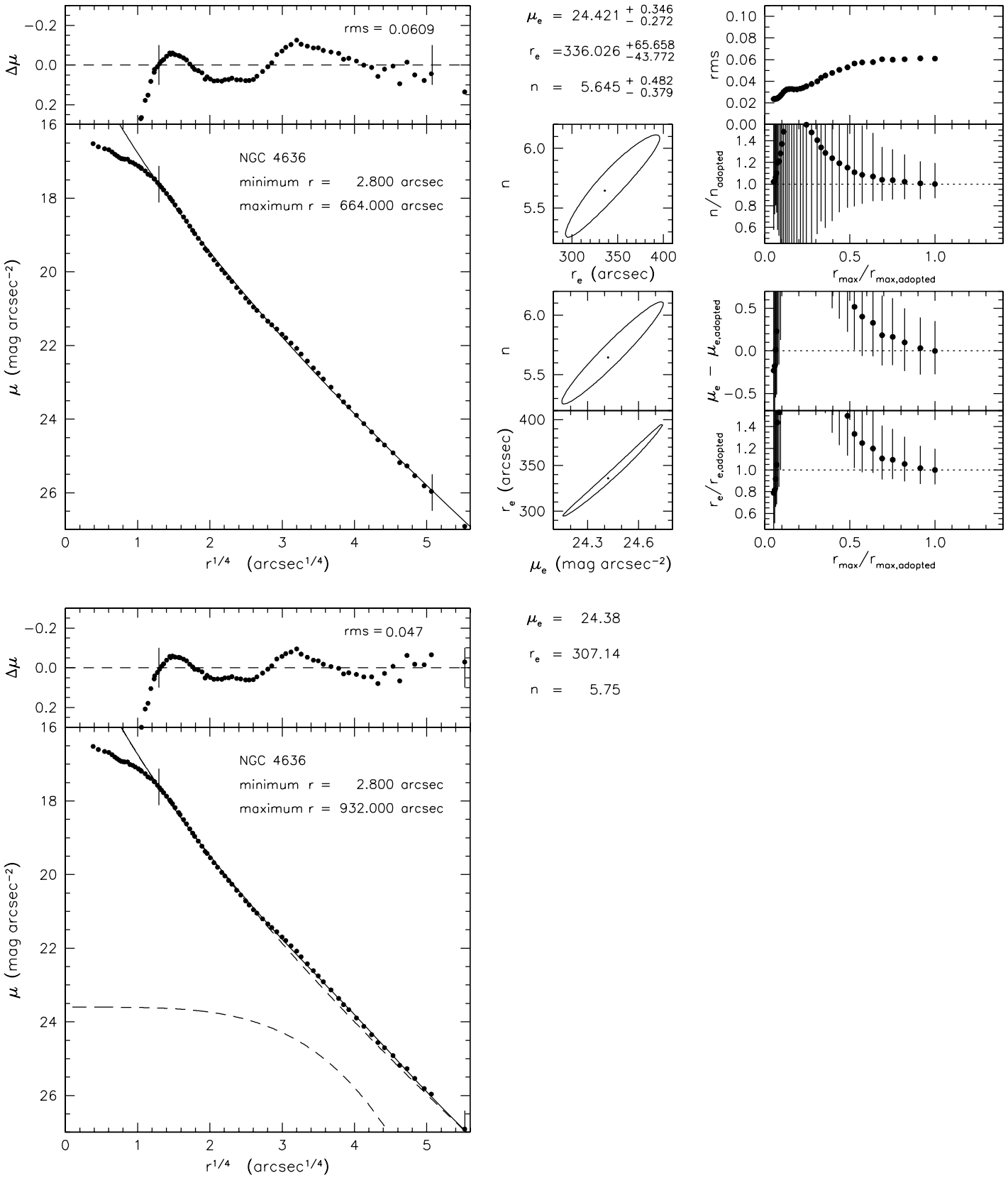

Figure 55. Sérsic function fits to the major-axis profile of NGC 4636. The layout is as in Figure 49. The adopted fit is at the top. The rms residual is slightly larger than normal, mostly because of a profile wiggle that is centered at $r^{1/4} \simeq 2.8$. The form of the wiggle (the model is too bright just inside the above radius and too faint just outside this radius) suggests the possibility that NGC 4636 may be a bulge-dominated S0, i.e., a face-on version of NGC 3115 (Hamabe 1982, Figure 5a). Therefore, the bottom panels show a decomposition into a Sérsic function bulge plus an exponential "disk" represented by the upper and lower dashed curves, respectively. Their sum is the solid curve. It fits the observed profile marginally better than does the adopted pure Sérsic fit, but the difference is not significant. In particular, the wiggle in the residual profile is not much reduced by the decomposition, because it happens over a smaller radius range than the exponential can accommodate. Thus there is no compelling evidence that NGC 4636 is an S0. In any case, the "disk" in the lower fit contributes only 8% of the total light, so the bulge parameters given by the decomposition are almost the same as those given by the adopted fit (see the keys).

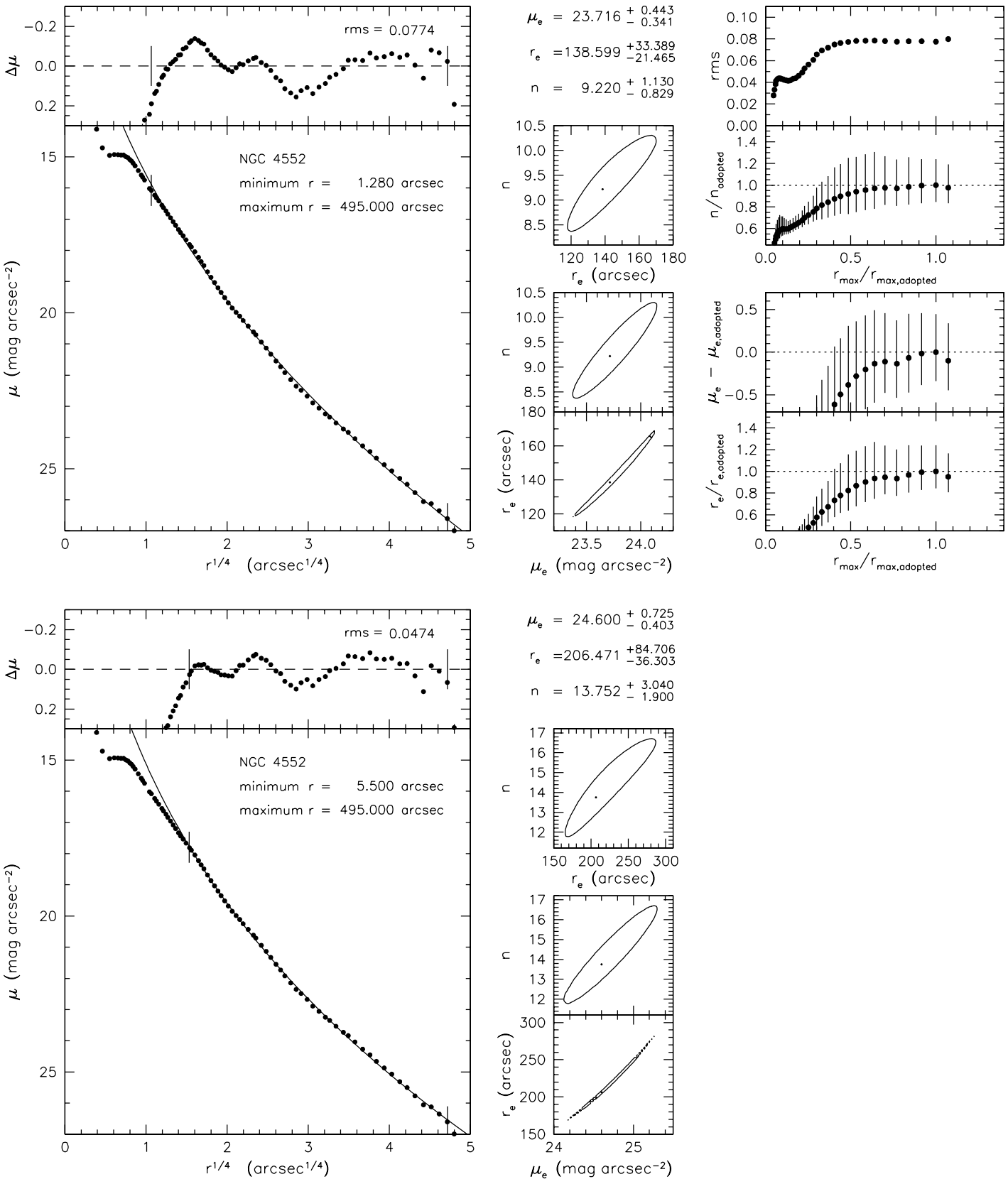

Figure 56. Sérsic function fits to the major-axis profile of NGC 4552. The layout is as in Figure 49. The adopted fit (top) has a higher-than-normal rms residual and a slightly concave-upward residual profile. It is possible that too much of the core region was included in the fit. Therefore, the bottom fit uses a restricted radius range; it results in smaller and nonsystematic residuals. The resulting core-within-a-core structure is intriguing but highly unusual. This fit may be an overinterpretation of the profile wiggles. We therefore adopt the top fit. The bottom fit is discussed in Appendix A.3 and used in Figure 74. Note that, at absolute magnitude $M_{VT} = -21.66$, NGC 4552 is the lowest-luminosity core elliptical in Virgo.

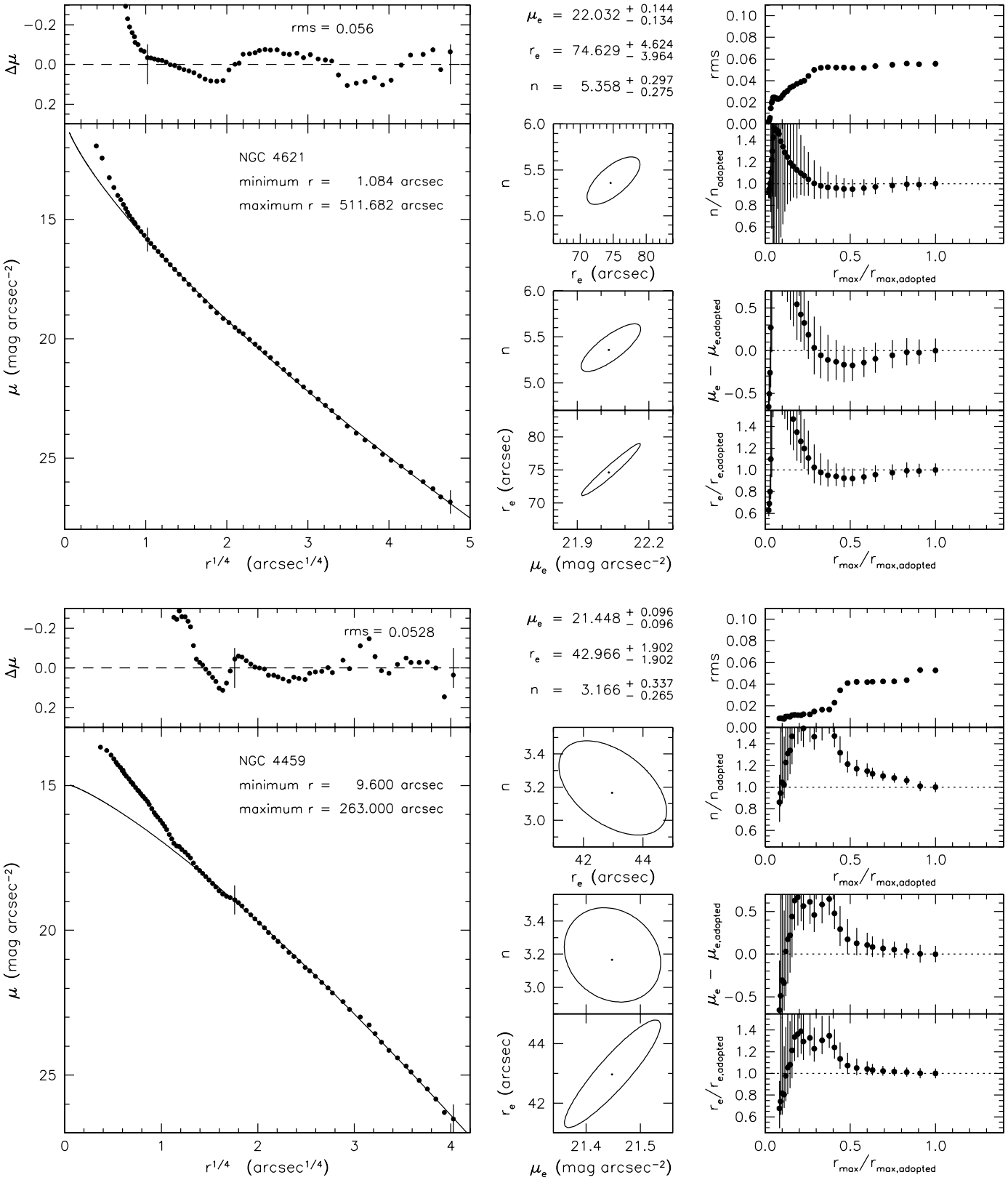

Figure 57. Sérsic function fits to the major-axis profiles of NGC 4621 and NGC 4459. The layout is as in Figure 49. In larger samples, core and power-law galaxies overlap in luminosity and NGC 4621 is in the overlap region (Faber et al. 1997). More accurate individual distances based on surface brightness fluctuations imply a luminosity such that *in the Virgo cluster* the separation between core and extra light ellipticals is fortuitously clean. At $M_{VT} = -21.54$, NGC 4621 is the brightest extra light elliptical in the cluster. NGC 4459 has a prominent dust disk between $r \sim 1''$ and $9''.6$ (e.g., Sandage 1961; Sandage & Bedke 1994; Ferrarese et al. 2006a); it is easily identified in the profile and has been omitted from the fit. The outer part of the galaxy is a very clean Sérsic function with $n < 4$ and no sign of an S0 disk. With respect to this fit—and in spite of any dust absorption—NGC 4459 clearly has extra light near the center.

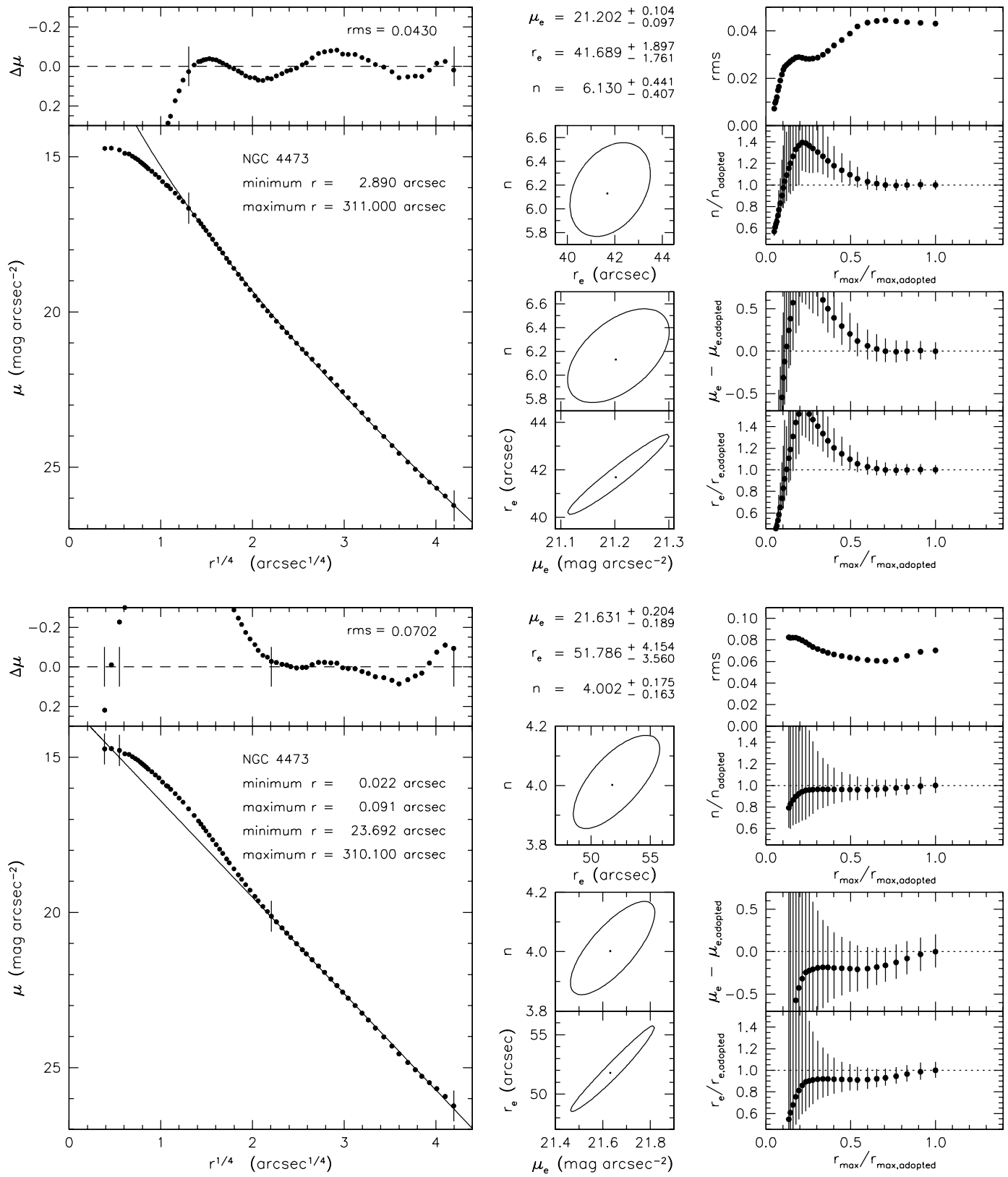

Figure 58. Sérsic function fits to the major-axis profile of NGC 4473. The layout is as in Figure 49. NGC 4473 is a tricky case. It dramatically illustrates the danger of purely "operational" analysis—in this case, least-squares fit of a Sérsic function that minimizes profile residuals—without taking other observations and their physical implications into account. The top fit looks beguilingly good, better than the bottom fit. If it were adopted, we would conclude that the galaxy has a core and a Sérsic index $n > 4$. However, we adopt the bottom fit. The reason is that SAURON observations show that the galaxy has a counter-rotating embedded disk (Cappellari & McDermid 2005; Cappellari et al. 2004, 2007, see Section 9.5). Figure 5 in Cappellari et al. (2007) shows that the counter-rotating disk is important from small radii out to $r \simeq 19''$ (that is, to $r^{1/4} \simeq 2.1$) but not at larger radii. We therefore fit the profile from $r \simeq 23''.7$ outward, excluding the counter-rotating disk. The inner edge of the fit range is determined by where the residuals from the outer Sérsic fit start to grow large, but they are consistent with the Cappellari results. We also include three points near the center to provide stability to the fit. Since stars in the embedded disk pass in front of the center, the surface brightness there is higher than that of the main body of the galaxy. Therefore the true Sérsic index is smaller than the value, $n \simeq 4.0 \pm 0.17$, that we derive. To illustrate this, we show in Figure 59 a decomposition of the profile into a Sérsic function main body and an exponential fit to the extra light.

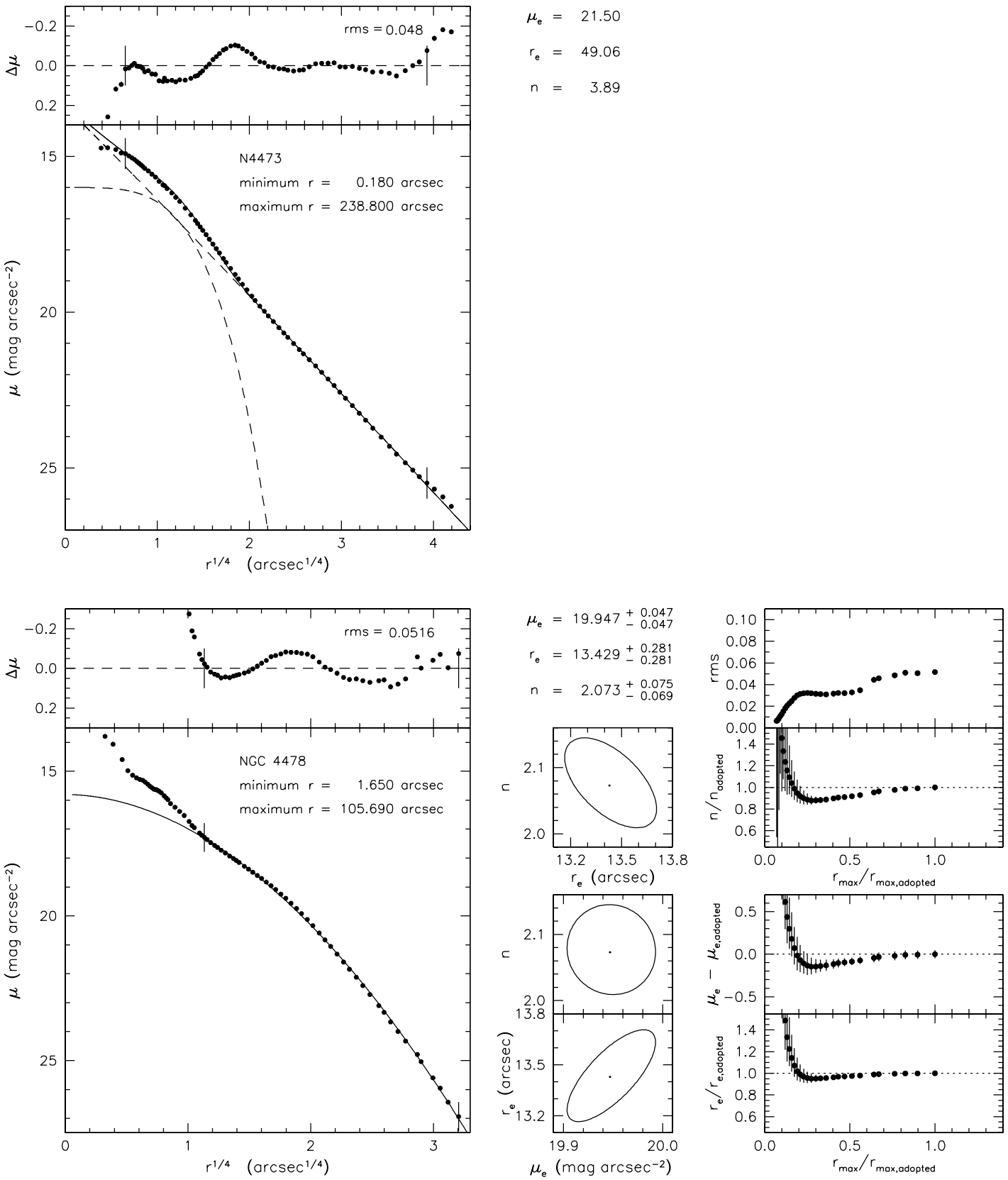

Figure 59. The top panels show a decomposition of the major-axis profile of NGC 4473 into an inner exponential fitted to the extra light (in essence, the counter-rotating disk) and an outer Sérsic function. The parameters of the main body of the galaxy are almost unchanged from the fit in Figure 58, but n drops slightly below 4, as expected. This decomposition is directly comparable to the Hopkins et al. (2009a) decomposition reproduced here in Figure 44. It gives a fractional contribution of the extra light of 9.1%, compared with 15% for the brighter and shallower disk fit by Hopkins. The bottom panels show our Sérsic function fit to the major-axis profile of NGC 4478. The layout is as in Figure 49.

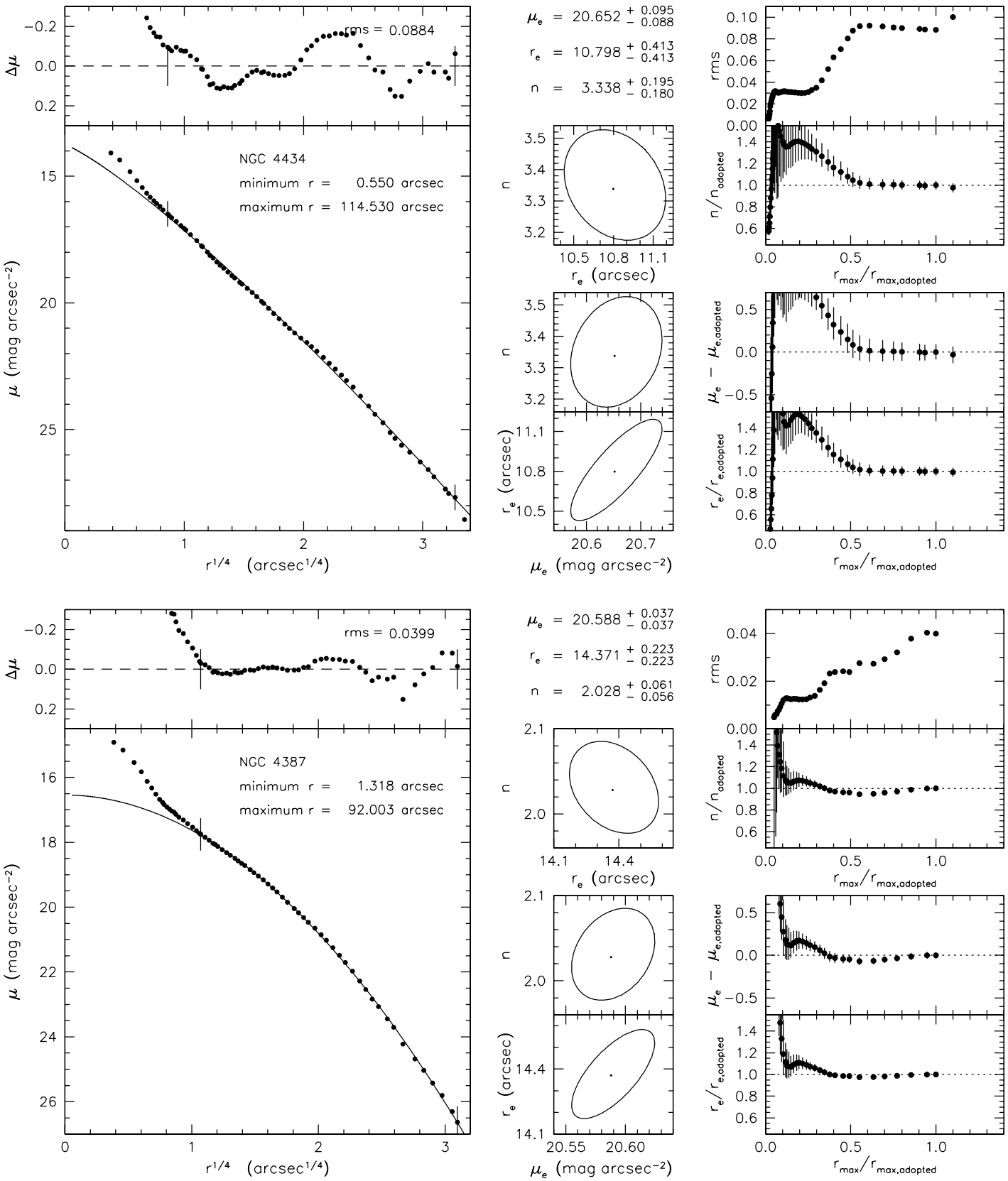

Figure 60. Sérsic function fits to the major-axis profiles of NGC 4434 and NGC 4387. The layout is as in Figure 49.

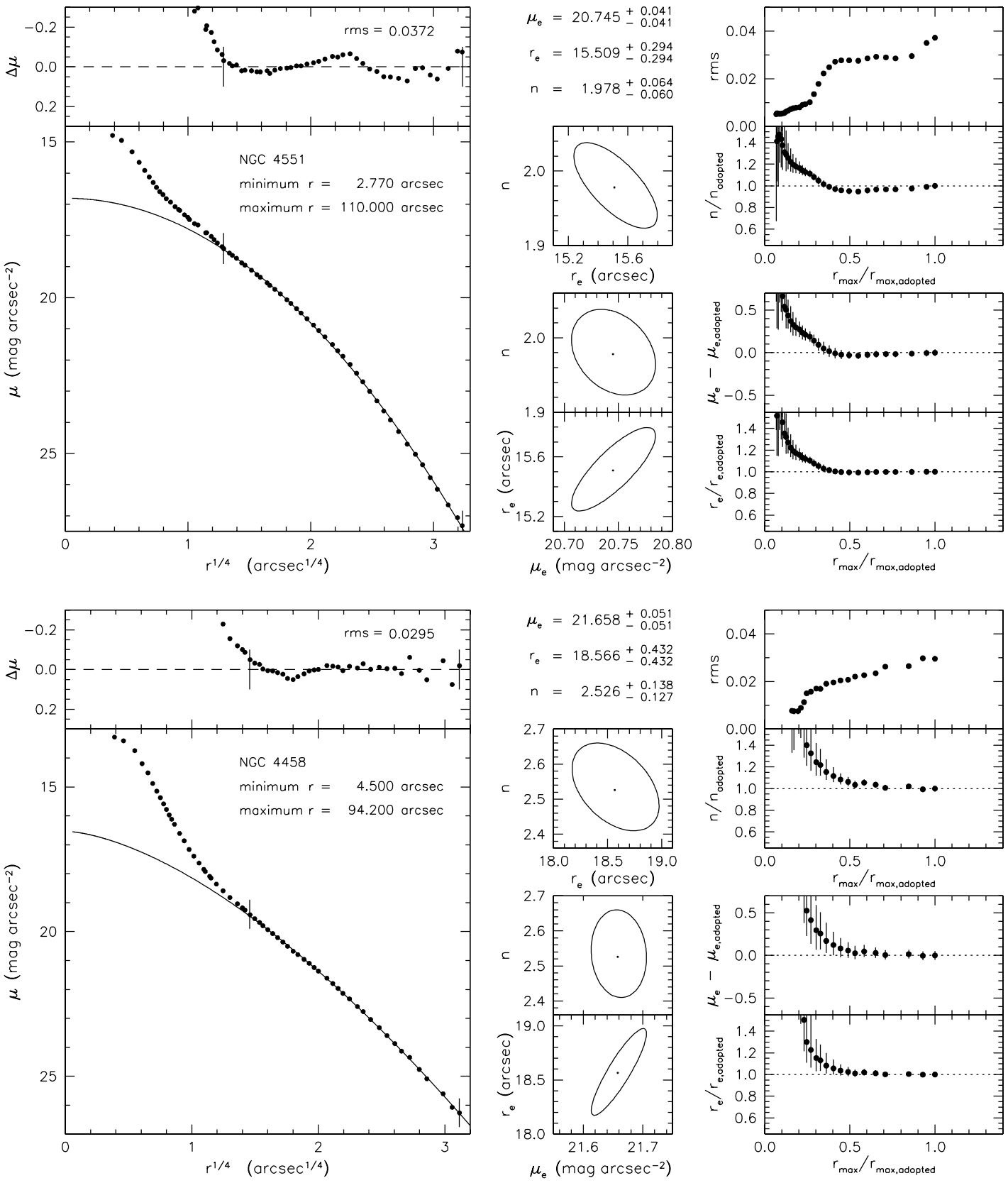

Figure 61. Sérsic function fits to the major-axis profiles of NGC 4551 and NGC 4458. The layout is as in Figure 49.

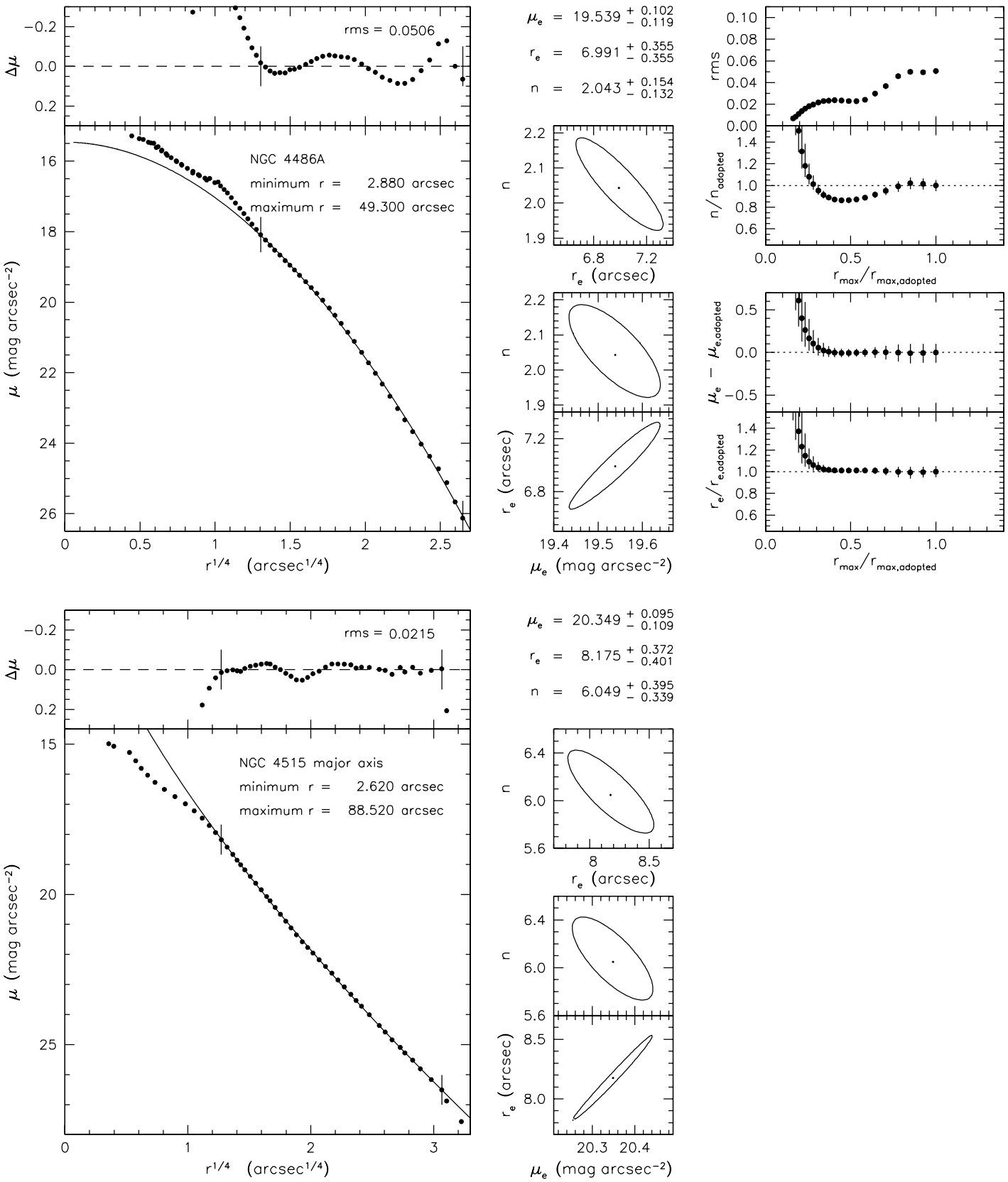

Figure 62. The top panels show our Sérsic function fit to the major-axis profile of NGC 4486A. The extra light is a particularly obvious nuclear disk bisected by a strong dust lane (see Figure 20 here and Kormendy et al. 2005) that produces the kink in the profile at $\sim 1''$. The bottom panels show a Sérsic fit to the major-axis profile of NGC 4515. This is superficially an excellent fit, with small rms deviations over a large radius range and a canonical combination of an apparent core (albeit with an unusually steep profile) and a Sérsic index $n > 4$. However, we do not adopt this fit. The reasons—and our adopted fit—are given in Figure 63.

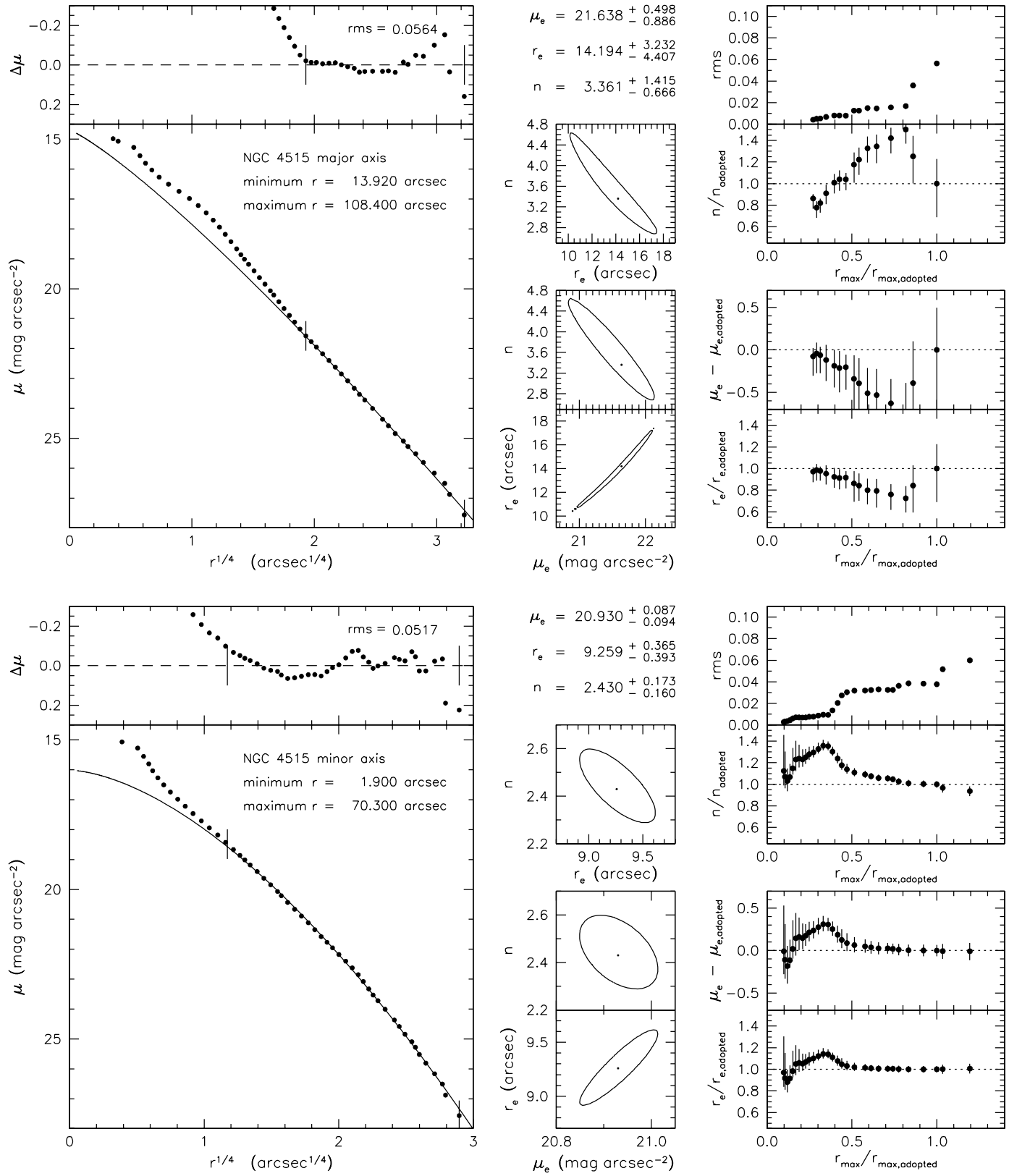

Figure 63. The top panels show our adopted Sérsic fit to the major-axis profile of NGC 4515 In our sample, this galaxy is the trickiest one to interpret. It is similar to NGC 4473. The ellipticity and a_4 profiles show the signature of an extended nuclear disk (Figure 21). But this disky central region shows almost no rotation ($V_{\rm rot} \lesssim 20$ km s^{-1}), a moderately high velocity dispersion ($\sigma \sim 90$ km s^{-1}) and hence an unusually low ratio of $V_{\rm rot}/\sigma$ for a low-luminosity elliptical (Bender & Nieto 1990). It would be interesting to look for counter-rotation. Given this situation, we are not persuaded by the superficially excellent fit in Figure 62. Instead, we adopt the top fit here, which omits the central disky structure. Is this reasonable? For an answer, we resort to the minor-axis profile (bottom panels). In all of our other galaxies, the major- and minor-axis profiles consistently both give $n < 4$ or both give $n > 4$. The minor-axis profile of NGC 4515 confirms that $n < 4$ and that extra light is detected. For this reason, we adopt the interpretation in the upper panels.

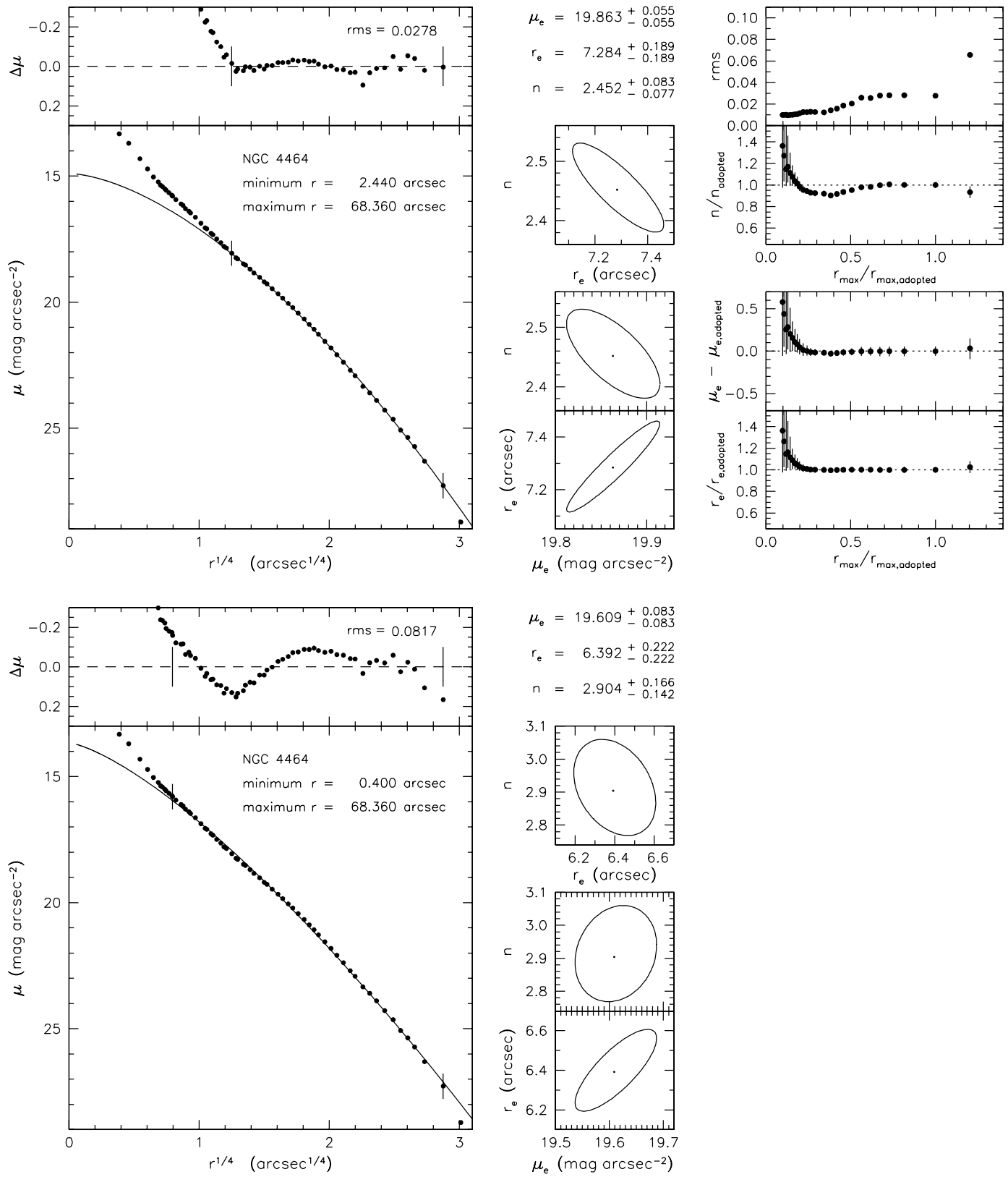

Figure 64. We use NGC 4464 to illustrate the robustness of our choice of the *inner* end of our fit range. That is, we use it as an example of how including extra light in the Sérsic fit produces systematic residuals that are unacceptable. The top panels show our adopted fit. In it, the upward residual produced by the extra light appears to start quite suddenly interior to the minimum radius 2.″44 used in the fit. But the change in curvature of the actual profile is subtle. Could we extend the fit to smaller radii? The bottom panels show that the answer is "no." If we add additional profile points inward to 0.″40, the resulting fit—while not extremely bad—has residuals that are substantially larger than our measurement errors. More tellingly, the residual profile still shows a strong kink at 2.″4, and it is systematically curved in a way that implies that we have included extra light in the fit. Therefore this fit is not acceptable. We emphasize the importance of the high accuracy and dynamic range of our profile data. Without it, we would be much less sure that the upper fit is valid while the lower fit is not. On the other hand, note that our scientific conclusions that $n < 4$ and that there is extra light are robust enough to be evident in both fits. Also, the parameters derived from the bottom fit would not significantly change our fundamental plane parameter correlations (Figures 34, 37, and 38).

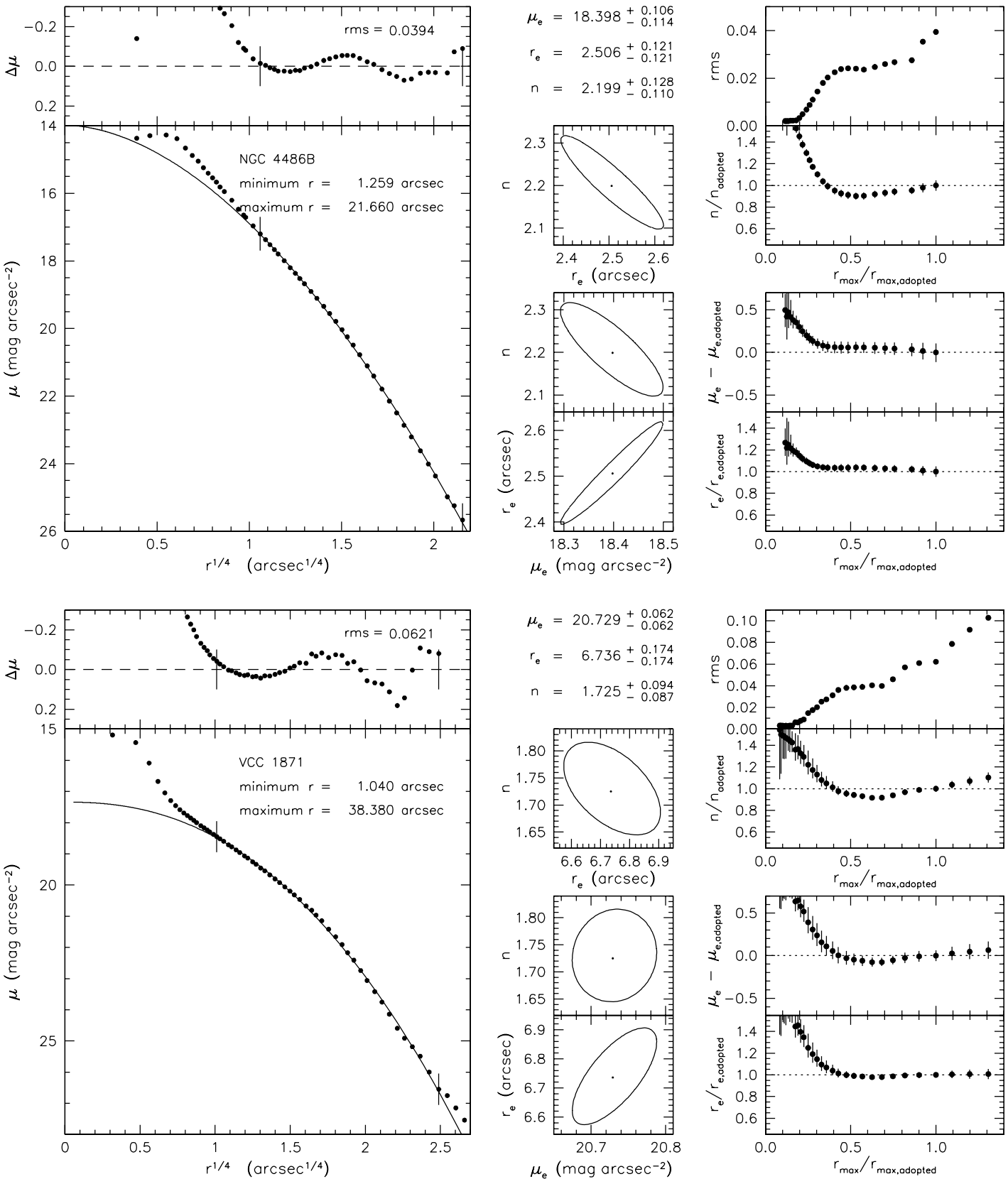

Figure 65. Sérsic function fits to the major-axis profiles of NGC 4486B and VCC 1871. When the well-known double nucleus of NGC 4486B (Lauer et al. 1996) is measured with a program that fits elliptical isophotes, the result looks like a core profile. However, the double nucleus actually is a feature inside the extra light component of a normal, tiny elliptical with a normal Sérsic function profile and a robust value of $n = 2.20^{+0.13}_{-0.11}$.

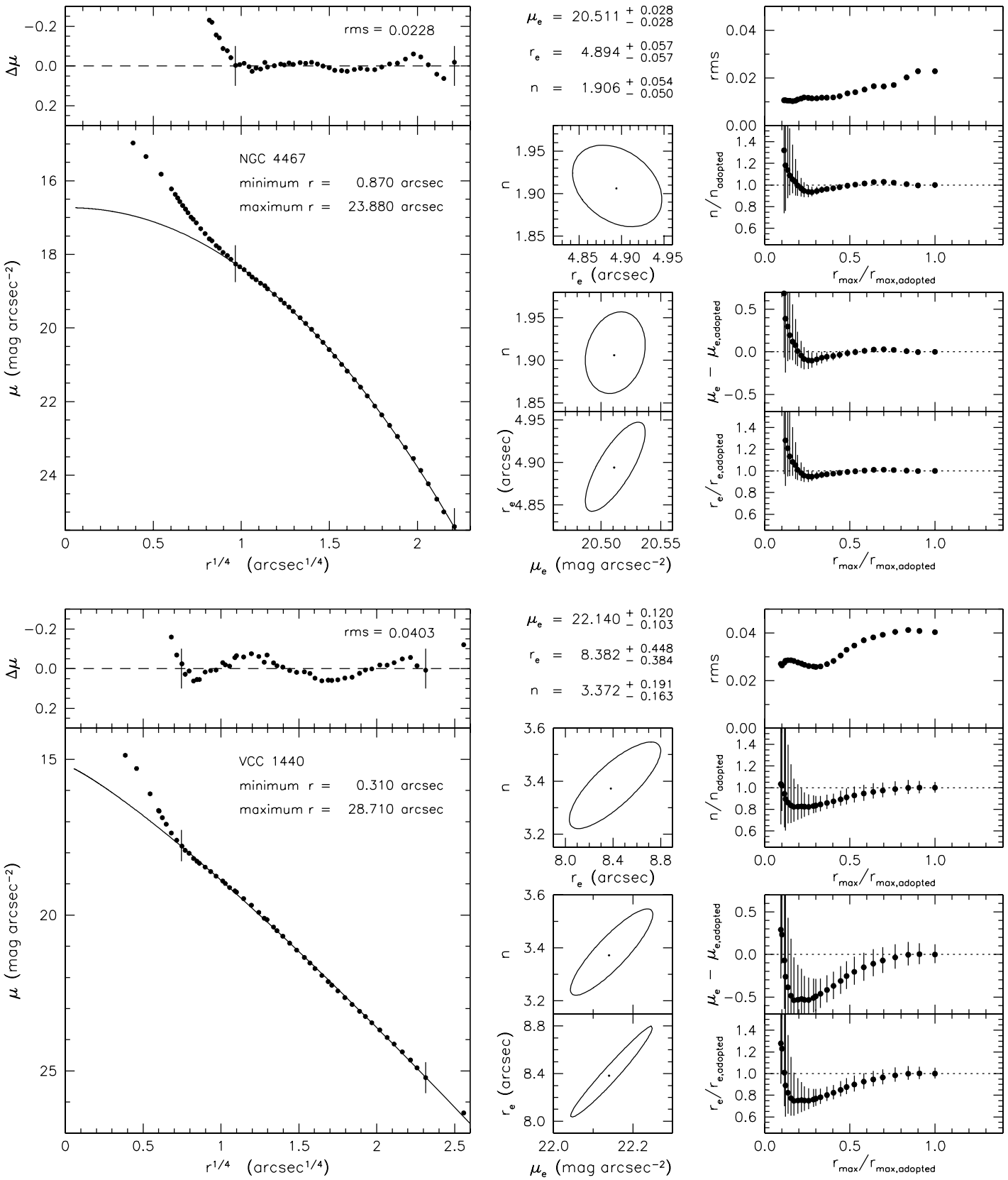

Figure 66. Sérsic function fits to the major-axis profiles of NGC 4467 and VCC 1440. They have $M_{VT} = -16.92$ and -16.85, respectively. That is, they are Virgo cluster analogs of M 32 ($M_{VT} = -16.69$).

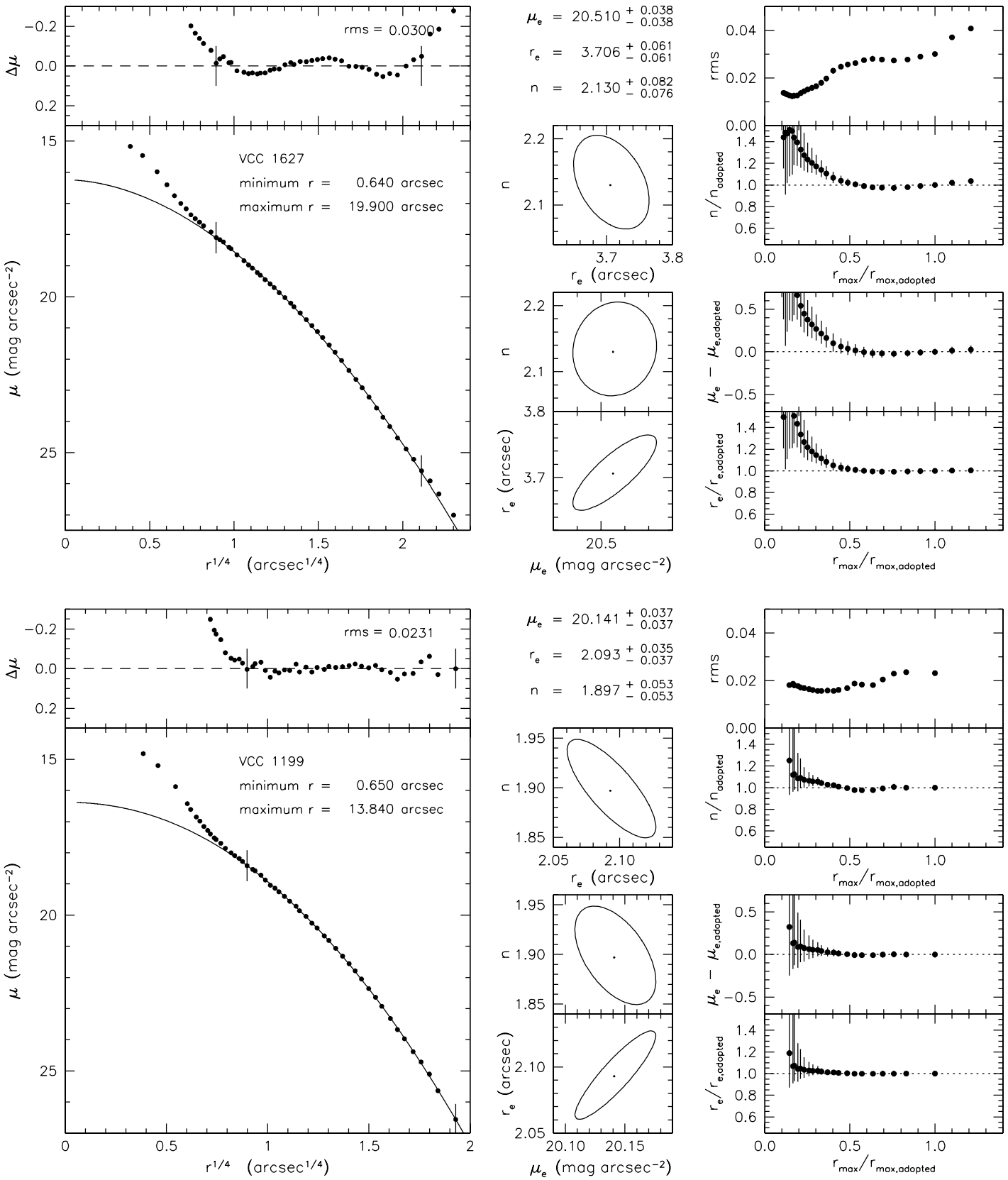

Figure 67. Sérsic function fits to the major-axis profiles of VCC 1627 and VCC 1199. The layout is as in Figure 49. At $M_{VT} = -16.44$ and -15.53, respectively, these are the lowest-luminosity (known) true ellipticals in Virgo. VCC 1199 is about 1 mag fainter than M 32 ($M_{VT} = -16.69$).

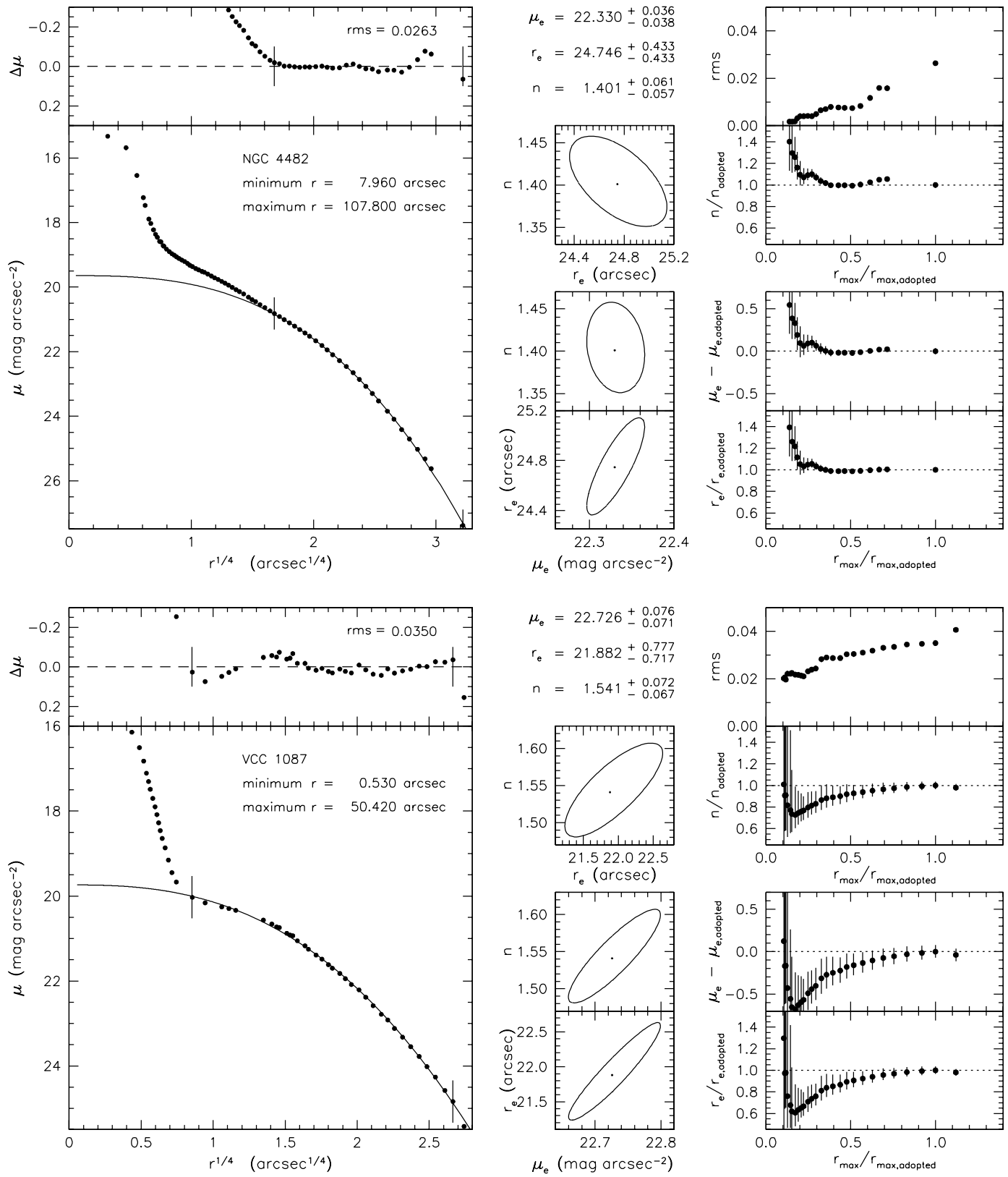

Figure 68. Sérsic function fits to the major-axis profiles of NGC 4482 and VCC 1087, the brightest spheroidal galaxies in our sample. The layout is as in Figure 49. Spheroidals show signs of more complication in their profiles than do ellipticals. The inner part of NGC 4482 outside the prominent nuclear star cluster is not fit by a Sérsic function. The fits for VCC 1087 (this figure), VCC 1355 (Figure 69), and VCC 1407 (Figure 71) show features similar to those of the "Type II" exponential profiles discussed by Freeman (1970). Our Sérsic fits have excellent to good, small rms residuals. But the profile data are accurate enough to show subtle systematic curvature in the residuals. The form of the curvature is such that a Sérsic function with a *slightly* higher n would fit better at large r. But then the inner profile outside the nucleus would drop below the inward extrapolation of the outer Sérsic fit, exactly as in a "Type II exponential." This is a subtle similarity to disk galaxies that we note in addition to the more obvious similarities revealed by the fundamental plane correlations (Figures 1, 34, 37, and 38; Sections 2.1 and 8).

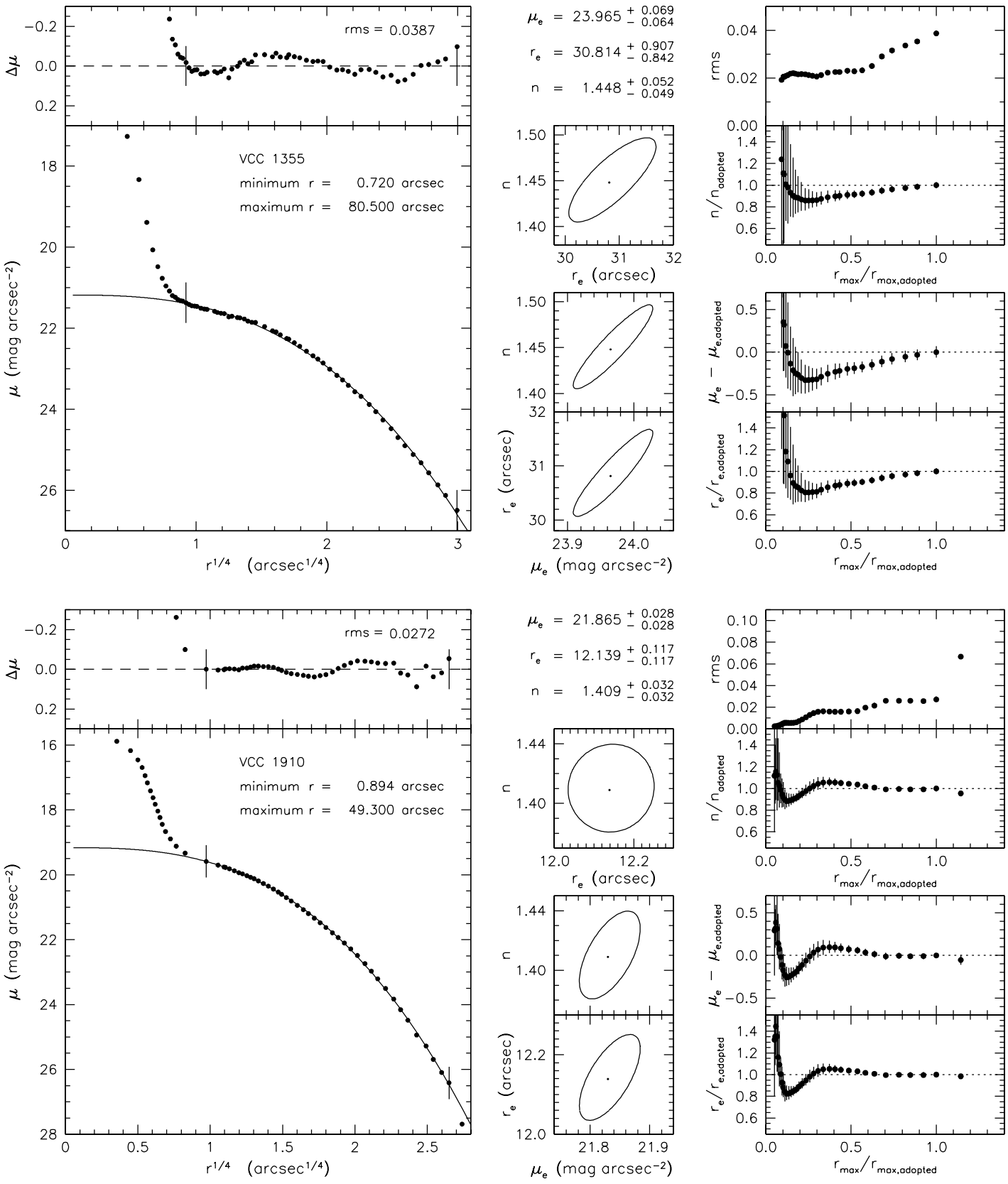

Figure 69. Sérsic function fits to the major-axis profiles of the spheroidal galaxies VCC 1355 and VCC 1910. The layout is as in Figure 49. VCC 1355 shows a hint of "Type II Sérsic function" behavior (see the caption to Figure 68).

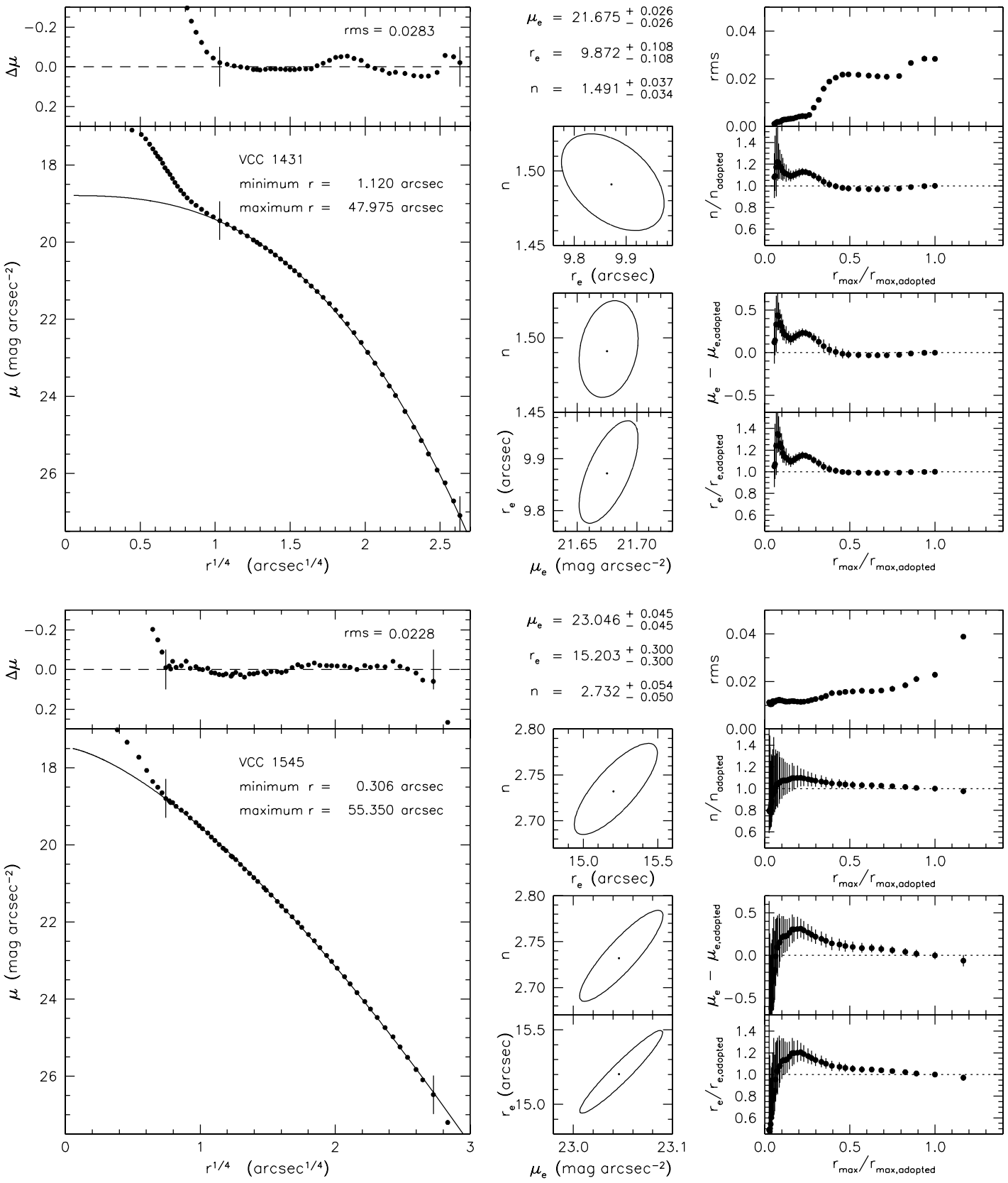

Figure 70. Sérsic function fits to the major-axis profiles of the spheroidal galaxies VCC 1431 and VCC 1545. The layout is as in Figure 49.

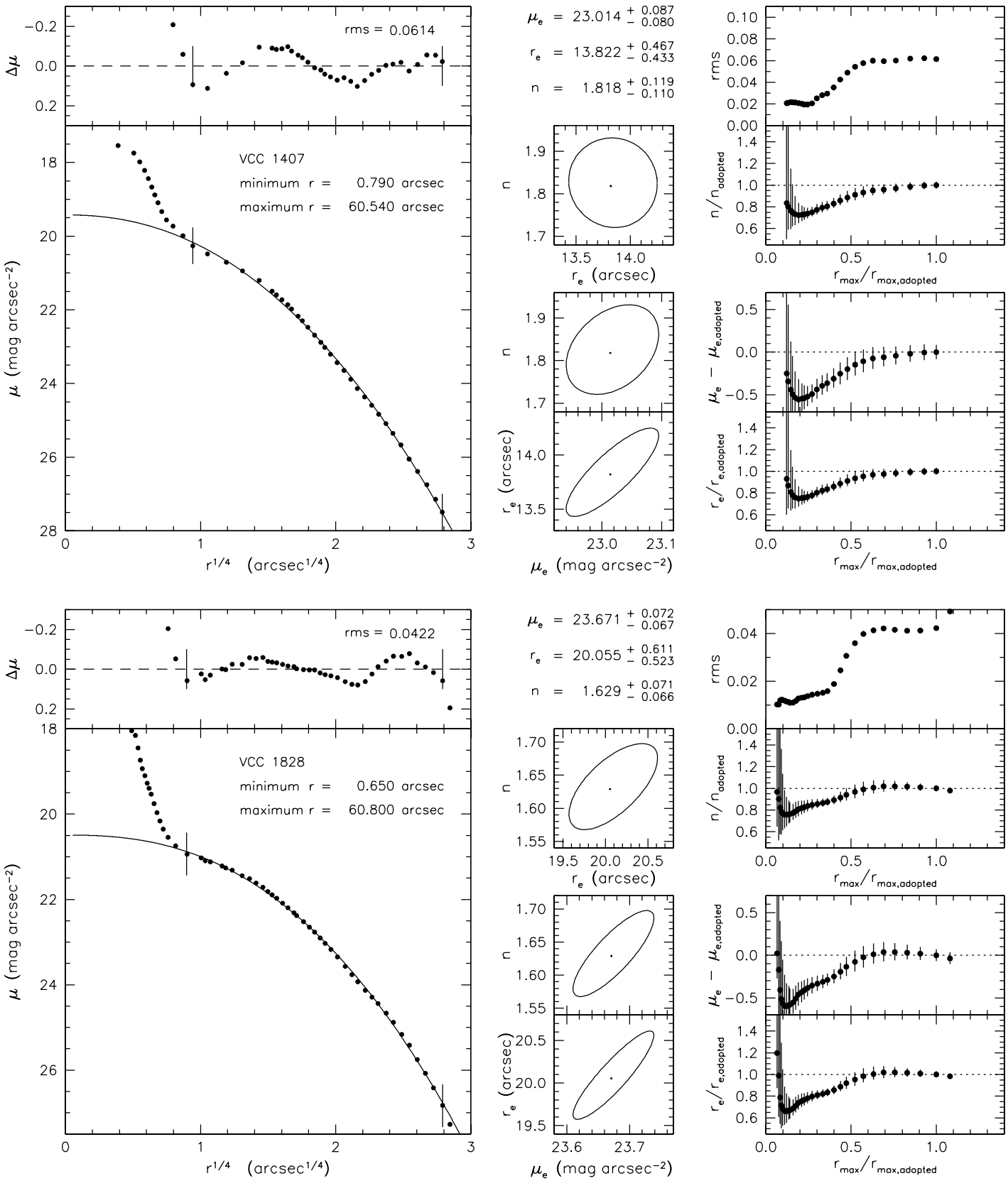

Figure 71. Sérsic function fits to the major-axis profiles of the spheroidal galaxies VCC 1407 and VCC 1828. The layout is as in Figure 49. VCC 1407 shows a hint of "Type II Sérsic function" behavior (see the caption to Figure 68). With $M_{VT} = -16.71$ and -16.61, respectively, these galaxies have almost the same luminosity as M 32 ($M_{VT} = -16.69$), but they have much lower Sérsic indices and central surface brightnesses.

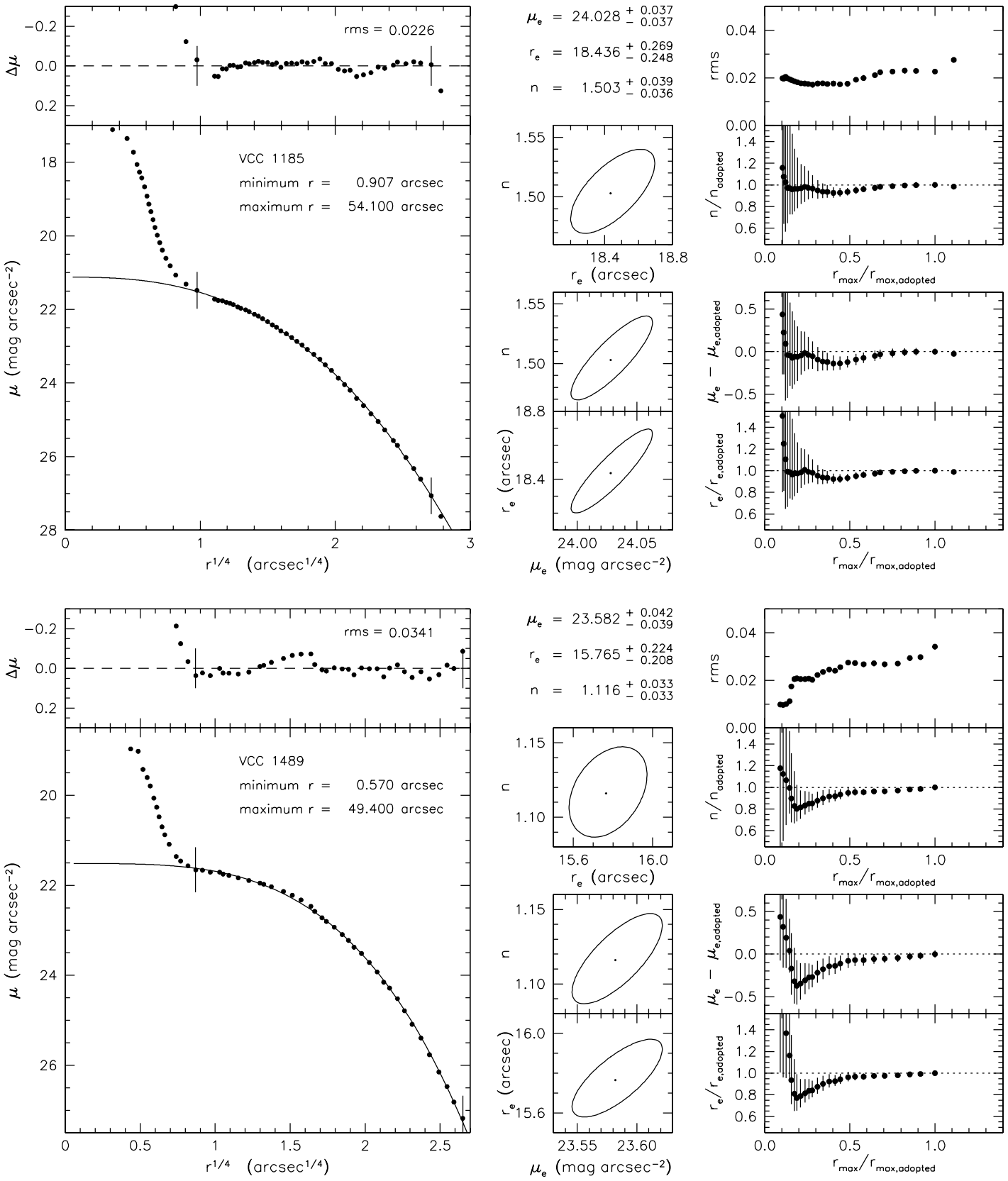

Figure 72. Sérsic function fits to the major-axis profiles of the spheroidal galaxies VCC 1185 and VCC 1489. The layout is as in Figure 49.

robustness of the fits to changes in the range of radii that are fitted. This is important because neither profile measurement errors nor errors associated with any failure of the function to describe the profiles are random. Fits can change substantially depending on whether particular wiggles in the profile are included or not. *How much dynamic range in a galaxy brightness profile is required to get a robust Sérsic fit?* With accurate profiles over large dynamic ranges, we can answer this for the Virgo cluster sample. The results should be useful as a general guide to interpreting the reliability of published and future Sérsic fits.

Figures 49–72 illustrate the fits. Consistent with Section 4.1, we fit Sérsic functions over the largest radius ranges over which they agree with the composite major-axis profiles. Fit tolerances are determined from the profile measurement errors implied by the scatter at each radius of the individual measurements illustrated in Figures 11–29 (top and bottom panels) and from the function fitting errors to the mean profile in Figures 49–72 (top-left panels). In general, the latter errors dominate. The median rms of the 27 fits is 0.040 V mag arcsec^{-2}. The mean rms is 0.046 V mag arcsec^{-2}, and the dispersion in rms values is 0.019 V mag arcsec^{-2}. Sérsic functions fit the main parts of the profiles of both E and Sph galaxies astonishingly well over large ranges in surface brightness.

Of course, the above rms values depend on our decisions on where to cut the fit ranges at small and large radii. At large radii, we prefer to keep deviations to < 0.1 mag arcsec^{-2}; as judged from the agreement between different sources, this is approximately the estimated profile error at large radii. However, in some cases, slightly larger deviations are accepted if doing so greatly increases the radius range of the fit. Our aim is to have the Sérsic fit describe as large a fraction of the total light of the galaxy as possible, consistent with measurement errors. Note that in almost all galaxies, the fit does not fail at large radii; rather, the profile ends where the S/N becomes too low, where sky subtraction becomes insecure, or where we reach the edge of the detector field of view. *For most galaxies, the Sérsic fits accurately describe the major-axis profiles over radius ranges that include* $\sim$ *93%–99% of the light of the galaxies* (see Figure 41).

At small radii r, the deviations of the profiles from the best fits become large and systematic, and they do so quite suddenly as r decreases. This indicates the presence of cores or extra light. Again, we cut the fit range where these deviations become comparable to the measurement errors. We tend to be slightly conservative: we often include radii where the fit departures associated with cores or extra light are starting to become apparent, again in order to include as much of the galaxy in the fit as possible.

For a few galaxies, small radius ranges near the center are excluded because of dust absorption. These do not significantly affect the fit results. Also, for a few galaxies, parts of the profile are excluded where large fit errors are associated with nonequilibrium structures that can be identified on physical grounds. These are discussed in Appendix A.3.

A.1. Parameter Errors Estimated Via χ^2 Ellipses

Figures 49–72 show two fits each, i.e., the top and bottom halves of each page. For each fit, the left two panels show the mean profile points, the fit range, the fit (as a solid curve), and the residuals $\Delta\mu$ from the fit, together with the rms within the fit range. Figures 11–29 are corresponding plots that show all of the original data sources. The middle column of each figure here shows the χ^2 ellipses and lists the fit parameters. The quoted parameter errors are the half-widths of each χ^2 ellipse in that parameter. The right-hand columns of figures explore robustness to changes in the fit range; they are discussed in Appendix A.2.

The best-fit Sérsic models were derived by minimizing

$$\chi^2 = \frac{1}{N_{\rm ind} - 3} \sum_{i=1}^{N_{\rm data}} \frac{[\mu_i(r_i) - \mu_S(r_i)]^2}{\sigma_{\mu,i}^2}, \qquad \text{(A2)}$$

where $\mu_i(r_i)$ is the observed surface brightness at radius r_i with measurement error $\sigma_{\mu,i}$, and where $\mu_S(r_i)$ is the surface brightness of the Sérsic model, Equation (A1), at r_i. Also, $N_{\rm data}$ is the number of data points, and $N_{\rm ind}$ is the number of independent data points. Estimating $N_{\rm ind}$ has always been one of the central uncertainties in profile fit error analysis. We are helped by the fact that we average many independent data sets from different telescopes and profile measurement techniques. On the other hand, closely spaced data points near galaxy centers are coupled by PSF smoothing; adjacent data points at large radii usually suffer from similar problems with large-scale flat fielding and sky subtraction, and it is common for profile measurement software to smooth images at large radii in order to improve S/N and to compensate for problems with masked or removed foreground stars and background galaxies. Therefore it is unrealistic to believe that all data points in our tabulated mean profiles are independent. After experimentation with the data sets for individual galaxies, we adopt the somewhat conservative assumption that $N_{\rm ind} \approx N_{\rm data}/2$.

The other uncertainty in applying Equation (A2) is the estimation of $\sigma_{\mu,i}$. Inherent in χ^2 minimization is the assumption that the errors in the fitted data points are random and uncorrelated. The residual plots show that both assumptions are almost always violated. A few profile wiggles are produced artificially when (for example) one profile data set starts to deviate from the others and, at some radius, suddenly gets omitted from the average. But examination of Figures 11–29 shows that most profile wiggles are real—they look the same in many data sets. They represent failures of the Sérsic function to describe the profiles at the few-percent level. Such failures are in no sense unexpected. In contrast, it is surprising that Sérsic functions work as well as they do. Nevertheless, the wiggles in the residual profiles—and, to a lesser extent, scatter in the residual profiles that is indicative of more-or-less random measurement errors—represent the ultimate limit on the accuracy of the Sérsic fits. We use the rms scatter of the fits (see the keys of Figures 49–72) as our estimate of $\sigma_{\mu,i}$. As long as this rms scatter—although partly systematic—is a few hundredths of a mag arcsec^{-2} and therefore comparable to profile measurement errors, this choice is reasonable and unlikely to lead us far astray. Nevertheless, the need for this choice of $\sigma_{\mu,i}$ means that our error analysis is necessarily approximate.

The rest of the job is engineering. The χ^2 minimum was determined with a simple grid search technique using three steps of successive refinement. Providing error estimates for the Sérsic parameters that reflect the fit quality in a meaningful way is tricky, because the errors of the three Sérsic parameters can be strongly coupled. Then the usual marginalized 1σ errors corresponding to $\Delta\chi^2 = 1$ around the minimum are misleadingly optimistic. We therefore decided to provide more realistic estimates for the fit uncertainties, namely the sizes of the three-dimensional 1σ error ellipsoids *as projected onto the parameter axes*. These ellipsoids are defined by $\Delta\chi^2 = 3.53$

(Press et al. 1986). The two-dimensional projections of the error ellipsoids are shown in the middle columns of plots in Figures 49–72. The corresponding parameter errors are listed in the keys above the plots. Note that these are calculated directly by interpolation in the χ^2 arrays, whereas the χ^2 ellipses are calculated "on the fly" by the `sm` contouring code. As a result, the illustrated χ^2 ellipses do not agree perfectly with the (more reliable) tabulated errors. Note also that extremely thin and elongated χ^2 "bananas" sometimes break up into isolated islands when the `sm` contouring program has trouble with the interpolation.

The error estimates listed in the keys above the χ^2 ellipses in Figures 49–72 are included in Table 1 and used in our analysis.

These error estimates are consistent with the results of our fit range tests as discussed in Appendix A.2.

A.2. Robustness of Sérsic Fits to Changes in the Radial Fit Range

Two kinds of fits are shown in Figures 49–72. Most illustrations show the adopted fit for each galaxy (e.g., top fit for NGC 4472 in Figure 49). A few alternative interpretations with different radial fit ranges are included to illustrate specific scientific points (e.g., bottom fit for NGC 4472 in Figure 49). These are discussed in the text, but their parameters are not included in Table 1.

For the adopted fits but not for the illustrative fits, the right-hand panels in Figures 49–72 test the effect of changing the outer radius $r_{\rm max}$ of the fit range from the adopted value $r_{\rm max,adopted}$ listed in the key of the large panel. As a function of $r_{\rm max}/r_{\rm max,adopted}$, they show how the rms residuals and the fit parameters (e.g., $r_{\rm e}$) change from the adopted value (e.g., $r_{\rm e,adopted}$) listed above the middle panels of χ^2 ellipses. The outer end of the fit range is changed by one tabulated profile point at a time, moving inward from the outermost tabulated point past the adopted point $r_{\rm max,adopted}$ (frequently the same as the outermost point) and on toward smaller r until the fit deviates drastically from the adopted one. For every choice of $r_{\rm max}$, a Sérsic fit is made and its results are illustrated. The plotted error bars are the half-widths of the χ^2 ellipses corresponding for that particular fit to the ones illustrated in the middle columns for the adopted fit. That is, the error bars take parameter coupling into account.

Examination of the fit range tests shows that our adopted Sérsic fits are very robust for almost every galaxy:

Sometimes the outermost data points (beyond $r_{\rm max,adopted}$) deviate suddenly above or below the adopted fit and would change that fit noticeably if included. But these points are very vulnerable to sky subtraction or flat-fielding errors. We include these points in the tabulated profiles in part because they result in more realistic total magnitudes but also so that readers can see our profile calculations begin to fail where they get difficult. We have no problem in discarding these points from the Sérsic fits.

More fundamental issues are these: as $r_{\rm max}$ is decreased, which wiggles in the composite profiles should we include in the fits? Are the fits sensitive to these choices? How much can we shrink the fit range and still derive reliable Sérsic parameters? That is, how much dynamic range in galaxy profiles is necessary for the confident use of Sérsic function fitting machinery?

Also, do the fit range tests support our error bars?

The figures provide clear answers to these questions. Fits derived with $r_{\rm max} \equiv f r_{\rm max,adopted} < r_{\rm max,adopted}$ differ by $\leqslant 1\sigma$ from the adopted fits in to about $f = 0.50$. More precisely, the limiting f has a mean of 0.48 ± 0.03 (dispersion $= 0.15$) and a median of 0.50 (quartiles $= 0.37, 0.59$). For somewhat smaller $r_{\rm max}$, the derived parameters still change only slightly as different profile wiggles are successively omitted from the fit. Of course, as $r_{\rm max}$ is decreased, the rms gets smaller, because the program struggles to fit fewer profile wiggles. Also, the parameter error bars grow, because their derivations are based on fewer data points. But *the changes in the parameters are consistent with the error bars given by the adopted fit. This confirms that our error analysis is realistic even though the profile fit errors are more systematic than random.* No conclusions of this paper are vulnerable to modest changes in fit ranges.

Eventually, as $r_{\rm max}$ is decreased well below $0.5\, r_{\rm max,adopted}$, the fits begin to deviate more significantly from the adopted ones. This is a sign that the dynamic range has become dangerously too small, i.e., that a very few profile wiggles are "torquing" the fit unrealistically. The degree to which this is a problem depends on Sérsic n. That is, the dynamic range in profile data that are needed for robust Sérsic fits depends on n. We illustrate both the dynamic range that we have in the present data and the reduced dynamic ranges that give fiducial errors in the Sérsic parameters as follows:

Figure 73 (left) summarizes the large dynamic range of our observations. Our Sérsic fits generally reach 25–27.5 V mag arcsec^{-2}. In many cases, the fit range extends to the faint limit of our photometry; in some cases, it ends where sky subtraction errors or overlapping objects affect the profiles. The Sérsic function almost never fails dramatically to fit low surface brightnesses. NGC 4406 is the main exception, but the outer profile may be affected by tidal shocking, or our measurements may be contaminated by the bracketing galaxies. The ranges of surface brightnesses that we fitted are shown in the middle-left panel, and the corresponding radial fit ranges are shown in the bottom panel. The inner end of each fit range is chosen to be where "missing light" in cores or extra light above the outer Sérsic fit becomes significant. The core galaxy with the unusually small $\Delta\mu_{V,\rm adopted}$ is NGC 4406, as discussed above. Nevertheless, the inner part of the galaxy is an excellent Sérsic function, and fit uncertainties do not affect our interpretation of fundamental plane correlations. The same is true of NGC 4382: nonequilibrium structure diagnostic of a not-yet-relaxed merger remnant create wiggles in the profile that can be fitted in various ways (three Sérsic fits are shown in Figure 53 and 54), but the plausible ones—the ones that fit large radius ranges—both lie in the derived parameter correlations. Our efforts to compile accurate profiles over large radius ranges have paid off in robust parameters that allow confident interpretation of the parameter correlations.

As a tool for users of Sérsic functions, we provide in Figure 73 (right) three summaries of the dynamic ranges needed for fits to the present data to give various fiducial parameter errors. They depend somewhat on Sérsic index, which is not known a priori. However, the dependence on n is weak enough so that a sufficiently good value can be derived with a preliminary fit. Therefore, we plot results as functions of n. There are two regimes. Fits that have $n \lesssim 3.5$ are very robust; a modest dynamic range is sufficient, and limitations on the fit come mostly from data quality and from decisions about the fit range and not from insufficient dynamic range. On the other hand, when $n \gg 4$, the fit is unstable and a generous dynamic range is necessary in order to get reliable results.

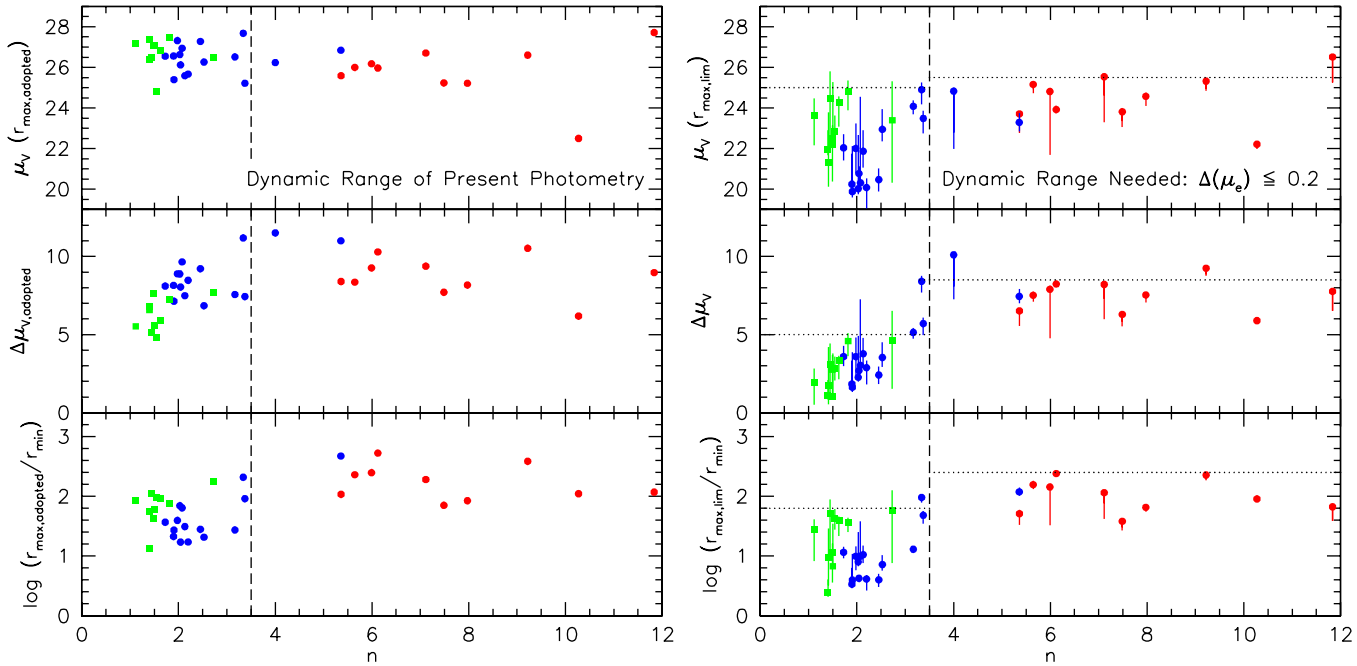

Figure 73. The left panels illustrate the dynamic range of the profile points used in our adopted Sérsic function fits; red points are for core ellipticals, blue points are for extra light ellipticals, and green points are for spheroidals. The right panels illustrate the reduced dynamic range that would, with the present, high-quality profile data, give Sérsic parameters that differ from our adopted ones by $\Delta(\mu_e) = 0.2$ mag arcsec^{-2}, a factor of 1.12 in r_e, and a factor of 1.10 in n (see the text). Upward-pointing "error bars" end at the minimum dynamic range required to give Sérsic fits that agree with our adopted ones to 1σ. Downward-pointing "error bars" end at the dynamic range required to give parameters that agree with our adopted ones to $\Delta(\mu_e) = 0.40$, a factor of 1.24 in r_e, and a factor of 1.19 in n. The top panels show the faint limit of the surface brightness range included in our fits (left) or required for $\Delta(\mu_e) \leqslant 0.2$ mag arcsec^{-2} (right). The middle panels show the surface brightness range of the profile data used in our fits (left) or required for $\Delta(\mu_e) \leqslant 0.2$ mag arcsec^{-2} (right). The bottom panels show the corresponding ratio of the radius of the outermost profile point included in the fit to the radius of innermost profile point included in the fit. The right-hand plots provide conservative criteria by which users of Sérsic functions can judge whether the dynamic range of their data is sufficient for robust fits (see the text for caveats). Approximate target dynamic ranges are indicated by horizontal dotted lines and depend somewhat on Sérsic index. For example (middle-right panel), for giant, core galaxies, which generally have $n \gtrsim 4$, it is almost always safe to have a surface brightness range of 8.5 mag arcsec^{-2} from just outside the core, where the fit becomes acceptable, to large radii, where the fit stops being good and/or where sky subtraction becomes a problem. In contrast, Sérsic fits are much more benign when $n < 3.5$, and progressively smaller surface brightness or radius ranges are sufficient, always assuming that the profile data are high enough in quality. One could choose a target dynamic range $\Delta\mu_V$ that decreases with n. We adopt the simpler approach of noting (dotted line) that $\Delta\mu_V \gtrsim 5$ mag arcsec^{-2} is essentially always safe.

Quantitatively, the right panels of Figure 73 were constructed as follows. From each fit range test (Figures 49–72), we determined the maximum fit radius $r_{\rm max,lim}$ at which the fitted μ_e differs from the adopted value by (say) 0.2 V mag arcsec^{-2}. Since the fits tend to preserve the total magnitude $V = \mu_e - 5\ \log r_e$ + constant, an error in μ_e of $\Delta(\mu_e) = 0.2$ mag arcsec^{-2} should correspond approximately to $\Delta(\log r_e) = 0.04$, i.e., a derived $r_{e,\rm lim} = 1.10\, r_{e,\rm adopted}$ or $r_{e,\rm lim} = (1/1.10)\, r_{e,\rm adopted}$ depending on the sign of $\Delta(\mu_e)$. The fit range tests confirm that the parameters are coupled in this way: removing the sign of $\Delta(\mu_e)$, the actual mean $\langle r_{e,\rm lim}/r_{e,\rm adopted}\rangle = 1.119 \pm 0.004$ $(\sigma/\sqrt{36})$. The corresponding error in n is $\langle n_{\rm lim}/n_{\rm adopted}\rangle = 1.096 \pm 0.010$ $(\sigma/\sqrt{36})$. These are the plotted points in the right panels of Figure 73. They show the fit ranges required with our data for 20% errors in effective brightness, 12% errors in effective radius, and 10% errors in Sérsic index. The χ^2 ellipses tell us that the errors are coupled so that fainter μ_e corresponds to larger r_e.

The points in the right-hand panels are plotted with "error bars" to show the fit ranges required for two different choices of $\Delta(\mu_e)$. The "error bars" that point toward larger dynamic range show the requirements for μ_e to agree with our adopted values to within our error bars. These fits were discussed earlier in this section. Corresponding error bars do not appear for many core ellipticals, because our errors in μ_e are already larger than the fiducial $\Delta(\mu_e) = 0.2$ mag arcsec^{-2} used for the plotted points. However, for extra light Es and for spheroidal galaxies, the Sérsic fits are very robust, our μ_e errors are small, and disagreeing with our adopted fits by only one error bar requires a larger dynamic range than disagreeing with our adopted fits by $\Delta(\mu_e) = 0.2$ mag arcsec^{-2}. In Figure 73, the "error bars" that point toward smaller dynamic range show the (easier) requirements for $\Delta(\mu_e) = 0.4$ mag arcsec^{-2}. The corresponding mean $\langle r_{e,\rm lim}/r_{e,\rm adopted}\rangle = 1.239 \pm 0.006$ $(\sigma/\sqrt{35})$ and $\langle n_{\rm lim}/n_{\rm adopted}\rangle = 1.189 \pm 0.025$ $(\sigma/\sqrt{35})$. Only 35 galaxies are included in the means because the formal errors on the NGC 4382 fits do not reach 0.4 mag arcsec^{-2} before we run out of points inside the annulus that was omitted from the fits. Again, the parameter coupling approximately preserves the total luminosity of the Sérsic function fit.

In the right panels of Figure 73, the horizontal dashed lines provide conservative estimates of safe dynamic ranges required to achieve the above parameter accuracies. The requirements depend somewhat on Sérsic index. For $n \leqslant 3.5$, dynamic range requirements are not severe, because small-n Sérsic fits are relatively stable. A range of 5 mag arcsec^{-2} in μ_V, corresponding to a range of a factor of about 60 in the ratio of the largest radius to the smallest radius fitted is almost always safe. Given typical amounts of extra light in the present galaxies, the above values correspond to a limiting surface brightness of 25 V mag arcsec^{-2}. Note that this is the limiting surface brightness to which the Sérsic function still fits adequately; the data may reach (and, in some of our galaxies, does reach) fainter surface brightnesses at which we no longer trust our sky or overlapping

galaxy subtraction. In general, the dynamic range requirements for small-n galaxies are not difficult to meet. Large-n galaxies are more of a challenge. Sometimes a dynamic range of a factor of 250 in surface brightness is enough, but other fits are less stable. A surface brightness range of 8.5 mag arcsec^{-2} is needed to make essentially all galaxies in the present sample have safe fits. This corresponds to a range of a factor of ~ 250 in radius.

We emphasize: *Dynamic range is only one requirement to get a good Sérsic fit. Equally important are the accuracy of the profile data and the decisions that are made about which profile points to include in the fit and which to omit because they are interpreted as showing missing light or extra light at small radii, S0 disks at intermediate radii, or sky subtraction errors at large radii.* The guidelines in Figure 73 are relevant only if the data are comparable in quality to those presented here. Also, they are only guidelines; for some of our galaxies, it is clearly sufficient to have less dynamic range than the dashed lines suggest.

It is important to note a final caveat: one of the main conclusions of this paper is that Sérsic functions fit the major-axis brightness profiles of Virgo cluster elliptical galaxies remarkably well. If this proves to be less true of ellipticals in a wider variety of environments—that is, if their profiles turn out to be more heterogeneous—then both the validity of Sérsic fits as analysis machinery and the right-hand panels of Figure 73 as guidelines to required dynamic ranges are compromised.

A.3. Robustness of Sérsic Fits: Comparison with Caon et al. (1993)

We illustrate two examples of the robustness (or not) of Sérsic fits. Figure 74 compares our results with those of Caon et al. (1993). Appendix B compares our results with those of Ferrarese et al. (2006a).

As noted in Section 3, Caon et al. (1993) were the first to establish the importance of Sérsic functions. They fitted B-band profiles of 52 early-type galaxies. The profiles were composites derived from deep Schmidt plates and CCD images of the central regions. They had large dynamic ranges; only three Caon fits for galaxies that we have in common do not satisfy the dynamic range requirements suggested in Appendix A.2 (circled points in Figure 74). The comparison of their major-axis n values with ours shows excellent agreement for almost all galaxies. The differences in n values are very large for three galaxies and moderately large for three more. For two of these, Caon et al. (1993) had less dynamic range than we found to be adequate. The rest can readily be understood:

We have noted that NGC 4486 (M 87) is a weak cD. As the fit range is increased, more cD halo gets included, and n looks larger. Our adopted fit uses a brightness range of 9.0 V mag arcsec^{-2} and gives $n = 11.8^{+1.8}_{-1.2}$. An alternative fit in Figure 50 includes less cD halo: the fit range is 6.0 V mag arcsec^{-2} and $n = 8.9^{+1.9}_{-1.3}$. Caon et al. (1993) had a fit range of 5.5 B mag arcsec^{-2} shifted away from the cD halo to higher surface brightnesses than those that we fit. Not surprisingly, they got a smaller Sérsic index, $n = 5.36$. We also would get a smaller Sérsic index if we reduced our fit range further.

NGC 4406 has a profile that is very accurately Sérsic out to $r = 153''$, the outer end of our fit range. Beyond this, the profile that we measure turns up suddenly. If we included the upturn in our fit, we would get a larger n. Caon et al. (1993) did this: they fitted the profile out to 1 mag arcsec^{-2} fainter than we did. Our composite profile is based on two different data sets that agree on the above deviations. Including the profile upturn in the Sérsic fit results in residuals that are not consistent with the accuracy of our profile.

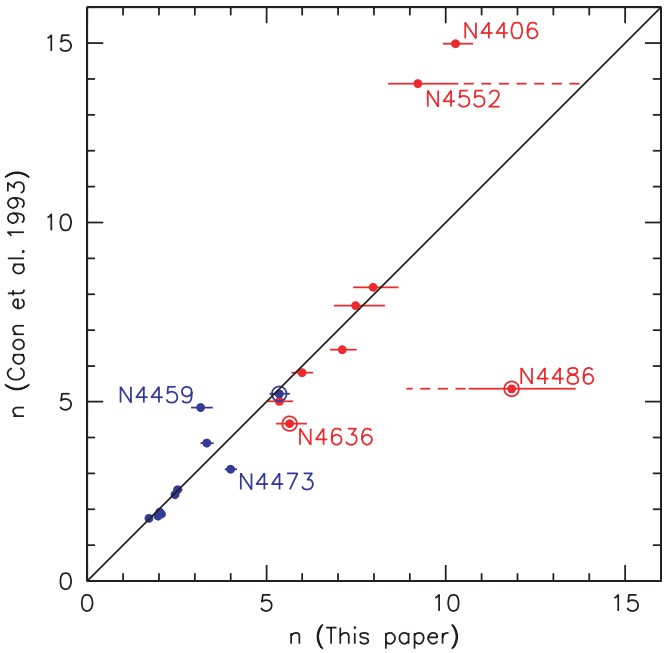

Figure 74. Comparison of our Sérsic n indices (Table 1) with those derived by Caon et al. (1993) for all 9 core ellipticals (red circles) and all 10 extra light ellipticals (blue circles) that we have in common. We have no spheroidals in common. Dashed lines point to our alternative fits as discussed in the text. Circled points indicate that the Caon et al. (1993) fits had less dynamic range than we found to be adequate for these galaxies from our fit range tests.

For NGC 4552, the difference between Caon's fit and ours is a matter of interpretation. We cannot prove that one fit is better than the other. But we can understand the difference. The residual plots in Figures 15 and 56 show that, for our chosen *inner* end of the fit range at $r = 1\farcs28$, the residuals look systematically concave-up from $r^{1/4} = 1.6$ ($r = 6\farcs5$) outward. The residuals are systematic (all data sets in Figure 15 agree) and they are larger than average. But they are not outside the range of what is reasonable. We chose $r = 1\farcs28$ as the inner end of our fit range because we wanted to fit as much of the galaxy light as possible. However, it could reasonably be argued that we should have chosen a larger minimum radius. If we choose $r = 5\farcs5$ (bottom fit in Figure 56), then the residuals no longer look systematic, the total rms is reduced from 0.0774 to 0.0474 mag arcsec^{-2}, and $n = 13.75^{+3.04}_{-1.90}$. This value is at the end of the dashed line from the NGC 4552 point in Figure 74. It agrees exactly with Caon's value. This is, in fact, exactly how they got their value: their B-band fit range corresponds to about 17–25.5 V mag arcsec^{-2} in Figures 15 and 56, i.e., essentially our modified fit range. No conclusions in this paper would significantly be changed if we adopted the modified fit range. The fundamental plane correlations would have slightly larger scatter, but the distinction between E and Sph galaxies would look stronger. The derived amount of missing light in the core would be substantially larger, suggestive of rather more than ~ 3 dry mergers.

NGC 4459 is deviant in Figure 74 because Caon et al. (1993) fitted parts of the inner profile that we, with our more accurate photometry, can confidently recognize as extra light. That is, the outer profile that we derive robustly has $n < 4$. Including extra light as Caon did would increase n to be greater than 4 as Caon found.

NGC 4473 is tricky because of the embedded counter-rotating disk. Our n is essentially fixed by our choice to include a few central points in the fit. We did this for reasons of stability: otherwise small wiggles in the outer profile render the fit unstable because then the fit range is too small. Given the precise fit range chosen by Caon et al. (1993), the slightly smaller n that they derive is understandable. Their value is plausible; we noted earlier that our value of n is an upper limit.

These few differences have taken a disproportionately large number of words to explain. In fact, the agreement between Caon's results and ours is excellent. Note that differences are not usually the result of dynamic range problems. Most differences result from different choices of which profile points to fit, consistent with the discussion in the previous section.

We used the Caon profiles for some of our galaxies, usually when we had problems with other data that we wanted to check. We did not systematically check all Caon data against our own. We were initially reluctant to use their data, partly because the B bandpass is bluer than most others used in this paper and partly because the outer profiles in Caon et al. (1993) are based on photographic plates. In retrospect, Figure 74 shows that we were too conservative: color gradients are less important than sky subtraction uncertainties at large radii, and the quality of the Caon et al. (1993) photometry is generally very good.

APPENDIX B

COMPARISON WITH FERRARESE ET AL. (2006A)

Ferrarese et al. (2006a) present photometry of 100 early-type galaxies in the Virgo cluster obtained with the *HST* as part of the ACS Virgo Cluster Survey (Côté et al. 2004). Their data reduction and ours generally agree to the extent that we can check them; e.g., their $g-z$ colors and ours agree well (Section 6.3, Equation (4)). Their paper and ours also agree on some results. For example, in some galaxies, they find central light excesses, although they call them "nuclei." But Ferrarese et al. (2006a) disagree with both dichotomies that are the focus of this paper. Since these dichotomies are our most important results, we concentrate on them.

B.1. The E–Sph Dichotomy

Ferrarese et al. (2006a, astro-ph/0602297 version) argue against the E–Sph dichotomy: "Once core galaxies are removed, dwarf and bright ellipticals display a continuum in their morphological parameters, contradicting some previous beliefs that the two belong to structurally distinct classes." Thus they echo papers reviewed in Section 2.1. They consider this to be a solved problem: "the structural dichotomy between dwarf and regular ellipticals as advocated by Kormendy (1985b) was likely the result of observational biases."

We disagree. Figures 34–38 provide strong confirmation of the E–Sph dichotomy, and Figure 41 illustrates it also. Kormendy (1985b, 1987b) had few galaxies in the magnitude range $M_V \sim -16$ to -17 (with the present distance scale) where the E and Sph sequences overlap, but the sequences were far apart and diverging from each other where they approached this magnitude range. The problem was not sample bias but rather (1) the luminosity functions (faint Es and bright Sphs are rare; Sandage et al. 1985a, 1985b) and (2) spatial resolution (except for M 32, tiny ellipticals were so poorly resolved with ground-based photometry that they could not be plotted in the parameter correlation diagrams). With *HST*, we can observe M 32 analogs in the Virgo cluster well enough to solve both problems. Figures 34–38 have many galaxies in the E–Sph overlap region. In a follow-up paper, Kormendy (2009) illustrates still more galaxies in the overlap region.

Moreover, far from being biased in favor of finding the dichotomy, our present sample is biased in favor of spheroidals that are similar to small ellipticals. This was deliberate: we targeted galaxies near the E–Sph transition because we wanted to know whether there are intermediate galaxies. Figures 34–38 show that we succeeded in mapping out the transition region: our Sph galaxies (green squares) approach closer to the E sequence than do the larger samples of Ferrarese et al. (2006a: green triangles) and Gavazzi et al. (2005, green crosses). Yet the E and Sph sequences remain distinct.

Why did Ferrarese et al. (2006a) not find this result? There are three main reasons: (1) our parameters measurements are more accurate, because composite profiles give us larger radius ranges over which to fit Sérsic functions while minimizing systematic errors at low surface brightnesses. (2) Ferrarese included S0 galaxies without doing bulge–disk decomposition. We show five large-bulge S0s *after bulge-disk decomposition* in Figure 37.

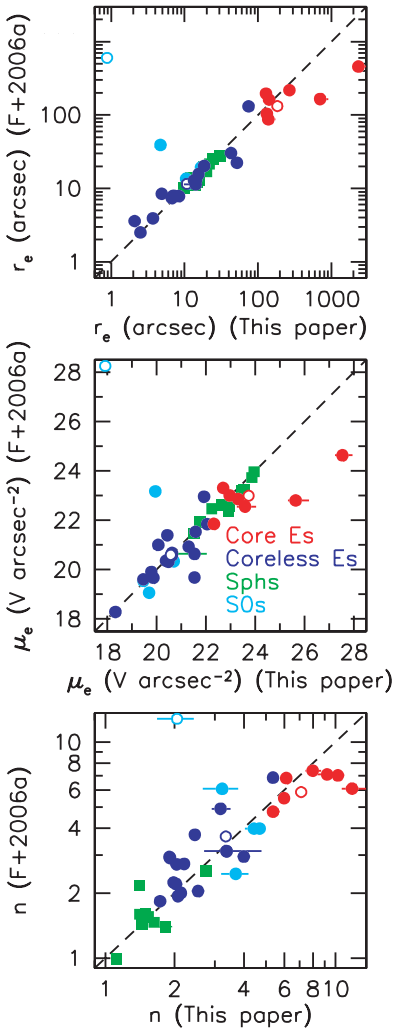

Figure 75. Comparison of Sérsic parameters fitted by Ferrarese et al. (2006a) with our Table 1 values. The Ferrarese values of r_e are converted from mean axis to major axis for consistency with our parameters. Also, g-band μ_e values are converted to V band using Equation (3) and $g-z$ values from Ferrarese's Table 4. The symbols are as in Figures 34 and 37–38. All of our parameters include error bars except r_e and μ_e for bulges. Most error bars are too small to be visible.

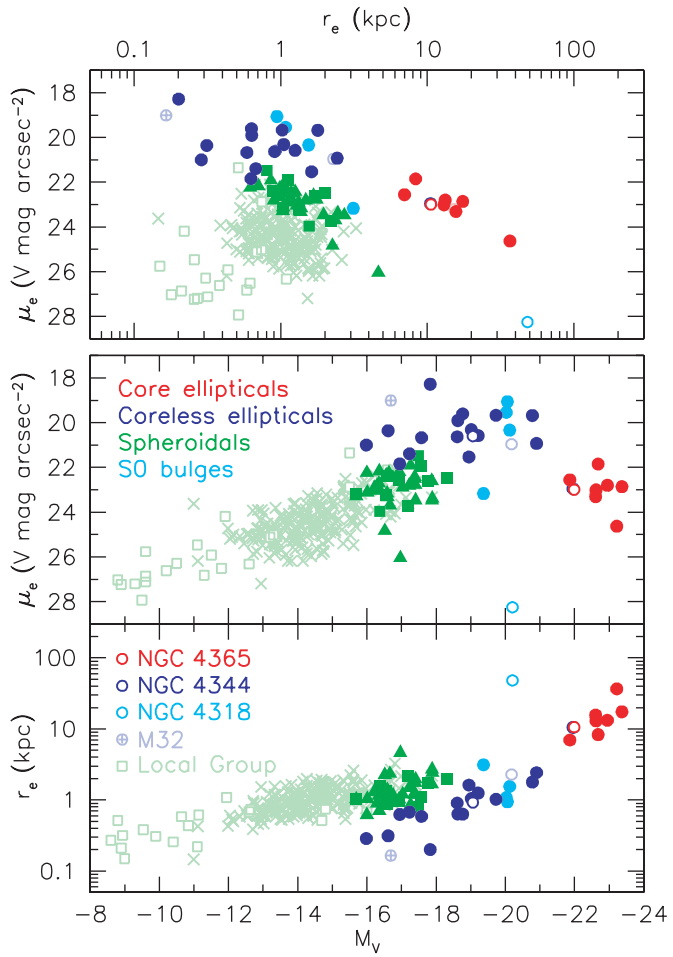

Figure 76. Global parameter correlations for elliptical and spheroidal galaxies using the galaxy sample, classifications, and symbols of our Figure 34 but with all parameters as measured by Ferrarese et al. (2006a). This figure can directly be compared with Figure 37. The two main differences between our analysis and that of Ferrarese et al. (2006a) are the treatment of the galaxy sample and the accuracy of the parameter measurements. This figure mainly tests the parameter measurements, while Figure 77 also tests the effects of sample differences. Here, the faint symbols show the parameters of galaxies that are not in Ferrarese's sample but that are in our sample, that of Gavazzi et al. (2005), or the Local Group. For consistency with these galaxies, Ferrarese's r_e values (their Table 3) have been converted from mean axis to major axis by dividing by $(1 - \langle\epsilon\rangle)^{1/2}$, where $\langle\epsilon\rangle$ values are mean ellipticities from their Table 4. The correction is approximate, because Sérsic n is not the same along the mean and major axes. This is insignificant except when $n \gg 4$ and has no effect on our conclusions.

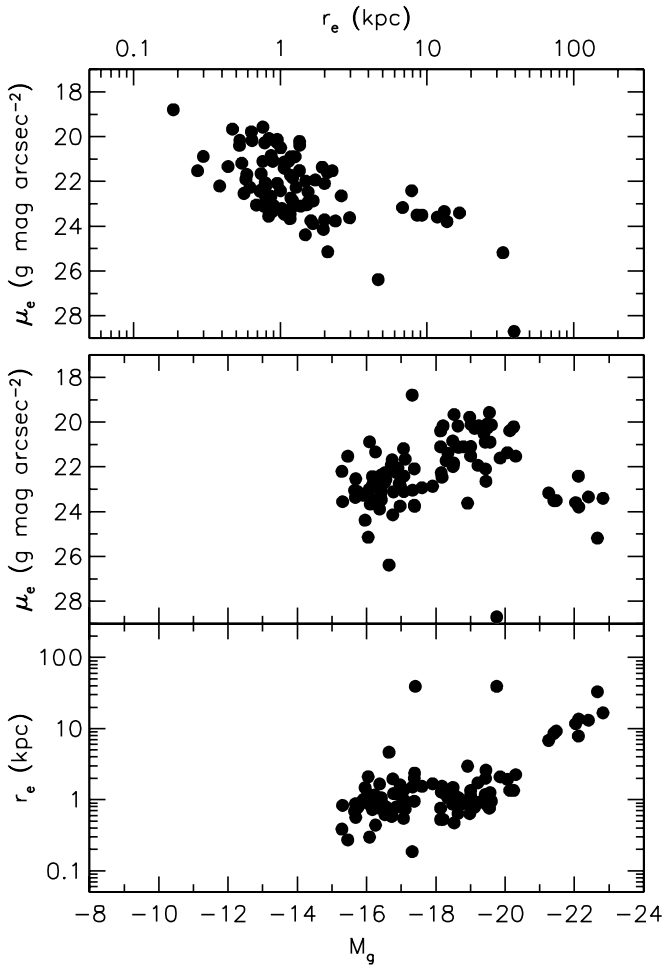

Figure 77. Global parameter correlations using the galaxy sample and parameter measurements of Ferrarese et al. (2006a). Different galaxy types are not distinguished. These are (from top to bottom) panels df, af, and ad of Figure 116 in Ferrarese et al. (2006a) with our figure orientations and parameter limits and with r_e in kpc to allow a direct comparison with Figures 37 and 76.

But in general, we omit S0s, because we have too little leverage on the bulge parameters. Including S0s without doing bulge–disk decomposition is certain to increase the scatter in the correlations. This makes it hard to distinguish the E and Sph sequences where they approach each other. (3) Ferrarese et al. (2006a) observed spheroidal galaxies over a range of only 2 mag in absolute magnitude, so they had too little luminosity leverage to see the *sequence* of spheroidals in parameter space. In addition, they did not plot parameters at the 10%-of-total-light radius, so they did not see the much larger separation of the sequences in our Figure 34.

Figure 75 compares Sérsic parameters derived by Ferrarese et al. (2006a) with our measurements. In many cases, the parameters agree well. This is particularly true of Sphs; they are small and have small n, so they are well observed with the small ACS field of view. However, for some galaxies, Ferrarese's parameters disagree with ours by much more than our estimated errors.

In Figure 75, the very discrepant turquoise point is for the S0 galaxy NGC 4318. Ferrarese's $n = 12.8$ fit includes the bulge and the inner part of the disk shown in Figure 32. However, outside the bulge, the disk is a well-defined exponential ($n = 1.11 \pm 0.11$). The other large discrepancy for an S0 galaxy is NGC 4489. But the small number of large discrepancies is not the main problem.

Figures 76 and 77 test how well Ferrarese et al. (2006a) could see the E–Sph dichotomy with their parameter measurements. Figure 76 shows Ferrarese's parameters but our galaxy classifications. A comparison with Figure 37 tests the effect of differences between their parameters and ours for the same sample of galaxies. One problem is immediately apparent. Ferrarese et al. (2006a) get μ_e values that are 1 mag arcsec^{-2} fainter than we do for three extra light ellipticals (Figure 75). Of these, NGC 4467 and VCC 1199 are M 32-like, faint Es that are especially important in Figures 37 and 38. Their small r_e and (in our data) bright μ_e help to define the extension of the E sequence toward more compact galaxies, left of where the Sph sequence approaches the ellipticals in Figure 37. Our profiles are based on four data sets each from three different telescopes; they agree well (Figures 23 and 24), and they support robust Sérsic fits with rms dispersions = 0.02 mag arcsec^{-2} (Figures 66 and 67). With Ferrarese's parameter values, these points lie close to the

Sph galaxies in Figure 76, and the extension of the E sequence to the left of the Sph sequence is less obvious.

Also, Ferrarese et al. (2006a) observed Sphs over only the brightest 2 mag of their luminosity function. Without the luminosity leverage provided by the fainter Sphs used in Figures 34, 37, and 38 and shown in Figure 76 by the ghostly points, one is not driven to conclude that there are separate, nearly perpendicular *linear sequences* of E and Sph galaxies in parameter space. So the luminosity bias in the Ferrarese sample contributes to their inability to distinguish the two types of galaxies. Nevertheless, guided by the ghostly points, it is possible to see the main features of Figure 37 in Figure 76. The ellipticals (blue and red points) define a fundamental plane, and the Sph galaxies approach the fundamental plane projection in the top panel near its middle, not near its end. A few faint ellipticals would be misclassified using Figure 76, but Ferrarese et al. (2006a) could have found the distinction between nearly perpendicular E and Sph sequences using their parameters.

(The same is true for Gavazzi et al. 2005. They argue against the E–Sph dichotomy, but it is apparent in their Figure 10. Core ellipticals [their dotted parallelograms] and faint ellipticals including M 32 define continuous linear sequences in parameter space that are clearly distinct from the sequence of spheroidals [mostly open circles].)

Figure 77 tests the importance of omitting S0 galaxies in Figure 76. It includes all galaxies in Ferrarese et al. (2006a), using r_e and μ_e from their Table 3 and total g-band magnitude from their Table 4. Unlike Figure 76, it does not use mean ellipticity to estimate major-axis parameters; Figure 77 shows parameters for the "mean axis" at 45° to the major axis. That is, Figure 77 shows (from top to bottom) panels df, af, and ad from Figure 116 of Ferrarese et al. (2006a). Comparison of Figure 77 with Figure 76 shows that the inclusion of S0 galaxies further increases the scatter in the E fundamental plane. Given this, and without guidance from the fainter spheroidals shown as ghostly points in Figure 76, it is easy to understand why Ferrarese et al. (2006a) concluded that E and Sph galaxies are continuous in parameter space. Still, it is interesting to note that there are two partly distinct clouds of points—in addition to the core ellipticals—in the middle and bottom panels of Figure 77. Therefore hints of the E–Sph dichotomy are still evident in Figure 77.

B.2. The E–E Dichotomy

Ferrarese et al. (2006a) also argue against the dichotomy of elliptical galaxies into "core" and "power-law" types. Their most compact statement is in the astro-ph/0602297 version: "The widely adopted separation of early-type galaxies between 'core' and 'power-law' types. . .prompted by the claim of a clearly bimodal distribution of [inner profile slope] values is untenable based on the present study." They then rediscover the dichotomy based on breaks in the surface brightness profiles from steep Sérsic functions at larger radii to shallow power laws at small radii: "In agreement with previous claims, the inner profiles. . .of eight of the 10 brightest galaxies, to which we will refer as "core" galaxies, are lower than expected based on an extrapolation of the outer Sérsic model, and are better described by a single power-law model. Core galaxies are clearly distinct in having fainter central surface brightness. . .and shallower logarithmic slope of the inner surface brightness profile. . .than expected based on the extrapolation of the trend followed by the rest of the sample. Large-scale, global properties also set core galaxies apart. . .."

However, cores have long been defined by many authors based on a central break in profile shape. As quoted in Section 9.2, the Abstract of Kormendy (1999) begins, "Elliptical galaxies are divided into two types: galaxies with steep profiles that show no breaks in slope or that have extra light at small radii compared to a Sérsic function fit and galaxies that show a break from steep outer profiles to shallow inner profiles." We use the same definition. The fact that "large-scale, global properties also set core galaxies apart" has always been central to descriptions of the E–E dichotomy (see the papers listed in Section 2.2).

The Nuker team also defined cores using the profile break: "At the 'break radius' r_b (formerly called the core radius r_c), the steep outer surface brightness profile turns down into a shallow inner power law" $I(r) \propto r^{-\gamma}$ (Kormendy et al. 1994) whose slope is observed to be $\gamma \simeq 0.1 \pm 0.1$. Lauer et al. (1995) included the profile slope in the definition, "We now define a *core* to be the region interior to a sharp turndown or break in the steep outer brightness profile, provided that the profile interior to the break has $\gamma < 0.3$." Including or not including a range of γ values in the definition has, it turns out, only minor effects on one's conclusions. Our definition based only on the profile break and the Lauer's definition that includes γ agree on most galaxies (Section 9.2).

Also, the distribution of central properties robustly shows a dichotomy, even though a few intermediate cases are found (Gebhardt et al. 1996; Lauer et al. 2007b; this paper).

Ferrarese et al. (2006a) do not find the E–E dichotomy in part because they treat Sph galaxies as ellipticals and then use the Lauer et al. (1995) definition of cores. They state, "Although the brightest [ellipticals] have shallow inner profiles, the shallowest profiles are found in faint dwarf systems." We discuss this point in Section 9.2. We agree that low-luminosity Sph galaxies have Sérsic $n \simeq 1$, which means that their central brightness profiles—outside any nuclei—satisfy the γ part of Lauer's definition. But most do not show a downward break from the outer Sérsic profile, so *Sph galaxies do not satisfy either our definition or Ferrarese's definition of a core.* Instead, these galaxies have almost-exponential profiles at all radii, highlighting again (see Section 2.1) their structural similarity to late-type galaxies. Section 8 confirms that Sph galaxies are not ellipticals. They should not cause difficulty in the definition of cores in ellipticals.

We emphasize another aspect of the E–E dichotomy which shows that it has physical meaning. The existence or otherwise of the dichotomy is not just about profile analysis. The distinction between core galaxies and extra light galaxies is also a distinction between many global physical properties, including isophote shape, the importance of rotation, hence also velocity distributions, and overall flattening. The discoveries of many of these correlations were based on a successful application of the Nuker definition of cores (Faber et al. 1997). Ferrarese et al. (2006a) ignore these successes. We find additional physical properties that are part of the E–E dichotomy, including stellar population ages and α element enhancements (Section 11.1).

Finally, we note that, when Ferrarese et al. (2006a) detected extra light, they considered it to be equivalent to nuclei and did not interpret it in the context of dissipative mergers. Meanwhile, Kormendy (1999) already detected extra light and interpreted it as the central, distinct stellar component predicted by the Mihos & Hernquist (1994) merger simulations. More recently, Côté et al. (2006, 2007) suggest that extra light in low-luminosity Es may be related to the "high-density cores" predicted by the Mihos & Hernquist models.

REFERENCES

Abazajian, K., et al. 2003, AJ, 126, 2081
Abazajian, K., et al. 2004, AJ, 128, 502
Abazajian, K., et al. 2005, AJ, 129, 1755
Aguilar, L. A., & White, S. D. M. 1986, ApJ, 307, 97
Arsenault, R., Salmon, D. A., Kerr, J. M., Rigaut, F. J., Crampton, D., & Grundmann, W. A. 1994, Proc. SPIE, 2201, 833
Baggett, S., & Gonzaga, S. 1998, WFPC2 Long-Term Photometric Stability, Instrument Science Report 98-03 (Space Telescope Science Institute), http://www.stsci.edu/hst/wfpc2/documents/isr/wfpc2_ isr9803.html
Balcells, M., & Quinn, P. J. 1990, ApJ, 361, 381
Baldry, I. K., Glazebrook, K., Brinkmann, J., Ivezić, Ž., Lupton, R. H., Nichol, R. C., & Szalay, A. S. 2004, ApJ, 600, 681
Balmaverde, B., & Capetti, A. 2006, A&A, 447, 97
Banse, K., Ponz, D., Ounnas, C., Grosbøl, P., & Warmels, R. 1988, in Instrumentation for Ground-Based Optical Astronomy: Present and Future, ed. L. B. Robinson (New York: Springer), 431
Barnes, J. E., & Hernquist, L. E. 1991, ApJ, 370, L65
Barnes, J. E., & Hernquist, L. 1996, ApJ, 471, 115
Barth, A. J., Greene, J. E., & Ho, L. C. 2008, AJ, 136, 1179
Barth, A. J., Ho, L. C., Rutledge, R. E., & Sargent, W. L. W. 2004, ApJ, 607, 90
Begelman, M. C., Blandford, R. D., & Rees, M. J. 1980, Nature, 287, 307
Bell, E. F., et al. 2004, ApJ, 608, 752
Bell, E. F., et al. 2006, ApJ, 640, 241
Bender, R. 1987, Mitt. Astr. Ges., 70, 226
Bender, R. 1988a, A&A, 193, L7
Bender, R. 1988b, A&A, 202, L5
Bender, R. 1990, A&A, 229, 441
Bender, R. 1992, in IAU Symp. 149, The Stellar Populations of Galaxies, ed. B. Barbuy & A. Renzini (Dordrecht: Kluwer), 267
Bender, R. 1996, in IAU Symp. 171, New Light on Galaxy Evolution, ed. R. Bender & R. L. Davies (Dordrecht: Kluwer), 181
Bender, R. 1997, in The Second Stromlo Symposium: The Nature of Elliptical Galaxies, ed. M. Arnaboldi, G. S. Da Costa, & P. Saha (San Francisco, CA: ASP), 11
Bender, R., Burstein, D., & Faber, S. M. 1992, ApJ, 399, 462
Bender, R., Burstein, D., & Faber, S. M. 1993, ApJ, 411, 153
Bender, R., Döbereiner, S., & Möllenhoff, C. 1987, A&A, 177, L53
Bender, R., Döbereiner, S., & Möllenhoff, C. 1988, A&AS, 74, 385
Bender, R., & Möllenhoff, C. 1987, A&A, 177, 71
Bender, R., & Nieto, J.-L. 1990, A&A, 239, 97
Bender, R., & Paquet, A. 1995, in IAU Symp. 164, Stellar Populations, ed. P. C. van der Kruit & G. Gilmore (Dordrecht: Kluwer), 259
Bender, R., Paquet, A., & Nieto, J.-L. 1991, A&A, 246, 349
Bender, R., Pierce, M., Tully, R. B., & Kormendy, J. 2008, in preparation
Bender, R., Saglia, R. P., & Gerhard, O. E. 1994, MNRAS, 269, 785
Bender, R., & Surma, P. 1992, A&A, 258, 250
Bender, R., Surma, P., Döbereiner, S., Möllenhoff, C., & Madejsky, R. 1989, A&A, 217, 35
Bender, R., et al. 2005, ApJ, 631, 280
Benson, A. J., Bower, R. G., Frenk, C. S., Lacey, C. G., Baugh, C. M., & Cole, S. 2003, ApJ, 599, 38
Benson, A. J., Cole, S., Frenk, C. S., Baugh, C. M., & Lacey, C. G. 2000, MNRAS, 311, 793
Bernardi, M., et al. 2003, AJ, 125, 1882
Best, P. N. 2006, Paper Presented at the Workshop on The Role of Black Holes in Galaxy Formation and Evolution, Potsdam, Germany, 2006 September 10–13 (see Cattaneo et al. 2009)
Best, P. N. 2007a, in ASP Conf. Ser., 379, Cosmic Frontiers, ed. M. Metcalfe & T. Shanks (San Francisco, CA: ASP), 213
Best, P. N. 2007b, New Astron. Rev., 51, 168
Best, P. N., Kaiser, C. R., Heckman, T. M., & Kauffmann, G. 2006, MNRAS, 368, L67
Best, P. N., Kauffmann, G., Heckman, T. M., Brinchmann, J., Charlot, S., Ivezić, Ž., & White, S. D. M. 2005, MNRAS, 362, 25
Best, P. N., von der Linden, A., Kauffmann, G., Heckman, T. M., & Kaiser, C. R. 2007, MNRAS, 379, 894
Binggeli, B. 1994, in ESO/OHP Workshop on Dwarf Galaxies, ed. G. Meylan & P. Prugniel (Garching: ESO), 13
Binggeli, B., & Cameron, L. M. 1991, A&A, 252, 27
Binggeli, B., Sandage, A., & Tammann, G. A. 1985, AJ, 90, 1681
Binggeli, B., Sandage, A., & Tammann, G. A. 1988, ARA&A, 26, 509
Binggeli, B., Tammann, G. A., & Sandage, A. 1987, AJ, 94, 251
Binney, J. 1976, MNRAS, 177, 19
Binney, J. 1978a, Comments Astrophys., 8, 27
Binney, J. 1978b, MNRAS, 183, 501
Binney, J. 2004, MNRAS, 347, 1093
Binney, J., & Tremaine, S. 1987, Galactic Dynamics (Princeton, NJ: Princeton Univ. Press)
Biretta, J. 2005, in The 2005 *HST* Calibration Workshop, ed. A. M. Koekemoer, P. Goudfrooij, & L. L. Dressel (Baltimore, MD: Space Telescope Science Institute), 109
Birnboim, Y., & Dekel, A. 2003, MNRAS, 345, 349
Blanton, E. L., Sarazin, C. L., & McNamara, B. R. 2003a, ApJ, 585, 227
Blanton, M. R., Eisenstein, D., Hogg, D. W., Schlegel, D. J., & Brinkmann, J. 2005, ApJ, 629, 143
Blanton, M. R., et al. 2003b, ApJ, 594, 186
Bohlin, R. C. 2007, Photometric Calibration of the ACS CCD Cameras, Instrument Science Report ACS 2007-06 (Space Telescope Science Institute), http://www.stsci.edu/hst/acs/documents/isrs
Böhringer, H., Briel, U. G., Schwarz, R. A., Voges, W., Hartner, G., & Trümper, J. 1994, Nature, 368, 828
Böhringer, H., Voges, W., Fabian, A. C., Edge, A. C., & Neumann, D. M. 1993, MNRAS, 264, L25
Böhringer, H., et al. 2001, A&A, 365, L181
Böker, T., Sarzi, M., McLaughlin, D. E., van der Marel, R. P., Rix, H.-W., Ho, L. C., & Shields, J. C. 2004, AJ, 127, 105
Bournaud, F., Jog, C. J., & Combes, F. 2007, A&A, 476, 1179
Bower, G. A., Heckman, T. M., Wilson, A. S., & Richstone, D. O. 1997, ApJ, 483, L33
Bower, R. G., Benson, A. J., Malbon, R., Helly, J. C., Frenk, C. S., Baugh, C. M., Cole, S., & Lacey, C. G. 2006, MNRAS, 370, 645
Bower, R. G., Lucey, J. R., & Ellis, R. S. 1992, MNRAS, 254, 601
Boylan-Kolchin, M., Ma, C.-P., & Quataert, E. 2004, ApJ, 613, L37
Boylan-Kolchin, M., Ma, C.-P., & Quataert, E. 2006, MNRAS, 369, 1081
Bregman, J. N. 2007, ARA&A, 45, 221
Buitrago, F., Trujillo, I., Conselice, C. J., Bouwens, R. J., Dickinson, M., & Yan, H. 2008, ApJ, 687, L61
Burkert, A., & Naab, T. 2003, in Lecture Notes in Physics 626, Galaxies and Chaos, ed. G. Contopoulos & N. Voglis (Berlin: Springer), 327
Burkert, A., Naab, T., Johansson, P. H., & Jesseit, R. 2008, ApJ, 685, 897
Burstein, D. 1979, ApJ, 234, 435
Byun, Y.-I., et al. 1996, AJ, 111, 1889
Caldwell, N. 1999, AJ, 118, 1230
Caon, N., Capaccioli, M., & D'Onofrio, M. 1993, MNRAS, 265, 1013
Caon, N., Capaccioli, M., & D'Onofrio, M. 1994, A&AS, 106, 199
Caon, N., Capaccioli, M., & Rampazzo, R. 1990, A&AS, 86, 429
Capaccioli, M., Caon, N., & D'Onofrio, M. 1993, in ESO/EIPC Workshop, Structure, Dynamics and Chemical Evolution of Elliptical Galaxies, ed. I. J. Danziger, W. W. Zeilinger, & K. Kjär (Garching: ESO), 43
Capaccioli, M., Vietri, M., Held, E. V., & Lorenz, H. 1991, ApJ, 371, 535
Capetti, A., & Balmaverde, B. 2006, A&A, 453, 27
Capetti, A., de Ruiter, H. R., Fanti, R., Morganti, R., Parma, P., & Ulrich, M.-H. 2000, A&A, 362, 871
Cappellari, M., & McDermid, R. M. 2005, Class. Quantum Grav., 22, S347
Cappellari, M., et al. 2004, in Carnegie Observatories Astrophysics Series 1, Coevolution of Black Holes and Galaxies, ed. L. C. Ho, http://www.ociw.edu/ociw/symposia/series/symposium1/proceedings.html
Cappellari, M., et al. 2006, MNRAS, 366, 1126
Cappellari, M., et al. 2007, MNRAS, 379, 418
Carlberg, R. G. 1986, ApJ, 310, 593
Carollo, C. M., Stiavelli, M., & Mack, J. 1998, AJ, 116, 68
Carter, D. 1978, MNRAS, 182, 797
Cattaneo, A., Dekel, A., Devriendt, J., Guideroni, B., & Blaizot, J. 2006, MNRAS, 370, 1651
Cattaneo, A., Dekel, A., Faber, S. M., & Guideroni, B. 2008, MNRAS, 389, 567
Cattaneo, A., et al. 2009, Nature, in press
Cawson, M. G. M. 1983, PhD thesis, Univ. Cambridge
Chilingarian, I., Cayette, V., Chemin, L., Durret, F., Laganá, T. F., Adami, C., & Slezak, E. 2007, A&A, 466, L21
Chilingarian, I. V., Cayette, V., Durret, F., Adami, C., Balkowski, C., Chemin, L., Laganá, T. F., & Prugniel, P. 2008, A&A, 486, 85
Chung, A., van Gorkom, J. H., Kenney, J. D. P., & Vollmer, B. 2007, ApJ, 659, L115
Ciotti, L. 1991, A&A, 249, 99
Ciotti, L., & Bertin, G. 1999, A&A, 352, 447
Ciotti, L., & Ostriker, J. P. 2001, ApJ, 551, 131
Côté, P., et al. 2004, ApJS, 153, 223
Côté, P., et al. 2006, ApJS, 165, 57
Côté, P., et al. 2007, ApJ, 671, 1456
Cox, T. J., Jonsson, P., Primack, J. R., & Somerville, R. S. 2006, MNRAS, 373, 1013

Da Costa, G. S. 1994, in ESO/OHP Workshop on Dwarf Galaxies, ed. G. Meylan & P. Prugniel (Garching: ESO), 221
Danforth, C. W., & Shull, J. M. 2008, ApJ, 679, 194
Dasyra, K. M., et al. 2006a, ApJ, 638, 745
Dasyra, K. M., et al. 2006b, ApJ, 651, 835
Dasyra, K. M., et al. 2006c, New Astron. Rev., 50, 720
Davies, R. L., Efstathiou, G., Fall, S. M., Illingworth, G., & Schechter, P. L. 1983, ApJ, 266, 41
Davies, R. L., et al. 2001, ApJ, 548, L33
Davis, L. E., Cawson, M., Davies, R. L., & Illingworth, G. 1985, AJ, 90, 169
Dekel, A., & Birnboim, Y. 2006, MNRAS, 368, 2
Dekel, A., & Birnboim, Y. 2008, MNRAS, 383, 119
Dekel, A., & Silk, J. 1986, ApJ, 303, 39
Dekel, A., & Woo, J. 2003, MNRAS, 344, 1131
De Lucia, G., Springel, V., White, S. D. M., Croton, D., & Kauffmann, G. 2006, MNRAS, 366, 499
D'Onofrio, M., Capaccioli, M., & Caon, N. 1994, MNRAS, 271, 523
de Vaucouleurs, G. 1948, Ann. d'Astrophys., 11, 247
de Vaucouleurs, G. 1959, Handbuch der Physik, 53, 275
de Vaucouleurs, G., & Nieto, J.-L. 1978, ApJ, 220, 449
de Zeeuw, P. T., et al. 2002, MNRAS, 329, 513
Diehl, S., & Statler, T. S. 2008, ApJ, 680, 897
Djorgovski, S. 1992, in Morphological and Physical Classification of Galaxies, ed. G. Longo, M. Capaccioli, & G. Busarello (Dordrecht: Kluwer), 337
Djorgovski, S., & Davis, M. 1987, ApJ, 313, 59
Djorgovski, S., de Carvalho, R., & Han, M.-S. 1988, in The Extragalactic Distance Scale, ed. S. van den Bergh & C. J. Pritchet (San Francisco, CA: ASP), 329
Djorgovski, S., & King, I. R. 1986, ApJ, 305, L61
Downes, D., & Solomon, P. M. 1998, ApJ, 507, 615
Doyon, R., Wells, M., Wright, G. S., Joseph, R. D., Nadeau, D., & James, P. A. 1994, ApJ, 437, L23
Draine, B. T., et al. 2007, ApJ, 663, 866
Dressler, A. 1979, ApJ, 231, 659
Dressler, A., Lynden Bell, D., Burstein, D., Davies, R. L., Faber, S. M., Terlevich, R. J., & Wegner, G. 1987, ApJ, 313, 42
Dressler, A., & Richstone, D. O. 1988, ApJ, 324, 701
Ebisuzaki, T., Makino, J., & Okamura, S. K. 1991, Nature, 354, 212
Ellis, S. C., & O'Sullivan, E. 2006, MNRAS, 367, 627
Elmegreen, D. M., Elmegreen, B. G., Chromey, F. R., & Fine, M. S. 2000, AJ, 120, 733
Emsellem, E., et al. 2004, MNRAS, 352, 721
Emsellem, E., et al. 2007, MNRAS, 379, 401
Fabbiano, G. 2006, ARA&A, 44, 323
Fabbiano, G., Kim, D.-W., & Trinchieri, G. 1992, ApJS, 80, 531
Faber, S. M. 1973, ApJ, 179, 423
Faber, S. M. 2005, in Nearly Normal Galaxies in a ΛCDM Universe, http://astro.ucsc.edu/~nng/webtalks/faber.pdf
Faber, S. M., Dressler, A., Davies, R. L., Burstein, D., Lynden-Bell, D., Terlevich, R., & Wegner, G. 1987, in Nearly Normal Galaxies: From the Planck Time to the Present, ed. S. M. Faber (New York: Springer), 175
Faber, S. M., & Jackson, R. E. 1976, ApJ, 204, 668
Faber, S. M., et al. 1997, AJ, 114, 1771
Faber, S. M., et al. 2007, ApJ, 665, 265
Fabian, A. C., Johnstone, R. M., Sanders, J. S., Conselice, C. J., Crawford, C. S., Gallagher, J. S., & Zweibel, E. 2008, Nature, 454, 968
Fabian, A. C., Sanders, J. S., Allen, S. W., Crawford, C. S., Iwasawa, K., Johnstone, R. M., Schmidt, R. W., & Taylor, G. B. 2003, MNRAS, 344, L43
Fabian, A. C., Sanders, J. S., Taylor, G. B., Allen, S. W., Crawford, C. S., Johnstone, R. M., & Iwasawa, K. 2006, MNRAS, 366, 417
Fabian, A. C., et al. 2000, MNRAS, 318, L65
Fabricant, D., & Gorenstein, P. 1983, ApJ, 267, 535
Farrah, D., Serjeant, S., Efstathiou, A., Rowan-Robinson, M., & Verma, A. 2002, MNRAS, 335, 1163
Ferrarese, L., Ford, H. C., & Jaffe, W. 1996, ApJ, 470, 444
Ferrarese, L., & Merritt, D. 2000, ApJ, 539, L9
Ferrarese, L., van den Bosch, F. C., Ford, H. C., Jaffe, W., & O'Connell, R. W. 1994, AJ, 108, 1598
Ferrarese, L., et al. 2006a, ApJS, 164, 334 (arXiv:astro-ph/0602297)
Ferrarese, L., et al. 2006b, ApJ, 644, L21
Filippenko, A. V., & Ho, L. C. 2003, ApJ, 588, L13
Fisher, D., Franx, M., & Illingworth, G. 1996, ApJ, 459, 110
Forman, W., et al. 2005, ApJ, 635, 894
Forman, W., et al. 2007, ApJ, 665, 1057
Franx, M., Illingworth, G., & Heckman, T. 1989a, AJ, 98, 538
Franx, M., Illingworth, G., & Heckman, T. 1989b, ApJ, 344, 613
Freeman, K. C. 1970, ApJ, 160, 811
Gallagher, J. S., & Ostriker, J. P. 1972, AJ, 77, 288
Garnett, D. R. 2002, ApJ, 581, 1019
Gavazzi, G., Donati, A., Cucciati, O., Sabatini, S., Boselli, A., Davies, J., & Zibetti, S. 2005, A&A, 430, 411
Gebhardt, K., et al. 1996, AJ, 112, 105
Gebhardt, K., et al. 2000, ApJ, 539, L13
Gebhardt, K., et al. 2003, ApJ, 583, 92
Gebhardt, K., et al. 2007, ApJ, 671, 1321
Geha, M., Guhathakurta, P., Rich, R. M., & Cooper, M. C. 2006, AJ, 131, 332
Geha, M., Guhathakurta, P., & van der Marel, R. P. 2002, AJ, 124, 3073
Geha, M., Guhathakurta, P., & van der Marel, R. P. 2003, AJ, 126, 1794
Genzel, R., Lutz, D., Moorwood, A. F. M., Rigopoulou, D., Spoon, H. W. W., Sternberg, A., Sturm, E., & Tran, D. 2000, in Lecture Notes in Physics 548, ISO Surveys of a Dusty Universe, ed. D. Lemke, M. Stickel, & K. Wilke (New York: Springer), 199
Genzel, R., Tacconi, L. J., Rigopoulou, D., Lutz, D., & Tecza, M. 2001, ApJ, 563, 527
Genzel, R., et al. 1998, ApJ, 498, 579
Gerhard, O., Kronawitter, A., Saglia, R. P., & Bender, R. 2001, AJ, 121, 1936
Gerola, H., Seiden, P. E., & Schulman, L. S. 1980, ApJ, 242, 517
González-García, A. C., Aguerri, J. A. L., & Balcells, M. 2005, A&A, 444, 803
Graham, A., & Colless, M. 1997, MNRAS, 287, 221
Graham, A., Lauer, T. R., Colless, M., & Postman, M. 1996, ApJ, 465, 534
Graham, A. W. 2001, AJ, 121, 820
Graham, A. W. 2004, ApJ, 613, L33
Graham, A. W., & Driver, S. P. 2005, PASA, 22, 118
Graham, A. W., & Driver, S. P. 2007, ApJ, 655, 77
Graham, A. W., Erwin, P., Trujillo, I., & Asensio Ramos, A. 2003, AJ, 125, 2951
Graham, A. W., Erwin, P., Trujillo, I., & Asensio Ramos, A. 2004, in Carnegie Observatories Astrophysics Series 1, Coevolution of Black Holes and Galaxies, ed. L. C. Ho, http://www.ociw.edu/ociw/symposia/series/symposium1/proceedings.html
Graham, A. W., & Guzmán, R. 2003, AJ, 125, 2936
Grebel, E. K. 2004, in Carnegie Observatories Astrophysics Series 4, Origin and Evolution of the Elements, ed. A. McWilliam & M. Rauch (Cambridge: Cambridge Univ. Press), 234
Greene, J. E., Barth, A. J., & Ho, L. C. 2006, New Astron. Rev., 50, 739
Greene, J. E., & Ho, L. C. 2004, ApJ, 610, 722
Greene, J. E., & Ho, L. C. 2007, ApJ, 670, 92
Gualandris, A., & Merritt, D. 2008, ApJ, 678, 780
Gunn, J. E. 1987, in Nearly Normal Galaxies: From the Planck Time to the Present, ed. S. M. Faber (New York: Springer), 455
Halliday, C., Davies, R. L., Kuntschner, H., Birkinshaw, M., Bender, R., Saglia, R. P., & Baggley, G. 2001, MNRAS, 326, 473
Hamabe, M. 1982, PASJ, 34, 423
Held, E. V., de Zeeuw, T., Mould, J., & Picard, A. 1992, AJ, 103, 851
Hensler, G., Theis, Ch., & Gallagher, J. S. 2004, A&A, 426, 25
Heyer, I., Richardson, M., Whitmore, B., & Lubin, L. 2004, The Accuracy of WFPC2 Photometric Zeropoints, Instrument Science Report WFPC2 2004-001 (Baltimore, MD: Space Telescope Science Institute), http://www.stsci.edu/hst/wfpc2/documents/isr/wfpc2_isr0401.html
Hibbard, J. E., Guhathakurta, P., van Gorkom, J. H., & Schweizer, F. 1994, AJ, 107, 67
Hibbard, J. E., & van Gorkom, J. H. 1996, AJ, 111, 655
Hill, G. J., Nicklas, H. E., MacQueen, P. J., Tejada, C., Cobos Duenas, F. J., & Mitsch, W. 1998, Proc. SPIE, 3355, 375
Ho, L. C. 2008, ARA&A, 46, 475
Hogg, D. W., et al. 2002, AJ, 124, 646
Hogg, D. W., et al. 2004, ApJ, 601, L29
Holtzman, J. A., Burrows, C. J., Casertano, S., Hester, J. J., Trauger, J. T., Watson, A. M., & Worthey, G. 1995, PASP, 107, 1065
Hopkins, P. F., Cox, T. J., Dutta, S. N., Hernquist, L., Kormendy, J., & Lauer, T. R. 2009a, ApJS, 181, 135
Hopkins, P. F., Cox, T. J., & Hernquist, L. 2008a, ApJ, 689, 17
Hopkins, P. F., Hernquist, L., Cox, T. J., di Matteo, T., Martini, P., Robertson, B., & Springel, V. 2005a, ApJ, 630, 705
Hopkins, P. F., Hernquist, L., Cox, T. J., di Matteo, T., Robertson, B., & Springel, V. 2006a, ApJS, 163, 1
Hopkins, P. F., Hernquist, L., Cox, T. J., Dutta, S. N., & Rothberg, B. 2008b, ApJ, 679, 156
Hopkins, P. F., Hernquist, L., Cox, T. J., Keres, D., & Wuyts, S. 2009b, ApJ, 691, 1424
Hopkins, P. F., Hernquist, L., Cox, T. J., Robertson, B., & Springel, V. 2006b, ApJS, 163, 50
Hopkins, P. F., Hernquist, L., Martini, P., Cox, T. J., Robertson, B., di Matteo, T., & Springel, V. 2005b, ApJ, 625, L71

Hopkins, P. F., Lauer, T. R., Cox, T. J., Hernquist, L., & Kormendy, J. 2009c, ApJS, 181, 486
Hubble, E. 1936, The Realm of the Nebulae (New Haven, CT: Yale Univ. Press)
Illingworth, G. 1977, ApJ, 218, L43
Jaffe, W., Ford, H. C., Ferrarese, L., van den Bosch, F., & O'Connell, R. W. 1993, Nature, 364, 213
Jaffe, W., Ford, H., Ferrarese, L., van den Bosch, F., & O'Connell, R. W. 1996, ApJ, 460, 214
Jaffe, W., Ford, H. C., O'Connell, R. W., van den Bosch, F. C., & Ferrarese, L. 1994, AJ, 108, 1567
Jarrett, T. H., Chester, T., Cutri, R., Schneider, S. E., & Huchra, J. P. 2003, AJ, 125, 525
Jedrzejewski, R., & Schechter, P. L. 1988, ApJ, 330, L87
Jedrzejewski, R., & Schechter, P. L. 1989, AJ, 98, 147
Jedrzejewski, R. I. 1987, MNRAS, 226, 747
Jerjen, H., & Binggeli, B. 1997, in The Second Stromlo Symposium: The Nature of Elliptical Galaxies, ed. M. Arnaboldi, G. S. Da Costa, & P. Saha (San Francisco, CA: ASP), 239
Jerjen, H., Binggeli, B., & Freeman, K. C. 2000, AJ, 119, 593
Jerjen, H., Kalnajs, A., & Binggeli, B. 2000, A&A, 358, 845
Jesseit, R., Naab, T., Peletier, R. F., & Burkert, A. 2007, MNRAS, 376, 997
Joner, M. D., & Taylor, B. J. 1990, PASP, 102, 1004
Jørgensen, I., Franx, M., & Kjærgaard, P. 1996, MNRAS, 280, 167
Joseph, R. D. 1999, Ap&SS, 266, 321
Joseph, R. D., & Wright, G. S. 1985, MNRAS, 214, 87
Kauffmann, G., & Haehnelt, M. 2000, MNRAS, 311, 576
Kauffmann, G., Heckman, T. M., & Best, P. N. 2008, MNRAS, 384, 953
Kauffmann, G., White, S. D. M., & Guideroni, B. 1993, MNRAS, 264, 201
Kauffmann, G., et al. 2003a, MNRAS, 341, 33
Kauffmann, G., et al. 2003b, MNRAS, 341, 54
Kelson, D. D., Zabludoff, A. I., Williams, K. A., Trager, S. C., Mulchaey, J. S., & Bolte, M. 2002, ApJ, 576, 720
Kennicutt, R. C. 1998a, ApJ, 498, 541
Kennicutt, R. C. 1998b, ARA&A, 36, 189
Kereš, D., Katz, N., Weinberg, D. H., & Davé, R. 2005, MNRAS, 363, 2
Khosroshahi, H. G., Jones, L. R., & Ponman, T. J. 2004, MNRAS, 349, 1240
Kim, E., Lee, M. G., & Geisler, D. 2000, MNRAS, 314, 307
King, I. R. 1971, PASP, 83, 199
Klypin, A., Kravtsov, A. V., Valenzuela, O., & Prada, F. 1999, ApJ, 522, 82
Komatsu, E., et al. 2009, ApJS, 180, 330
Kormendy, J. 1973, AJ, 78, 255
Kormendy, J. 1977, ApJ, 218, 333
Kormendy, J. 1980, in ESO Workshop on Two Dimensional Photometry, ed. P. Crane & K. Kjär (Geneva: ESO), 191
Kormendy, J. 1982, in Twelfth Advanced Course of the Swiss Society of Astronomy and Astrophysics, Morphology and Dynamics of Galaxies, ed. L. Martinet & M. Mayor (Sauverny: Geneva Obs.), 113
Kormendy, J. 1984, ApJ, 287, 577
Kormendy, J. 1985a, ApJ, 292, L9
Kormendy, J. 1985b, ApJ, 295, 73
Kormendy, J. 1987a, in IAU Symp. 127, Structure and Dynamics of Elliptical Galaxies, ed. T. de Zeeuw (Dordrecht: Reidel), 17
Kormendy, J. 1987b, in Nearly Normal Galaxies: From the Planck Time to the Present, ed. S. M. Faber (New York: Springer), 163
Kormendy, J. 1988, ApJ, 325, 128
Kormendy, J. 1989, ApJ, 342, L63
Kormendy, J. 1993, Paper Presented at an Aspen Workshop on Galaxy Formation
Kormendy, J. 1999, in Galaxy Dynamics: A Rutgers Symposium, ed. D. Merritt, J. A. Sellwood, & M. Valluri (San Francisco, CA: ASP), 124
Kormendy, J. 2004, in Carnegie Observatories Astrophysics Series 1, Coevolution of Black Holes and Galaxies, ed. L. C. Ho (Cambridge: Cambridge Univ. Press), 1
Kormendy, J. 2009, in Galaxy Evolution: Emerging Insights and Future Challenges, ed. S. Jogee, L. Hao, G. Blanc, & I. Marinova (San Francisco, CA: ASP), in press (arXiv:0812.0806)
Kormendy, J., & Bahcall, J. N. 1974, AJ, 79, 671
Kormendy, J., & Bender, R. 1994, in ESO/OHP Workshop on Dwarf Galaxies, ed. G. Meylan & P. Prugniel (Garching: ESO), 161
Kormendy, J., & Bender, R. 1996, ApJ, 464, L119
Kormendy, J., & Bender, R. 1999, ApJ, 522, 772
Kormendy, J., & Bender, R. 2009, ApJ, 691, L142
Kormendy, J., Bender, R., Evans, A. S., & Richstone, D. 1998, AJ, 115, 1823
Kormendy, J., & Djorgovski, S. 1989, ARA&A, 27, 235
Kormendy, J., & Gebhardt, K. 2001, in The 20th Texas Symposium on Relativistic Astrophysics, ed. J. C. Wheeler & H. Martel (New York: AIP), 363
Kormendy, J., Gebhardt, K., Fisher, D. B., Drory, N., Macchetto, F. D., & Sparks, W. B. 2005, AJ, 129, 2636
Kormendy, J., & Illingworth, G. 1982, ApJ, 256, 460
Kormendy, J., & McClure, R. D. 1993, AJ, 105, 1793
Kormendy, J., & Richstone, D. 1995, ARA&A, 33, 581
Kormendy, J., & Sanders, D. B. 1992, ApJ, 390, L53
Kormendy, J., & Stauffer, J. 1987, in IAU Symp. 127, Structure and Dynamics of Elliptical Galaxies, ed. T. de Zeeuw (Dordrecht: Reidel), 405
Kormendy, J., et al. 1994, in ESO/OHP Workshop on Dwarf Galaxies, ed. G. Meylan & P. Prugniel (Garching: ESO), 147
Kormendy, J., et al. 1996a, in IAU Symp. 171, New Light on Galaxy Evolution, ed. R. Bender & R. L. Davies (Dordrecht: Kluwer), 105
Kormendy, J., et al. 1996b, ApJ, 459, L57
Kormendy, J., et al. 1997, ApJ, 482, L139
Krajnović, D., et al. 2008, MNRAS, 390, 93
Kronawitter, A., Saglia, R. P., Gerhard, O., & Bender, R. 2000, A&AS, 144, 53
Kuntschner, H., et al. 2006, MNRAS, 369, 497
Laine, S., van der Marel, R. P., Lauer, T. R., Postman, M., O'Dea, C. P., & Owen, F. N. 2003, AJ, 125, 478
Landolt, A. U. 1983, AJ, 88, 439
Lauer, T. R. 1985a, ApJS, 57, 473
Lauer, T. R. 1985b, ApJ, 292, 104
Lauer, T. R. 1985c, MNRAS, 216, 429
Lauer, T. R., Faber, S. M., Ajhar, E. A., Grillmair, C. J., & Scowen, P. A. 1998, AJ, 116, 2263
Lauer, T. R., et al. 1992a, AJ, 103, 703
Lauer, T. R., et al. 1992b, AJ, 104, 552
Lauer, T. R., et al. 1993, AJ, 106, 1436
Lauer, T. R., et al. 1995, AJ, 110, 2622
Lauer, T. R., et al. 1996, ApJ, 471, L79
Lauer, T. R., et al. 2002, AJ, 124, 1975
Lauer, T. R., et al. 2005, AJ, 129, 2138
Lauer, T. R., et al. 2007a, ApJ, 662, 808
Lauer, T. R., et al. 2007b, ApJ, 664, 226
Le Floc'h, E., et al. 2005, ApJ, 632, 169
Light, E. S., Danielson, R. E., & Schwarzschild, M. 1974, ApJ, 194, 257
Lin, D. N. C., & Faber, S. M. 1983, ApJ, 266, L21
Lisker, T., & Fuchs, B. 2009, A&A, in press (arXiv:0903.2474)
Lisker, T., Glatt, K., Westera, P., & Grebel, E. K. 2006, AJ, 132, 2432
Liu, Y., Zhou, X., Ma, J., Wu, H., Yang, Y., Li, J., & Chen, J. 2005, AJ, 129, 2628
Lugger, P. M., Cohn, H. N., Cederbloom, S. E., Lauer, T. R., & McClure, R. D. 1992, AJ, 104, 83
Lutz, D., Spoon, H. W. W., Rigopoulou, D., Moorwood, A. F. M., & Genzel, R. 1998, ApJ, 505, L103
Lutz, D., et al. 1996, A&A, 315, L137
Magorrian, J., et al. 1998, AJ, 115, 2285
Makino, J., & Ebisuzaki, T. 1996, ApJ, 465, 527
Makino, J., & Funato, Y. 2004, ApJ, 602, 93
Martel, A. R., Turner, N. J., Sparks, W. B., & Baum, S. A. 2000, ApJS, 130, 267
Mateo, M. 1998, ARA&A, 36, 435
Matteucci, F. 1994, A&A, 288, 57
Matthews, T. A., Morgan, W. W., & Schmidt, M. 1964, ApJ, 140, 35
McClure, R. D., et al. 1989, PASP, 101, 1156
McConnachie, A. W., & Irwin, M. J. 2006, MNRAS, 365, 1263
McDermid, R. M., et al. 2006, MNRAS, 373, 906
McNamara, B. R., & Nulsen, P. E. J. 2007, ARA&A, 45, 117
McNamara, B. R., Nulsen, P. E. J., Wise, M. W., Rafferty, D. A., Carilli, C., Sarazin, C. L., & Blanton, E. L. 2005, Nature, 433, 45
McNamara, B. R., et al. 2000, ApJ, 534, L135
Mei, S., et al. 2007, ApJ, 655, 144
Merritt, D. 2006, ApJ, 648, 976
Merritt, D., & Ferrarese, L. 2001, MNRAS, 320, L30
Merritt, D., Mikkola, S., & Szell, A. 2007, ApJ, 671, 53
Merritt, D., Milosavljević, M., Favata, M., Hughes, S. A., & Holz, D. E. 2004, ApJ, 607, L9
Michard, R. 1985, A&AS, 59, 205
Mihos, J. C., Harding, P., Feldmeier, J., & Morrison, H. 2005, ApJ, 631, L41
Mihos, J. C., & Hernquist, L. 1994, ApJ, 437, L47
Mihos, J. C., & Hernquist, L. 1996, ApJ, 464, 641
Milosavljević, M., & Merritt, D. 2001, ApJ, 563, 34
Milosavljević, M., Merritt, D., Rest, A., & van den Bosch, F. C. 2002, MNRAS, 331, L51
Möllenhoff, C., & Bender, R. 1987a, in IAU Symp. 127, Structure and Dynamics of Elliptical Galaxies, ed. T. de Zeeuw (Dordrecht: Reidel), 409
Möllenhoff, C., & Bender, R. 1987b, A&A, 174, 63

Moore, B., Katz, N., Lake, G., Dressler, A., & Oemler, A. 1996, Nature, 379, 613
Moore, B., Lake, G., & Katz, N. 1998, ApJ, 495, 139
Morelli, L., et al. 2004, MNRAS, 354, 753
Morgan, W. W., & Lesh, J. R. 1965, ApJ, 142, 1364
Naab, T., & Burkert, A. 2003, ApJ, 597, 893
Naab, T., Burkert, A., & Hernquist, L. 1999, ApJ, 523, L133
Naab, T., Burkert, A., Johansson, P. H., & Jesseit, R. 2008, in IAU Symp. 245, Formation and Evolution of Galaxy Bulges, ed. M. Bureau, E. Athanassoula, & B. Barbuy (Cambridge: Cambridge Univ. Press), 47
Naab, T., Jesseit, R., & Burkert, A. 2006a, MNRAS, 372, 839
Naab, T., Johansson, P. H., Ostriker, J. P., & Efstathiou, G. 2007, ApJ, 658, 710
Naab, T., Khochfar, S., & Burkert, A. 2006b, ApJ, 636, L81
Naab, T., & Ostriker, J. P. 2009, ApJ, 690, 1452
Naab, T., & Trujillo, I. 2006, MNRAS, 369, 625
Nardini, E., Risaliti, G., Salvati, M., Sani, E., Imanishi, M., Marconi, A., & Maiolino, R. 2008, MNRAS, 385, L130
Navarro, J. F. 1990, MNRAS, 242, 311
Navarro, J. F., Eke, V. R., & Frenk, C. S. 1996, MNRAS, 283, L72
Netzer, H., et al. 2007, ApJ, 666, 806
Nieto, J.-L., & Bender, R. 1989, A&A, 215, 266
Nieto, J.-L., Bender, R., & Surma, P. 1991, A&A, 244, L37
Nipoti, C., & Binney, J. 2007, MNRAS, 382, 1481
Nipoti, C., Londrillo, P., & Ciotti, L. 2003, MNRAS, 342, 501
Nowak, N., Saglia, R. P., Thomas, J., Bender, R., Pannella, M., Gebhardt, K., & Davies, R. I. 2007, MNRAS, 379, 909
Oemler, A. 1976, ApJ, 209, 693
Ostriker, J. P. 1980, Comments Astrophys., 8, 177
Ostriker, J. P., & Ciotti, L. 2005, Phil. Trans. R. Soc. A, 363, 667
O'Sullivan, E., Forbes, D. A., & Ponman, T. J. 2001, MNRAS, 328, 461
Pasquali, A., van den Bosch, F. C., Mo, H. J., Yang, X., & Somerville, R. 2009, MNRAS, 394, 38
Paturel, G., Petit, C., Prugniel, Ph., Theureau, G., Rousseau, J., Brouty, M., Dubois, P., & Cambrésy, L. 2003, A&A, 412, 45
Pedraz, S., Gorgas, J., Cardiel, N., Sánchez-Blázquez, P., & Guzmán, R. 2002, MNRAS, 332, L59
Peiris, H. V., & Tremaine, S. 2003, ApJ, 599, 237
Peletier, R. F., Davies, R. L., Illingworth, G. D., Davis, L. E., & Cawson, M. 1990, AJ, 100, 1091
Pellegrini, S. 1999, A&A, 351, 487
Pellegrini, S. 2005, MNRAS, 364, 169
Peterson, B. M., et al. 2005, ApJ, 632, 799
Press, W. H., Flannery, B. P., Teukolsky, S. A., & Vetterling, W. T. 1986, Confidence Limits on Estimated Model Parameters, in Numerical Recipes: The Art of Scientific Computing (Cambridge: Cambridge Univ. Press), chapter 14.5
Prugniel, Ph., & Héraudeau, Ph. 1998, A&AS, 128, 299
Quillen, A. C., Bower, G. A., & Stritzinger, M. 2000, ApJS, 128, 85
Quinlan, G. D. 1996, NewA, 1, 35
Quinlan, G. D., & Hernquist, L. 1997, New Astron., 2, 533
Racine, R., & McClure, R. D. 1989, PASP, 101, 731
Ravindranath, S., Ho, L. C., & Filippenko, A. V. 2002, ApJ, 566, 801
Ravindranath, S., Ho, L. C., Peng, C. Y., Filippenko, A. V., & Sargent, W. L. W. 2001, AJ, 122, 653
Renzini, A. 2006, ARA&A, 44, 141
Rest, A., van den Bosch, F. C., Jaffe, W., Tran, H., Tsvetanov, Z., Ford, H. C., Davies, J., & Schafer, J. 2001, AJ, 121, 2431
Richstone, D. O. 1976, ApJ, 204, 642
Rigopoulou, D., Spoon, H. W. W., Genzel, R., Lutz, D., Moorwood, A. F. M., & Tran, Q. D. 1999, AJ, 118, 2625
Rix, H.-W., & White, S. D. M. 1990, ApJ, 362, 52
Rix, H.-W., & White, S. D. M. 1992, MNRAS, 254, 389
Robertson, B., Cox, T. J., Hernquist, L., Franx, M., Hopkins, P. F., Martini, P., & Springel, V. 2006, ApJ, 641, 21
Rothberg, B., & Joseph, R. D. 2004, AJ, 128, 2098
Rothberg, B., & Joseph, R. D. 2006, AJ, 131, 185
Saglia, R. P, Bender, R., & Dressler, A. 1993, A&A, 279, 75
Saito, M. 1979a, PASJ, 31, 181
Saito, M. 1979b, PASJ, 31, 193
Sandage, A. 1961, The Hubble Atlas of Galaxies (Washington, DC: Carnegie Institution of Washington)
Sandage, A., & Bedke, J. 1994, The Carnegie Atlas of Galaxies (Washington, DC: Carnegie Institution of Washington)
Sandage, A., & Binggeli, B. 1984, AJ, 89, 919
Sandage, A., Binggeli, B., & Tammann, G. A. 1985a, in ESO Workshop on the Virgo Cluster, ed. O.-G. Richter & B. Binggeli (Garching: ESO), 239
Sandage, A., Binggeli, B., & Tammann, G. A. 1985b, AJ, 90, 1759
Sanders, D. B. 1999, Ap&SS, 266, 331
Sanders, D. B., & Mirabel, I. F. 1996, ARA&A, 34, 749
Sanders, D. B., Soifer, B. T., Elias, J. H., Madore, B. F., Matthews, K., Neugebauer, G., & Scoville, N. Z. 1988a, ApJ, 325, 74
Sanders, D. B., Soifer, B. T., Elias, J. H., Neugebauer, G., & Matthews, K. 1988b, ApJ, 328, L35
Sanders, J. S., & Fabian, A. C. 2007, MNRAS, 381, 1381
Sarzi, M., Rix, H.-W., Shields, J. C., Rudnick, G., Ho, L. C., McIntosh, D. H., Filippenko, A. V., & Sargent, W. L. W. 2001, ApJ, 550, 65
Scannapieco, E., Silk, J., & Bouwens, R. 2005, ApJ, 635, L13
Schild, R. E. 1983, PASP, 95, 1021
Schlegel, D. J., Finkbeiner, D. P., & Davis, M. 1998, ApJ, 500, 525
Schmidt, M. 1959, ApJ, 129, 243
Schombert, J. M. 1986, ApJS, 60, 603
Schombert, J. M. 1987, ApJS, 64, 643
Schombert, J. M. 1988, ApJ, 328, 475
Schweitzer, M., et al. 2006, ApJ, 649, 79
Schweizer, F. 1980, ApJ, 237, 303
Schweizer, F. 1982, ApJ, 252, 455
Schweizer, F. 1987, in Nearly Normal Galaxies: From the Planck Time to the Present, ed. S. M. Faber (New York: Springer), 18
Schweizer, F. 1990, in Dynamics and Interactions of Galaxies, ed. R. Wielen (New York: Springer), 60
Schweizer, F. 1996, AJ, 111, 109
Schweizer, F. 1998, in 26th Advanced Course of the Swiss Society of Astronomy and Astrophysics, Galaxies: Interactions and Induced Star Formation, ed. D. Friedli, L. Martinet, & D. Pfenniger (New York: Springer), 105
Schweizer, F., & Seitzer, P. 1992, AJ, 104, 1039
Scorza, C., & Bender, R. 1995, A&A, 293, 20
Scorza, C., Bender, R., Winkelmann, C., Capaccioli, M., & Macchetto, D. F. 1998, A&AS, 131, 265
Sérsic, J. L. 1968, Atlas de Galaxias Australes (Cordoba: Observatorio Astronomico, Univ. Cordoba)
Shields, J. C., Walcher, C. J., Böker, T., Ho, L. C., Rix, H.-W., & van der Marel, R. P. 2008, ApJ, 682, 104
Silk, J. 2005, MNRAS, 364, 1337
Silk, J., & Rees, M. J. 1998, A&A, 331, L1
Simien, F., & Prugniel, Ph. 1997, A&AS, 126, 15
Simien, F., & Prugniel, Ph. 1998, A&AS, 131, 287
Simien, F., & de Vaucouleurs, G. 1986, ApJ, 302, 564
Sirianni, M., et al. 2005, PASP, 117, 1049
Skrutskie, M. F., et al. 2006, AJ, 131, 1163
Smith, J. A., et al. 2002, AJ, 123, 2121
Somerville, R. S., & Primack, J. R. 1999, MNRAS, 310, 1087
Spoon, H. W. W., Marshall, J. A., Houck, J. R., Elitzur, M., Hao, L., Armus, L., Brandl, B. R., & Charmandaris, V. 2007, ApJ, 654, L49
Springel, V. 2000, MNRAS, 312, 859
Springel, V., Di Matteo, T., & Hernquist, L. 2005, ApJ, 620, L79
Springel, V., & Hernquist, L. 2005, ApJ, 622, L9 (arXiv:astro-ph/041379)
Statler, T. S. 1999, ApJ, 524, L87
Statler, T. S., Emsellem, E., Peletier, R. F., & Bacon, R. 2004, MNRAS, 353, 1
Statler, T. S., King, I. R., Crane, P., & Jedrzejewski, R. I. 1999, AJ, 117, 894
Steinmetz, M., & Navarro, J. F. 2002, New Astron., 7, 155
Stoughton, C., et al. 2002, AJ, 123, 485
Stover, R. J. 1988, in Instrumentation for Ground-Based Optical Astronomy: Present and Future, ed. L. B. Robinson (New York: Springer), 443
Strateva, I., et al. 2001, AJ, 122, 1861
Surma, P., & Bender, R. 1995, A&A, 298, 405
Tacconi, L. J., Genzel, R., Lutz, D., Rigopoulou, D., Baker, A. J., Iserlohe, C., & Tecza, M. 2002, ApJ, 580, 73
Terndrup, D. M. 1993, in The Minnesota Lectures on the Structure and Dynamics of the Milky Way, ed. R. M. Humphreys (San Francisco, CA: ASP), 9
Thomas, D., Bender, R., Hopp, U., Maraston, C., & Greggio, L. 2003, Ap&SS, 284, 599
Thomas, D., Brimioulle, F., Bender, R., Hopp, U., Greggio, L., Maraston, C., & Saglia, R. P. 2006, A&A, 445, L19
Thomas, D., Greggio, L., & Bender, R. 1998, MNRAS, 296, 119
Thomas, D., Greggio, L., & Bender, R. 1999, MNRAS, 302, 537
Thomas, D., Maraston, C., & Bender, R. 2002, Ap&SS, 281, 371
Thomas, D., Maraston, C., Bender, R., & Mendez de Oliveira, C. 2005, ApJ, 621, 673
Thomas, J., Saglia, R. P., Bender, R., Thomas, D., Gebhardt, K., Magorrian, J., Corsini, E. M., & Wegner, G. 2007, MNRAS, 382, 657
Thornton, C. E., Barth, A. J., Ho, L. C., Rutledge, R. E., & Greene, J. E. 2008, ApJ, 686, 892

Tonry, J. L., Dressler, A., Blakeslee, J. P., Ajhar, E. A., Fletcher, A. B., Luppino, G. A., Metzger, M. R., & Moore, C. B. 2001, ApJ, 546, 681
Toomre, A. 1964, ApJ, 139, 1217
Toomre, A. 1977, in The Evolution of Galaxies and Stellar Populations, ed. B. M. Tinsley & R. B. Larson (New Haven: Yale Univ. Obs.), 401
Toomre, A., & Toomre, J. 1972, ApJ, 178, 623
Tran, Q. D., et al. 2001, ApJ, 552, 527
Tremaine, S. 1981, in The Structure and Evolution of Normal Galaxies, ed. S. M. Fall & D. Lynden Bell (Cambridge: Cambridge Univ. Press), 67
Tremaine, S. 1995, AJ, 110, 628
Tremaine, S., et al. 2002, ApJ, 574, 740
Tremblay, B., & Merritt, D. 1996, AJ, 111, 2243
Tremonti, C. A., et al. 2004, ApJ, 613, 898
Trujillo, I., Asensio Ramos, A., Rubiño-Martín, J. A., Graham, A. W., Aguerri, J. A. L., Cepa, J., & Gutiérrez, C. M. 2002, MNRAS, 333, 510
Trujillo, I., Erwin, P., Asensio Ramos, A., & Graham, A. W. 2004, AJ, 127, 1917
Trujillo, I., Graham, A. W., & Caon, N. 2001, MNRAS, 326, 869
van Albada, T. S. 1982, MNRAS, 201, 939
van den Bosch, R. C. E., van de Ven, G., Verolme, E. K., Cappellari, M., & de Zeeuw, P. T. 2008, MNRAS, 385, 647
van der Marel, R. P. 1991, MNRAS, 253, 710
van der Wel, A., Holden, B. P., Zirm, A. W., Franx, M., Rettura, A., Illingworth, G. D., & Ford, H. C. 2008, ApJ, 688, 48
van Dokkum, P. G. 2005, AJ, 130, 2647
van Dokkum, P. G., & Franx, M. 1995, AJ, 110, 2027
van Zee, L., Barton, E. J., & Skillman, E. D. 2004a, AJ, 128, 2797
van Zee, L., Skillman, E. D., & Haynes, M. P. 2004b, AJ, 128, 121
Vega, O., Clemens, M. S., Bressan, A., Granato, G. L., Silva, L., & Panuzzo, P. 2008, A&A, 484, 631
Veilleux, S., Cecil, G., & Bland-Hawthorn, J. 2005, ARA&A, 43, 769
Veilleux, S., et al. 2006, ApJ, 643, 707
Verdoes Kleijn, G. A., Baum, S. A., de Zeeuw, P. T., & O'Dea, C. P. 1999, AJ, 118, 2592
Véron-Cetty, M.-P., & Véron, P. 1988, A&A, 204, 28
Wagner, S. J., Bender, R., & Möllenhoff, C. 1988, A&A, 195, L5
Wehner, E. H., & Harris, W. E. 2006, ApJ, 644, L17
White, S. D. M., & Rees, M. J. 1978, MNRAS, 183, 341
Wirth, A., & Gallagher, J. S. 1984, ApJ, 282, 85
Worthey, G. 2004, AJ, 128, 2826
Worthey, G., Faber, S. M., & Gonzalez, J. J. 1992, ApJ, 398, 69